

**CFD Determination of Fluid and Geometry Related
Localized Heat Transfer Phenomena for
Supercritical Water Flow**

By

Amjad Farah

Thesis Submitted in Partial Fulfillment of the Requirements
for the Degree of Doctor of Philosophy

In

The Faculty of Energy Systems and Nuclear Science

Nuclear Engineering

University of Ontario Institute of Technology

April, 2017

©Amjad Farah, 2017

Executive Summary

The proposed concept of Supercritical Water-cooled Reactor (SCWR) as part of the Generation IV International Forum aims to improve the thermal efficiency over current power plants by utilizing cooling water at pressures and temperature above the critical point. At supercritical conditions, however, the properties of the fluid can vary rapidly in response to changes in temperature and pressure, and without a phase change. One example is the specific heat, which exhibits a sharp peak at a point defined as the pseudocritical temperature.

Computational Fluid Dynamics (CFD) is a numerical approach to model fluids in multidimensional space using the Navier-Stokes equations and databases of fluid properties to arrive at a full simulation of a fluid dynamics and heat transfer system. Turbulence models employed in CFD are a set of equations that determine the turbulence transport terms in the mean flow equations. They are based on hypotheses about the process of turbulence, and as such require empirical input in the form of constants or functions, in order to achieve closure.

This work is conducted to further develop an understanding of supercritical water (SCW) flow by analyzing the flow- and geometry-dependent localized phenomena under supercritical conditions using CFD turbulence models. The numerical study employed the Realizable k - ϵ and the SST k - ω turbulence models. The created meshes are three dimensional to capture the multi-dimensional effects of SCW heat transfer phenomena.

In the first part of the study, the turbulent Pr number effect on SCW heat transfer characteristics is determined by analyzing changes in fluid properties such as temperature profiles, turbulence intensity, and velocity in response to varying the turbulent Pr values in the CFD models. This investigation has shown the energy turbulent Pr to have the most effect on improving SCW heat transfer simulation

results under the deteriorated heat transfer regime, by affecting the turbulence production in the fluid due to buoyancy forces. Buoyancy forces were also studied in downward flow under the same conditions and were shown to reduce the deterioration in heat transfer observed in upward flow.

The second part involved an investigation of fluid property effects in complex geometries to determine important flow parameters that capture localized flow phenomena effects. Two geometries are considered: an annular channel with helical fins, and a tube with a sudden area change. The helicity of the first geometry did not appear to induce additional turbulence in the flow, compared to bare geometries. On the other hand, the sudden area change introduced large levels of turbulence, and while it dissipated quickly, it did show an enhancement in the heat transfer and lowered the outlet wall temperatures. These results can be used as a design input for SCWR fuel geometry design.

As a result, this study contributes to the understanding of the SCW heat transfer fundamentals under normal and deteriorated regimes in bare and complex geometries, and identifies the areas of improvement in the related experimental work. Significant experimental work is needed to verify the findings of CFD simulations, and to provide empirical input into the turbulence models.

Acknowledgements

I am deeply grateful to my supervisors, Dr. Glenn Harvel and Dr. Igor Pioro, for their constant support and encouragement in my research and the writing of this thesis.

I would like to thank my colleagues Jeffrey Samuel, Adam Lipchitz, Juan Carlos Jouvin, Neema Kakkuzhiyil, Khalil Sidawi, John Zoidberg, Kelvin Seto and Jelena Vucicevic for their support, valuable insight, and discussions. I am also indebted to the members of the Nuclear Design Laboratory at UOIT for giving me the perfect working atmosphere.

To Dr. Glenn Harvel, thank you for your guidance, support and assistance for the entire duration this work. Thank you for your valuable discussions, for providing me with ideas, materials, and most importantly for the opportunity.

My supervisory committee Dr. Eleodor Nichita and Dr. Jennifer McKellar for your valuable discussions, your guidance and your support.

Financial support from the NSERC/NRCan/AECL Generation IV Energy Technologies Program and NSERC Discovery Grants is gratefully acknowledged.

Finally, I am thankful to my family; my parents, Karim Farah and Fadia Asber, and my brother, Loujain Farah for helping me through the difficult times and for being a source of inspiration during the course of my research and throughout my university education.

Table of Contents

List of Tables	iv
List of Figures	v
Nomenclature	xv
Glossary	xvii
Chapter 1: Introduction	1
1.1 Computational Fluid Dynamics.....	3
1.2 Objectives	4
Chapter 2: Literature Review.....	5
2.1 Generation IV Reactors.....	5
2.2 Physical Properties of SCW	5
2.3 Heat Transfer in Supercritical Fluids	7
2.4 Empirical Correlations.....	9
2.5 CFD Theory for Fluid Flow	12
2.6 CFD for SCW Flow.....	17
2.6.1 RANS - Two-Equation Models.....	19
2.6.2 Boundary Layer Resolution.....	23
2.7 Turbulent Prandtl Number.....	25
2.8 Integration of Numerical Model in Computational Domain.....	31
2.9 Geometry Considerations	33
2.9.1 Nuclear Fuel Bundle.....	33
2.9.2 Endplate Geometry	34
2.9.3 Other Studies	36
Chapter 3: Methodology.....	37
3.1 Bare Tube Experimental Dataset and Test Facility.....	38
3.2 Annular Channel Experimental Dataset and Test Facility.....	44
3.3 Meshing Methodology	47
3.3.1 Bare Tube Geometry and Mesh.....	48
3.3.2 Annular Channel with Helical Fins Geometry and Mesh.....	54
3.3.3 Bare Tube with Sudden Area Change Geometry and Mesh.....	64
3.4 FLUENT Methodology.....	68

3.4.1	Viscous Models.....	68
3.4.2	Material Properties.....	70
3.4.3	Solution Methods and Controls	72
3.4.4	Convergence	74
3.4.5	Test Matrices for Simulations	75
Chapter 4:	Simple Tube Results.....	86
4.1	Assessment of Simple Tube 3D Flow and Thermal Distributions	90
4.1.1	NHT Regime Results	90
4.1.2	DHT Regime Results.....	97
4.1.3	Subcritical Flow Results	110
4.2	Turbulent Prandtl Number Variations Results.....	115
4.3	Downward flow results.....	133
4.4	Summary	138
Chapter 5:	Annular Channel with Helical Fins.....	139
5.1	Case 1 - SST Model, Free Mesh, Heated Fins	141
5.2	Case 1 - SST Model, 3D Blocking Mesh.....	167
5.3	Case 1 - RKE Model, Free Mesh	172
5.4	Case 1 - Straight Fins, SST Model, Free Mesh	182
5.5	Case 1 - No Fins, SST Model, Free Mesh.....	189
5.6	Case 5 - SST Model, Free Mesh.....	206
5.7	Sources of Uncertainties.....	214
Chapter 6:	Sudden Area Change Geometry	217
Chapter 7:	Concluding Remarks and Recommendations.....	236
7.1	Concluding Remarks	236
7.2	Contribution to Knowledge.....	239
7.3	Future Work.....	239
References	241
Appendix A:	Summary of Publications and Awards	248
Relevant Publications	248
Awards, Scholarships and Research Grants.....		249
Appendix B:	Bare Tube Results - NHT, RKE Model	250

Appendix C: Turbulent Pr number variations for RKE and SST	255
Appendix D: Axial locations of thermocouples in the helically finned annular flow channel.....	257

List of Tables

Table 3-1: Kirillov et al. Dataset Ranges [52].....	41
Table 3-2: Uncertainties of primary parameters [52].....	41
Table 3-3: Maximum Uncertainties of Measured and Calculated Parameters [55]	46
Table 3-4: Test Matrix for Simple Tube Simulations, RKE and SST Models.....	75
Table 3-5: Standard and Modified Values for RKE Turbulent Pr Numbers.....	76
Table 3-6: Standard and Modified Values for SST Turbulent Pr Numbers	76
Table 3-7: Test Matrix for Turbulent Pr variations study, RKE and SST Models. P: 24.1 MPa, $G = 1496 \text{ kg/m}^2\text{s}$, $q = 1235 \text{ kW/m}^2$, $L = 1\text{-}3 \text{ m}$, $T_{\text{in}} = 366^\circ\text{C}$, $T_{\text{out}} = 386^\circ\text{C}$	76
Table 3-8: Test matrix for annular channel with helical fins simulations	80
Table 3-9: Test Matrix for Tube with Sudden Area Change Simulations, RKE and SST Models	85
Table 5-1: Operating Parameters for Annular Channel with Helical Fins Experiments.	139
Table 5-2: Specific heat variation with temperature at a constant pressure	213
Table 6-1: Test matrix of tube with orifice geometry simulations.....	233

List of Figures

Figure 2-1: Thermo-physical properties of water in the supercritical conditions.....	6
Figure 2-2: Flow layers from the wall to the fully developed stream according to Y^+ values [27]	24
Figure 2-3: Solution domain division into control volumes	32
Figure 2-4: CANDU fuel bundle geometry, courtesy of W. Peiman	33
Figure 2-5: Stair-step mesh study on endplate geometry [50]	34
Figure 2-6: Visualization of flow through two half-bundles with an endplate in the center of the flow length [50].....	35
Figure 2-7: Cross-sectional flow visualization through endplate geometry [50]	35
Figure 2-8: An Example of a Subchannel CFD analysis for SCWR rod bundle [51].....	36
Figure 2-9: An Example of a 3-Rod Bundle Inter-subchannel CFD analysis [52]	36
Figure 3-1: SKD-1 loop schematic : 1-Circulating pump, 2-mechanical filter, 3-regulating valves, 4-electrical heater, 5-flowmeter, 6-test section, 7-throttling valve, 8-mixer-cooler, 9-discharge tank, 10-heat exchangers-main coolers, 11-feedwater tank, 12-volume compensator, and 13-feedwater pump [53].....	40
Figure 3-2: Sample experimental run from the Kirillov et al. dataset [53], with bulk-fluid, wall temperatures and heat transfer coefficients.....	43
Figure 3-3: General Schematic of SCW Experimental Setup [56].	44
Figure 3-4: Illustration of Heated Central Rod Annular Channel [56]	45
Figure 3-5: Sample Experimental Run from Razumovskiy et al. [56].....	47
Figure 3-6: A graphical representation of the mesh geometry (not to scale).....	48
Figure 3-7: 3D Bounding Box Block for the Geometry.....	50
Figure 3-8: Modifying the Blocks to Fit the Geometry.....	51
Figure 3-9: ICEM CFD mesh for 1/8 tube geometry	52
Figure 3-10: Mesh view in the XY plane	53
Figure 3-11: Boundary layer for mesh.....	54
Figure 3-12: Cross Sectional View and Dimensions of the Annular Channel Geometry [56].....	55
Figure 3-13: A See-through View of the Annular Channel Geometry	56
Figure 3-14: Cut-plane View of the Annular Channel Geometry. Solid is Flow Volume. .	56
Figure 3-15: The Geometry Imported by ICEM CAD Interface.....	57
Figure 3-16: 3D blocking of the Annular Channel Geometry	58
Figure 3-17: Block Edges for the Annular Channel. Red colored edges have matching curves in the geometry, and black edges have no association.	59
Figure 3-18: 3D Mesh (3D blocking) of Annular Channel with Helical Ribs - Front View	60
Figure 3-19: 3D Mesh (3D blocking) of Annular Channel with Helical Ribs- Isometric View	60
Figure 3-20: 3D Mesh (3D blocking) of Annular Channel with Helical Ribs - Close-up View	61

Figure 3-21: 3D Mesh (Free Multi-zone blocking) of Annular Channel with Helical Ribs - Front View.....	62
Figure 3-22: 3D Mesh (Free Multi-zone blocking) of Annular Channel with Helical Ribs- Isometric View	62
Figure 3-23: 3D Mesh (Free Multi-zone blocking) of Annular Channel with Helical Ribs - Close-up View	63
Figure 3-24: Inflation Parameters on a Free Mesh of Annular Channel with Helical Ribs - Close-up View	64
Figure 3-25: Graphical representation of the 3-D mesh for vertical tube with an orifice. (not to scale)	66
Figure 3-26: (a) Front and (b) Side Views of the Area Change Geometry and its Dimensions	67
Figure 3-27: ICEM CFD Mesh for 1/8 Tube Geometry with a Sudden Area Change.....	68
Figure 3-28: Illustration of the finned rod dimensions	78
Figure 4-1: An experimental dataset sample from Kirillov et al. dataset [53] showing NHT, and the simulation result of RKE and SST models for wall temperatures and heat transfer coefficients.....	87
Figure 4-2: An experimental dataset sample from Kirillov et al. dataset [53] showing DHT, and the simulation result of RKE and SST models for wall temperatures and heat transfer coefficients.....	89
Figure 4-3: Reference case from Kirillov et al. dataset [53] for the 3D mesh of a simple tube geometry	91
Figure 4-4: 3D Fluid temperature plot for a case with: $P = 24$ MPa, $G = 1002$ kg/m ² s, and $q = 391$ kW/m ² , using the SST model (NHT).....	92
Figure 4-5: 3D density plot for a case with: $P = 24$ MPa, $G = 1002$ kg/m ² s, and $q = 391$ kW/m ² , using the SST model.....	93
Figure 4-6: 3D viscosity plot for a case with $P = 24$ MPa, $G = 1002$ kg/m ² s, and $q = 391$ kW/m ² , using the SST model.....	93
Figure 4-7: 3D specific heat plot for a case with: $P = 24$ MPa, $G = 1002$ kg/m ² s, and $q = 391$ kW/m ² , using the SST model.....	94
Figure 4-8: 3D turbulent kinetic energy plot for a case with $P = 24$ MPa, $G = 1002$ kg/m ² s, and $q = 391$ kW/m ² , using the SST model	94
Figure 4-9: 3D turbulence intensity plot for a case with: $P = 24$ MPa, $G = 1002$ kg/m ² s, and $q = 391$ kW/m ² , using the SST model.....	96
Figure 4-10: DHT case for the 3D mesh of a simple tube geometry	98
Figure 4-11: 3D Temperature plot for a case with: $P = 24.1$ MPa, $G = 1496$ kg/m ² s, and $q = 1235$ kW/m ² , using the RKE model (DHT).....	99
Figure 4-12: 3D Temperature plot for a case with: $P = 24.1$ MPa, $G = 1496$ kg/m ² s, and $q = 1235$ kW/m ² , using the SST model (DHT)	100
Figure 4-13: 3D Density plot for a case with: $P = 24.1$ MPa, $G = 1496$ kg/m ² s, and $q = 1235$ kW/m ² , using the RKE model.....	101

Figure 4-14: 3D Density plot for a case with: $P = 24.1$ MPa, $G = 1496$ kg/m ² s, and $q = 1235$ kW/m ² , using the SST model.....	101
Figure 4-15: 3D Viscosity plot for a case with: $P = 24.1$ MPa, $G = 1496$ kg/m ² s, and $q = 1235$ kW/m ² , using the RKE model.....	103
Figure 4-16: 3D Viscosity plot for a case with: $P = 24.1$ MPa, $G = 1496$ kg/m ² s, and $q = 1235$ kW/m ² , using the SST model.....	103
Figure 4-17: 3D Velocity plot for a case with: $P = 24.1$ MPa, $G = 1496$ kg/m ² s, and $q = 1235$ kW/m ² , using the RKE model.....	104
Figure 4-18: 3D Velocity plot for a case with: $P = 24.1$ MPa, $G = 1496$ kg/m ² s, and $q = 1235$ kW/m ² , using the SST model.....	104
Figure 4-19: 3D Specific heat plot for a case with: $P = 24.1$ MPa, $G = 1496$ kg/m ² s, and $q = 1235$ kW/m ² , using the RKE model.....	105
Figure 4-20: 3D Specific heat plot for a case with: $P = 24.1$ MPa, $G = 1496$ kg/m ² s, and $q = 1235$ kW/m ² , using the SST model.....	105
Figure 4-21: 3D Thermal conductivity plot for a case with: $P = 24.1$ MPa, $G = 1496$ kg/m ² s, and $q = 1235$ kW/m ² , using the RKE model.....	106
Figure 4-22: 3D Thermal conductivity plot for a case with: $P = 24.1$ MPa, $G = 1496$ kg/m ² s, and $q = 1235$ kW/m ² , using the SST model.....	106
Figure 4-23: 3D Turbulent kinetic energy plot for a case with: $P = 24.1$ MPa, $G = 1496$ kg/m ² s, and $q = 1235$ kW/m ² , using the RKE model.....	108
Figure 4-24: 3D Turbulent intensity plot for a case with: $P = 24.1$ MPa, $G = 1496$ kg/m ² s, and $q = 1235$ kW/m ² , using the RKE model.....	108
Figure 4-25: 3D Turbulent kinetic energy plot for a case with: $P = 24.1$ MPa, $G = 1496$ kg/m ² s, and $q = 1235$ kW/m ² , using the SST model.....	109
Figure 4-26: 3D Turbulence intensity plot for a case with: $P = 24.1$ MPa, $G = 1496$ kg/m ² s, and $q = 1235$ kW/m ² , using the SST model.....	109
Figure 4-27: 3D Temperature plot for a case with: $P = 1$ MPa, $G = 1496$ kg/m ² s, and $q = 1235$ kW/m ² , using the SST model.....	111
Figure 4-28: 3D Density plot for a case with: $P = 1$ MPa, $G = 1496$ kg/m ² s, and $q = 1235$ kW/m ² , using the SST model.....	112
Figure 4-29: 3D Viscosity plot for a case with: $P = 1$ MPa, $G = 1496$ kg/m ² s, and $q = 1235$ kW/m ² , using the SST model.....	112
Figure 4-30: 3D Specific heat plot for a case with: $P = 1$ MPa, $G = 1496$ kg/m ² s, and $q = 1235$ kW/m ² , using the SST model.....	113
Figure 4-31: 3D Turbulent kinetic energy plot for a case with: $P = 1$ MPa, $G = 1496$ kg/m ² s, and $q = 1235$ kW/m ² , using the SST model.....	113
Figure 4-32: 3D Turbulence intensity plot for a case with: $P = 1$ MPa, $G = 1496$ kg/m ² s, and $q = 1235$ kW/m ² , using the SST model.....	114
Figure 4-33: 3D Velocity plot for a case with: $P = 1$ MPa, $G = 1496$ kg/m ² s, and $q = 1235$ kW/m ² , using the SST model.....	114
Figure 4-34: Effect of turbulent Pr number on wall temperature profiles, RKE model..	117

Figure 4-35: Effect of turbulent Pr number on temperature profiles, for SST model	118
Figure 4-36: Errors in Simulated Wall Temperatures for RKE Model.....	120
Figure 4-37: Errors in Simulated Wall Temperatures for SST Model	121
Figure 4-38: 3D Temperature plot for a case with: $P = 24.1$ MPa, $G = 1496$ kg/m ² s, and $q = 1235$ kW/m ² , using the RKE model and Energy $Pr_t = 0.75$	125
Figure 4-39: 3D Temperature difference plot (Energy Pr_t 0.85 - 0.75) for a case with: $P = 24.1$ MPa, $G = 1496$ kg/m ² s, and $q = 1235$ kW/m ² , using the RKE model	125
Figure 4-40: 3D Density plot for a case with: $P = 24.1$ MPa, $G = 1496$ kg/m ² s, and $q = 1235$ kW/m ² , using the RKE model and Energy $Pr_t = 0.75$	126
Figure 4-41: 3D Specific heat plot for a case with: $P = 24.1$ MPa, $G = 1496$ kg/m ² s, and $q = 1235$ kW/m ² , using the RKE model and Energy $Pr_t = 0.75$	126
Figure 4-42: 3D Thermal conductivity plot for a case with: $P = 24.1$ MPa, $G = 1496$ kg/m ² s, and $q = 1235$ kW/m ² , using the RKE model and Energy $Pr_t = 0.75$	127
Figure 4-43: 3D Viscosity plot for a case with: $P = 24.1$ MPa, $G = 1496$ kg/m ² s, and $q = 1235$ kW/m ² , using the RKE model and Energy $Pr_t = 0.75$	127
Figure 4-44: 3D Turbulent kinetic energy plot for a case with: $P = 24.1$ MPa, $G = 1496$ kg/m ² s, and $q = 1235$ kW/m ² , using the RKE model and Energy $Pr_t = 0.75$	129
Figure 4-45: 3D Turbulence intensity plot for a case with: $P = 24.1$ MPa, $G = 1496$ kg/m ² s, and $q = 1235$ kW/m ² , using the RKE model and Energy $Pr_t = 0.75$	129
Figure 4-46: 3D Turbulent kinetic energy difference (Energy Pr_t 0.85 - 0.75) for a case with: $P = 24.1$ MPa, $G = 1496$ kg/m ² s, and $q = 1235$ kW/m ² , using the RKE model	130
Figure 4-47: 3D Turbulence intensity difference (Energy Pr_t 0.85 - 0.75) for a case with: $P = 24.1$ MPa, $G = 1496$ kg/m ² s, and $q = 1235$ kW/m ² , using the RKE model.....	130
Figure 4-48: Temperature profiles for a case with: 24.1 MPa, $G = 1496$ kg/m ² s, and $q = 1235$ kW/m ² , $P =$ using the RKE model with Energy $Pr_t = 0.75$	131
Figure 4-49: Temperature profiles for a case with: $P = 24.1$ MPa, $G = 1488$ kg/m ² s, and $q = 1256$ kW/m ² , using the unmodified RKE model and with Energy $Pr_t = 0.75$	132
Figure 4-50: 3D Temperature plot for a case with: $P = 24.1$ MPa, $G = 1496$ kg/m ² s, and $q = 1235$ kW/m ² , flowing downwards, using the RKE model and Energy $Pr_t = 0.75$	134
Figure 4-51: 3D Density plot for a case with: $P = 24.1$ MPa, $G = 1496$ kg/m ² s, and $q = 1235$ kW/m ² , flowing downwards, using the RKE model and Energy $Pr_t = 0.75$	134
Figure 4-52: 3D Specific heat plot for a case with: $P = 24.1$ MPa, $G = 1496$ kg/m ² s, and $q = 1235$ kW/m ² , flowing downwards, using the RKE model and Energy $Pr_t = 0.75$	135
Figure 4-53: 3D Viscosity plot for a case with: $P = 24.1$ MPa, $G = 1496$ kg/m ² s, and $q = 1235$ kW/m ² , flowing downwards, using the RKE model and Energy $Pr_t = 0.75$	135
Figure 4-54: 3D Thermal conductivity plot for a case with: $P = 24.1$ MPa, $G = 1496$ kg/m ² s, $q = 1235$ kW/m ² , flowing downwards, using the RKE and Energy $Pr_t = 0.75$..	136
Figure 4-55: 3D Turbulence intensity plot for a case with: $P = 24.1$ MPa, $G = 1496$ kg/m ² s, $q = 1235$ kW/m ² , flowing downwards, using the RKE and Energy $Pr_t = 0.75$	136

Figure 4-56: 3D Turbulence kinetic energy plot for a case with: $P = 24.1$ MPa, $G = 1496$ kg/m ² s, and $q = 1235$ kW/m ² , flowing downwards, RKE model with Energy $Pr_t = 0.75$	137
Figure 4-57: 3D Turbulence intensity difference (Downwards - upwards) for a case with: $P = 24.1$ MPa, $G = 1496$ kg/m ² s, and $q = 1235$ kW/m ² , RKE with Energy $Pr_t = 0.75$	137
Figure 5-1: Illustration of the finned rod surfaces names	140
Figure 5-2: Sample Experimental Run for the Annular Channel with Helical Fins, with bulk-fluid and wall temperatures [56]	141
Figure 5-3: Temperature Contour for the Fluid at the Walls of the Annular Channel Using the SST Model ($P = 22.6$ MPa, $G = 2000$ kg/m ² s, $q = 1.543$ MW/m ²)	142
Figure 5-4: Close-up of Temperature Contour for the Fluid at the Walls of the Annular Channel Using the SST Model ($P = 22.6$ MPa, $G = 2000$ kg/m ² s, $q = 1.543$ MW/m ²)	143
Figure 5-5: Simulated Temperatures for the Fluid at Three Walls of the Inner Tube of the Flow Channel Using the SST Model ($P = 22.6$ MPa, $G = 2000$ kg/m ² s, $q = 1.543$ MW/m ²)	145
Figure 5-6: Simulated Temperatures for the Fluid at the Three Walls of a Helical Fin (Fin 1) Using the SST Model ($P = 22.6$ MPa, $G = 2000$ kg/m ² s, $q = 1.543$ MW/m ²)	146
Figure 5-7: Simulated Temperatures for the Fluid at the Three Walls of a Helical Fin (Fin 2) Using the SST Model ($P = 22.6$ MPa, $G = 2000$ kg/m ² s, $q = 1.543$ MW/m ²)	147
Figure 5-8: Simulated Temperatures for the Fluid at Two Walls of the Inner Flow Tube, and Two Helical Fin Walls (Side and Top) Using the SST Model ($P = 22.6$ MPa, $G = 2000$ kg/m ² s, $q = 1.543$ MW/m ²)	149
Figure 5-9: Simulated Temperatures for the Fluid at All Heated Walls of the Annular Channel (SST Model, $P = 22.6$ MPa, $G = 2000$ kg/m ² s, $q = 1.543$ MW/m ²), and the Average Temperature Profile Using Curve Fitting	150
Figure 5-10: Temperature Contour for the Fluid at Various Cross Sections in the Annular Channel (SST Model, $P = 22.6$ MPa, $G = 2000$ kg/m ² s, $q = 1.543$ MW/m ²)	152
Figure 5-11: Close-up of Temperature Contour for the Fluid at a Radial Cross Section in the Annular Channel (SST Model, $P = 22.6$ MPa, $G = 2000$ kg/m ² s, $q = 1.543$ MW/m ²)	153
Figure 5-12: Close-up of Temperature Contour for the Fluid at a Radial Cross Section in the Annular Channel (SST Model, $P = 22.6$ MPa, $G = 2000$ kg/m ² s, $q = 1.543$ MW/m ²)	153
Figure 5-13: Close-up of Temperature Contour and Mesh at a Radial Cross Section in the Annular Channel (SST Model, $P = 22.6$ MPa, $G = 2000$ kg/m ² s, $q = 1.543$ MW/m ²)	154
Figure 5-14: Close-up of Temperature Contour and Mesh at a Radial Cross Section in the Annular Channel (SST Model, $P = 22.6$ MPa, $G = 2000$ kg/m ² s, $q = 1.543$ MW/m ²)	155
Figure 5-15: Turbulence Kinetic Energy Contour for the Fluid at a longitudinal Cross Section (SST Model, $P = 22.6$ MPa, $G = 2000$ kg/m ² s, $q = 1.543$ MW/m ²)	156
Figure 5-16: Close-up of Turbulence Kinetic Energy Contour for the Fluid at a Radial Cross Section (SST Model, $P = 22.6$ MPa, $G = 2000$ kg/m ² s, $q = 1.543$ MW/m ²)	157
Figure 5-17: Turbulence Intensity Contour for the Fluid at Various Radial Cross Sections (SST Model, $P = 22.6$ MPa, $G = 2000$ kg/m ² s, $q = 1.543$ MW/m ²)	158

Figure 5-18: Velocity Contour for the Fluid at a longitudinal Cross Section (SST Model, $P = 22.6$ MPa, $G = 2000$ kg/m ² s, $q = 1.543$ MW/m ²)	159
Figure 5-19: Velocity Contour for the Fluid at a Radial Cross Section (SST Model, $P = 22.6$ MPa, $G = 2000$ kg/m ² s, $q = 1.543$ MW/m ²).....	160
Figure 5-20: Velocity Streamlines for the Fluid in the Flow Domain (SST Model, $P = 22.6$ MPa, $G = 2000$ kg/m ² s, $q = 1.543$ MW/m ²).....	161
Figure 5-21: Radial Velocity Component Contour for the Fluid at a Radial Cross Section (SST Model, $P = 22.6$ MPa, $G = 2000$ kg/m ² s, $q = 1.543$ MW/m ²).....	162
Figure 5-22: Density Contour for the Fluid at the Walls of the Annular Channel (SST Model, $P = 22.6$ MPa, $G = 2000$ kg/m ² s, $q = 1.543$ MW/m ²)	163
Figure 5-23: Density Contour for the Fluid at a longitudinal Cross Section in the Annular Channel (SST Model, $P = 22.6$ MPa, $G = 2000$ kg/m ² s, $q = 1.543$ MW/m ²).....	163
Figure 5-24: Density Contour for the Fluid at Various Cross Sections in the Annular Channel (SST Model, $P = 22.6$ MPa, $G = 2000$ kg/m ² s, $q = 1.543$ MW/m ²).....	164
Figure 5-25: Specific Heat Contour for the Fluid at the Walls of the Annular Channel (SST Model, $P = 22.6$ MPa, $G = 2000$ kg/m ² s, $q = 1.543$ MW/m ²).....	165
Figure 5-26: Specific Heat Contour for the Fluid at a Longitudinal Cross Section (SST Model, $P = 22.6$ MPa, $G = 2000$ kg/m ² s, $q = 1.543$ MW/m ²)	166
Figure 5-27: Simulated Temperatures for the Fluid at All Heated Walls of the Annular Channel (SST Model, 3D Blocking Mesh).....	168
Figure 5-28: Temperature Contour for the Fluid at Various Cross Sections in the Annular Channel (SST Model, $P = 22.6$ MPa, $G = 2000$ kg/m ² s, $q = 1.543$ MW/m ²).....	169
Figure 5-29: Temperature Contour for the Fluid at a Radial Cross Section in the Annular Channel (SST Model, $P = 22.6$ MPa, $G = 2000$ kg/m ² s, $q = 1.543$ MW/m ²).....	169
Figure 5-30: Temperature Contour for the Fluid at a Radial Cross Section in the Annular Channel (SST Model, $P = 22.6$ MPa, $G = 2000$ kg/m ² s, $q = 1.543$ MW/m ²).....	170
Figure 5-31: Close-up of Temperature Contour for the Fluid at a Radial Cross Section in the Annular Channel (SST Model, $P = 22.6$ MPa, $G = 2000$ kg/m ² s, $q = 1.543$ MW/m ²).....	171
Figure 5-32: Simulated Temperatures for the Fluid at All Heated Walls of the Annular Channel (RKE Model), and the Average Temperature Profile Using Curve Fitting.....	173
Figure 5-33: Temperature Contour for the Fluid at the Walls of the Annular Channel (RKE Model, $P = 22.6$ MPa, $G = 2000$ kg/m ² s, $q = 1.543$ MW/m ²)	174
Figure 5-34: Temperature Contour for the Fluid at a Longitudinal Cross Section in the Annular Channel (RKE Model, $P = 22.6$ MPa, $G = 2000$ kg/m ² s, $q = 1.543$ MW/m ²)	174
Figure 5-35: Temperature Contour with Mesh Lines at a Radial Cross Section in the Annular Channel (RKE Model, $P = 22.6$ MPa, $G = 2000$ kg/m ² s, $q = 1.543$ MW/m ²)	175
Figure 5-36: Close-up of Temperature Contour at a Radial Cross Section in the Annular Channel (RKE Model, $P = 22.6$ MPa, $G = 2000$ kg/m ² s, $q = 1.543$ MW/m ²)	176
Figure 5-37: Turbulent Kinetic Energy Contour at Various Radial Cross Sections in the Annular Channel (RKE Model, $P = 22.6$ MPa, $G = 2000$ kg/m ² s, $q = 1.543$ MW/m ²)	177

Figure 5-38: Turbulent Kinetic Energy Contour at a Radial Cross Section in the Annular Channel (RKE Model, $P = 22.6$ MPa, $G = 2000$ kg/m ² s, $q = 1.543$ MW/m ²)	177
Figure 5-39: Turbulence Intensity Contour at Various Radial Cross Sections in the Annular Channel (RKE Model, $P = 22.6$ MPa, $G = 2000$ kg/m ² s, $q = 1.543$ MW/m ²)	178
Figure 5-40: Velocity Contour at a Longitudinal Cross Sections in the Annular Channel (RKE Model, $P = 22.6$ MPa, $G = 2000$ kg/m ² s, $q = 1.543$ MW/m ²)	179
Figure 5-41: Velocity Contour at a Radial Cross Sections in the Annular Channel (RKE Model, $P = 22.6$ MPa, $G = 2000$ kg/m ² s, $q = 1.543$ MW/m ²)	180
Figure 5-42: Velocity Streamlines for the Fluid in the Annular Channel (RKE Model, $P = 22.6$ MPa, $G = 2000$ kg/m ² s, $q = 1.543$ MW/m ²).....	181
Figure 5-43: Simulated temperature for the fluid at all heated walls of the annular channel with straight fins (SST model), and the average temperature profile using curve fitting.....	183
Figure 5-44: Temperature Contour for the Fluid at the Walls of the Annular Channel with Straight Fins (SST Model, $P = 22.6$ MPa, $G = 2000$ kg/m ² s, $q = 1.543$ MW/m ²)	184
Figure 5-45: Temperature contours for the fluid at various cross sections in the annular channel with straight fins (SST model, $P = 22.6$ MPa, $G = 2000$ kg/m ² s, $q = 1.543$ MW/m ²)	185
Figure 5-46: Turbulent kinetic energy contours for the fluid at various cross sections in the annular channel with straight fins (SST model, $P = 22.6$ MPa, $G = 2000$ kg/m ² s, $q = 1.543$ MW/m ²)	186
Figure 5-47: Turbulence intensity contours for the fluid at various cross sections in the annular channel with straight fins (SST model, $P = 22.6$ MPa, $G = 2000$ kg/m ² s, $q = 1.543$ MW/m ²)	187
Figure 5-48: Velocity contours for the fluid at various cross sections in the annular channel with straight fins (SST model, $P = 22.6$ MPa, $G = 2000$ kg/m ² s, $q = 1.543$ MW/m ²)	188
Figure 5-49: Velocity streamlines for the fluid in the annular channel with straight fins (SST model, $P = 22.6$ MPa, $G = 2000$ kg/m ² s, $q = 1.543$ MW/m ²).....	188
Figure 5-50: Simulated temperature for the fluid at the heated wall of the annular channel with no fins (SST model, same ID and OD of case with helical fins), and the average temperature profile using curve fitting.....	190
Figure 5-51: Temperature contours for the fluid at various cross sections in the annular channel with no fins (SST model, $P = 22.6$ MPa, $G = 2000$ kg/m ² s, $q = 1.543$ MW/m ²) .	191
Figure 5-52: Temperature contour and mesh at a radial cross section in the annular channel with no fins (SST model, $P = 22.6$ MPa, $G = 2000$ kg/m ² s, $q = 1.543$ MW/m ²) .	192
Figure 5-53: Turbulent kinetic energy contour at longitudinal cross section in the annular channel with no fins (SST model, $P = 22.6$ MPa, $G = 2000$ kg/m ² s, $q = 1.543$ MW/m ²) .	194
Figure 5-54: Turbulence kinetic energy contour at a radial cross section in the annular channel with no fins (SST model, $P = 22.6$ MPa, $G = 2000$ kg/m ² s, $q = 1.543$ MW/m ²) .	195

Figure 5-55: Turbulence intensity contours at a longitudinal cross section in the annular channel with no fins (SST model, $P = 22.6$ MPa, $G = 2000$ kg/m ² s, $q = 1.543$ MW/m ²).	196
Figure 5-56: Turbulence intensity contour at a radial cross section in the annular channel with no fins (SST model, $P = 22.6$ MPa, $G = 2000$ kg/m ² s, $q = 1.543$ MW/m ²).....	197
Figure 5-57: Velocity contour at a longitudinal cross section in the annular channel with no fins (SST model, $P = 22.6$ MPa, $G = 2000$ kg/m ² s, $q = 1.543$ MW/m ²).....	197
Figure 5-58: Velocity streams for the fluid in the annular channel with no fins (SST model, $P = 22.6$ MPa, $G = 2000$ kg/m ² s, $q = 1.543$ MW/m ²).....	198
Figure 5-59: Simulated temperature for the fluid at the heated wall of the annular channel with no fins (SST model, equivalent power (2 MW/m ²)), and the average temperature profile using curve fitting.....	200
Figure 5-60: Simulated temperature for the fluid at the heated wall of the annular channel with no fins (SST model, same equivalent hydraulic diameter as the geometry with helical fins), and the average temperature profile using curve fitting	201
Figure 5-61: Simulated temperature for the fluid at the heated wall of the annular channel with no fins (SST model, same equivalent hydraulic diameter as the geometry with helical fins, equivalent power (2 MW/m ²)), and the average temperature profile using curve fitting	202
Figure 5-62: Simulated temperature for the fluid at the heated wall of the annular channel with no fins (SST model, same flow area as the geometry with helical fins), and the average temperature profile using curve fitting	203
Figure 5-63: Simulated temperature for the fluid at the heated wall of the annular channel with no fins (SST model, same flow area as the geometry with helical fins, equivalent power (2 MW/m ²)), and the average temperature profile using curve fitting	204
Figure 5-64: Comparison of average simulated temperatures for the fluid at the heated wall of the annular channel with helical fins and no fins (SST model)	205
Figure 5-65: Simulated temperature for the fluid at all heated walls of the annular channel with straight fins (SST model), and the average temperature profile using curve fitting.....	207
Figure 5-66: Density contours at the heated walls in the annular channel with helical fins (SST model, $P = 22.6$ MPa, $G = 2000$ kg/m ² s, $q = 2.547$ MW/m ²).....	208
Figure 5-67: Density contours at a longitudinal cross section in the annular channel with helical fins (SST model, $P = 22.6$ MPa, $G = 2000$ kg/m ² s, $q = 2.547$ MW/m ²).....	208
Figure 5-68: Turbulence intensity contours at a longitudinal cross section in the annular channel with helical fins (SST model, $P = 22.6$ MPa, $G = 2000$ kg/m ² s, $q = 2.547$ MW/m ²)	209
Figure 5-69: Velocity contours at a longitudinal cross section in the annular channel with helical fins (SST model, $P = 22.6$ MPa, $G = 2000$ kg/m ² s, $q = 2.547$ MW/m ²).....	209
Figure 5-70: Velocity streams for the fluid in the annular channel with helical fins (SST model, $P = 22.6$ MPa, $G = 2000$ kg/m ² s, $q = 2.547$ MW/m ²).....	210

Figure 5-71: Specific heat contours at the heated wall in the annular channel with helical fins (SST model, $P = 22.6$ MPa, $G = 2000$ kg/m ² s, $q = 2.547$ MW/m ²)	212
Figure 5-72: Specific heat contours at a longitudinal cross section in the annular channel with helical fins (SST model, $P = 22.6$ MPa, $G = 2000$ kg/m ² s, $q = 2.547$ MW/m ²).....	212
Figure 5-73: Specific heat for the fluid at the heated walls in the annular channel with helical fins (SST model, $P = 22.6$ MPa, $G = 2000$ kg/m ² s, $q = 2.547$ MW/m ²).....	213
Figure 6-1: 3D temperature contour plot for a tube with an orifice in the entrance region with: $P = 24$ MPa, $G = 1002$ kg/m ² s, and $q = 391$ kW/m ² , using the RKE model	218
Figure 6-2: Center plane in the 3D mesh of 1/8 tube with an orifice in the entrance region	218
Figure 6-3: 3D temperature plot for a tube with an orifice in the entrance region with: $P = 24$ MPa, $G = 1002$ kg/m ² s, and $q = 391$ kW/m ² , using the RKE model	219
Figure 6-4: 3D temperature scatter plot for a tube with an orifice in the entrance region with: $P = 24$ MPa, $G = 1002$ kg/m ² s, and $q = 391$ kW/m ² , using the RKE model	220
Figure 6-5: Close-up of the orifice geometry with the mesh lines showing the higher density around the orifice walls.....	222
Figure 6-6: 3D turbulent kinetic energy scatter plot for a tube with an orifice in the entrance region: $P = 24$ MPa, $G = 1002$ kg/m ² s, and $q = 391$ kW/m ² , using the RKE model	222
Figure 6-7: 3D cutout of turbulent kinetic energy plot for a tube with an orifice in the entrance region: $P = 24$ MPa, $G = 1002$ kg/m ² s, and $q = 391$ kW/m ² , RKE model	223
Figure 6-8: 3D 3D turbulence intensity scatter plot for a tube with an orifice in the entrance region: $P = 24$ MPa, $G = 1002$ kg/m ² s, and $q = 391$ kW/m ² , RKE model	223
Figure 6-9: 3D cutout of turbulence intensity plot for a tube with an orifice in the entrance region: $P = 24$ MPa, $G = 1002$ kg/m ² s, and $q = 391$ kW/m ² , RKE model	224
Figure 6-10: 3D Specific heat scatter plot for a tube with an orifice in the entrance region: $P = 24$ MPa, $G = 1002$ kg/m ² s, and $q = 391$ kW/m ² , RKE model.....	224
Figure 6-11: 3D Velocity scatter plot for a tube with an orifice in the entrance region: $P = 24$ MPa, $G = 1002$ kg/m ² s, and $q = 391$ kW/m ² , using the RKE model	225
Figure 6-12: 3D Velocity scatter plot for the tube entrance region with an orifice: $P = 24$ MPa, $G = 1002$ kg/m ² s, and $q = 391$ kW/m ² , using the RKE model	225
Figure 6-13: 3D Temperature heat plot for a tube with an orifice 20 cm into the heated length with: $P = 24$ MPa, $G = 1002$ kg/m ² s, and $q = 391$ kW/m ² , using the RKE model	228
Figure 6-14: 3D Specific heat plot for a tube with an orifice 20 cm into the heated length with: $P = 24$ MPa, $G = 1002$ kg/m ² s, and $q = 391$ kW/m ² , using the RKE model	228
Figure 6-15: 3D Velocity plot for a tube with an orifice 20 cm into the heated length with: $P = 24$ MPa, $G = 1002$ kg/m ² s, and $q = 391$ kW/m ² , using the RKE model.....	229
Figure 6-16: 3D cutout of Velocity plot for a tube with an orifice 20 cm into the heated length with: $P = 24$ MPa, $G = 1002$ kg/m ² s, and $q = 391$ kW/m ² , using the RKE model	229
Figure 6-17: Velocity streams visualization around the orifice 20 cm into the heated length with: $P = 24$ MPa, $G = 1002$ kg/m ² s, and $q = 391$ kW/m ² , using the RKE model	230

Figure 6-18: Velocity streams visualization around the orifice 20 cm into the heated length with: $P = 24$ MPa, $G = 1002$ kg/m ² s, and $q = 391$ kW/m ² , using the RKE model	231
Figure 6-19: 3D Turbulence intensity plot for a tube with an orifice 20 cm into the heated length with: $P = 24$ MPa, $G = 1002$ kg/m ² s, and $q = 391$ kW/m ² , RKE model.....	232
Figure 6-20: 3D Turbulence intensity plot for a tube after the orifice 20 cm into the heated length with: $P = 24$ MPa, $G = 1002$ kg/m ² s, and $q = 391$ kW/m ² , RKE model.....	232
Figure 6-21: Wall temperature results for simple tube and tube with orifice in entrance region, $P = 24.1$, $G = 1500$ kg/m ² s, and $q = 1022$ kW/m ² , using the RKE model	234
Figure 6-22: Wall temperature results for simple tube and tube with orifice in entrance region, $P = 24.1$, $G = 1489$ kg/m ² s, and $q = 1164$ kW/m ² , using the RKE model	235
Figure B-1: 3D Temperature plot for a case with: $P = 24$ MPa, $G = 1002$ kg/m ² s, and $q = 391$ kW/m ² , using the RKE model.....	250
Figure B-2: 3D Density plot for a case with: $P = 24$ MPa, $G = 1002$ kg/m ² s, and $q = 391$ kW/m ² , using the RKE model.....	251
Figure B-3: 3D Specific heat plot for a case with: $P = 24$ MPa, $G = 1002$ kg/m ² s, and $q = 391$ kW/m ² , using the RKE model.....	251
Figure B-4: 3D Thermal conductivity plot for a case with: $P = 24$ MPa, $G = 1002$ kg/m ² s, and $q = 391$ kW/m ² , using the RKE model	252
Figure B-5: 3D Viscosity plot for a case with: $P = 24$ MPa, $G = 1002$ kg/m ² s, and $q = 391$ kW/m ² , using the RKE model.....	252
Figure B-6: 3D Turbulence kinetic energy plot for a case with: $P = 24$ MPa, $G = 1002$ kg/m ² s, and $q = 391$ kW/m ² , using the RKE model	253
Figure B-7: 3D Turbulence intensity plot for a case with: $P = 24$ MPa, $G = 1002$ kg/m ² s, and $q = 391$ kW/m ² , using the RKE model	253
Figure B-8: 3D Velocity plot for a case with: $P = 24$ MPa, $G = 1002$ kg/m ² s, and $q = 391$ kW/m ² , using the RKE model.....	254
Figure C-1: Effect of Turbulent Pr Number on Wall Temperature Profiles for RKE Model	255
Figure C-2: Effect of Turbulent Pr Number on Wall Temperature Profiles for SST Model	256
Figure D-1: Cut planes illustrating the axial locations of thermocouples in the helically finned annular flow channel	257

Nomenclature

A	area, m ²	q	heat flux, W/m ²
c_p	specific heat, J/kg K	r	radius, m
\bar{c}_p	averaged specific heat within the range of $(T_w - T_b)$; $\left(\frac{H_w - H_b}{T_w - T_b}\right)$, J/kg K	S	user-defined source term
C_μ	empirical constant	T	temperature, °C, K
$C2\varepsilon$	empirical constant	t	time, s
D	diameter, m	u	velocity(x-direction), m/s
e	internal energy, J	V	volume, Total velocity, m/s
F	force, N	v	velocity (y-direction), m/s
f_μ	dampening function	w	velocity (z-direction), m/s
G	mass flux, kg/m ² s	x	position on x-axis, m
G_k	gravitational production term	Y	dissipation term
g	gravitational acceleration constant, m/s ²	y^+	dimensionless wall distance
H	heat transfer coefficient, W/m ² K	z	position on the z axis, m
h	enthalpy, J/kg		
k	turbulent kinetic energy, J/kg		
k	thermal conductivity, W/m k		
L	Length, m		
m	mass, kg		
P	pressure, Pa		
P	production term due to mean velocity gradient		
p	perimeter, m		
\dot{Q}	heat transfer rate, W		

Greek Letters

β	thermal expansion coefficient, 1/K
δV	volume element, m ³
δm	mass element, kg
ε	turbulent kinetic energy dissipation rate, m ² /s ³
μ	dynamic viscosity, Pa s
μ_t	turbulent viscosity, Pa s
μ_e	effective viscosity, Pa s
μ^*	frictional velocity, m/s

ρ	density, kg/m ³
∇	gradient
τ	shear stress, Pa
ω	specific turbulent kinetic energy dissipation rate, 1/s

Dimensionless numbers

Nu	Nusselt number $\left(\frac{H \cdot D_{hy}}{k}\right)$
Pr	Prandtl number $\left(\frac{\mu \cdot c_p}{k}\right)$
$\overline{\text{Pr}}$	average Prandtl number $\left(\frac{\mu \cdot \bar{c}_p}{k}\right)$
Re	Reynolds $\left(\frac{G \cdot D_{hy}}{\mu}\right)$

Subscripts and Superscripts

b	bulk
cr	critical
exp	experimental
fl	flow
hy	hydraulic
in	inlet
pc	pseudocritical
hy	hydraulic
p	pressure
vl	volumetric
w	wall
wet	wetted

Acronyms and Abbreviations

CAD	Computer Aided Design
CHF	Critical Heat Flux
CFD	Computational Fluid Dynamics
DHT	Deteriorated Heat Transfer
DNS	Direct Numerical Simulation
Exp.	Experimental
GIF	Generation IV International Forum

ID	Inside diameter
IHT	Improved Heat Transfer
IPPE	Institute of Physics and Power Engineering
LES	Large Eddy Simulation
MUSCL	Monotone Upstream-Centered Schemes for Conservation Laws
NHT	Normal Heat Transfer
NIST	National Institute of Standards and Technology
OD	Outer diameter
PISO	Pressure-Implicit with Splitting of Operators
PRESTO	Pressure Staggering Options
PWR	Pressurized Water Reactor
RANS	Reynolds-Averaged Navier-Stokes
REFPROP	Reference Fluid Thermodynamic and Transport Properties
RKE	Realizable k- ϵ
RNG	Re-Normalization Group
SCW	SuperCritical Water
SCWR	Super-Critical Water-cooled Reactor
SDR	Specific Dissipation Rate
SIMPLE	Semi-Implicit Method for Pressure-Linked Equations
SS	Stainless steel
SST	Shear Stress Transport
TDR	Turbulent Dissipation Rate
Temp.	Temperature
TKE	Turbulent Kinetic Energy
UDF	User Defined Function
UGS	UniGraphics computer aided design software

Glossary

Compressed fluid is the fluid at a pressure above the critical pressure, but at a temperature below the critical temperature.

Critical point (also called a *critical state*) is the point in which the distinction between the liquid and gas (or vapor) phases disappears, i.e., both phases have the same temperature, pressure and specific volume or density. The *critical point* is characterized with the phase-state parameters: T_{cr} , P_{cr} and v_{cr} (or ρ_{cr}), which have unique values for each pure substance.

Fluid is a substance that continually deforms (flows) under an applied shear stress. Fluids are a subset of the phases of matter and include liquids, gases, plasmas, and, to some extent, plastic solids. Fluids are substances that have zero shear modulus or, in simpler terms, a fluid is a substance, which cannot resist any shear force applied to it. Although the term "fluid" includes both the liquid and gas phases, in common usage, "fluid" is often used as a synonym for "liquid", with no implication that gas could also be present.

Near-critical point is actually a narrow region around the critical point, where all thermo-physical properties of a pure fluid exhibit rapid variations.

Pseudocritical line is the line, which consists of pseudocritical points.

Pseudocritical point (characterized with P and T_{pc}) is the point at a pressure above the critical pressure and at a temperature ($T_{pc} > T_{cr}$) corresponding to the maximum value of specific heat at this particular pressure.

Supercritical fluid is the fluid at pressures and temperatures that are higher than the critical pressure and critical temperature. However, in the present Chapter, the term *supercritical fluid* usually includes both terms – a *supercritical fluid* and *compressed fluid*.

Supercritical "steam" is actually supercritical water, because at supercritical pressures fluid is considered as a single-phase substance. However, this term is widely (and incorrectly) used in the literature in relation to supercritical-"steam" generators and turbines.

Supercritical "vapor" is actually supercritical fluid, because at supercritical pressures fluid is considered as a single-phase substance.

Superheated steam is the steam at pressures below the critical pressure, but at temperatures above the critical temperature.

Superheated vapor is the vapor at pressures below the critical pressure, but at temperatures above the critical temperature.

Triple point is the state at which all three phases coexist in equilibrium.

Deteriorated Heat Transfer (DHT) is characterized with lower values of the heat transfer coefficient compared to those for normal heat transfer; and, hence, has higher values of wall temperature within some part of a test section or within the entire test section.

Improved Heat Transfer (IHT) is characterized with higher values of the heat transfer coefficient compared to those for normal heat transfer; and hence, lower values of wall temperature within some part of a test section or within the entire test section. The improved heat-transfer regime or mode includes peaks or “humps” in the heat transfer coefficient near the critical or pseudocritical points.

Normal Heat Transfer (NHT) can be characterized in general with heat transfer coefficients similar to those of subcritical convective heat transfer far from the critical or pseudocritical regions, when they are calculated according to the conventional single-phase Dittus-Boelter-type correlations: $\mathbf{Nu} = 0.023 \mathbf{Re}^{0.8} \mathbf{Pr}^{0.4}$.

Pseudo-boiling is a physical phenomenon similar to subcritical-pressure nucleate boiling, which may appear at supercritical pressures. Due to heating of a supercritical fluid with a bulk-fluid temperature below the pseudocritical temperature (high-density fluid, i.e., “liquid”), some layers near the heating surface may attain temperatures above the pseudocritical temperature (low-density fluid, i.e., “gas”). This low-density “gas” leaves the heating surface in a form of variable density (bubble) volumes. During the pseudo-boiling, the heat transfer coefficient usually increases (improved heat-transfer regime).

Pseudo-film boiling is a physical phenomenon similar to subcritical-pressure film boiling, which may appear at supercritical pressures. At pseudo-film boiling, a

low-density fluid (a fluid at temperatures above the pseudocritical temperature, i.e., “gas”) prevents a high-density fluid (a fluid at temperatures below the pseudocritical temperature, i.e., “liquid”) from contacting (“rewetting”) a heated surface. Pseudo-film boiling leads to the deteriorated heat-transfer regime.

Chapter 1: Introduction

Computational Fluid Dynamics (CFD) modeling of SuperCritical Water (SCW) heat transfer is currently used in nuclear engineering to predict heat transfer coefficients and temperature profiles [1], in support of the development of both conventional and nuclear type supercritical water power plants. However, since the conception of the idea of using SCW as a coolant, the focus has been shifted away from this research until recently, when the introduction of a Supercritical Water-cooled Reactor (SCWR) concept was brought forward, as part of the Generation IV International Forum (GIF).

The move towards Gen IV reactor concepts is meant to address the issues facing current and Generation III+ nuclear power plants. While nuclear energy provides reliable and continuous electricity generation, with lower greenhouse gas emissions compared to thermal power plants (coal-fired, combined cycle gas-fired, etc.), they are not very competitive in terms of thermal efficiency [2]. 96% of current reactors are water-cooled designs that have thermal efficiencies in the range of 32 to 36%, compared to advanced thermal power plants which reach up to 62%. SCWR designs aim to increase the efficiency into the range of 40-50%, by utilizing water at pressures and temperatures above the critical point.

A fluid remains in the same phase, regardless of the temperature variations once the pressure has exceeded the thermal critical value (supercritical pressure). However, the properties of the fluid can vary rapidly in response to changes in temperature and pressure. Particularly, the specific heat exhibits a sharp peak at the pseudocritical temperature. Density, thermal conductivity, and viscosity also vary significantly within a small temperature window in the vicinity of the pseudocritical temperature.

The diffusion of heat, both by molecular and turbulent action, can be greatly affected by the property variations. For example the variation of density can affect

turbulence production, either by changing the flow acceleration due to thermal expansion, or due to the influence of buoyancy.

The current methods of predicting the mechanics of SCW flow as well as temperature and heat transfer coefficients profiles associated with it are lacking in accuracy, and even in the understanding of the underlying phenomena behind the flow mechanism. The most accurate 1-D correlations do not predict heat transfer phenomena accurately, and those designed for fuel bundles are very geometry specific. Furthermore, 1-D methods do not provide any insight to the multidimensional phenomena in the flow and thus are not capable of describing the basic physics of flow in these conditions.

Furthermore, heat transfer coefficients (HTCs) in supercritical water are lower than those in subcritical water in current reactors. Thus there is a need to introduce turbulence in the flow, and simple geometries such as bare tubes cannot be used in the reactor core. This brings forward the need to study more complex geometries (similar to fuel bundles) that are capable of enhancing flow turbulence.

However, due to the uniqueness of each bundle design, experimental determination of the heat transfer effects can get very costly and time-consuming. An approach such as CFD, once validated for certain flow conditions, can be used to explain the various phenomena in different geometries without the need for separate physical experiments in each one.

The research hypotheses are twofold: 1) the transition in SCW heat transfer regimes is influenced by the level of buoyancy-induced turbulence in the flow. 2) Introducing high turbulence in SCW flow by means of geometric perturbations is necessary to enhance heat transfer and increase the margin to deterioration.

This research will work towards developing an accurate description of the SCW flow by studying the multidimensional effects of changing properties in normal and deteriorated heat transfer regimes, and in different geometries that introduce

various levels of turbulence in the flows. The study will be conducted using CFD 2-equation turbulence models in 3-D simulations of supercritical water flow through a bare tube, annular channels with helical fins, and sudden area change geometries.

Simulations in bare tubes will aid in understanding the fundamental phenomena occurring in normal and deteriorated heat transfer regimes in simple geometries and will be validated by comparing the results to bare tube data. The next step is to analyze a complex geometry in the form of an annular flow channel with helical fins and compare the results to experimental wall temperatures to establish the effects of geometric perturbations on SCW flow and heat transfer. The last step is analyzing a sudden area change geometry

1.1 Computational Fluid Dynamics

CFD is a set of numerical methods applied to obtain approximate or exact solutions of fluid dynamics and heat transfer in multi-dimensional space and time. CFD involves applying the conservation equations and transport of certain properties to obtain a full description of the flow property fields.

By solving the conservation equations in a chosen flow, CFD simulations then output distributed properties [3], which are described in fields such as velocity, temperature, and density as functions of position and time. Ultimately, all flow and heat transfer characteristics desired from the solution, such as the rate of heat transfer or the heat transfer coefficients, are derived from these distributed fields.

The advantages of CFD methods are generally attributed to the relatively low cost (compared to physical experiments), the level of detail available, and the early insight into phenomena that may arise in engineering applications. CFD provides a platform to identify and guide design decisions in the early stages before a potential problem could delay or deter the experimental process. An additional

benefit is the safety aspect of analyzing high risk systems, such as nuclear power plants and their components, without physical hazards [3].

The level of detail that CFD simulations provide is higher than any other approach to solve the same problem. Compared to other computational and experimental techniques, entire distributions of properties within a body or a flow field can be determined and accounted for, and the various available models allow for the study of turbulence at multiple length and time scales [3]. The cost of such level of detail is the increase in computational resources owing to the complexity of the governing equations. For most CFD applications the equations are non-linear partial differential equations and the level of complexity rises with the desired accuracy of the solution.

1.2 Objectives

The objective of this work is to further develop an understanding of SCW flow by analyzing the flow- and geometry-dependent localized phenomena under supercritical conditions using CFD turbulence models.

The main objective will be accomplished by:

- (1) Analysis of various turbulence models and the empirical constants involved in simplifying the conservation equation for generalized flow (e.g. turbulent Pr number), and determining their effect on flow characteristics; such as temperature profiles, turbulence intensity, velocity, etc.
- (2) CFD investigation of fluid property effects around geometrical perturbations to determine important flow parameters that capture localized flow phenomena effects.

The study would be a comprehensive examination of the localized phenomena, as there is a need to look at both the geometry and the fluid properties to understand the underlying physics involved in SCW flow.

Chapter 2: Literature Review

2.1 Generation IV Reactors

A group of countries, including Canada, EU, Japan, Russia, USA and others have combined efforts to develop the next generation of nuclear reactors (Generation IV reactors). The ultimate goal of developing these reactors is to increase the thermal efficiencies of nuclear power plants from the current range of 30 - 36% to 45 - 50% or higher. This increase in efficiency would result in a much higher generation of electricity compared to current fleet of reactors per unit input of uranium mass [4].

The Generation IV International Forum (GIF) Program has narrowed design options of nuclear reactors to six concepts; 1) Gas-cooled Fast Reactor (GFR) or High Temperature Reactor (HTR), 2) Very High Temperature Reactor (VHTR), 3) Sodium-cooled Fast Reactor (SFR), 4) Lead-cooled Fast Reactor (LFR), 5) Molten Salt Reactor (MSR), and 6) SuperCritical Water-cooled Reactor (SCWR). These nuclear-reactor concepts differ one from each other in terms of their design, neutron spectrum, coolant, moderator, operating temperatures and pressures [5].

Supercritical water-cooled reactors use water above the critical point as a coolant, resulting in higher thermodynamic efficiency. Some of the other reactors use other fluids in their supercritical state such as CO₂ and helium. Before these concepts can be built and operated however, a profound understanding of how the fluids at these conditions behave under the proposed conditions must be gathered.

2.2 Physical Properties of SCW

Supercritical Water exists in the region above the critical point (~22.064 MPa, and 374°C), and those conditions it behaves in a much different manner than subcritical water.

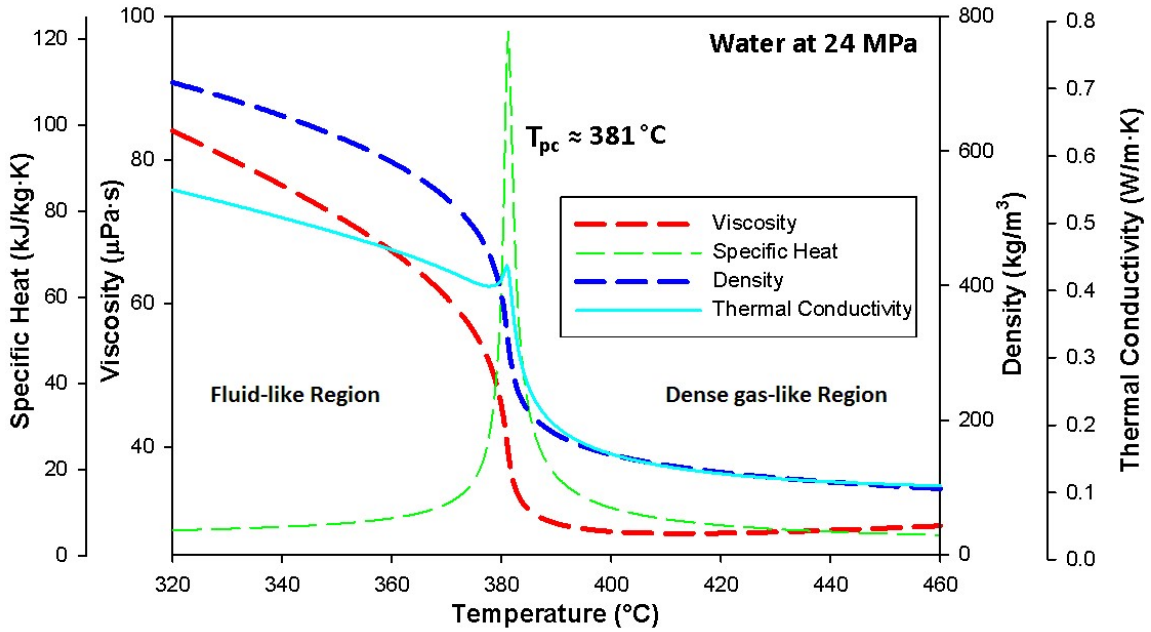


Figure 2-1: Thermo-physical properties of water in the supercritical conditions

As Figure 2-1 depicts, the properties of SCW range from liquid-like region then undergo steep changes in properties in approximately $\pm 25^\circ\text{C}$ around the pseudocritical point (where the highest value of specific heat is reached).

The changes in density, thermal conductivity and dynamic viscosity of the fluid show a dramatic drop near the pseudocritical point, and since the proposed operating conditions for SCWRs involve passing through the pseudocritical point, accurate prediction of the SCW behaviour is much needed in these conditions.

More to the point, in complicated geometries, the fluid passes the pseudocritical region at multiple points throughout the geometry, which brings about more complicated behaviour, as the rapid change in properties and the corresponding effects (flow acceleration, pressure drops, potential heat transfer deterioration, etc.) occurs more than once throughout the flow domain.

2.3 Heat Transfer in Supercritical Fluids

After the fluid passes the critical thermodynamic point, the heat transfer phenomena in water follows three regimes depending on the operating conditions; normal heat transfer (NHT), deteriorated heat transfer (DHT), and Improved/Enhanced Heat Transfer (IHT) [4]. The exact conditions at which the regimes change are not yet known, although there are some empirical equations that attempt to correlate the onset of DHT based on heat flux, mass flux, and geometric properties [6].

In normal heat transfer regime, the heat transfer coefficients are similar to those in conditions of subcritical convective heat transfer, and improved heat transfer is characterized by higher coefficients in comparison to the normal heat transfer regimes.

Deteriorated Heat Transfer (DHT) is the phenomenon resulting in a reduction of the heat transfer coefficient at the wall, which consequently raises the wall temperature. The most contributing factors to DHT are the heat flux, mass flux, and the geometry; where many authors attribute the ratio of heat to mass fluxes to be major factor for the creation of DHT conditions [7] [8] [9]. What is agreed on is that DHT is caused by the local changes of the physical properties of water near the heated wall.

Experimentally, the deterioration in heat transfer is observed in cases where the flow is in the upwards direction. Downward flow experiments with the same operating conditions do not result in any deterioration, and the wall temperature increase consistently, similar to that of a NHT regime in upwards flow [9].

Cheng et al. [10] argue two situations of DHT occurrence. One occurrence is when the mass flux is higher than a certain value, the heat transfer coefficient decreases consistently.

When the mass flux is lower than this certain value, however, the heat transfer coefficients (HTCs) decrease abruptly at certain heat flux values and gradually increase after. This is possibly due to the buoyancy forces; when the heat flux increases; the buoyancy force becomes stronger near the heated wall which leads to a flattening of the velocity profile radially. As the generation of turbulence energy is proportional to the gradient of the mean velocity, turbulence is then suppressed. Consequently, this results in the reduction of HTC. Once the heat transfer is increased further, the buoyancy force undergoes further enhancement which causes a velocity peak near the heated wall. This in turn results in higher turbulence because of the newly found gradient and the heat transfer is improved again. This means the HTC will be enhanced with mixing; that is when the fluid near the wall mixes with the bulk fluid.

In downward flows, the buoyancy is opposed to the flow and does not distort the velocity profiles, preserving the relatively large turbulent kinetic energy difference along the heated length, thus mitigating the presence of DHT.

Shiralkar and Griffith compiled data for heat transfer deterioration based on papers by over 15 researchers who conducted experiments in water, oxygen, carbon dioxide and nitrogen tetroxide, under a wide range of flow rates, heat fluxes, test section sizes and pressures [7]. Based on the data provided, the conditions under which the deterioration has been observed are reported by Shiralkar and Griffith as:

- 1- The wall temperature must be above, and the bulk temperature must be below the pseudocritical temperature.
- 2- The heat flux must be above a certain value, dependant on the flow rate and the pressure.

Another interesting potential explanation for the phenomenon is pseudo-boiling. It is a similar to subcritical pressure nucleate boiling, which may appear at

supercritical pressures. Due to heating of supercritical fluid with a bulk-fluid temperature below the pseudocritical temperature (high-density fluid), some layers near a heating surface may reach temperatures above the pseudocritical temperature (low-density fluid). This low-density gas-like fluid leaves the heating surface in the form of variable density (bubble) volumes. During the pseudo-boiling, the wall heat transfer coefficient usually increases (improved heat-transfer regime).

Pseudo-film boiling is a physical phenomenon similar to subcritical-pressure film boiling, which may appear at supercritical pressures. At pseudo-film boiling, a low-density fluid above the pseudocritical temperature prevents a high density fluid below the pseudocritical temperature from contacting a heated surface leading to the deterioration of heat-transfer.

Experimental data suggests the increase in temperature as a result of DHT is slower and more stable than the corresponding temperature increase for CHF in subcritical flows.

While there are numerous suggestions that local phenomena are important, there is insufficient evidence to support them, and the actual impact of the localized effects is not yet known. Studying geometrical perturbations will aid in bridging the knowledge gap in this area.

2.4 Empirical Correlations

In the case of nuclear power plants, the ability to predict correctly heat-transfer coefficients along a fuel-bundle string is essential for the reactor design. There is however a lack of experimental data and correspondingly empirical correlations for heat transfer in fuel bundles. Only one correlation is known for a helically-finned, 7-element bundle by Dyadyakin and Popov, developed in 1977 [11].

$$\text{Nu}_x = 0.0021 \text{Re}_x^{0.8} \overline{\text{Pr}}_x^{0.7} \left(\frac{\rho_w}{\rho_b}\right)_x^{0.45} \left(\frac{\mu_b}{\mu_{in}}\right)_x^{0.2} \left(\frac{\rho_b}{\rho_{in}}\right)_x^{0.1} \left(1 + 2.5 \frac{D_{hy}}{x}\right) \quad [2-1]$$

Where x is the axial location along the heated length of the test section (in meters) and D_{hy} is the hydraulic equivalent diameter; calculated as:

$$D_{hy} = \frac{4 \cdot A_{ft}}{p_{wet}} \quad [2-2]$$

This test bundle was designed for applications in transport (naval) reactors, and not for power reactor. Moreover, heat transfer correlations for bundles are usually very sensitive to a particular bundle design, which makes the correlation inadequate for other bundle geometries.

To overcome the problem, attempts at developing wide-range heat-transfer correlations based on bare-tube data have been conducted to serve as a conservative approach. The conservative approach is based on the fact that HTC's are generally lower in bare tubes than in bundle geometries, where the heat transfer is enhanced with appendages such as endplates, bearing pads, spacers, etc.

As a result, a number of empirical correlations, based on experimentally obtained datasets, have been proposed to calculate the HTC in forced convection for various fluids including water at supercritical conditions. These bare-tube correlations are available in the open literature, however, differences in HTC values can be up to several hundred percent [4].

The developed correlations differ by the dataset upon which they were based, and by the base temperature for the dimensionless parameters, be it bulk, wall or film temperatures.

Of the most widely used correlations for supercritical conditions, the Bishop et al. correlation is the most notable, in the form:

$$\mathbf{Nu}_b = \mathbf{0.0069 Re}_b^{0.9} \overline{\mathbf{Pr}}_b^{0.66} \left(\frac{\rho_w}{\rho_b} \right)_x^{0.43} \left(\mathbf{1 + 2.4 \frac{D}{x}} \right) \quad [2-3]$$

Where the last term accounts for the entrance region effect in the test section, however, since it is related to the particular experimental apparatus for the dataset, it is not often applicable to other conditions, where the flow is already developed in the test section. Therefore, the correlation is mainly used in the form:

$$\mathbf{Nu}_b = \mathbf{0.0069 Re}_b^{0.9} \overline{\mathbf{Pr}}_b^{0.66} \left(\frac{\rho_w}{\rho_b} \right)_x^{0.43} \quad [2-4]$$

The operating parameters in which the experimental dataset was collected are: pressure: 22.8 – 27.6 MPa, bulk-fluid temperature: 282 – 527°C, mass flux: 651 – 3662 kg/m²s, and heat flux: 0.31 – 3.46 MW/m². The accuracy of the fit for experimental data was ±15% [12].

As the correlation was developed in the 1960s, and properties of water have been updated since then, a new correlation was proposed by Mokry et al. in 2009, based on the same approach as Bishop et al. correlation. The correlation was based on experimental data collected in the supercritical conditions, for SCW flowing upwards in a 4-m long vertical bare tube. The operating pressure was approximately 24 MPa, mass flux ranged from 200 – 1500 kg/m²s, coolant inlet temperatures from 320 – 350°C, and heat flux up to 1250 kW/m² [13].

$$\mathbf{Nu}_b = \mathbf{0.0061 Re}_b^{0.904} \overline{\mathbf{Pr}}_b^{0.684} \left(\frac{\rho_w}{\rho_b} \right)_x^{0.564} \quad [2-5]$$

The Bishop et al. and Mokry et al. correlations are based on the bulk fluid properties to calculate the Reynolds and Prandtl numbers. Another approach is to use the wall temperatures instead; however there is a significantly smaller number of correlations developed using this method. Of the most accurate correlations in that aspect is the Swenson et al. correlation:

$$\mathbf{Nu}_w = \mathbf{0.00459 Re}_w^{0.923} \overline{\mathbf{Pr}}_w^{0.613} \left(\frac{\rho_w}{\rho_b} \right)^{0.231} \quad [2-6]$$

The experimental data was obtained at pressures: 22.8 – 41.4 MPa, bulk-fluid temperatures: 75 – 576°C, wall temperatures: 93 – 649°C and mass flux: 542 – 2150 kg/m²s. The prediction of experimental data was also within ±15% [14].

Heat-transfer correlations based on bare-tube data can be used as a preliminary conservative approach. The main problem with the experiments and models developed to date is that only 1-D effects have been captured. Only one point is taken into consideration at any given cross section with averaged values for said cross section. This means none of the localized effects are included in these numerical models. As the heat is transferred from the heated element radially throughout the fluid, the temperature along the cross section varies, and crosses the pseudocritical point at different points. Averaging the temperatures and properties lead to results that may not represent the real behaviour of the fluid, as apparent by the results of simulations using correlations to predict experimental values.

Furthermore, the experimental data which is used to develop and test these correlations do not include measurements for any localized effects, even in bundle geometries. As such, the only way to gain insight into these effects currently is through 3D CFD simulations.

2.5 CFD Theory for Fluid Flow

Generally, there are three approaches to solving fluid flow and heat transfer problems; theoretical, experimental, and numerical. The theoretical approach uses governing equations to find exact analytical solutions, while the numerical approach relies on computational procedures to find the best approximation of the solution. The experimental approach involves staging a carefully constructed experiment using a model of the real object to build on.

CFD resides in the numerical approach category, where it employs the use of multi-equation turbulence models (based on partial differential equations) to describe almost any fluid flow and heat transfer process. The number of equations is a result of assumptions and simplifications made to the Navier-Stokes equations for computational purposes.

As in any numerical code for flow dynamics and heat transfer, the governing equations are simply versions of the conservation laws of classic physics;

- Conservation of mass,
- Conservation of momentum, and
- Conservation of energy

In some cases, additional equations might be needed to account for other phenomena such as electromagnetism or entropy transport.

The fluid can be considered as a continuous medium, which consists of infinitesimally small elements. The conservation laws must be satisfied by every element in the fluid. These elements move around, rotate, and deform under the forces acting on the flow [3]. The most used approach in CFD is the Eulerian approach, in which the conservation principles applied to the volume elements are formulated in terms of the distributed properties mentioned earlier in section 1.1 (density $\rho(x,t)$, temperature $T(x,t)$, velocity $v(x,t)$, etc...).

Taking one property and generalizing the result for the rest, the differentiation of density for example, with respect to time would give the rate of change of density within the fluid element

$$\frac{\partial \rho}{\partial t} + \frac{\partial \rho}{\partial x} \frac{dx(t)}{dt} + \frac{\partial \rho}{\partial y} \frac{dy(t)}{dt} + \frac{\partial \rho}{\partial z} \frac{dz(t)}{dt} = \frac{\partial \rho}{\partial t} + u \frac{\partial \rho}{\partial x} + v \frac{\partial \rho}{\partial y} + w \frac{\partial \rho}{\partial z} \quad [2-7]$$

Where the derivatives of the position components are simplified as the local velocity vector resulting in:

$$\mathbf{V} = u\mathbf{i} + v\mathbf{j} + w\mathbf{k} \quad [2-8]$$

By using the local velocity vectors and the gradient of density with respect to position, equation 2-7 simplifies further to:

$$\frac{D\rho}{Dt} = \frac{\partial\rho}{\partial t} + \mathbf{V} \cdot \nabla\rho \quad [2-9]$$

Similarly, the rate of change of other properties such as velocity components, and even the temperature would be:

$$\frac{Du}{Dt} = \frac{\partial u}{\partial t} + \mathbf{V} \cdot \nabla u \quad [2-10]$$

$$\frac{DT}{Dt} = \frac{\partial T}{\partial t} + \mathbf{V} \cdot \nabla T \quad [2-11]$$

This means every rate of change of any distributed property for the fluid varies in two components, one due to the time variation of the property at any location, and one due to the motion of the element in the flow medium available for that element.

Knowing this approach, the governing equations can be written to explain the fluid motion; starting with the conservation of mass. For the given density and velocity vectors, and a volume of element δV , the mass element $\delta m = \rho\delta V$ must be constant;

$$\frac{d(\rho\delta v)}{dt} = \delta v \frac{D\rho}{Dt} + \rho \frac{d(\delta v)}{dt} = 0 \quad [2-12]$$

By dividing by the volume of the element, the continuity equation is obtained:

$$\frac{D\rho}{Dt} + \rho \cdot \nabla \mathbf{V} = 0 \quad [2-13]$$

This equation can be rewritten as:

$$\frac{\partial\rho}{\partial t} + \mathbf{V} \cdot \nabla\rho + \rho \cdot \nabla\mathbf{V} = \frac{\partial\rho}{\partial t} + \nabla(\rho\mathbf{V}) = 0 \quad [2-14]$$

Alternatively, in cylindrical coordinates, the equation can be written as:

$$\frac{1}{r} \left\{ \frac{\partial}{\partial x} (r\rho u) + \frac{\partial}{\partial r} (r\rho v) \right\} = 0 \quad [2-15]$$

In incompressible fluids, the density can be considered constant, in which the equation simplifies further to just a gradient of volume. However, in SCW, this is not the case due to the significant density changes through the pseudocritical point. Thus, the equation remains as is.

The next conservation equation concerns momentum, as stated by Newton's second law; the rate of change of momentum of a body is equal to the net force acting on it:

$$\frac{d}{dt} (mV) = F \quad [2-16]$$

For a fluid element in a flow medium the left-hand side of the equation becomes:

$$\rho \frac{D}{Dt} (V) = \rho \left[\frac{\partial}{\partial t} (V) + (V \cdot \nabla) V \right] \quad [2-17]$$

In the Cartesian coordinates, the velocity term has three components (u, v, w) and the equation can be rewritten in terms of each component. For an analysis in the 2D plane, and using the cylindrical system, the equations become:

$$\frac{1}{r} \left\{ \frac{\partial}{\partial x} (r\rho u^2) + \frac{\partial}{\partial r} (r\rho v u) \right\} = -\frac{\partial p}{\partial x} + \rho g + \frac{1}{r} \left\{ 2 \frac{\partial}{\partial x} \left[r\mu_e \left(\frac{\partial u}{\partial x} \right) \right] + \frac{\partial}{\partial r} \left[r\mu_e \left(\frac{\partial u}{\partial r} + \frac{\partial v}{\partial x} \right) \right] \right\} \quad [2-18]$$

$$\frac{1}{r} \left\{ \frac{\partial}{\partial x} (r\rho u v) + \frac{\partial}{\partial r} (r\rho v^2) \right\} = -\frac{\partial p}{\partial x} + \frac{1}{r} \left\{ \frac{\partial}{\partial x} \left[r\mu_e \left(\frac{\partial v}{\partial x} + \frac{\partial u}{\partial r} \right) \right] + 2 \frac{\partial}{\partial r} \left[r\mu_e \left(\frac{\partial v}{\partial r} \right) \right] \right\} - \frac{2\mu_e v}{r^2} \quad [2-19]$$

The term μ_e is the effective viscosity defined by $\mu_e = \mu + \mu_t$ where the turbulent viscosity is defined as:

$$\mu_t = \rho C_\mu f_\mu \left(\frac{k^2}{\varepsilon} \right) \quad [2-20]$$

, where f_μ is a dampening function to account for the near wall effects (varies with each viscous model), and C_μ is an empirical constant.

Thus, the forces acting on the fluid element can be broken down into two categories; body forces and surface forces.

Body forces act on the mass of the fluid element directly, coming from an external source such as gravity, magnets, electric, etc. whereas the surface forces originate from the pressure and friction forces between the fluid elements themselves, and between the fluid and the walls. The momentum equation can be rewritten to express the flow in many ways depending on the assumptions made for each particular case, such as incompressible or inviscid fluids.

Similar to the case of mass and momentum, energy conservation can be expressed for fluid elements as:

$$\rho \frac{De}{Dt} = -\nabla \cdot q - p(\nabla \cdot V) + \dot{Q} \quad [2-21]$$

Where $e(x,t)$ is the internal energy per unit mass, and $q(x,t)$ is the heat flux vector. This can also be written in terms of specific enthalpy ($h = e + p/\rho$):

$$\rho \frac{Dh}{Dt} = \frac{Dp}{Dt} + \dot{Q} - \nabla \cdot q \quad [2-22]$$

The energy equation in the cylindrical coordinates can be rewritten as:

$$\frac{1}{r} \left\{ \frac{\partial}{\partial x} (r\rho u h) + \frac{\partial}{\partial r} (r\rho v h) \right\} = \frac{1}{r} \left\{ \frac{\partial}{\partial x} \left[r \left(\frac{\mu}{Pr} + \frac{\mu_T}{Pr_t} \right) \left(\frac{\partial h}{\partial x} \right) \right] + \frac{\partial}{\partial r} \left[r \left(\frac{\mu}{Pr} + \frac{\mu_T}{Pr_t} \right) \left(\frac{\partial h}{\partial r} \right) \right] \right\} \quad [2-23]$$

Where Pr is the molecular Prandtl number and Pr_t is the turbulent Prandtl number, it is usually used as a constant of 0.9.

After the definition of the conservation equations, boundary conditions must be defined. Boundary conditions are of great importance to CFD solutions since numerical methods cannot be solved without them. In any physical space, a finite control volume is selected for the simulation, and then the boundaries for that volume must be defined accurately for an adequate solution to be obtained.

Generally the boundaries can be defined as walls, inlet and outlet conditions. These, in turn, branch out into many conditions such as rigid or moving walls, inlet-vent, intake fan, mass-flow inlet, outlet, pressure outlet; etc... more on this subject will be discussed throughout the document.

2.6 CFD for SCW Flow

The prediction of turbulent flow is a very complicated computation, as turbulence is a fluctuation in the flow field in time and space. It is a complicated phenomenon because it is unsteady in three dimensions and consisting of multiple scales [15]. The same difficulty applies to experimental techniques as well. This is where numerical methods seem to have more promise, however it is still very hard to justify the solutions and verify them.

To reach solutions without relying on analytical methods, one can use simulations and modelling to approach the problem. The methods for simulations are direct numerical simulation (DNS) and large eddy simulations (LES), whereas the modelling consists of an approach named Reynolds-averaged Navier-Stokes (RANS) [3].

The DNS method is the most direct approach as it solves the Navier-Stokes equations without any modifications or simplifying assumptions. This results in a complete picture of every property field in the fluid domain, however it comes at the price of computational time. Even in the simplest of cases, the problem would take unrealistically large computational grids and would take a very long computational time, which renders it impractical.

This is where LES comes in to simplify the approach. The equations are solved for spatially filtered variables that represent the behaviour of the flow on relatively large length scales. The effects of the small-scale fluctuations add additional terms to the equations. These terms cannot be calculated directly; instead they have to be approximated.

On the other hand, modelling isn't intended to compute the actual realization of the flow, but rather the model system of equations for mean flow quantities, such as the velocity, pressure, Reynolds stresses, and so on. This would result in the flow characteristics that are averaged over many iterations, and hence the name, Reynolds Averaged Navier-Stokes. This method is very efficient computationally compared to LES and DNS, however that comes at the price of increasing errors introduced by the assumptions and approximations in the RANS model.

In practical engineering applications, RANS is the most used method, for its relative simplicity (less computational effort) and because mean flow characteristics are often sufficient for engineering problems. For more fundamental studies of flow physics, DNS is preferred, for its ability to completely simulate the flow behaviour. However, unless the analysis is done for small Reynolds numbers and in very limited and simplified flow domains, DNS is not a practical approach, and requires far greater computational resources than what is currently available. Since most flows exist in moderate to high Reynolds numbers, they are beyond the reach of DNS.

The LES approach is becoming more attractive recently for its ability to be used for fundamental science (with awareness of the errors it produces). Although it is still more expensive to conduct than RANS (this problem can be overcome with supercomputers), LES can add important information on moderate and large flow fluctuations and provides more accuracy than RANS.

2.6.1 RANS - Two-Equation Models

The turbulence models differ in accuracy and thus computational resources and time consumption. Some turbulence models are more suited to particular applications than others. Early work in understanding turbulent phenomena leading to CFD codes was more qualitative in nature [16], relying on high speed photography and measurement of thermos-physical properties within boundary layers to lay the groundwork for assumptions to be made regarding the modeling of turbulent boundary layers. The work contained in the thesis will employ the use of two-equation turbulence models in RANS; as such, these models are the focus of discussion in this document.

Turbulence models modify the unsteady Navier-Stokes equations by introducing averaged and fluctuating terms to produce the Reynolds Averaged Navier-Stokes equations, which model the mean values for flow quantities [17]. The averaging procedure introduces additional unknown terms containing products of the fluctuating quantities, which act like additional stresses in the fluid. These terms, called turbulent or Reynolds stresses, are difficult to determine directly and so become further unknowns.

The Reynolds stresses need to be modeled by additional equations of known quantities in order to achieve closure. Closure means that there are a sufficient number of equations for all the unknowns. The equations used to close the system define the type of turbulence model.

The most well-known two-equation energy transport turbulence model in the RANS method is the k - ϵ turbulence model developed by Jones & Launder [18]. The variables k and ϵ represent the total turbulent kinetic energy and the dissipation rate of said energy respectively. These variables account for the amount of kinetic energy present within an eddy, and the rate at which that energy is dissipated to the flowing fluid. The model works by conserving the energy contained within a turbulent region through transport equations that carry that

total energy (and its dissipation) along a geometrical flow path. The two quantities are described as follows:

$$k = \frac{\overline{u_x'^2} + \overline{u_y'^2} + \overline{u_z'^2}}{2} \quad \left(\frac{m^2}{s^2} \right) \quad [2-24]$$

Where u , v , and z represent the velocity components of the fluid contained within the three dimensional domain. The variable ϵ is dependent on k as well as a quantity called the eddy viscosity. Eddy viscosity governs the transport of kinetic turbulent energy, and is analogous to how molecular viscosity governs the transport of momentum of in a flowing fluid. The dissipative energy term ϵ is defined as follows:

$$\epsilon = \rho C_\mu \frac{k^2}{\mu_t} \quad \left(\frac{m^2}{s^3} \right) \quad [2-25]$$

Where ρ is the density of the fluid, μ_t is the eddy viscosity, and C_μ is a dimensionless proportionality constant (taken to be 0.09 as defined by the standard k - ϵ model). The definition of ϵ can be written in a more compact form:

$$\epsilon = \frac{k^{3/2}}{l} \quad \text{where} \quad l = \frac{\rho C_\mu}{\mu_t \sqrt{k}} \quad [2-26]$$

Where l is the characteristic turbulent length scale, representing the maximum diameter of an energy-containing eddy. The k - ϵ model is the most basic and documented turbulence model. Though it is able to solve many complex flows, it suffers deficiencies when attempting to solve certain types of problems including those with adverse pressure gradients in boundary layers, separated flows, and large re-circulating zones. Discrepancies between mathematical solutions and reality arise in part due to the k - ϵ model's dependence on a single turbulent length scale; l . To improve the accuracy of the k - ϵ model, the k - ω turbulence model was developed by Wilcox [19]. The k - ω turbulence model introduces a specific turbulent energy dissipation rate; ω . This quantity is a ratio of the terms k and ϵ :

$$\omega = \frac{\varepsilon}{k} \quad (s^{-1}) \quad [2-27]$$

The definition of the k - ω model removes the dependence of the single turbulent length scale, allowing for solutions encompassing any size of turbulent eddy generation. This allows for a more accurate description of fluid flow as the k - ε model can struggle to resolve very fine boundary layers near walls as the mesh in this region is often stretched out. The k - ω model however is able to resolve small distances near walls and the no-slip boundary condition at the wall is conserved. The k - ω model is better at resolving fine details contained within the boundary layer. The k - ω model is however sensitive to free stream values of ω far from the boundary layer at the wall, and so the k - ω Shear Stress Transport (SST) model was developed to overcome this deficiency [20]. This model hinges on Bradshaw's assumption, that the turbulent shear stress near the wall is proportional to the amount of turbulent kinetic energy present [21]. The k - ω SST model is essentially a blend of standard k - ε and k - ω models, utilizing the boundary layer treatment of the k - ω and far from the wall treatment of k - ε to better represent a fluid flow.

The general form of the models can be expressed as:

$$\left\{ \frac{\partial}{\partial x} (\rho u k) + \frac{1}{r} \frac{\partial}{\partial r} (r \rho v k) \right\} = \frac{\partial}{\partial x} \left[\left(\mu + \frac{\mu_t}{\sigma_k} \right) \frac{\partial k}{\partial x} \right] + \frac{1}{r} \frac{\partial}{\partial r} \left[r \left(\mu + \frac{\mu_t}{\sigma_k} \right) \frac{\partial k}{\partial r} \right] + P_k + G_k - \rho(\varepsilon - D) \quad [2-28]$$

P_k is the production term due to the mean velocity gradient:

$$P_k = \mu_t \left[2 \left\{ \left(\frac{\partial u}{\partial x} \right)^2 + \left(\frac{\partial v}{\partial r} \right)^2 + \left(\frac{v}{r} \right)^2 \right\} + \left(\frac{\partial u}{\partial r} + \frac{\partial v}{\partial x} \right)^2 \right] \quad [2-29]$$

The gravitational production term is computed by the equation:

$$G_k = \overline{\rho' u'} g_x = c_\theta \beta \rho g x \frac{k}{\varepsilon} \left[\mu_T \left(\frac{\partial u}{\partial r} + \frac{\partial v}{\partial x} \right) \left(\frac{\partial T}{\partial r} \right) + \left(2 \mu_T \frac{\partial u}{\partial x} - \frac{2}{3} \rho k \right) \left(\frac{\partial T}{\partial x} \right) \right] \quad [2-30]$$

Where $g_x = -g$ for upward flow, $g_x = g$ for downward flow and $c_\theta = 0.3$.

Turbulent dissipation rate is represented as:

$$\left\{ \frac{\partial}{\partial x} (\rho u \epsilon) + \frac{1}{r} \frac{\partial}{\partial r} (r \rho v \epsilon) \right\} = \frac{\partial}{\partial x} \left[\left(\mu + \frac{\mu_t}{\sigma_\epsilon} \right) \left(\frac{\partial \epsilon}{\partial x} \right) \right] + \frac{1}{r} \frac{\partial}{\partial r} \left[r \left(\mu + \frac{\mu_t}{\sigma_\epsilon} \right) \left(\frac{\partial \epsilon}{\partial r} \right) \right] + C_{\epsilon 1} f_1 \left(\frac{1}{T_t} \right) (P_k + G_k) - C_{\epsilon 2} f_2 \left(\frac{\rho \epsilon}{T_t} \right) + \rho E \quad [2-31]$$

The constants $C_{\epsilon 1}$ and $C_{\epsilon 2}$ and the functions f_1 and f_2 are model specific. In a similar manner, the specific dissipation rate is:

$$\left\{ \frac{\partial}{\partial x} (\rho u \omega) + \frac{1}{r} \frac{\partial}{\partial r} (r \rho v \omega) \right\} = \frac{\partial}{\partial x} \left[\left(\mu + \frac{\mu_t}{\sigma_\omega} \right) \left(\frac{\partial \omega}{\partial x} \right) \right] + \frac{1}{r} \frac{\partial}{\partial r} \left[r \left(\mu + \frac{\mu_t}{\sigma_\omega} \right) \left(\frac{\partial \omega}{\partial r} \right) \right] + G_\omega - Y_\omega + S_\omega + D_\omega \quad [2-32]$$

G_ω is the generation of ω , Y_ω is the dissipation of ω , S_ω is a user defined source term, and D_ω is a cross diffusion term.

One more topic of importance in computational fluid dynamics is that of how the boundary layer solutions are obtained. The variable *wall* y^+ , also known as the dimensionless wall distance, defines the structure of the boundary layer and gives a measure of how accurately it is resolved. The definition of y^+ follows:

$$y^+ = \frac{\rho \mu_* y}{\mu} \quad [2-33]$$

Where ρ , μ , and y represent the density, molecular viscosity, and physical distance from the wall, while μ_* is the frictional velocity of the flow and is defined as:

$$\mu_* = \sqrt{\frac{\tau_{wall}}{\rho}} \quad [2-34]$$

With τ_{wall} being the shear stress at the wall, and again ρ represents the density of the fluid. A generally accepted value of *wall* $y^+ < 5$ indicates an adequately resolved boundary layer. It is however recommended to modify the boundary layer of a mesh such that its values of *wall* y^+ fall near the value of unity at the wall.

An earlier analysis has been done by Sharabi [22] [23], for the prediction of heat transfer in an experimental dataset provided by Pis'menny [24]. The experimental dataset was for supercritical water in bare tubes flowing both upwards and downwards. At an operating pressure of 23.5 MPa, it is in the proposed range for SCWR's. The test section was a stainless tube heated uniformly by direct electric current. The study involved both $k-\epsilon$ and $k-\omega$ models with low-reynolds correction to estimate the wall temperatures in the steady state environment.

The results from that analysis show that the models reasonably simulate the heat transfer conditions in the low heat and mass fluxes regions.

Even though the $k-\epsilon$ is able to detect the deterioration of heat transfer when the wall temperatures exceed the pseudo-critical temperature, it overestimates the wall temperatures after the deterioration region and do not recover sufficiently after the peak.

The $k-\omega$ model is much less reliable in predicting the same conditions, and produces discontinuities along the heated length in deteriorated conditions. Analysis was then also conducted using STAR-CCM+ code which showed very similar results in using the $k-\epsilon$ with the low-Re corrections.

Another study, conducted by Gu et al. [25] proved the same results again near the deteriorated heat transfer regime. The $k-\omega$ SST however produced more accurate results when using the full buoyancy effects in the model.

2.6.2 Boundary Layer Resolution

The next topic to consider is the dimensionless wall distance, y^+ . In some ways, the y^+ concept is analogous to the Reynolds number. The y^+ is used generally in CFD to describe how coarse or fine the mesh is for a flow pattern. It is important in turbulence modeling to determine the proper size of the cells near the wall to arrive at accurate solutions from the viscous models.

Near-wall regions have large gradients in the solution variables, and the momentum transport occurs more actively [26]; from Figure 2-2 it can be seen that viscosity affected region (the boundary layer of the flow) can be made up of three zones, according to their y^+ values:

- Viscous sublayer, $y^+ < 5$.
- Buffer layer (blending region), $5 < y^+ < 30$.
- Fully turbulent (log-law region), $30 < y^+$.

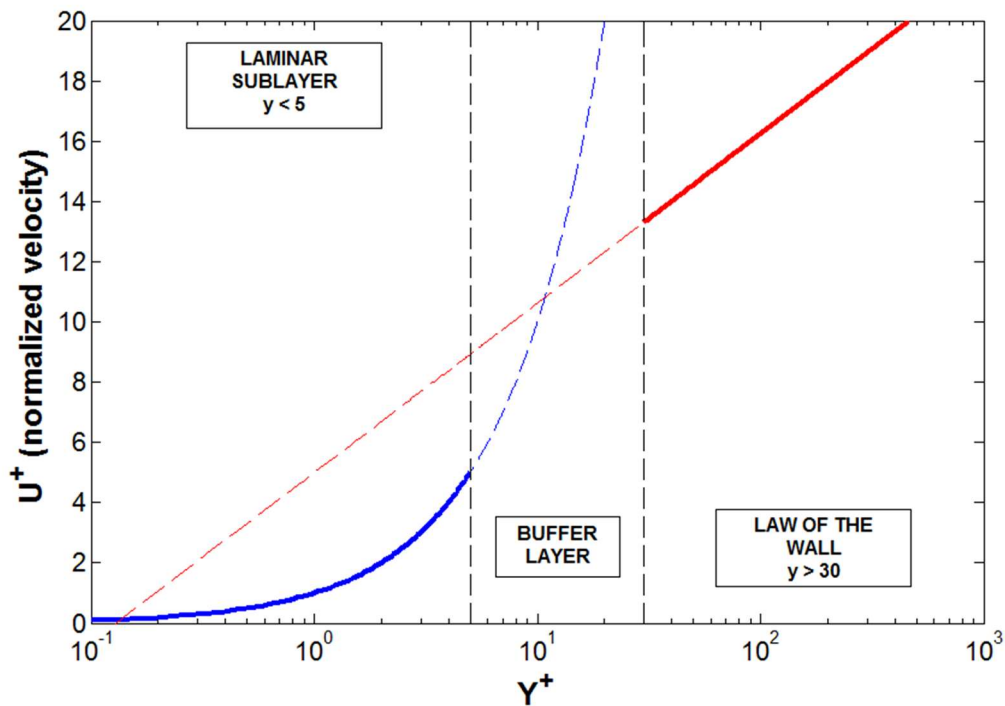


Figure 2-2: Flow layers from the wall to the fully developed stream according to Y^+ values [27]

Thus the y^+ is often used in CFD to describe the ratio between turbulent and laminar influences in a computational cell. Very close to the wall, the viscous dampening reduces the velocity fluctuations, however near the outer layer the velocity has larger gradients which aids in creating more turbulence (as the turbulence production is proportional to the gradient of velocity).

Different models have different restrictions on the y^+ value at the wall. For example the $k-\epsilon$ uses wall functions to estimate the properties near the wall and thus requires wall y^+ values in the order of ~ 30 . The $k-\omega$ shear stress transport model on the other hand is better suited for resolving near wall effects and thus a y^+ value of ~ 1 is much more appropriate for its use [27] [28].

The y^+ calculation is used to define the first node in the mesh near the wall; however the density of the mesh in the boundary layer is of great importance as well. A 3-D mesh is proposed for some of the following work, so the layers can be composed of prism cells in the boundary layer and tetrahedral cells in the free stream region. Analysis will be conducted on the best density for each viscous model, to conclude which model provides an accurate solution at the best computational cost.

2.7 Turbulent Prandtl Number

The work on turbulent Pr number is important in the context of supercritical water simulations, due to the fact that all CFD turbulence models were developed for applications involving generalized subcritical flows [29] [30].

The turbulence models themselves are a set of equations that determine the turbulence transport terms in the mean flow equations. They are based on hypotheses about the process of turbulence (which is not fully understood yet), and as such require empirical input in the form of constants or functions, in order to achieve closure. Closure in this context means having sufficient equations for the number of unknowns to be solved. By introducing a set of empirical constants to a model, that model then becomes valid for certain flow conditions, or for a range of flows.

Of those constants, the turbulent Prandtl number appears in multiple equations; energy, momentum, turbulent kinetic energy, turbulent kinetic energy dissipation rate, etc... and the value it takes in each equation is different and chosen

empirically to fit a wide range of flows in the subcritical region. The studies that attempt to find the effect of varying the Pr_t number on simulation results, often only mention one number; presumably the one that appears in the energy equation (although it is never explicitly explained) [31] [32]. The rest of the constants are treated as universally acceptable for generalized flow (even in cases of subcritical flow) and not tested for their effect on flow parameters.

In this work, an attempt is made to explore the effects of these turbulent Pr numbers, in order to understand their significance, and to build on previous knowledge to modify the turbulence models and achieve higher accuracy in simulating experimental conditions.

The semi-empirical models use constants and coefficients developed for general use for a large multitude of fluids, flow conditions and geometries. A better understanding of the physical importance of these coefficients is required to improve the models' accuracy and provide realistic profiles for the fluid temperatures, as well as the associated fluid and flow properties.

The formation of the turbulent Pr number stems from solving the conservation equations. To arrive at the definition, a case of constant fluid properties and viscous dissipation can be considered. The differential equations that must be satisfied in the boundary layer flow can be expressed as:

Continuity:

$$\frac{\partial u}{\partial x} + \frac{\partial v}{\partial y} = 0 \quad [2-35]$$

Momentum:

$$u \frac{\partial u}{\partial x} + v \frac{\partial u}{\partial y} + \left(\frac{1}{\rho}\right) \frac{dP}{dx} = \frac{\partial}{\partial y} \left(\nu \frac{\partial u}{\partial y} - \overline{u'v'} \right) \quad [2-36]$$

Energy:

$$u \frac{\partial t}{\partial x} + v \frac{\partial t}{\partial y} = \frac{\partial}{\partial y} \left(\alpha \frac{\partial t}{\partial y} - \overline{t'v'} \right) \quad [2-37]$$

The eddy diffusivity concept defines the two quantities:

$$\overline{u'v'} = -\epsilon_M \left(\frac{\partial u}{\partial y} \right) \quad [2-38]$$

$$\overline{t'v'} = -\epsilon_H \left(\frac{\partial t}{\partial y} \right) \quad [2-39]$$

Where $\overline{u'v'}$ and $\overline{t'v'}$ are the turbulent shear stress and the turbulent heat flux respectively, which are products of the time averaged values for instantaneous fluctuation of velocity and temperature terms. ϵ_M and ϵ_H are the eddy diffusivity terms for momentum and heat respectively.

If placed in equations for momentum and energy, they become:

$$u \frac{\partial u}{\partial x} + v \frac{\partial u}{\partial y} + \left(\frac{1}{\rho} \right) \frac{dP}{dx} = \frac{\partial}{\partial y} \left((\nu + \epsilon_m) \frac{\partial u}{\partial y} \right) \quad [2-40]$$

$$u \frac{\partial t}{\partial x} + v \frac{\partial t}{\partial y} = \frac{\partial}{\partial y} \left((\alpha + \epsilon_H) \frac{\partial t}{\partial y} \right) \quad [2-41]$$

By relating to the molecular Pr number:

$$Pr = \frac{\nu}{\alpha} = \frac{\text{viscous diffusion rate}}{\text{thermal diffusion rate}} = \frac{c_p \mu}{k} \quad [2-42]$$

The turbulent Pr number can be defined as the ratio of the momentum eddy diffusivity (eddy viscosity) and the heat transfer eddy diffusivity.

$$Pr_t = \frac{\epsilon_m}{\epsilon_h} \quad [2-43]$$

By substituting back into the energy equation:

$$u \frac{\partial t}{\partial x} + v \frac{\partial t}{\partial y} = \frac{\partial}{\partial y} \left(\nu \left[\frac{1}{Pr} + \frac{\epsilon_M}{\nu} \right] \frac{\partial t}{\partial y} \right) \quad [2-44]$$

If a solution to the momentum equation was available, then the values u , v , and ϵ_M will follow in the energy equation. The only term needed then to solve the energy equation is the turbulent Pr number.

Knowing the correct turbulent Pr number is necessary for accurate description of the flow and heat transfer characteristics of the flow in the boundary layer, especially in two-dimensional boundary layer problems or flows in a long pipe or ducts [33]. In such cases the most important turbulent heat diffusion is only in the direction normal to the flow, thus using higher level turbulence models becomes extremely complicated. These models use a very large number of experimentally determined constants, a lot of which have not been accurately determined yet.

The use of the turbulent Pr number which implements the eddy diffusivity of momentum and heat is much simpler on the other hand, and is capable of accurately predicting the boundary layer behavior in most engineering related situations [34] [35] [36].

The simplest model to describe the turbulent heat transfer results in:

$$\epsilon_H = \epsilon_M \rightarrow Pr_t = 1$$

This is known as the Reynolds analogy between shear stress and heat transfer [37]. In experimental cases for gas streams, this relationship seems to apply with good agreement if the molecular Prandtl number is near 1.0. When applied to liquids however, this analogy is known to be invalid [38].

Study of the literature shows a gap in the understanding of the turbulent Pr number effect, especially as it has many variants in each of the models, such as turbulent kinetic energy Pr, turbulent dissipation rate Pr, energy Pr, and wall Pr. This is related to a different empirical approximation for the Pr number for turbulent flow eddies in different area of the flow; near wall boundary layer, large

eddies near the bulk fluid, or approximations for the equations for turbulent kinetic energy and its dissipation rate [17] [33] [39].

The numbers were selected as empirical constants for generalized flows and thus do not necessarily apply to fluids with a large variance of Pr numbers. From gases to water and to liquid metal for example yields changes in Pr at 2 orders of magnitude. The corresponding change in turbulent Pr numbers is much less dramatic, and falls in intervals as small as 0.7-0.9 [33] [40].

The various turbulent Prandtl numbers that appear in the Realizable k- ϵ and k- ω SST are shown below [28]:

- TKE Prandtl Number:

(Standard or Realizable k- ϵ model, the standard or SST k- ω model) is the effective Prandtl number for transport of turbulence kinetic energy. This effective Prandtl number defines the ratio of the momentum diffusivity to the diffusivity of turbulence kinetic energy via turbulent transport.

- TKE (Inner) Prandtl:

(Only for the SST k- ω model) is the effective Prandtl number for the transport of turbulence kinetic energy, inside the near-wall region.

- TKE (Outer) Prandtl:

(Only for the SST k- ω model) is the effective Prandtl number for the transport of turbulence kinetic energy, outside the near-wall region.

- TDR Prandtl Number:

(For the standard or realizable k- ϵ model) is the effective Prandtl number for transport of the turbulent dissipation rate. This effective Prandtl number defines the ratio of the momentum diffusivity to the diffusivity of turbulence dissipation via turbulent transport.

(For the standard k- ω model) the TDR Prandtl Number is the effective Prandtl number for the transport of the specific dissipation rate.

- SDR (Inner) Prandtl:

(Only for the SST $k-\omega$ model) is the effective Prandtl number for the transport of the specific dissipation rate, inside the near-wall region.

- SDR (Outer) Prandtl:

(Only for the SST $k-\omega$ model) is the effective Prandtl number for the transport of the specific dissipation rate, outside the near-wall region.

- Energy Prandtl Number:

(For both $k-\epsilon$ and $k-\omega$ models) is the turbulent Prandtl number for energy, in the energy production due to buoyancy equation.

- Wall Prandtl Number:

(For all turbulence models) is the turbulent Prandtl number at the wall, in temperature wall functions equations.

- $C2\epsilon$:

(For Realizable $k-\epsilon$ model) is an empirical constant used in the transport equation for ϵ .

Recently, there have been a number of papers published about the topic of a variable turbulent Pr number to aid supercritical water simulations [41] [42] [43]. By using empirical and DNS data, it can be seen that the turbulent Pr number, which is a property of the flow, changes from about 0.7 in the core flow to 1.1 near the wall, for fluids such as air and water at normal pressures. The premise of these studies was to formulate an expression to capture the variability of Pr_t in supercritical flow. However, due to the lack of any experimental data in supercritical conditions, the formulation had to be purely mathematical in nature, and reliant on empirical weights of various variables, such as pressure, diameter of flow channel, and the molecular weight of the fluid material.

The approach is somewhat similar to that taken by the developers of empirical Nusselt number correlations discussed earlier. While this method has shown improvement in the prediction of heat transfer against standard models, the

deviations from experimental data was still upwards of 30% for wall temperatures and heat transfer coefficients. Another concern is the lack of clarity when it comes to defining the turbulent Pr number modified in the numerical model. As shown earlier, there are multiple Pr_t numbers, and no study mentions which one is modified or which equation they appear in.

Due to these issues, it is very difficult to replicate the findings, due to the ambiguity in the creation of the variable expression, and its usage in the numerical model.

Finally, in the analysis of the modified models, the studies show the comparison between the wall temperatures predicted by each model, but without any indication of the effects on the fluid flow properties, such as turbulence levels, pseudocritical point propagation, velocity profiles, etc.

2.8 Integration of Numerical Model in Computational Domain

The numerical models, are used to calculate the fluid properties in the computational domain, or grid. The grid shape and cell count depends on the case, the geometry, and the accuracy required from the solution.

The most common numerical methods used in the CFD programs to reach a solution are:

- The finite volume method has the broadest applicability (~ 80% of cases)
- Finite element (~15%)

There are many other approaches used less commonly in commercial CFD programs such as finite difference, boundary element, vorticity based methods, etc. [44].

The finite difference is the oldest method of the mentioned above, and was used for the first numerical solution in a flow over a circular cylinder. It is very popular due to its simplicity, however it has the disadvantage of being restricted to simple grids and does not conserve momentum, energy and mass on coarse grids.

Finite element method (FEM) on the other hand is used mostly for analyzing structural mechanics problems. It was adapted later for fluid flow, with the advantage of high accuracy on coarse grids especially for viscous flow problems. However it is slow for large problems and not very well suited for turbulent flows.

This brings the attention to finite volume method which was developed after the two mentioned approaches, and gained approval due to the conservation of mass, momentum and energy even when the variables go through discontinuities in the grid. In addition, the memory usage and speed are enhanced over large grids, higher speed flows, and turbulent flows [44].

The basic methodology in finite volume is the following [45]:

- Divide the domain into control volumes.
- Integrate the differential equation over the control volume.
- Values at the control volume faces are used to evaluate the derivative terms, using assumptions to how the value varies.
- The result is a set of linear algebraic equations; one for each control volume.
- The equations are solved iteratively or simultaneously until convergence is achieved.

Figure 2-3 shows how the solution domain is divided into a finite number of small control volumes (cells).

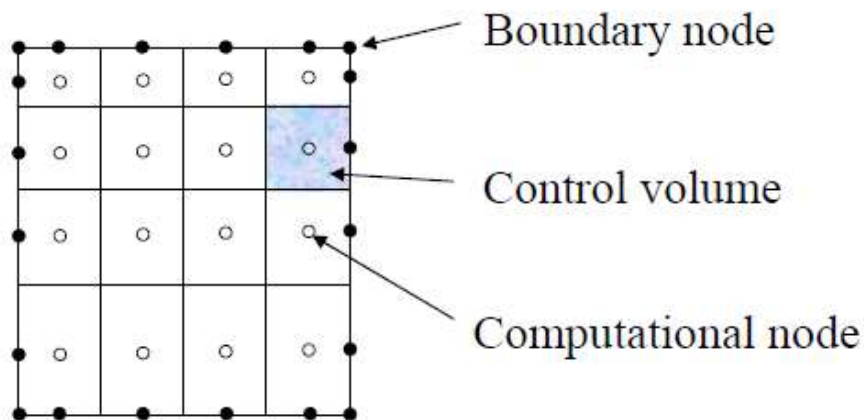


Figure 2-3: Solution domain division into control volumes

2.9 Geometry Considerations

2.9.1 Nuclear Fuel Bundle

The geometry in a nuclear fuel bundle is a complicated one. The proposed designs for the SCWR fuel bundles are similar in nature to the current geometries in CANDU reactors, and both have the following features:

- end plates,
- end caps,
- bearing pads, and
- spacers.

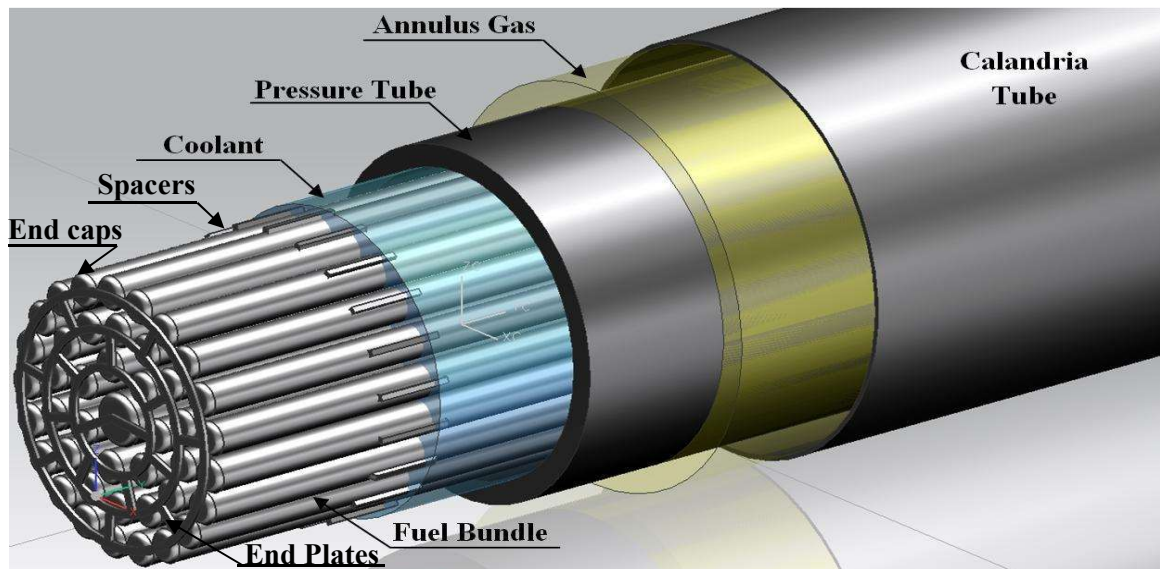


Figure 2-4: CANDU fuel bundle geometry, courtesy of W. Peiman

By analyzing the flow through these geometric perturbations, a flow pattern that resembles the flow through an orifice emerges. Consequently, Idelchik's orifice equations are used for fuel bundle loss coefficient calculations [46] [47], as an application of sudden area change treatment to appendages.

The rest of the fuel channel includes further obstacles, such as flow measuring and control devices. A common control device in CANDU-type reactors is a variable

flow orifice plates at channel inlets, adopted in CANDU6 and Darlington reactors [48].

In the latest SCWR designs, the flow will enter a plenum, which then diverts the flow into individual fuel channels using orifices to control the flow and maintain an outlet temperature of 625°C for all channels [49].

2.9.2 Endplate Geometry

Previous work has been done on fuel bundle geometries to establish geometry effects on SCW flow. One problem that affects simulations on SCW flow in complex geometries, is the immense computational time and resources needed for such simulations, even under the simplest flow conditions. As such a study by Jesse Saunders et al. [50] using computational sources available at UOIT, could only produce viable results using adiabatic conditions in a stair-step mesh setup as illustrated in Figure 2-5. Figure 2-6 shows the test section, which consists of two bare half-bundles with an endplate in halfway through the flow length. The test is adiabatic at supercritical conditions, and the velocity fields are studied to show areas of blockage and flow acceleration.

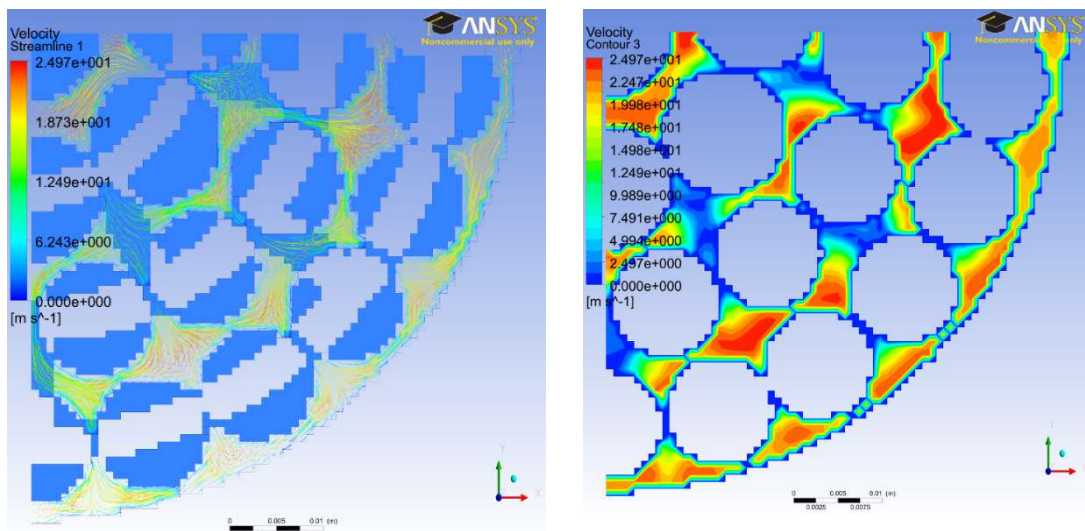


Figure 2-5: Stair-step mesh study on endplate geometry [50]

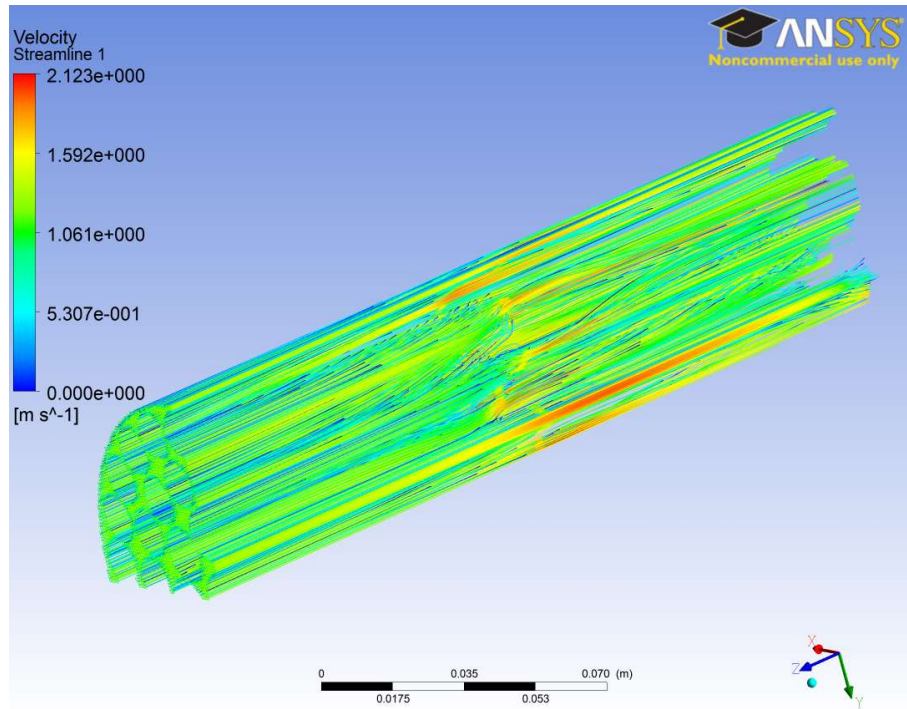


Figure 2-6: Visualization of flow through two half-bundles with an endplate in the center of the flow length [50]

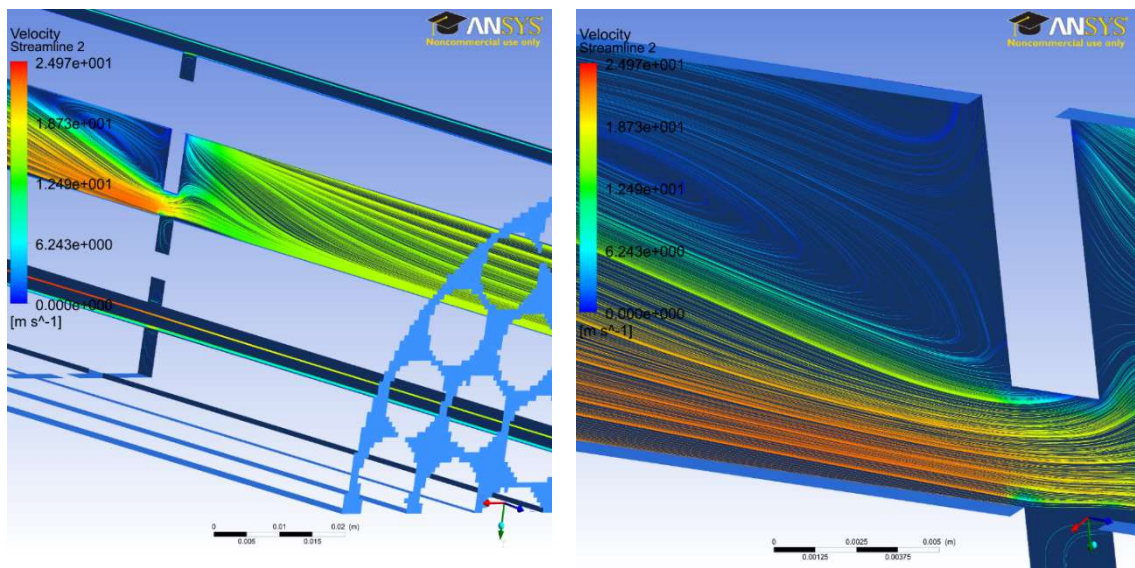


Figure 2-7: Cross-sectional flow visualization through endplate geometry [50]

Analyzing the flow by means of cross sectional visualization around the endplate, the flow behavior is shown to mimic that of an orifice geometry; producing a sudden area change. The flow is contracted, followed by a sudden expansion,

producing flow stagnation and recirculation at the blockage and acceleration through the open flow area.

2.9.3 Other Studies

The problem with adding complex geometries to CFD simulations is a universal one, and many authors address it in their studies. The result is most studies analyze phenomena such as single- and multi-subchannel flows (examples shown in Figure 2-8 and Figure 2-9) in smooth, bare geometries without flow obstacles [51] [52].

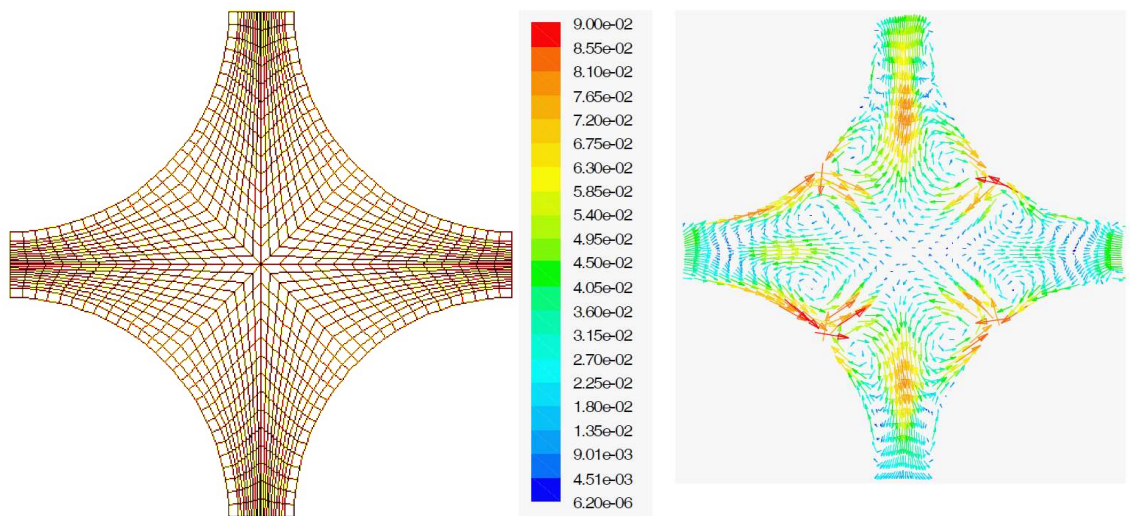


Figure 2-8: An Example of a Subchannel CFD analysis for SCWR rod bundle [51]

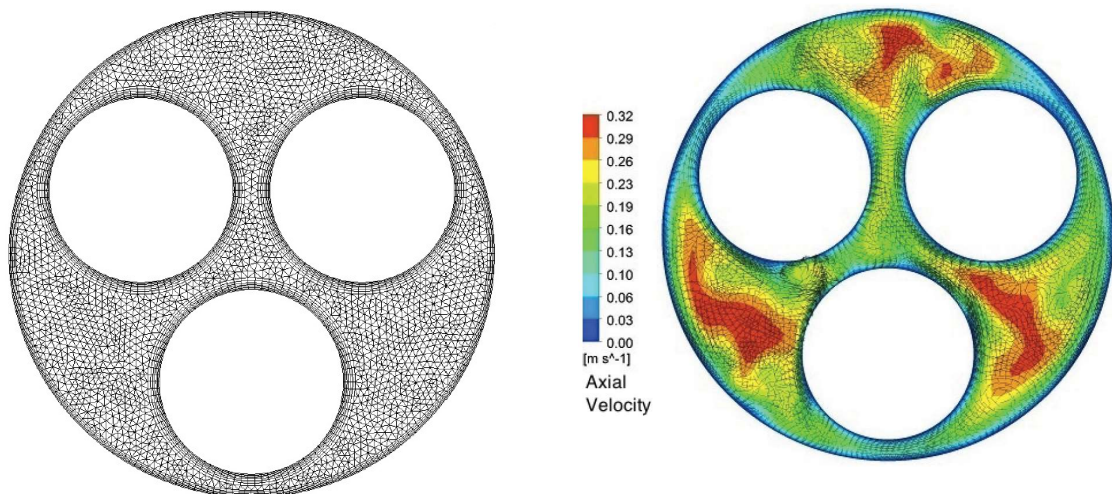


Figure 2-9: An Example of a 3-Rod Bundle Inter-subchannel CFD analysis [52]

Chapter 3: Methodology

In order to achieve the objectives set out for this work, a methodology was developed to describe the needed tasks and how they relate to their corresponding objectives. The focus of the work is on utilizing CFD models in FLUENT to simulate the flow of SCW in various geometries and under different conditions.

The first step is to compare the simulations to a benchmark in the form of existing experimental data. By verifying the results against the experimental data, they can be then evaluated for capturing the physical phenomena occurring at or near the supercritical region. A set of experimental data for SCW flow in vertical bare tubes is used as the reference model and for select model sensitivity analysis. A second set of experimental data for SCW flow in an annular channel with helical ribs is used for assessment of geometrical effects.

The next step in meeting objective #1 - empirical constants analysis - is to observe and analyze the effects on the simulation results in response to modifying key model parameters. By varying the turbulent Pr number for example, the flow characteristics will change, and those changes can be compared to the benchmark data.

Finally, to study a more realistic approximation of the geometrical perturbations that might be found in a reactor setting, a simple pipe geometry can be modified with appendages such as a sudden area change (as explained in section 2.9) to determine the important flow parameters that capture the localized flow phenomena as part of meeting objective #2.

Sections 3.1 and 3.2 describe the bare tube experimental dataset and the annular channel experimental dataset. Section 3.3 provides the methodology for meshing each geometry. Section 3.4 provides the methodology for analysis using FLUENT.

3.1 Bare Tube Experimental Dataset and Test Facility

A large dataset was made available by the Institute for Physics and Power Engineering (Obninsk, Russia), with conditions similar to those of pressure tube type Supercritical Water-cooled Reactor (SCWR) concepts currently proposed by Canada [53]. This dataset includes 80 configurations of heat and mass flux. The experiments conducted by Kirillov et al. [53] with SCW provide data which can be used to benchmark the ability of the FLUENT code to solve heat and mass transfer problems in the supercritical region.

The SKD-1 loop, shown in Figure 3-1, is a high-temperature and high-pressure pumped loop, capable of achieving 28 MPa and outlet temperatures of up to 500°C [4]. The working fluid is distilled and de-ionized water. The test section consists of a four-meter long vertically oriented pipe of inner and outer diameters of 10 mm and 14 mm respectively. The diameter is close to the 7.26 mm hydraulic-equivalent diameter of the proposed 62-element SCWR fuel assembly [54]. The pipe wall material is stainless steel of 12Kh18N10T type, with an average surface roughness height of 0.63-0.8 μm . The experiments encompass a wide range of operating parameters at a pressure of 24 MPa with inlet temperatures ranging from 320°C to 350°C. Mass fluxes range from 200 – 1,500 kg/m²s while heat fluxes up to 1,250 kW/m² were used for several combinations of wall and bulk-fluid temperatures that were at, below, or just above the pseudocritical temperature. Table 3-1 identifies the range of conditions for the Kirillov et al. Experiments. The highlighted regions are the ones closely related to the proposed conditions for SCWR's operation and hence of most interest to this work.

Compressed water was pumped upwards through the test section at four different mass flux groupings of 200, 500, 1,000, and 1,500 kg/m²s. Each group of mass flux was pumped through the test section and heated by passing an electrical current through the pipe (600 kW AC power supply, provided by copper clamps on each end of the tube), creating a uniform heat flux distribution. The test section is

wrapped with thermal insulation to minimize heat loss. The effective surface heat flux varied in the range 73–1,250 kW/m² with the lowest heat flux corresponding to the lower mass flux groups and vice versa. All experiments were performed at an inlet pressure of 24±0.1 MPa. For each group of mass flux, the inlet temperature was varied so that the enthalpy increase along the length of the pipe varied within the group. The inlet temperature was set to less than 25°C from the pseudocritical point in each case to capture subtle changes that occur when approaching the pseudocritical point. Some of the low heat flux cases were modeled so that the pseudocritical point is located just before the fluid exits the heated length.

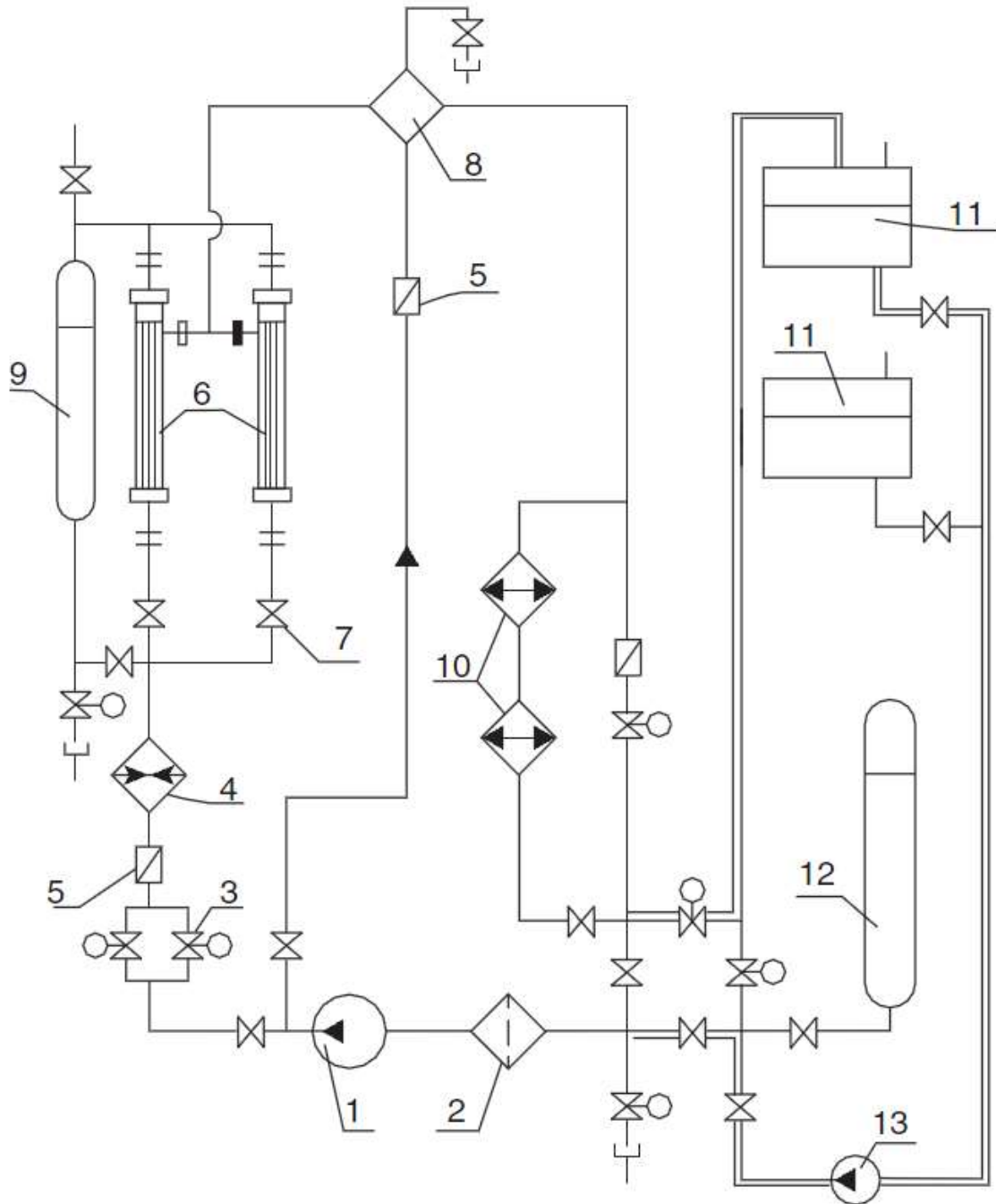


Figure 3-1: SKD-1 loop schematic : 1-Circulating pump, 2-mechanical filter, 3-regulating valves, 4-electrical heater, 5-flowmeter, 6-test section, 7-throttling valve, 8-mixer-cooler, 9-discharge tank, 10-heat exchangers-main coolers, 11-feedwater tank, 12-volume compensator, and 13-feedwater pump [53]

Table 3-1: Kirillov et al. Dataset Ranges [53]

Mass Flux ($\frac{kg}{m^2s}$)	Pressure Range (MPa)	Bulk Fluid Temperature (°C)	Heat Flux Range ($\frac{kW}{m^2}$)
200	24.0 - 24.2	320 - 450	73 - 214
500	24.0 - 24.2	325 - 450	141 - 454
1,000	23.9 - 24.1	325 - 425	392 - 826
1,500	24.0 - 24.1	320 - 425	489 - 1,256

*Highlighted regions closest to proposed SCWR normal operating conditions

Table 3-2: Uncertainties of primary parameters [53]

Parameter	Maximum Uncertainty
Test-section power	±1.0%
Inlet pressure	±0.25%
Wall temperatures	±3.0°C
Mass-flow rate	±1.5%
Heat loss	≤ 3%

Eighty-one chromel-alumel thermocouples were used to measure the outer wall temperature of the pipe at intervals of 5 mm spaced axially. The inner wall temperature was calculated by using a correlation to provide theoretical inner wall temperatures, assuming uniformly distributed heat-generation sources [55]:

$$T_w^{int} = T_w^{ext} + \frac{q_{vl}}{4k_w} \left[\left(\frac{D_{ext}}{2} \right)^2 - \left(\frac{D}{2} \right)^2 \right] - \frac{q_{vl}}{2k_w} \left(\frac{D_{ext}}{2} \right)^2 \ln \left(\frac{D_{ext}}{D} \right) \quad [3-1]$$

Where k_w is the thermal conductivity of the wall, and q_{vl} represents the volumetric heat flux depicted as;

$$q_{vl} = \frac{Q}{\frac{\pi}{4}(D_{ext}^2 - D^2)L_l} \quad [3-2]$$

The term L_l represents the local heated length, and Q is the measured power calculated as the product of the voltage and current through the tube wall. The data provided for the analysis consists only of the calculated inner-wall temperatures. A typical set of inside-wall temperature points are shown in red (•) in Figure 3-2.

With this information, and the inlet and outlet temperatures of the water, bulk fluid temperatures were calculated from the enthalpy rise using a heat balance equation (blue line in Figure 3-2). Knowing the inner wall and the bulk fluid temperatures, calculations of the effective heat transfer coefficient (black points ♦ in Figure 3-2) were performed using the equation:

$$HTC = \frac{q}{T_{wall} - T_{bulk}} \quad \left(\frac{kW}{m^2K} \right) \quad [3-3]$$

An empirical correlation was proposed for deteriorated heat-flux calculations in which the DHT appears (for details, see reference [6]):

$$q_{dht} = -58.97 + 0.745 G, \text{ kW/m}^2 \quad [3-4]$$

The experimentally estimated heat transfer coefficients and those calculated using empirical correlations can be compared to the results from FLUENT simulations to determine the accuracy of FLUENT in SCW conditions and establish a benchmark for comparison.

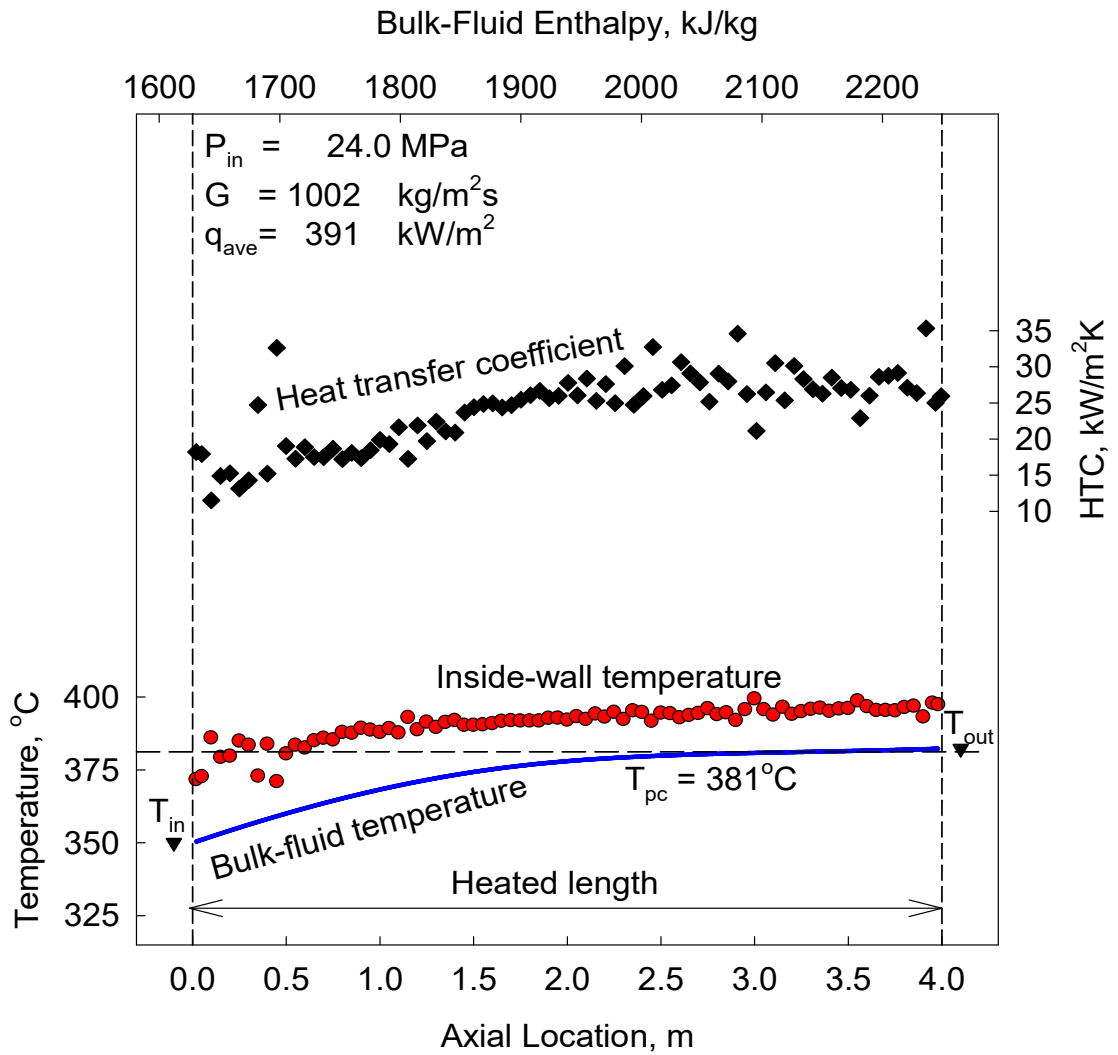


Figure 3-2: Sample experimental run from the Kirillov et al. dataset [53], with bulk-fluid, wall temperatures and heat transfer coefficients

3.2 Annular Channel Experimental Dataset and Test Facility

The second set of experimental data originated from the work at the National Technical University of Ukraine, Kiev Polytechnic Institute [56]. The SCW experimental setup is a stainless-steel loop operating at pressures up to 28 MPa and temperatures up to 700°C. The coolant used is a chemically desalinated water flowing upwards in a vertical test section, and heated directly with a 90 kW AC power supply. The experimental setup diagram is shown in Figure 3-3 for reference.

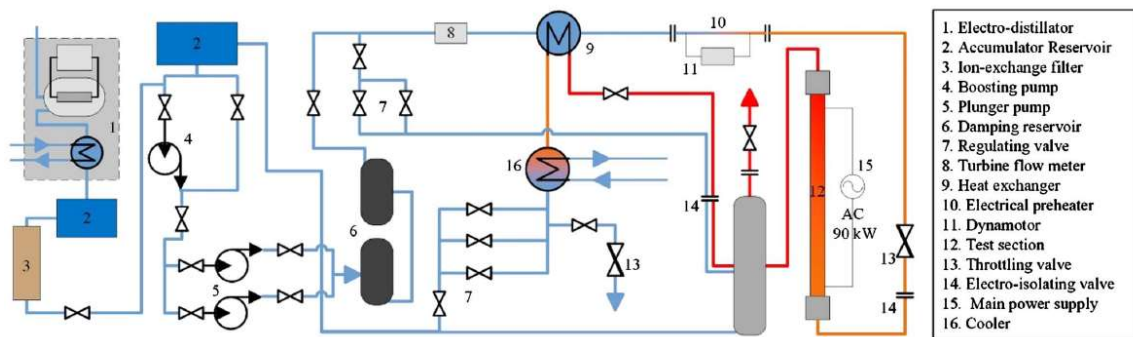


Figure 3-3: General Schematic of SCW Experimental Setup [56].

The heated element in the test section is a 485-mm long cylindrical rod with 4 helical ribs wound over a 400-mm pitch, as shown in Figure 3-4. SCW flows in the gap between the heated rod and the outer tube, in an equivalent hydraulic diameter of 2.7 mm, as calculated by:

$$D_{hy} = \frac{4 \cdot A_{fl}}{P_{wet}} \quad [3-5]$$

Wall temperatures in the test sections are measured using 7 thermocouples which are installed along the heated length of the inner surface of the heated rod (which is in fact a thin-walled tube) at 95, 195, 255, 315, 375, 415 and 475 mm from the inlet of the heated section. The first thermocouple is placed beyond the calculated entrance region of $L/D_{hy} > 25$. Each thermocouple is engraved into a copper plug of a diameter equal to the inner diameter of the inner tube. The plugs are then covered with a heat-resistant silicone resin that provides electrical insulation. This

method of installing the thermocouples allows for measurements of the average temperature in each cross section. The thermocouples are calibrated within the temperature range of 20-450°C.

As the measured wall temperatures were inside the heated rod, the outer-wall temperatures had to be determined numerically, by obtaining a general solution for a temperature distribution in a tube with uniform volumetric heat generation. By assuming steady-state conditions and one-dimensional radial heat conduction, equation (3-1) mentioned earlier can be utilized again.



Figure 3-4: Illustration of Heated Central Rod Annular Channel [56]

Bulk-fluid temperatures on the other hand were measured using chromel-alumel ungrounded sheathed thermocouples of 0.2-mm diameter inserted into the fluid

flow inside mixing chambers. Mixing chambers are used to minimize the non-uniformity in a cross-sectional temperature distribution and to dampen the pressure pulsations within the test sections. Inlet and outlet sections of hydrodynamic stabilization were provided.

The experimental parameters are varied for different runs to capture the various flow and heat transfer phenomena in SCW. The inlet temperature was varied from 125-352°C, the heat flux ranged from 1.03-3.45 MW/m², while the mass flux was altered from 800-3000 kg/m²s.

Experimental data were recorded using a Data Acquisition System once the required power levels and flow conditions were reached and stabilized (steady-state conditions). The maximum uncertainties of primary parameters of the experiment are listed in Table 3-3.

Table 3-3: Maximum Uncertainties of Measured and Calculated Parameters [56]

Parameter	Maximum Uncertainty
Bulk-fluid temperatures	±3.4%
Inlet pressure	±0.2%
Wall temperatures	±3.2%
Mass-flow rate	±2.3%
Heat loss	≤ 3.4%
Heat flux	±3.5%
HTC	±12.7%

A sample of the experimental results is shown in Figure 3-5, similarly structured to the sample shown for the bare tube results.

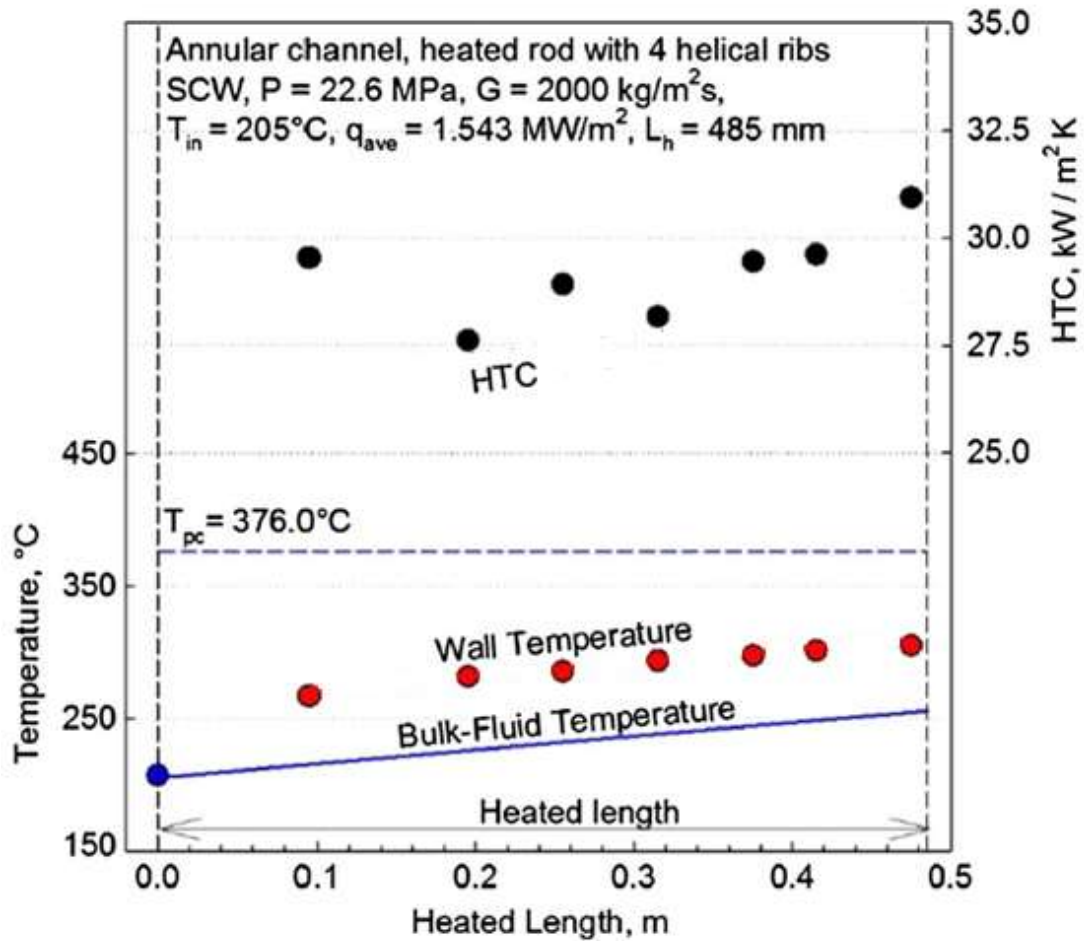


Figure 3-5: Sample Experimental Run from Razumovskiy et al. [56]

3.3 Meshing Methodology

The geometries and meshes constructed for analysis in FLUENT are built using ICEM CFD software. The meshing techniques vary for different geometries and complexities.

The main method meshing in ICEM is called blocking. This method involves creating blocks that conform to the CAD geometry and then creating the mesh using these blocks. Throughout the following sections, the meshing methodologies will be discussed for each geometry. The meshes are tested for the quality of the cells, the angles between the cell faces, and any errors in the creation of the mesh. The node density is increased and tested in the solver until the results do not vary anymore, at which point mesh independence is achieved.

3.3.1 Bare Tube Geometry and Mesh

The first mesh is to be constructed for a bare tube, with an entrance region, to simulate the flow of SCW in the experiments by Kirillov et al. However to reduce computational resources, while maintaining the ability to capture 3-D effects of the turbulent flow, a 1/8 slice is modelled. Figure 3-6 shows a graphical representation of the geometry.

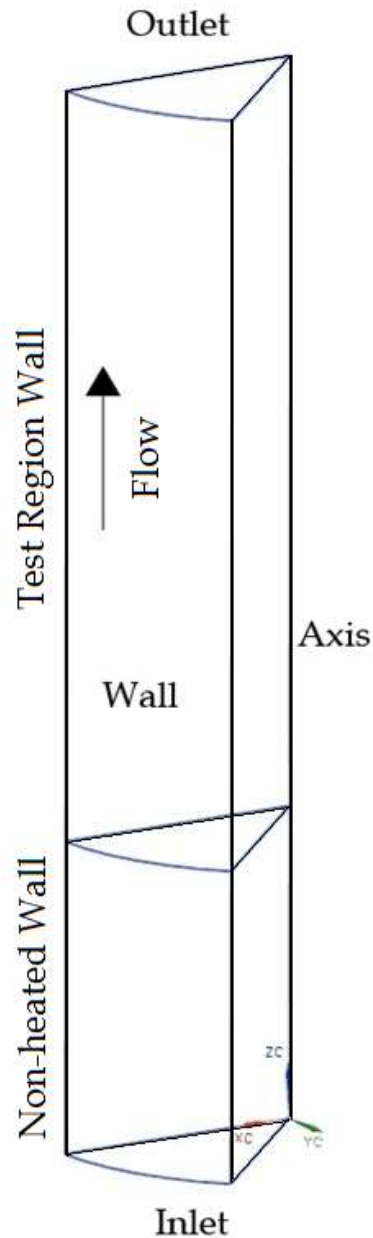


Figure 3-6: A graphical representation of the mesh geometry (not to scale)

To start meshing in ICEM, for a simple geometry such as a bare tube, the geometry is constructed using the geometry editor in ICEM itself. The process for creating a geometry in ICEM involves creating points, then lines and finally surfaces that enclose the lines. ICEM is a surface modeller and doesn't "know" what a volume is. It can only see points, lines and surfaces. After a set of surfaces is modelled, a "material point" can then be specified within these surfaces to represent the volume to be meshed. As such, the approach to building a geometry and meshing it in ICEM is rather different than conventional meshing software. It lacks the ability to carry out Boolean operations for example, since it doesn't recognize volumes. This will be explained further in the following sections as more complex geometries are discussed.

After the geometry is created, each component can be named and placed into a "part". Extra parts that are unnamed or unmeshed will not be exported to the solver. ICEM exports only the mesh information and structure and none of the geometry, which only serves to guide the mesh generation process.

To create the mesh itself, the technique is called blocking, in which a block is created then modified to fit the geometry. The meshing parameters are then applied to the block edges and faces to create the final mesh. Figure 3-7 shows the 3D bounding box which is created initially. For this geometry, the faces at the inlet and outlet need only 3 edges, so the two bottom vertices of the block are merged to create a block with 3 edges. The block is then split along the axial length to create two blocks, one for the entrance region, and one for the heated flow as shown in Figure 3-8. This step is needed since the wall is divided into two sections, and only one of them is heated. As such, to create the correct boundary conditions to be exported to FLUENT, the two walls need to be in separate parts, and meshed separately.

The next step is to associate the blocking with the geometry. This involves associating block edges with geometry curves, and block faces with geometry surfaces. Finally, the part mesh setup is used to define the maximum size for cells in each part, as well as the inflation parameters (the boundary layer) such as the first node height, height ratio, and number of layers.

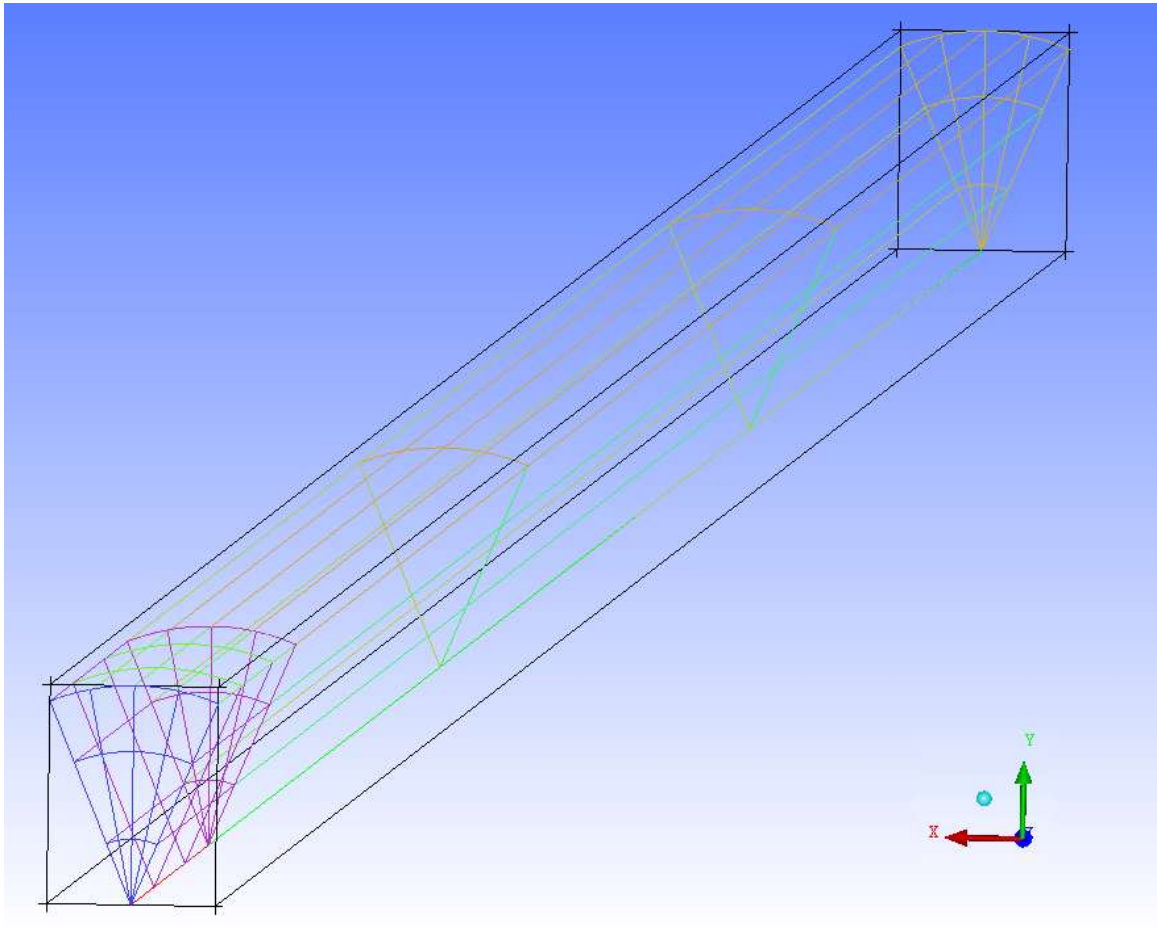


Figure 3-7: 3D Bounding Box Block for the Geometry

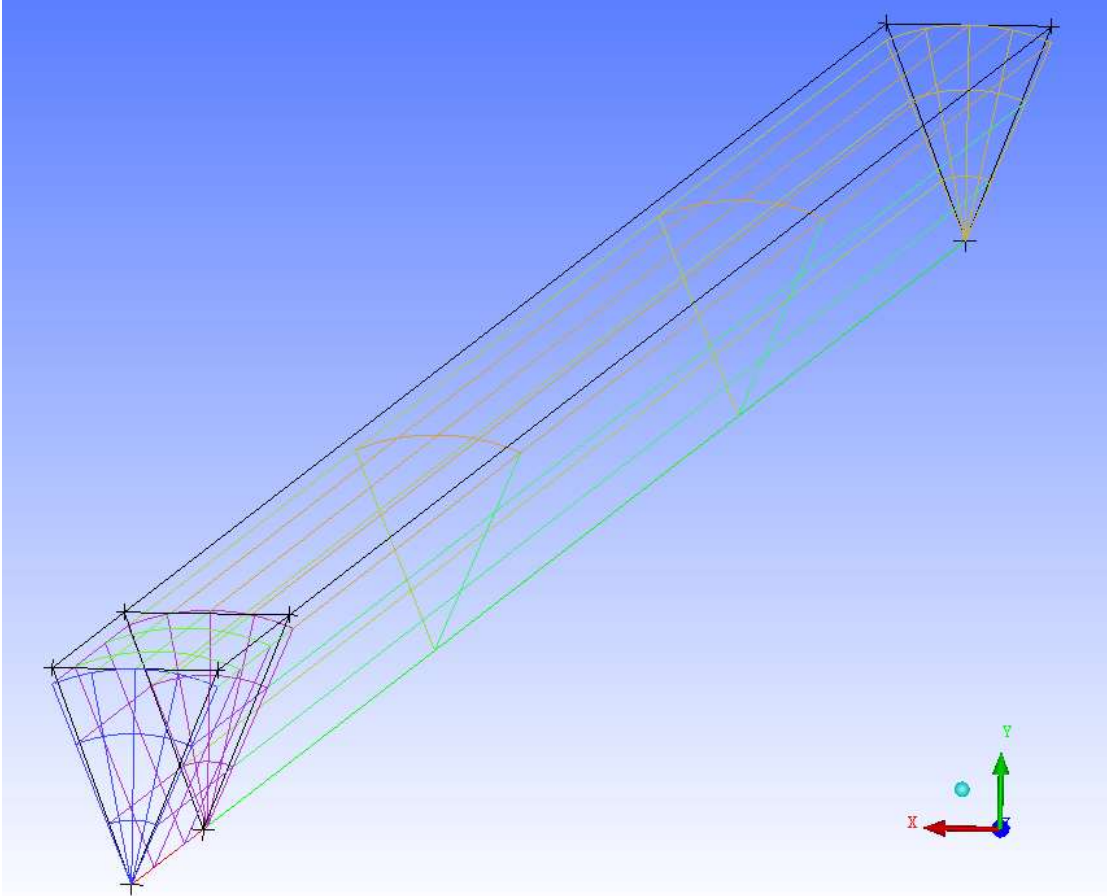


Figure 3-8: Modifying the Blocks to Fit the Geometry

Figure 3-9 shows the actual mesh as constructed in ICEM. The mesh is quad dominant, with tri elements used for sharp edges. The node sizes in the mesh are selected to be uniform throughout the mesh at 0.4 mm, leading to a total node count of 5000 in the axial direction and 33 in the radial direction (includes 20 cells in the boundary layer). Any increase in node density beyond this amount does not produce a difference in results or convergence.

The quality of the mesh is best in the quad region, where it is constructed evenly and the angles between the mesh cells are closer to 90°. The center of the tube (around the axis) has cells with acute angles making for a lower quality mesh at that region, however it is sufficient for the simulation purposes as the bulk fluid

temperature profile does not change greatly near the axis and the simulations generate the same profile as a higher quality mesh.

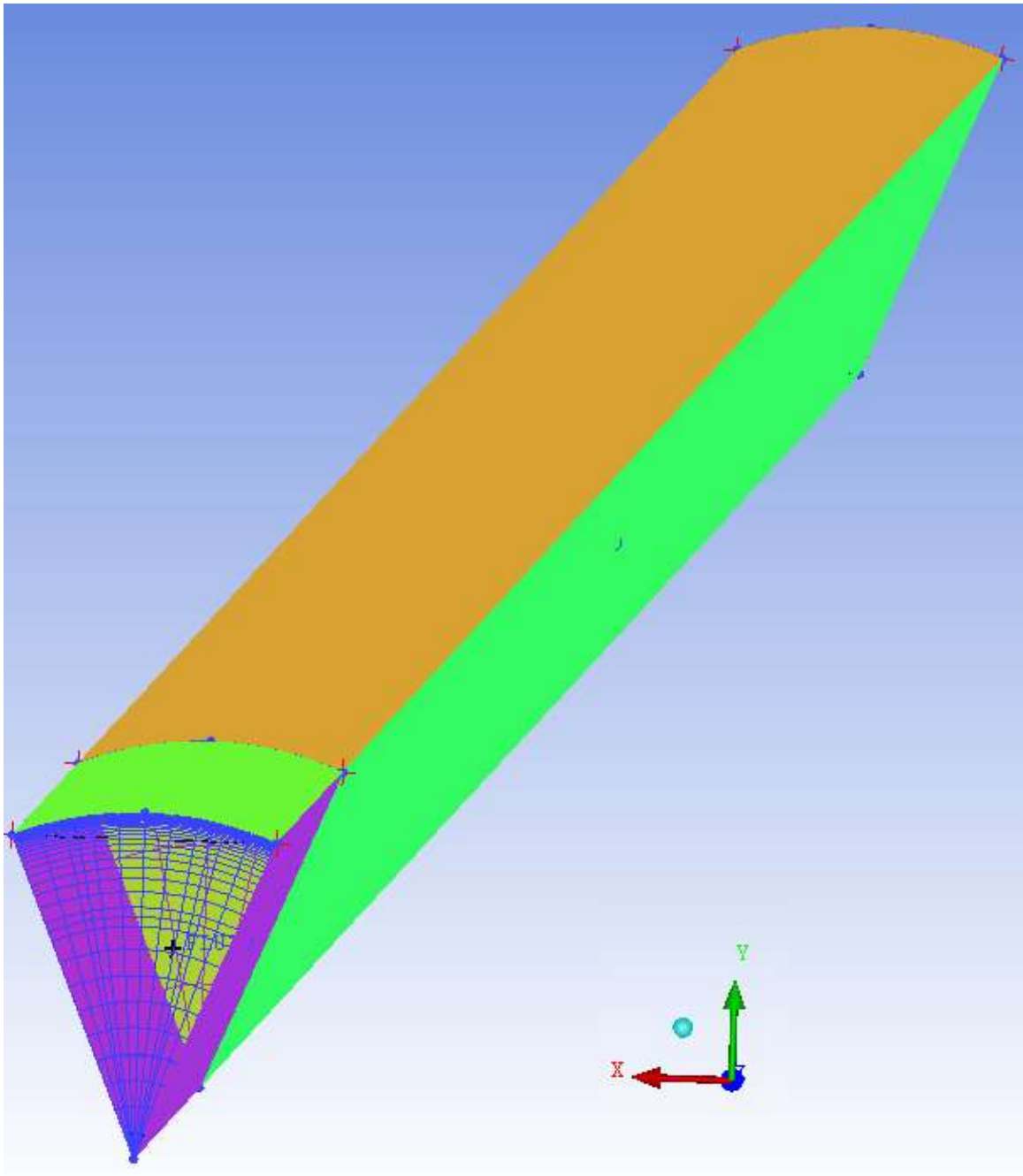


Figure 3-9: ICEM CFD mesh for 1/8 tube geometry

A front view representation is shown in Figure 3-10 for the mesh in the XY plane, to show the computational cells. The figure also shows the gradual increase in cell height away from the wall. The boundary layer is constructed such that the first cell is 2 microns from the wall, with a height ratio of 1.2 and 20 layers total. The simulation results confirm the Y^+ value to be between 0.55 and 1 along the length of the wall. Figure 3-11 also shows a close up of the boundary layer and the relative cell sizes.

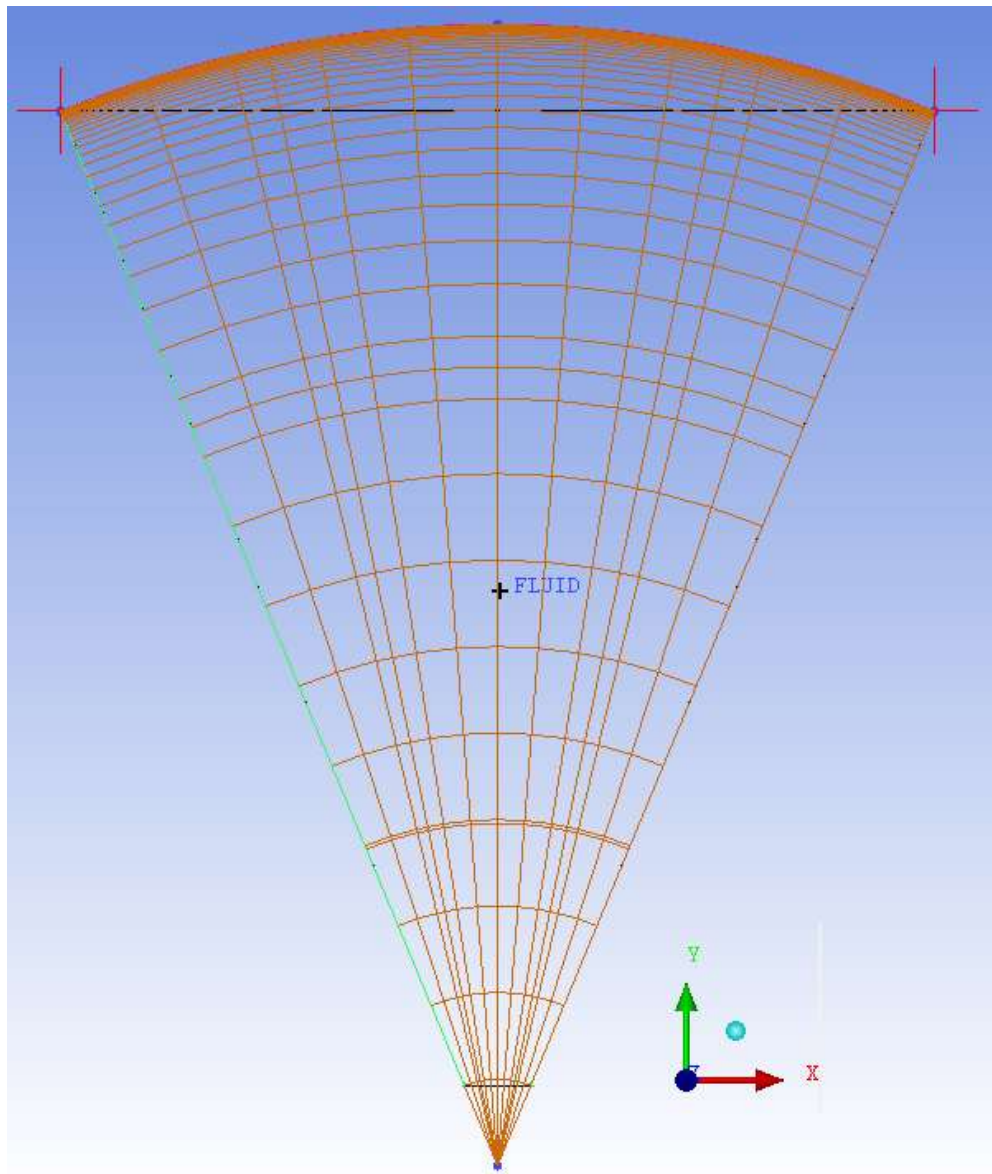


Figure 3-10: Mesh view in the XY plane

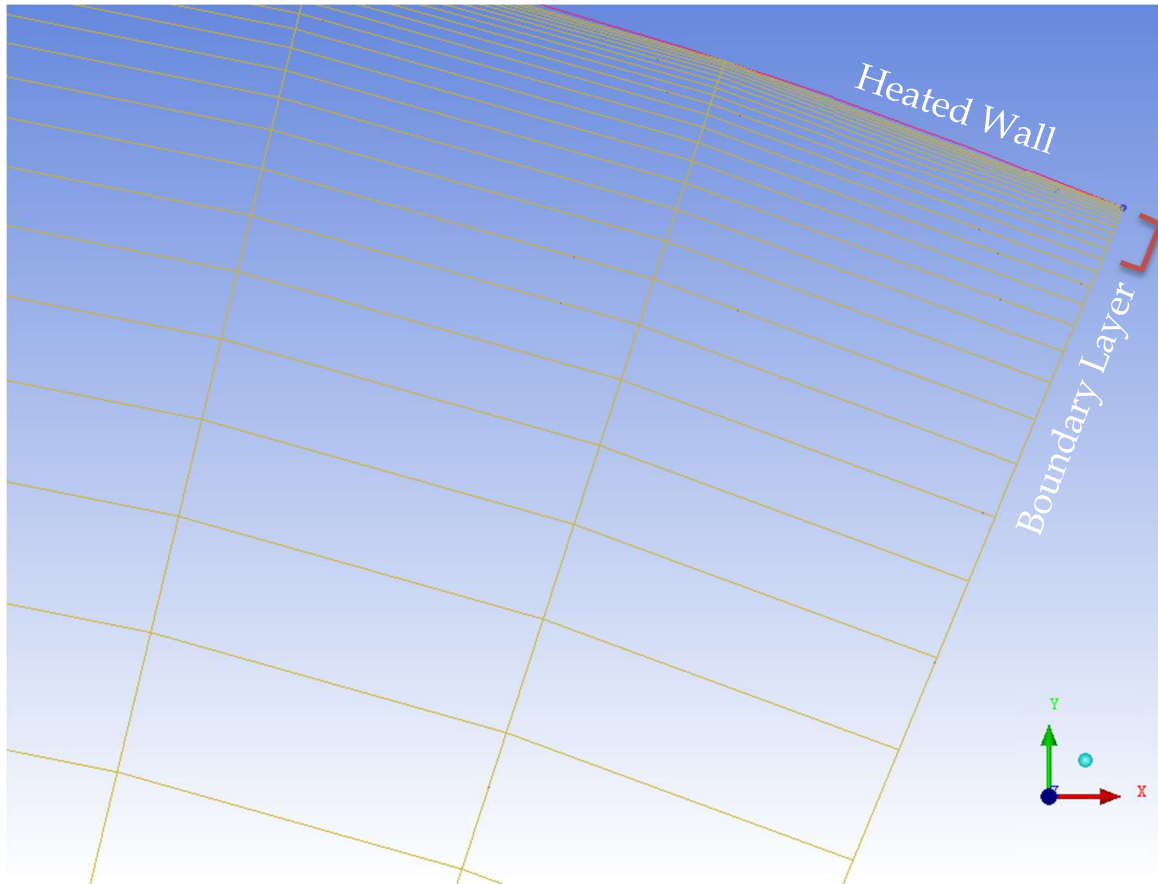


Figure 3-11: Boundary layer for mesh

A mesh independence study was carried out to confirm the additional refinement of the computational domain does not lead to any further change in the convergence levels or the values of the output variables (e.g. outlet and surface temperatures).

3.3.2 Annular Channel with Helical Fins Geometry and Mesh

The annular channel geometry is quite complicated compared to the bare tube discussed earlier. The complexity stems from the addition of the helical fins wound over the inner tube. Due to the fact that the geometry builder in ICEM is quite difficult to use for this type of geometry (creating helices and sweeping surfaces along them), and the lack of ability to construct and manipulate volumes (e.g. Boolean operations) UGS NX software was used instead to create the geometry.

The channel is 485 mm long with helical ribs wound over a pitch of 400 mm. The cross sectional view along with the dimensions of the channel are shown in Figure 3-12.

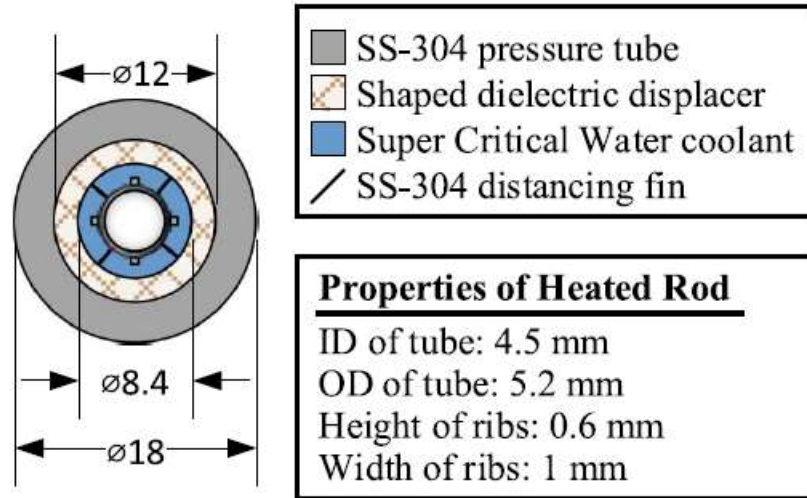


Figure 3-12: Cross Sectional View and Dimensions of the Annular Channel Geometry [56]

The geometry created in NX represents the flow volume of the fluid. An entrance region was added as well to develop the flow before entering the heated section. Figure 3-13 shows a see-through view of the geometry.

The flow volume is created by extruding a cylinder representing the volume inside the outer pipe, and then subtracting the volume of the inner tube with the helical ribs. Figure 3-14 shows a cut-plane view to illustrate the final geometry to be exported to ICEM CFD.

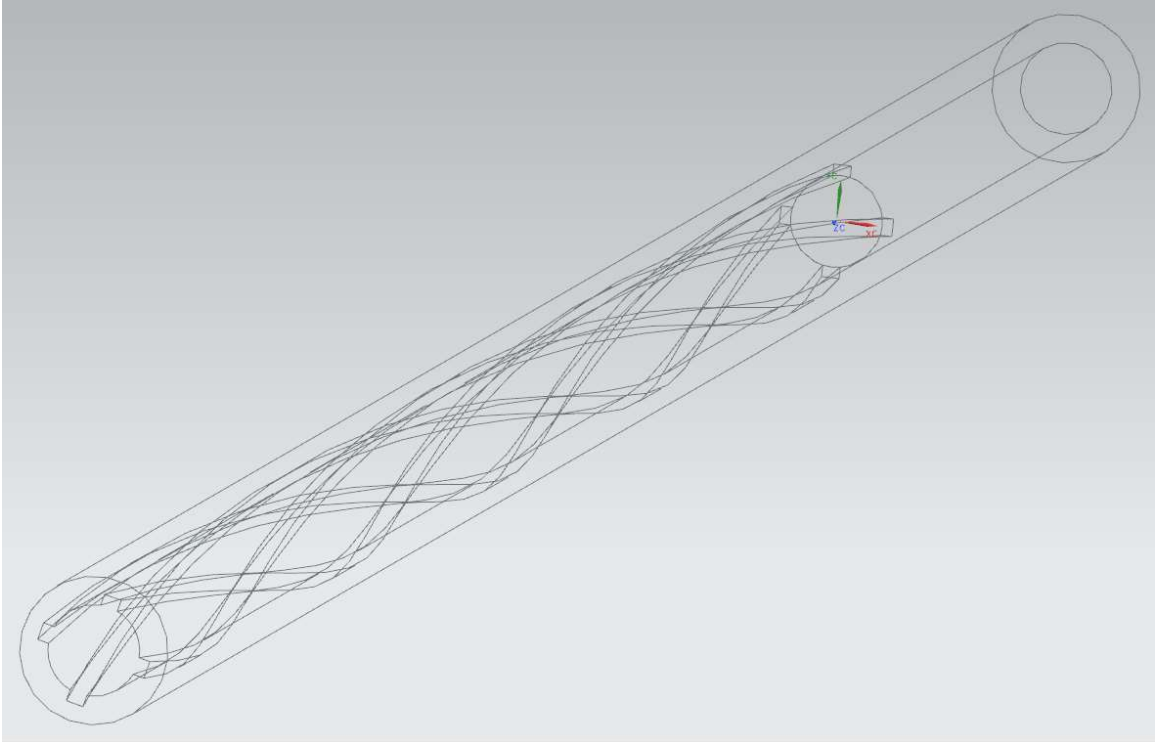


Figure 3-13: A See-through View of the Annular Channel Geometry

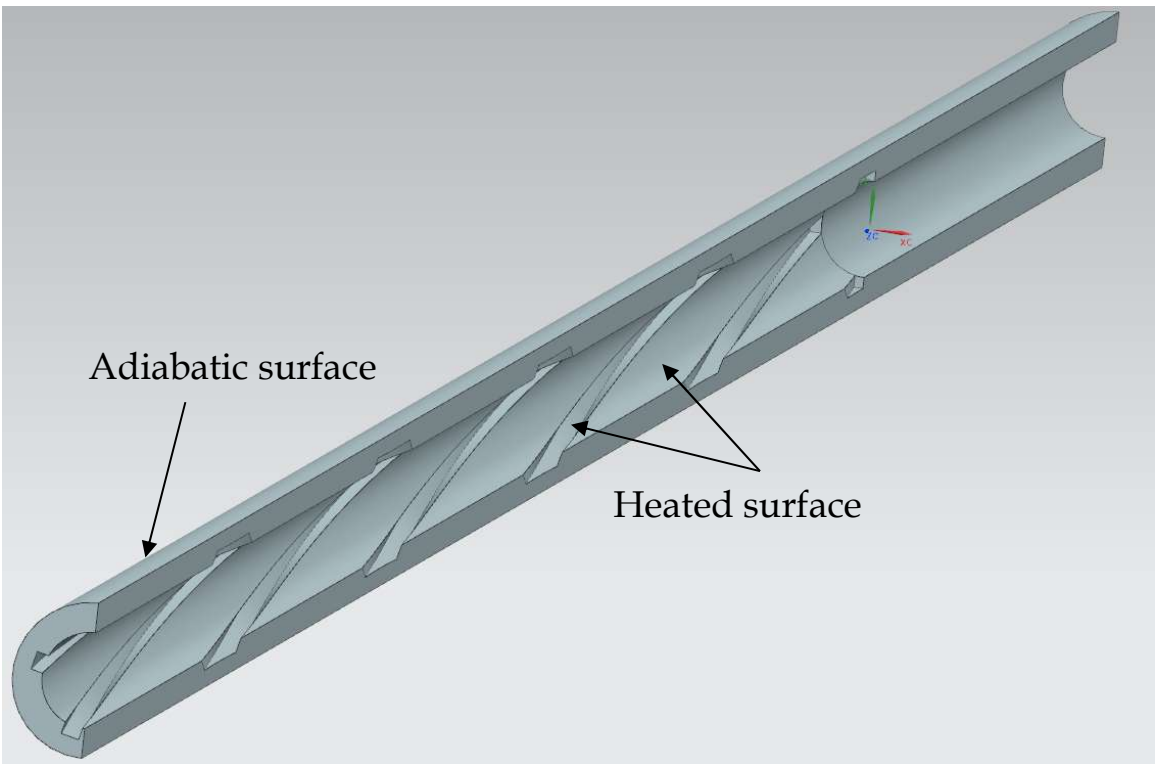


Figure 3-14: Cut-plane View of the Annual Channel Geometry. Solid is Flow Volume.

Due to the complexity of the geometry and lack of symmetry, the mesh has to be constructed for the full flow volume. The entire geometry is then imported by ICEM using the ANSYS CAD interface, which reads the NX file and reconstructs the geometry in ICEM using points, curves and surfaces as shown in Figure 3-15. As mentioned earlier, ICEM is a surface modeller, and thus the final step in creating the geometry is to create a “material point” to represent the volume intended for the mesh.

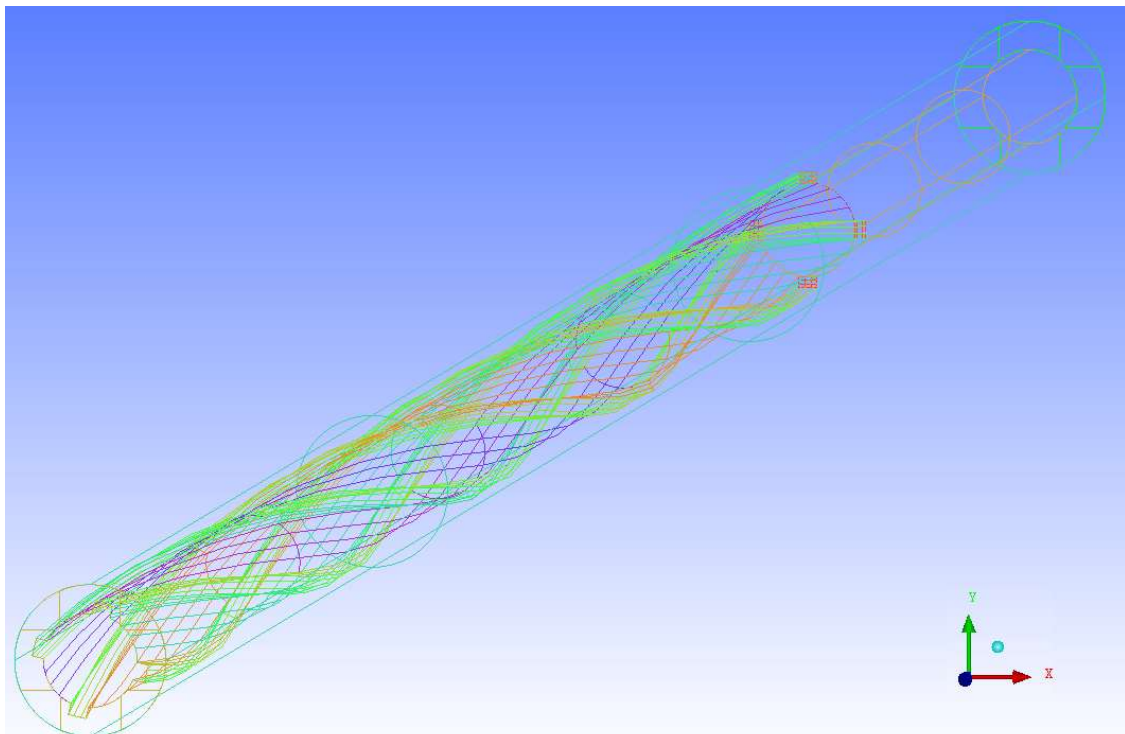


Figure 3-15: The Geometry Imported by ICEM CAD Interface

To create the mesh for this type of geometry, using the ICEM blocking technique is quite problematic, as the initial bounding box has to be cut several times to account for “empty” region in the center of the annular channel, as well as the space left by the helical ribs, as shown in Figure 3-16.

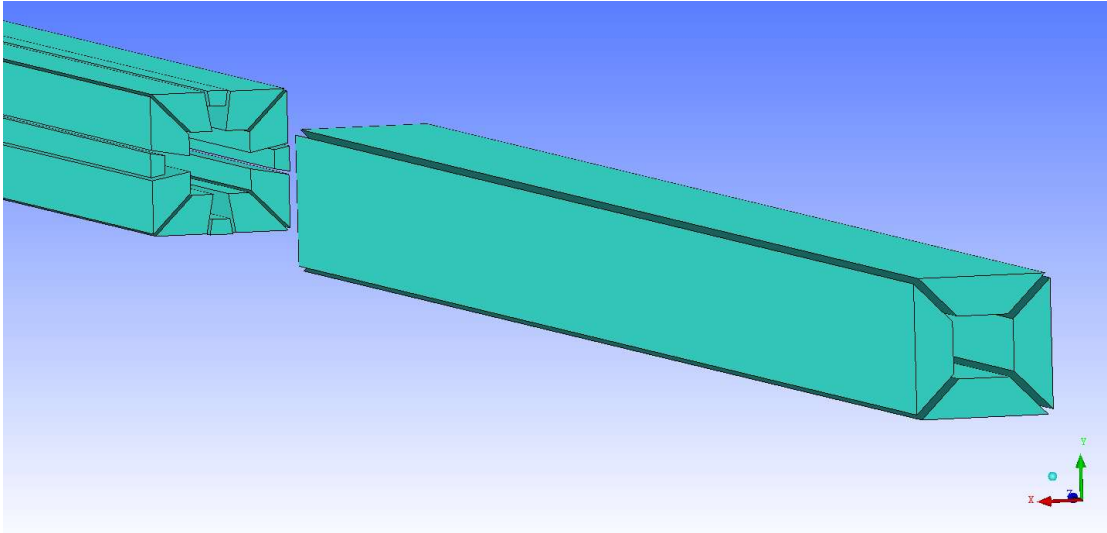


Figure 3-16: 3D blocking of the Annular Channel Geometry

To create a blocking representation of an annular region, ICEM uses a method of block splitting called O-Grid, which creates the blocks shown on the right side of Figure 3-16. The same is done for the heated section, but as it involves helical ribs as well, more splitting has to be done in order to shape the blocks to match the geometry.

The problem stems from the fact that each time the block is split, more edges and faces are created from the blocks, and as they have to be associated to the geometry, and then meshed, this will result in many edges that do not have curves in the geometry to be associated with. Figure 3-17 shows the block edges, with the red colored edges representing those with geometry association and the black colored edges with no matching geometry. This would not be a problem if the fins were straight, as the resulting mesh would not be dependent on those edges, but as they are wound around the surface of the inner tube, this results in “orphan” edges with no association, which create a mesh that does not match the geometry.

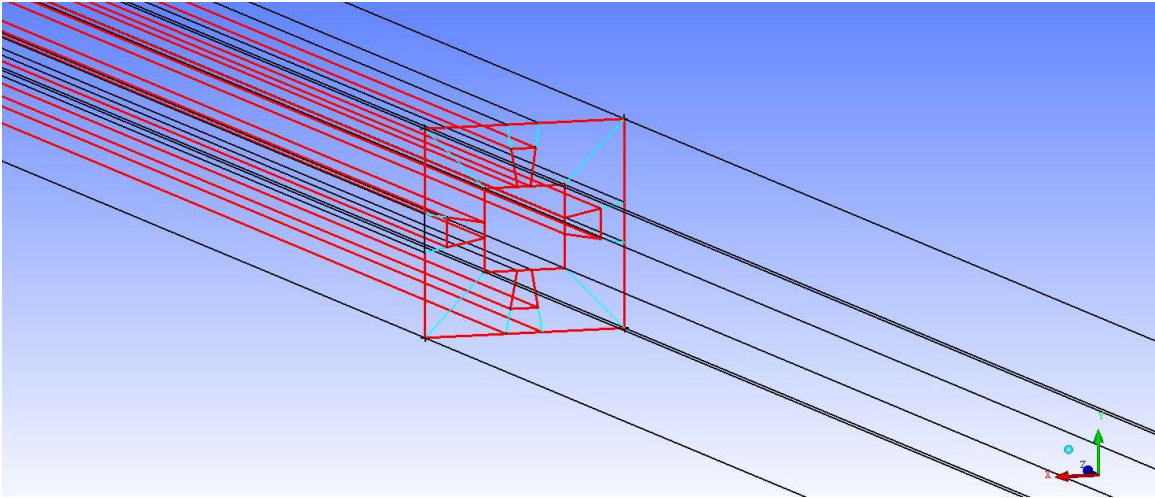


Figure 3-17: Block Edges for the Annular Channel. Red colored edges have matching curves in the geometry, and black edges have no association.

An attempt to solve this issue, by capitalizing on the fact that the geometry itself is neglected when the mesh is exported to the solver, is to create extra curves matching the helicity those of the ribs and associating the extra edges with them. The additional problem here is that all association is done manually by inspecting the geometry and selecting the edges and curves on screen. This procedure tends to get somewhat difficult when dealing with (in this case) 32 helical edges.

After the association and assigning a maximum cell size of 0.25 mm to the edges, the preliminary mesh was constructed as shown in Figure 3-18, Figure 3-19, and Figure 3-20.

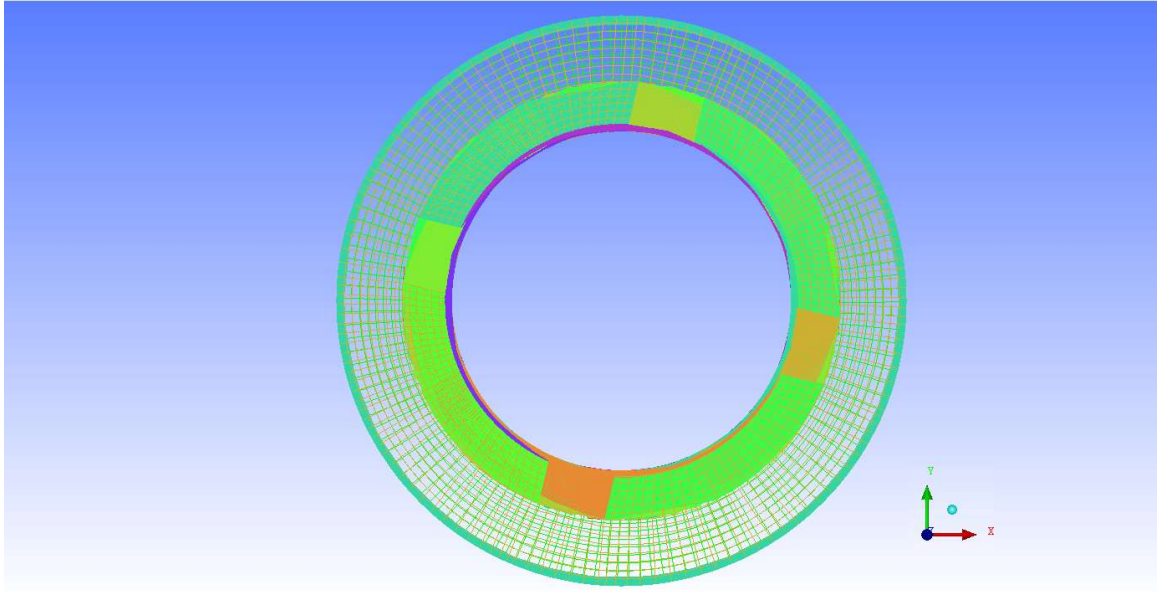


Figure 3-18: 3D Mesh (3D blocking) of Annular Channel with Helical Ribs - Front View

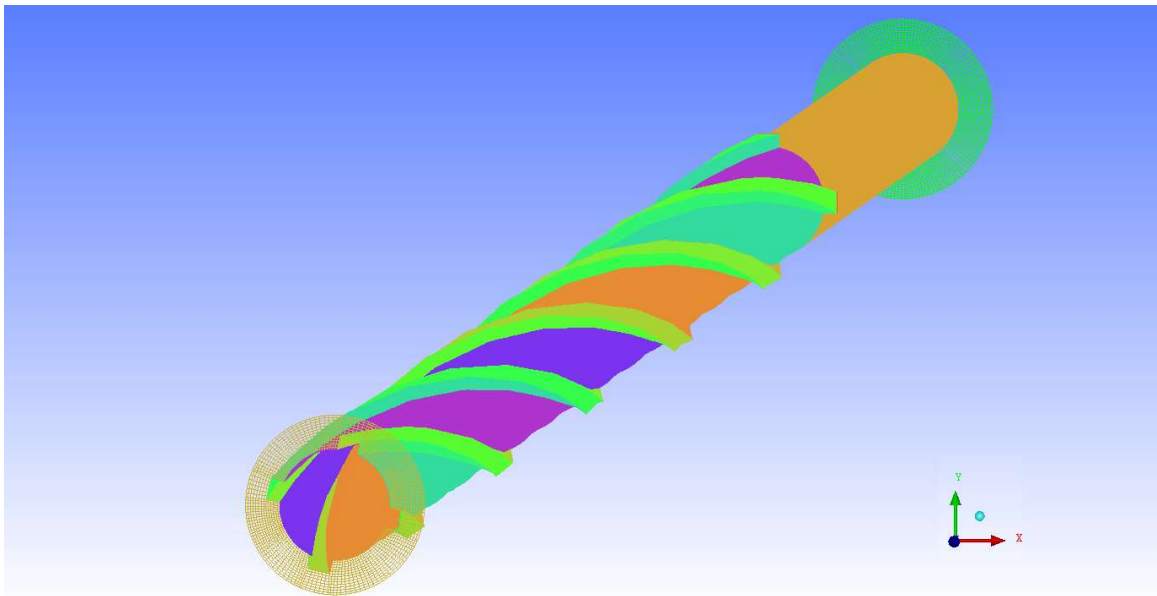


Figure 3-19: 3D Mesh (3D blocking) of Annular Channel with Helical Ribs- Isometric View

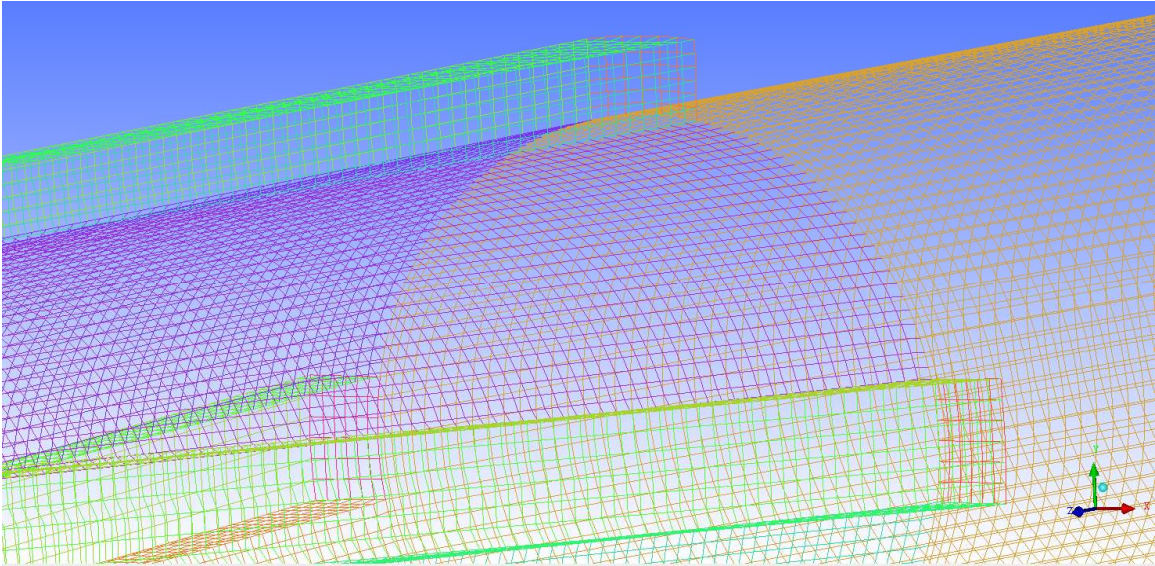


Figure 3-20: 3D Mesh (3D blocking) of Annular Channel with Helical Ribs – Close-up View

By testing the quality of the mesh, it was apparent that due to the high curvature of the geometry, there are cells with high skewness and high aspect ratio faces. Preventing the possibility of having small cells near the wall (boundary layer). Simulations with this type of mesh proved to be unreliable; reaching lower convergence levels than anticipated (discussed in 3.4.4) and required the use of modified under-relaxation factors (discussed in 3.4). There was also a need to run a mesh-check and fixing algorithm in the solver itself, which provided further warnings that the mesh may not be fully fixed after the operation.

Another approach to block and mesh the geometry, uses multi-zone blocking technique. This involves 2D surface blocking; by creating blocks for each surface, and then creating a 3D block using ICEM's algorithms to mesh the volume. This eliminates the need for slicing the geometry and the blocks, by automating the geometry decomposition. The three options for this method: Mapped, Swept, or Free. Mapped and swept create structured meshes using quad or tri cells. Whereas "Free" creates less structured cells while maintaining the maximum allowable size. Figure 3-21, Figure 3-22 and Figure 3-23 show different views of the free mesh.

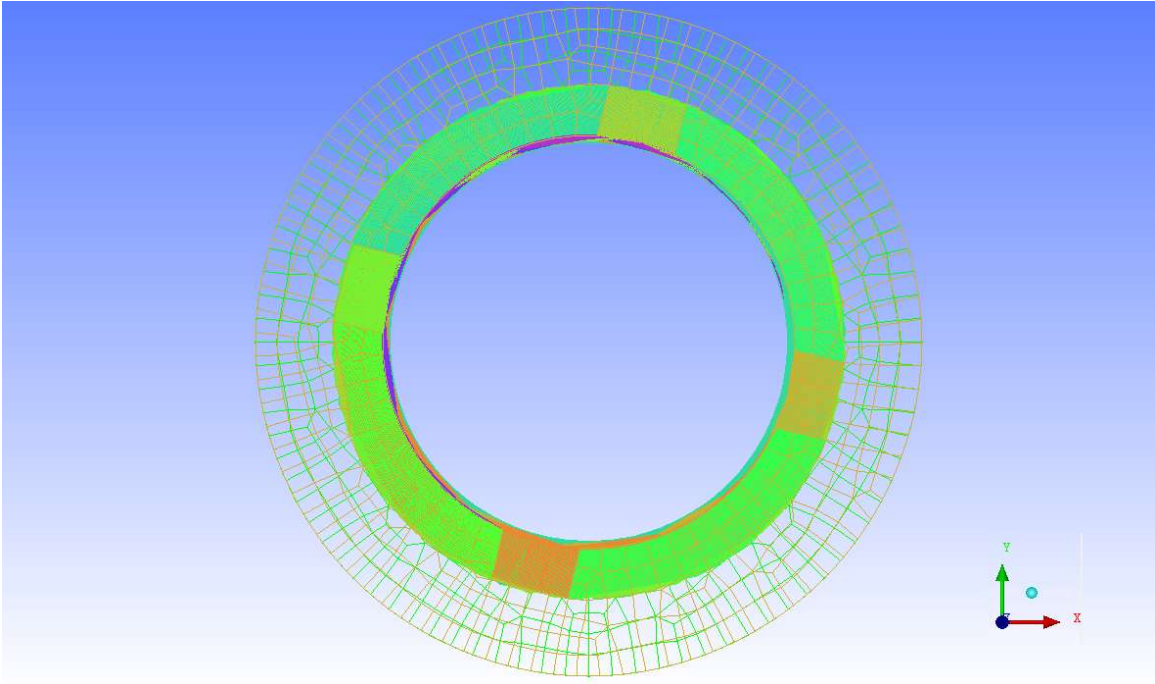


Figure 3-21: 3D Mesh (Free Multi-zone blocking) of Annular Channel with Helical Ribs - Front View

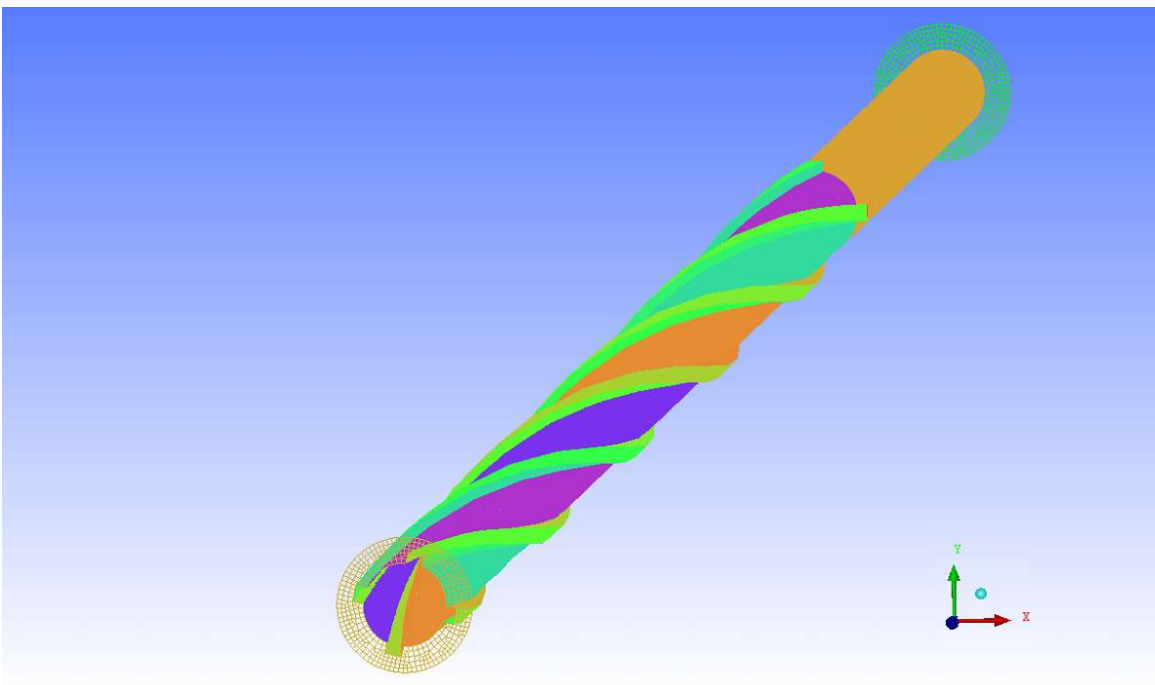


Figure 3-22: 3D Mesh (Free Multi-zone blocking) of Annular Channel with Helical Ribs- Isometric View

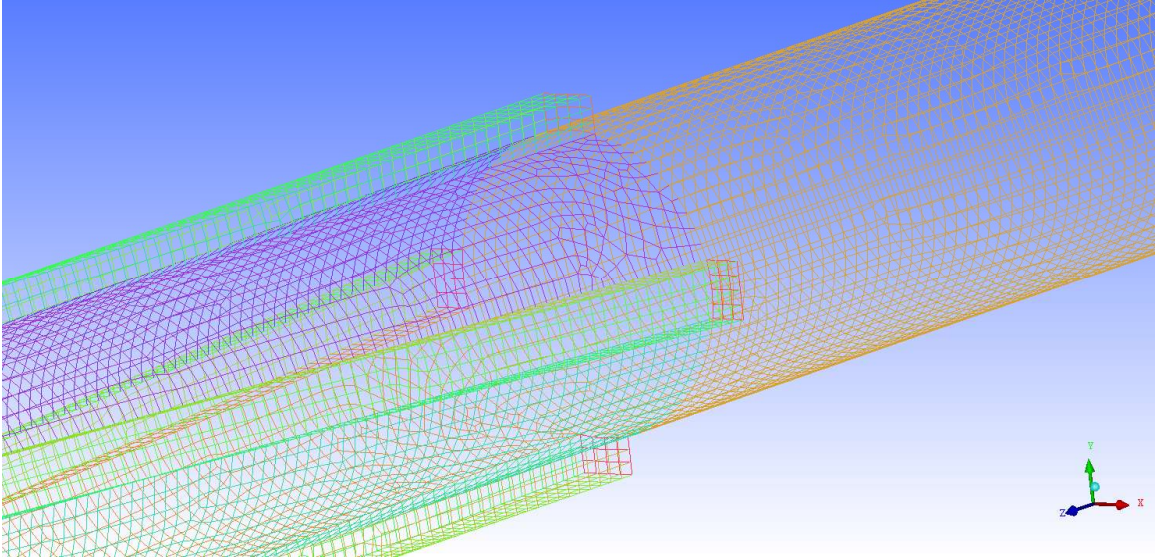


Figure 3-23: 3D Mesh (Free Multi-zone blocking) of Annular Channel with Helical Ribs - Close-up View

Only the Free 2-D surface blocking was successful in creating a mesh for this geometry, due to the high curvature and the complexity of the geometry. This type of mesh creates cells that are of higher quality and lower skewness than the ones created using the 3D blocking shown earlier. The problem with this mesh however, is the difficulty in creating a structured boundary layer. Specifying the first node distance, the ratio of growth and the number of layers is the approach to creating a boundary layer from an edge or a surface, however, when applied to the free mesh, the edge doesn't "carry" the inflation parameter. Instead, the inflation is localized as shown in Figure 3-24. The implications and the impact on results is discussed in Chapter 5: .

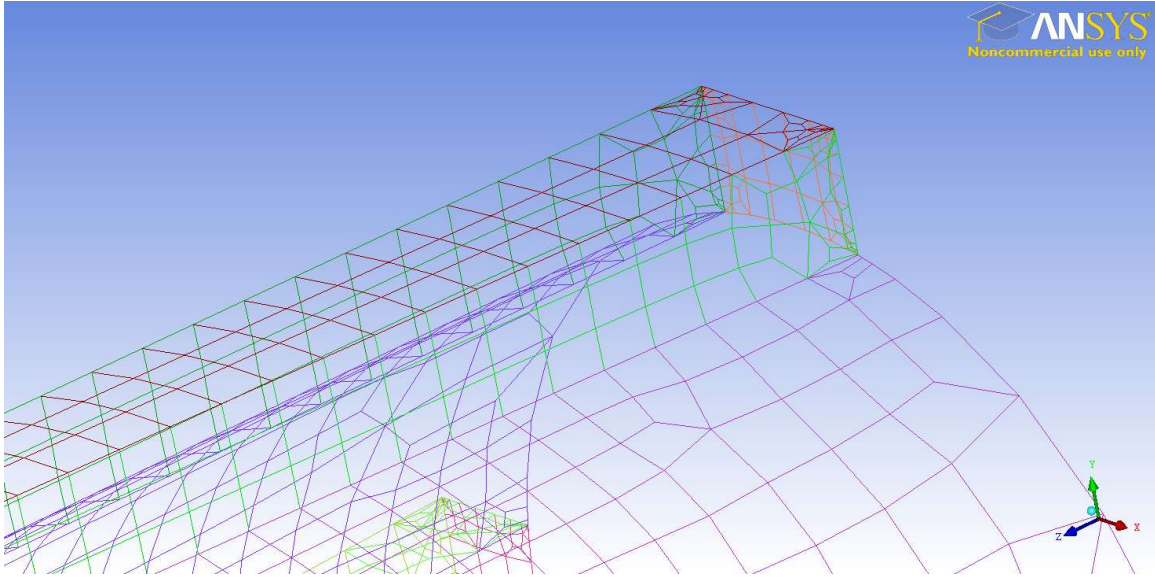


Figure 3-24: Inflation Parameters on a Free Mesh of Annular Channel with Helical Ribs - Close-up View

3.3.3 Bare Tube with Sudden Area Change Geometry and Mesh

The analysis of a helically ribbed annular channel is an important step to examine the capabilities of the FLUENT code to simulate the flow and heat transfer phenomena in a complex geometry. The existence of the experimental data makes it a viable option to validate the code for applications beyond the simple bare tube. As seen from initial results however (to be discussed in detail in Chapter 5:), there does not appear to be much induction of turbulence energy and the resulting Reynolds numbers are in the order of 10^4 . As such, the benefits of these simulations do not extend to modelling realistic reactor geometries.

To remedy this issue, and to study the effects of geometry perturbations on the SCW flow without the limitations of creating a complex fuel channel or a full-bundle geometry analysis, a sudden area change is selected as a representative for a real reactor geometry, as well as shedding some light on possible flow characteristics through the fuel bundle's sudden area change. As mentioned earlier in section 2.9, the current method of analyzing the nuclear fuel bundle

geometry, is by treating the perturbations as sudden area changes, and applying the applicable equations.

Due to the symmetrical nature of the geometry, the sudden area change is represented as a gap in the continuous fluid domain as shown in Figure 3-25. The location of the sudden area change can be varied by either constructing a new mesh to place it in a different position relative to the entrance region and outlet, or by changing the boundary conditions in the solver.

The bare tube data discussed in section 3.1 is modeled with the addition of a sudden area change at various lengths and heat transfer regimes to assess the effect this geometry would have on SCW flow.

The geometry and the mesh are based on a 1/8 slice of the pipe, to capture the 3D effects without consuming excessive computational resources.

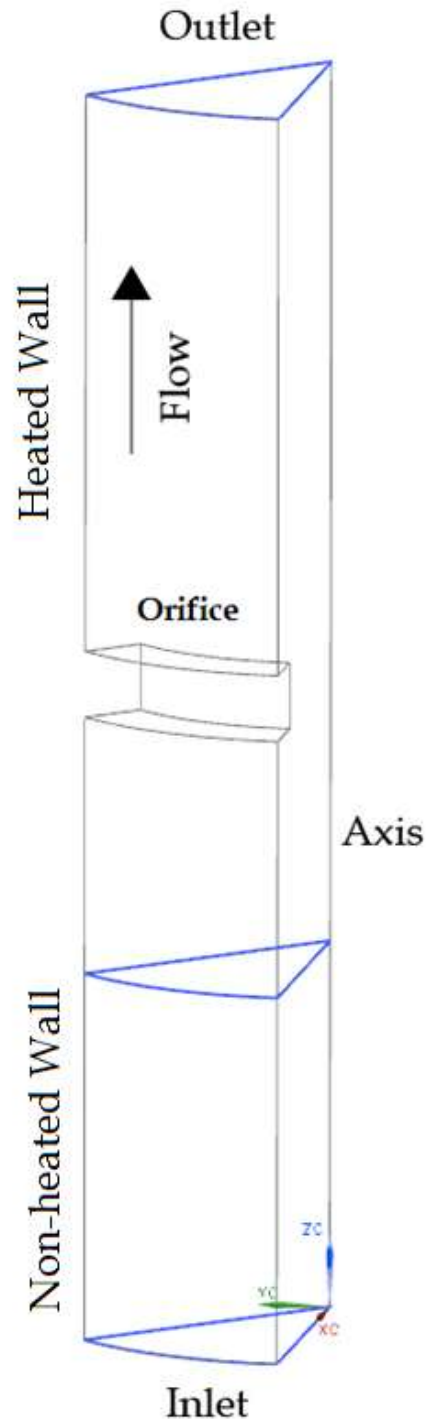


Figure 3-25: Graphical representation of the 3-D mesh for vertical tube with an orifice. (not to scale)

The dimensions of the sudden area change were taken to conform to a thin orifice geometry (shown in Figure 3-26) and were selected based on ASME orifice design guidelines [57] and Idelchik's Handbook of Hydraulic Resistance [47].

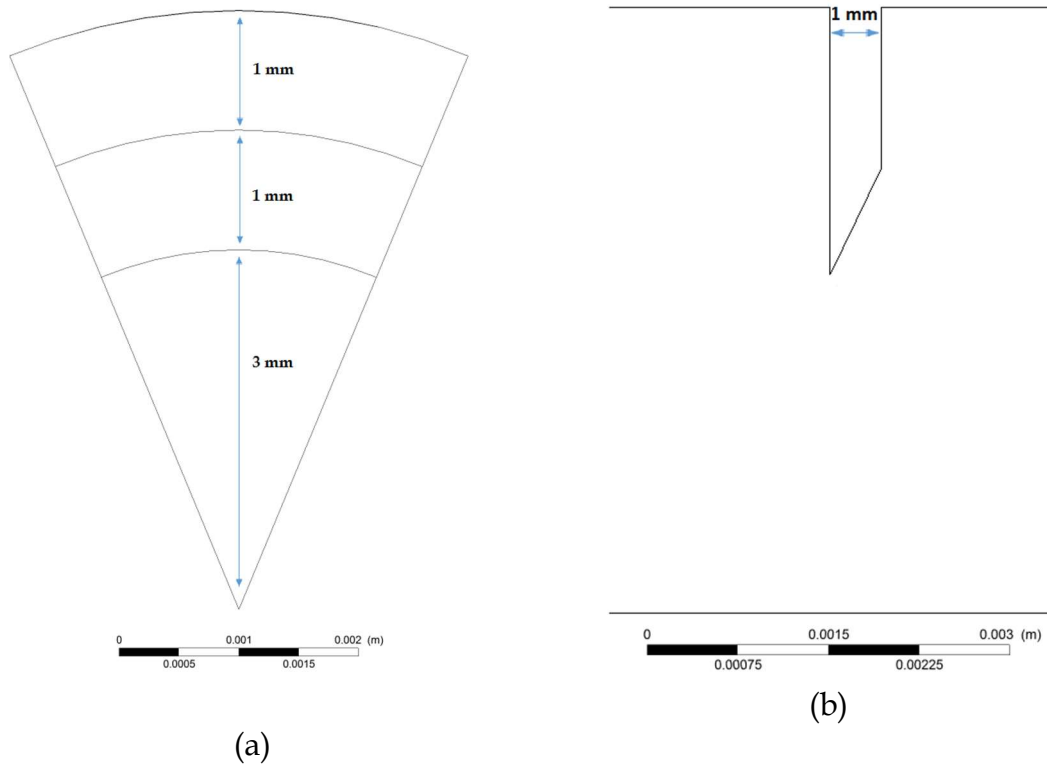


Figure 3-26: (a) Front and (b) Side Views of the Area Change Geometry and its Dimensions

To create a mesh for this geometry, the same approach is taken as the simple pipe meshing methodology, with the additional step of splitting the block further to account for the gap in the flow where the sudden area change is.

A close-up of the mesh around the sudden area change is shown in Figure 3-27. The same mesh density as the simple pipe configuration is used. The boundary layer is grown from each of the walls, and as such, the resulting mesh around the perturbation has a higher node density wherever the mean flow cells intersect with the boundary layer cells.

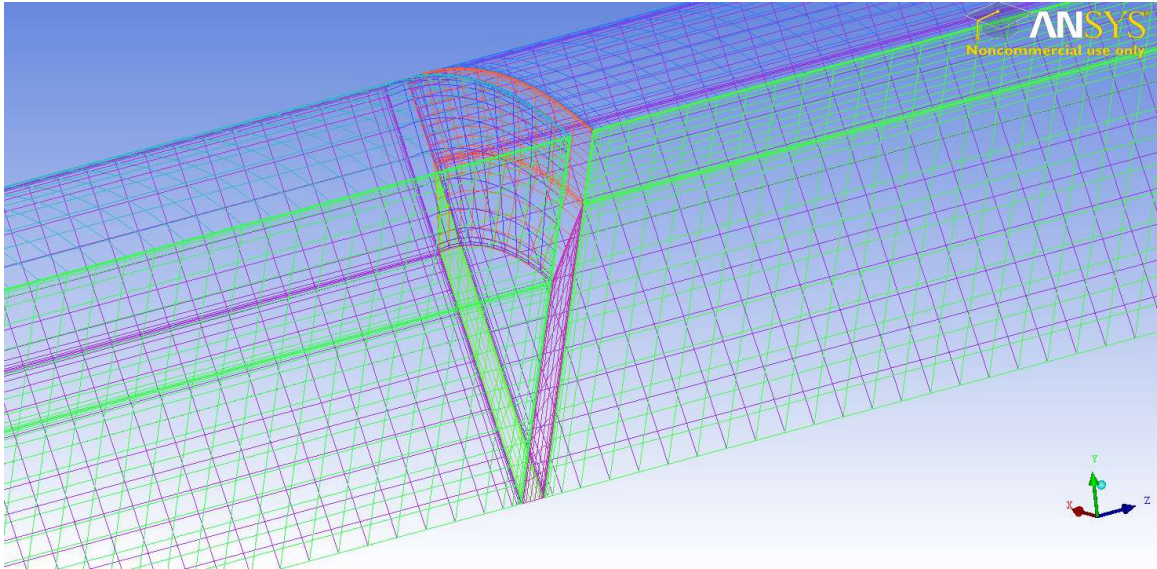


Figure 3-27: ICEM CFD Mesh for 1/8 Tube Geometry with a Sudden Area Change

3.4 FLUENT Methodology

After creating a mesh and exporting it into a format readable by FLUENT, the solver can be started and the case can be setup.

At the start-up, options are given for the case to be solved in 3D or 2D environments, as well as the use of double precision and the number of parallel processes to be run simultaneously. After selecting the appropriate configuration for the case, the problem setup follows.

3.4.1 Viscous Models

The first step is to select the viscous model for the solution. The options are given for 1-, 2-, 3-, 4- and 5-equation models. For this study, the 2-equation models will be used. The 3-equation models and higher are used usually for flows including transitions in turbulent state; this is not the case in the current study. Additionally, the choice of these models will increase the computational time greatly and often results in early divergence in the solver.

The 2-equation models are as stated earlier; the $k-\omega$ and $k-\varepsilon$. For each model, there are options for fine tuning the equations for certain applications.

The $k-\varepsilon$ model has three variations; standard, RNG and realizable $k-\varepsilon$. All three models have similar forms, with transport equations for k and ε . The major differences are as follows [28]:

- The method of calculating turbulent viscosity,
- The turbulent Prandtl numbers governing the turbulent diffusion of k and ε , and
- The generation and destruction terms in the ε equation.

The features that are essentially common in all models include turbulent production, generation due to buoyancy, accounting for effects of compressibility, and modelling heat and mass transfer.

The standard $k-\varepsilon$ model is a semi-empirical model where the equation for k is derived from an exact equation, while the transport equation for ε was obtained using physical reasoning and does not highly resemble its mathematically exact counterpart. In the derivation of the $k-\varepsilon$ model, it is assumed that the flow is fully turbulent and it neglects the effects of molecular viscosity, thus it is only valid for fully turbulent flows.

The RNG-based $k-\varepsilon$ model is derived from the instantaneous Navier-Stokes equations, using a method called Renormalization Group (RNG). This analytical derivation results in different constants than those present in the standard model.

In addition to the two previous models, FLUENT includes a realizable $k-\varepsilon$ model, in which the realizable term means that the model satisfies certain mathematical constraints on the normal stresses, which is consistent with the physics of turbulent flows. This model, first proposed by Shih et al. [58], was intended to

address the deficiencies in the traditional k - ϵ models, which lies in the definition of the dissipation rate (ϵ).

Within each of the aforementioned models, there are multiple options for near-wall treatment as well as options to account for the pressure gradients and thermal effects, including viscous heating and buoyancy effects.

Similarly to the k - ϵ mode, the k - ω model has variations that are based on similar forms for the transport equation for k and ω . Two models exist for k - ω ; the standard and shear-stress transport (SST). The major differences between the two models are:

- Gradual change from the normal k - ω model in the inner region of the boundary layer near the wall to a variant of the k - ϵ model with high-Reynolds emphasis in the outer part of the boundary layer.
- The turbulent viscosity term is modified to account for the transport effects due to the turbulent shear stress.

Theoretically then, the application of the SST k - ω should provide the best of the two approaches; k - ω and k - ϵ for turbulent flow with high Reynolds numbers.

As in the case of the k - ϵ model, the k - ω has options for low-Re corrections and viscous heating effects near the wall.

3.4.2 Material Properties

The material properties to be defined consist of the fluid and wall materials. The walls are taken as standard stainless steel, and the surface roughness is modified in the options to match that listed in the experimental setup as mentioned in section 3.1.

As for the fluid properties; the water properties in the FLUENT material database does not extend beyond the critical point, which calls for an alternative method of importing the fluid properties.

FLUENT provides multiple input methods for material properties; including direct input at a specific point, continuous functions over a defined interval, or importing databases from external sources.

The single point entry is not useful, as the water properties change massively in the pseudocritical region as shown earlier. The function inputs have much more merit and can be very useful for simple to moderate changes in the properties over the desired range of temperatures. If the function was to be specified in FLUENT itself, then the options are limited mainly to polynomials. This approach might be sufficient for most fluids in the sub-critical region, however it does not represent the behaviour of SCW accurately. User-defined functions (UDFs) can be written in an external program such as C++ and then imported as a script to FLUENT. This method allows for a wider range of functions to be used, such as logarithmic and Gaussian functions. This naturally allows for more accuracy in replicating the properties (error < 5%).

The abovementioned approaches are very effective when a direct link cannot be established between FLUENT and an external database. Fortunately, a built-in script allows for interfacing of FLUENT and NIST REFPROP database of fluid properties [59], disregarding the need for UDFs in this work.

By employing the following commands in the FLUENT command line area, the link is established, after which the fluid (water) is selected from a list of the fluids and the application of both liquid and vapour phases is added.

```
'define/user-defined/real-gas-models/nist-real-gas-model'  
  
'use NIST real gas? [no] yes'  
  
'select real-gas data file [" "] "water.fld" '  
  
'define/user-defined/real-gas-models/set-phase'  
  
'Select vapour phase (else liquid)? [yes]'
```

This method allows for the solver to use the water properties up to 2000 K and pressures well in excess of the operational conditions (theoretical limit of 1000 MPa in REFPROP [59]).

3.4.3 Solution Methods and Controls

The solver type is pressure-based, and in the solution methods section, there are multiple options for pressure-velocity coupling schemes:

- Semi-Implicit Method for Pressure-Linked Equations (SIMPLE): The default scheme in FLUENT, and is robust for most applications.
- SIMPLE-Consistent (SIMPLEC): Allows faster convergence for simple problems such as laminar flows.
- Pressure-Implicit with Splitting of Operators (PISO): Useful for unsteady flow problems or for meshes containing cells with higher than average skewness.

The SIMPLE scheme is used unless there are issues with convergence, such as in the case of the annular channel with helical ribs, where the cells have high skewness due to the curvature of the geometry.

Discretization (Interpolation methods) are used for field variables (stored at cell centers) which must be interpolated to the faces of the control volumes, using one

of the following schemes for momentum, turbulent kinetic energy, (specific) dissipation rate, and energy:

- First order upwind: Easiest to converge, only first-order accurate
- Second-order upwind: Uses larger stencils for 2nd order accuracy, essential with tri-tet mesh, or when flow is not aligned with grid. Convergence may be slower.
- Monotone Upstream-Centered Schemes for Conservation Laws (MUSCL): 3rd order convection discretization scheme for unstructured meshes; more accurate in predicting secondary flows, vortices, forces, etc.

The meshes exported by ICEM CFD are unstructured, and thus MUSCL is used for discretization in the solver. In the case of the simple tube, second-order upwind was used with no convergence issues.

The interpolation methods for face pressure are:

- Standard: The default scheme, reduced accuracy for flows exhibiting large surface-normal pressure gradients near boundaries. Should not be used when steep pressure changes are present in the flow.
- PRESTO: Used for highly swirling flows, flows with steep pressure gradients, or in strongly curved domains.
- Linear: Used when other options result in convergence difficulties, or unphysical behaviour.
- Second-order: Used for compressible flows, not to be used with porous media, fans, jumps, or multi-phase models.

For the annular channel and the sudden area change geometries, PRESTO was selected due to its applicability to swirling flows with pressure gradients and strongly curved domains, as well as the convergence problems with the standard scheme.

3.4.4 Convergence

The solution is completed when the convergence criteria is satisfied. At convergence, the following must be obtained:

- All discrete conservation equations are obeyed in all cells to a specific tolerance or the solution no longer changes with subsequent iterations.
- Overall mass, momentum and energy balances are achieved.

To monitor the convergence, residual history is used, and generally a decrease in residuals by three orders of magnitude indicates at least qualitative convergence. At which point, all flow features should be established. The energy residual must decrease to 10^{-6} for the pressure based solver.

Additional monitors can be added to establish trends for variables or functions at a boundary or any defined surface. For example in the simulations conducted in this study, pressure monitors are placed on the inlet and outlet boundaries to confirm the change in pressure and to modify it in the solution setup if found to be different from the initial approximation. Monitors for the temperature at the outlet and the maximum temperature at the heated surfaces are also used to confirm the outlet bulk fluid temperature is as calculated from the heat balance, and the maximum surface temperature doesn't exceed the experimental values by a large margin or the temperature limit of the NIST database.

In some cases, even with a good case setup and choosing the appropriate solution methods for the simulation, divergence can occur quickly, and variable can get out of bound, such as temperature or viscosity exceeding their theoretical limits in the solver. In such cases, an attempt can be made to alter the under-relaxation factors to stabilize the iterative process.

Variables are updated at each iteration and their values in their corresponding equations should get closer and closer together until convergence is achieved. The under-relaxation factors are used to suppress oscillations and increase stability in

the flow solution that result from numerical errors. For a change in a variable (ϕ), the under-relaxation factor (α) would be represented as:

$$\phi = \phi_{old} + \alpha\Delta\phi \quad [3-6]$$

Under-relaxation factors that are too small will significantly slow down convergence, to the extent that it might appear that the solution has converged when in fact it has not. The opposite is also true; by increasing the under-relaxation factors, the convergence might be accelerated at the expense of solution stability.

The general approach is to start with the default under-relaxation factors, which are applicable to a wide range of flow conditions, and only modify them if needed to achieve convergence. In all simulations in this study, the energy under-relaxation factor had to be reduced from 1 to 0.99 (and in some cases 0.9) to achieve convergence. In the cases of sudden area change and annular channel geometries, the momentum value had to be reduced from 0.75 to around 0.5.

3.4.5 Test Matrices for Simulations

3.4.5.1 Bare tube and Pr_t simulations

For the benchmark analysis, since the mesh for the bare tube is 2 m in length and the test section is 4 m, three simulations were needed, from 0-2, 1-3 and 2-4 meters of heated length. The simulations are conducted in the NHT and DHT regimes. Both RKE and SST models were used as shown in the test matrix in Table 3-4. The results are compared to each other, as well as to a subcritical flow case.

Table 3-4: Test Matrix for Simple Tube Simulations, RKE and SST Models

Sim.	P, MPa	G, kg/m ² s	q, MW/m ²	T _{in} , °C	L, m	Model
1	24	1002	391	350	0-2	RKE
2	24	1002	391	350	0-2	SST
3	24	1002	391	368	1-3	RKE
4	24	1002	391	368	1-3	SST
5	24	1002	391	378	2-4	RKE
6	24	1002	391	378	2-4	SST

7	24.1	1496	1235	322	0-2	RKE
8	24.1	1496	1235	322	0-2	SST
9	24.1	1496	1235	367	1-3	RKE
10	24.1	1496	1235	367	1-3	SST
11	24.1	1496	1235	381	2-4	RKE
12	24.1	1496	1235	381	2-4	SST
13	1	1496	1235	25	N/A	RKE
14	1	1496	1235	25	N/A	SST

The values for the turbulent Pr number in the RKE and SST models are shown in Table 3-5 and Table 3-6 and the test matrix for the simulations is shown in Table 3-7.

Table 3-5: Standard and Modified Values for RKE Turbulent Pr Numbers

Parameter	Value for RKE	Modified range
Turbulent kinetic energy Pr	1	0.9 - 1.1
Turbulent dissipation rate Pr	1.2	0.9 - 1.3
Energy Pr	0.85	0.75 - 0.95
Wall Pr	0.85	0.75 - 0.95

Table 3-6: Standard and Modified Values for SST Turbulent Pr Numbers

Parameter	Value for SST	Modified range
Turbulent kinetic energy Pr (inner)	1.176	1.1 - 1.3
Turbulent kinetic energy Pr (outer)	1	0.9 - 1.1
Specific dissipation rate Pr (inner)	2	1.8 - 2.4
Specific dissipation rate Pr (outer)	1.168	1.1 - 1.3
Energy Pr	0.85	0.75 - 0.95
Wall Pr	0.85	0.75 - 0.95

Table 3-7: Test Matrix for Turbulent Pr variations study, RKE and SST Models. P: 24.1 MPa, G = 1496 kg/m²s, q = 1235 kW/m², L = 1-3 m, T_{in} = 366°C, T_{out} = 386°C

RKE parameter change	SST parameter change
TDR Pr = 0.9	Energy Pr = 0.75
TDR Pr = 1	Energy Pr = 0.95
TDR Pr = 1.3	TKE Inner Pr = 1.1
Energy Pr = 0.75	TKE Inner Pr = 1.3

TKE Pr = 0.9	TKE Outer Pr = 0.9
Wall Pr = 0.75	TKE Outer Pr = 1.1
$C_{2\varepsilon} = 2.1$	Wall Pr = 0.75
TDR Pr = 0.9, Energy Pr = 0.75	Wall Pr = 0.95
TDR Pr = 1, Energy Pr = 0.75	SDR Inner Pr = 1.8
TDR Pr = 1, $C_{2\varepsilon} = 2.1$	SDR Inner Pr = 2.2
TDR Pr = 1, Energy Pr = 0.75, $C_{2\varepsilon} = 2.1$	SDR Outer Pr = 1.1
TDR Pr = 1, Energy Pr = 0.75, $C_{2\varepsilon} = 1.85$	Energy Pr = 0.75, SDR Inner Pr = 2.2
	Energy Pr = 0.75, SDR Inner Pr = 2.4

3.4.5.2 Annular channel with helical fins

As mentioned earlier in this chapter, the wall temperatures for this dataset were measured using thermocouples engraved in copper plugs inside the inner tube, and the temperatures were averaged for each cross section. This presents a source of uncertainty for the true wall temperature of the fluid, as the existence of the helical fins adds a variable thickness to the wall, and the calculated values for the fluid temperatures at the wall will not in fact be uniform. The fundamental role of the fins is to increase the heat transfer area and remove more heat compared to a bare wall. In addition, due to the heat generation in the solid structure, and the angles between the fins and the tube surface, the heat flux distribution will not be uniform (radially or axially) and there will be areas of higher heat flux to the fluid, causing higher temperatures, which will not be reflected in the experimental points.

The heat flux variation due to thickness and temperature fluctuations is mentioned by the authors [56], however, only an average heat flux is given for each case. This means the actual values are not known and the differences between the heat flux at the flow tube and the fin surfaces (sides and top) are not known either. This creates a problem in recreating the experimental conditions using CFD. Due to the ambiguity of the heat flux description, three methods of simulating the experimental setup were taken, based on different assumptions and interpretations of the heat generation relationship to the heat flux in the geometry:

- 1) Full heat flux out of every heated surface: if the average heat flux reported by the authors is indeed averaged for every surface.
- 2) Unheated fins: as the thickness of the heated rod is 0.35mm compared to the height of the fin 0.6mm, the electric current is likely to take the path of least resistance through the base and mostly bypass the thickness of the fins.
- 3) 0.5 heat flux out of the fin surfaces: the base of the fin is 1 mm wide, and with a thickness of 0.6 mm, the perimeter is 2.2 mm compared to a base of 1 mm if the fin did not exist. Thus, the heat that would have otherwise been generated out of 1 mm section is now being released out of 2.2 mm, resulting in a reduction of roughly 0.5 the original heat flux out of the base.

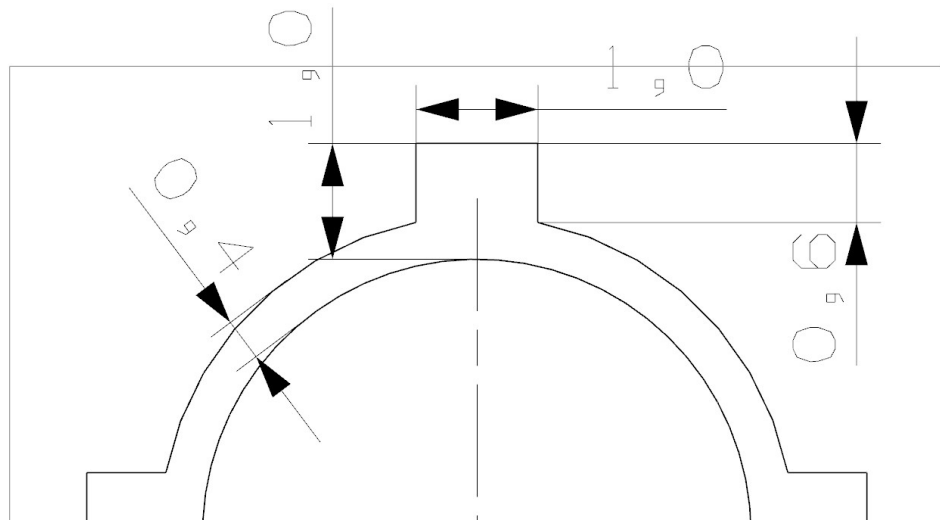


Figure 3-28: Illustration of the finned rod dimensions

The test matrix for all simulations is shown in Table 3-8. The simulations range from the standard geometry of the annular channel with helical fins using the SST and RKE models, to the same geometry with straight fins, and finally an annular channel with no fins. The change in geometry will establish the differences the fins introduce to the results, and whether they have an impact on the temperature profiles, heat transfer, turbulence production, etc.

When comparing to an annular channel with no fins, the area change has to be considered, so a set of simulations is conducted for an annular channel with the

same inner and outer diameters, same hydraulic equivalent diameter, and finally the same flow area. Another point of comparison is the heat introduced to the fluid. Tests were done for the same heat flux, and for the same total power (resulting in a higher flux).

Table 3-8: Test matrix for annular channel with helical fins simulations

Sim. #	Case #	P, MPa	G, kg/m ² s	q, MW/m ²	T _{in} , °C	HT regime	Model	Geom.	Heat flux model	H _{out} , kJ/kg	T _{out} , °C
1	1	22.6	2000	1.543	205	NHT	SST	Helical fins	Heated fins	1133	260
2	1	22.6	2000	1.543	205	NHT	RKE	Helical fins	Heated fins	1133	260
3	1	22.6	2000	1.543	205	NHT	SST	Helical fins	Unheated fins	1029	237
4	1	22.6	2000	1.543	205	NHT	RKE	Helical fins	Unheated fins	1029	237
5	1	22.6	2000	1.543	205	NHT	SST	Helical fins	0.5 flux fins	1082	249
6	1	22.6	2000	1.543	205	NHT	RKE	Helical fins	0.5 flux fins	1082	249

7	1	22.6	2000	1.543	205	NHT	SST	Straight fins	Heated fins	1132.8	259.7
8	1	22.6	2000	1.543	205	NHT	RKE	Straight fins	Heated fins	1132.8	259.7
9	1	22.6	2000	1.543	205	NHT	SST	Straight fins	0.5 flux fins	1081.7	248.7
10	1	22.6	2000	1.543	205	NHT	SST	Straight fins	Unheated fins	1028.8	236.8
11	1	22.6	2000	1.543	205	NHT	SST	No fins, same ID, OD	Same flux : 1.543 MW/m ²	1062.3	244.7
12	1	22.6	2000	1.543	205	NHT	SST	No fins, same D _{hy}	Same flux : 1.543 MW/m ²	1106.5	254.2
13	1	22.6	2000	1.543	205	NHT	SST	No fins, same ID, OD	Same power: 2 MW/m ²	1115.3	256.2

14	1	22.6	2000	1.543	205	NHT	SST	No fins, same D_{hy}	Same power: 2 MW/m ²	1172.5	267.9
15	1	22.6	2000	1.543	205	NHT	SST	No fins, same A_{flow}	Same flux : 1.543 MW/m ²	1076.3	247.7
16	1	22.6	2000	1.543	205	NHT	SST	No fins, same A_{flow}	Same power: 2 MW/m ²	1133.4	259.9
17	2	22.6	2000	1.758	207	NHT	SST	Helical Fins	Heated fins	1176.6	268.9
18	2	22.6	2000	1.758	207	NHT	RKE	Helical Fins	Heated fins	1176.6	268.9
19	2	22.6	2000	1.758	207	NHT	SST, Energy $Pr_t = 0.75$	Helical Fins	Heated fins	1176.6	268.9
20	2	22.6	2000	1.758	207	NHT	SST, Energy $Pr_t = 0.75$, SDR $Pr_t = 2.4$	Helical Fins	Heated fins	1176.6	268.9

21	3	22.6	2000	2.033	208	NHT	SST	Helical Fins	Heated fins	1225.5	278.9
22	3	22.6	2000	2.033	208	NHT	RKE	Helical Fins	Heated fins	1225.5	278.9
23	3	22.6	2000	2.033	208	NHT	SST, Energy $Pr_t = 0.75$, SDR $Pr_t = 2.4$	Helical Fins	Heated fins	1225.5	278.9
24	3	22.6	2000	2.033	208	NHT	RKE, Energy $Pr_t = 0.75$	Helical Fins	Heated fins	1225.5	278.9
25	4	22.6	2000	2.547	214	DHT	SST	Helical fins	Heated fins	1335.3	300.5
26	4	22.6	2000	2.547	214	DHT	RKE	Helical fins	Heated fins	1335.3	300.5
27	4	22.6	2000	2.547	214	DHT	SST	Straight fins	Heated fins	1334.9	300.3

28	4	22.6	2000	2.547	214	DHT	SST, Energy $Pr_t = 0.75$	Helical fins	Heated fins	1335.3	300.5
29	4	22.6	2000	2.547	214	DHT	SST, Energy $Pr_t = 0.75,$ SDR $Pr_t = 2.4$	Helical fins	Heated fins	1335.3	300.5
30	4	22.6	2000	2.547	214	DHT	RKE, Energy $Pr_t = 0.75$	Helical fins	Heated fins	1335.3	300.5
31	N/A	1	2000	1.543	205	Subcritical	SST	Helical fins	Heated fins	3089.9	317.9

3.4.5.3 Sudden area change geometry

The following test matrix shows the simulations on this geometry under the normal and deteriorated heat transfer conditions, with the turbulent models developed through the results of the analysis on the bare tubes and helical fin geometry.

Table 3-9: Test Matrix for Tube with Sudden Area Change Simulations, RKE and SST Models

Sim.	P, MPa	G, kg/m ² s	q, MW/m ²	T _{in} , °C	L, m	Model	Orifice location, m
1	24	1002	391	350	0-2	RKE	0.1, ent. region
2	24	1002	391	350	0-2	SST	0.1, ent. region
3	24	1002	391	368	1-3	RKE	0.1, ent. region
4	24	1002	391	368	1-3	SST	0.1, ent. region
5	24	1002	391	378	2-4	RKE	0.1, ent. region
6	24	1002	391	378	2-4	SST	0.1, ent. region
7	24	1002	391	350	0-2	RKE	0.2, heated region
8	24	1002	391	350	0-2	SST	0.2, heated region
9	24	1002	391	368	1-3	RKE	0.2, heated region
10	24	1002	391	368	1-3	SST	0.2, heated region
11	24	1002	391	378	2-4	RKE	0.2, heated region
12	24	1002	391	378	2-4	SST	0.2, heated region
13	24.1	1496	1235	322	0-2	RKE	0.1, ent. region
14	24.1	1496	1235	322	0-2	SST	0.1, ent. region
15	24.1	1496	1235	367	1-3	RKE	0.1, ent. region
16	24.1	1496	1235	367	1-3	SST	0.1, ent. region
17	24.1	1496	1235	381	2-4	RKE	0.1, ent. region
18	24.1	1496	1235	381	2-4	SST	0.1, ent. region
19	24.1	1496	1235	322	0-2	RKE	0.2, heated region
20	24.1	1496	1235	322	0-2	SST	0.2, heated region
21	24.1	1496	1235	367	1-3	RKE	0.2, heated region
22	24.1	1496	1235	367	1-3	SST	0.2, heated region
23	24.1	1496	1235	381	2-4	RKE	0.2, heated region
24	24.1	1496	1235	381	2-4	SST	0.2, heated region

Chapter 4: Simple Tube Results

The work done in this chapter is concentrated on studying the turbulent Pr number effect on simulation results as part of meeting the first objective of empirical constants analysis. The second part, in chapters 5 and 6, is concerned with the flow in an annular channel with helical fins and a pipe with a sudden area change as part of the investigation of geometrical perturbations on SCW flow.

The turbulent Pr number analysis shows the effect of the different variations of turbulent Pr on the simulation results in the form of temperature and fluid properties in the flow. It establishes the expected trends from each of the variations, as well as aiding to select specific constants for further study.

The analysis of the geometrical perturbations showcases the ability of the CFD models to simulate SCW flow under artificial turbulence inducing geometry. The results of which will be used to further understand the flow of SCW in a reactor-simulating geometry.

To start with the simple tube analysis, a sample case was selected from the Kirillov et al. experimental dataset [53], to represent the NHT regime in SCW flow as shown in Figure 4-1. The models developed through previous studies, with the unmodified turbulent Pr numbers [60] provide a very good fit for experimental data, with less than 5% deviation from experimental wall temperatures for the realizable k - ϵ and the SST k - ω models. Before the bulk fluid passes the pseudocritical point, the fluid is essentially a compressed liquid and the heat transfer phenomenon is relatively straight-forward. It can be solved using empirical correlations (even ones developed for subcritical flows), and standard two-equation CFD models.

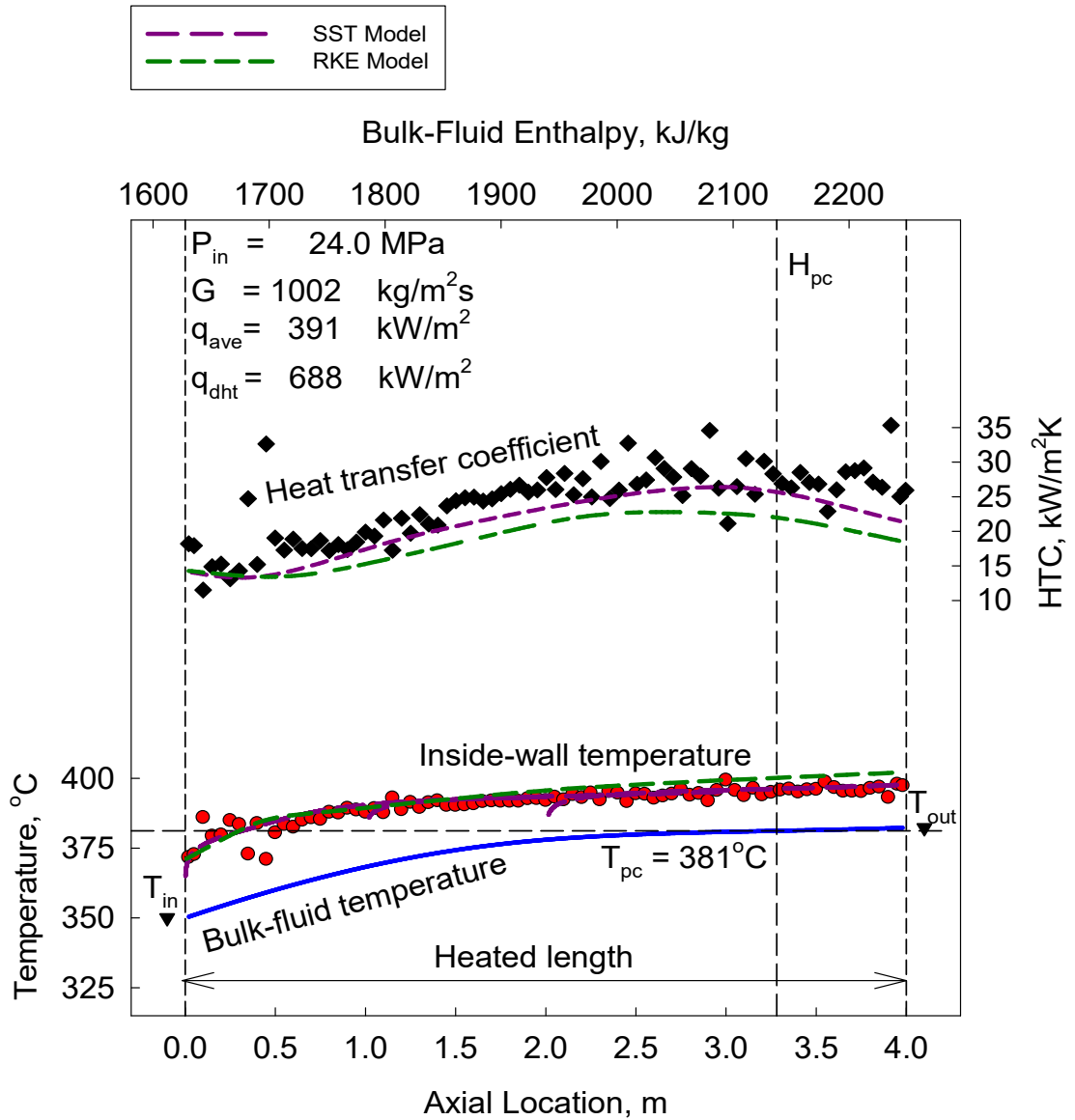


Figure 4-1: An experimental dataset sample from Kirillov et al. dataset [53] showing NHT, and the simulation result of RKE and SST models for wall temperatures and heat transfer coefficients

Figure 4-2 shows an experimental test with a higher heat flux to mass flux ratio, which results in a wall-temperature profile resembling a DHT phenomenon. As the fluid crosses the pseudocritical point, heat transfer is reduced to the bulk-fluid and the wall temperatures rise as a result. It is at this region that the empirical correlation do not produce valid results (producing incorrect trends), and as shown in the same figure, the CFD results for the RKE and SST models show a deviation from experimental data as well. This suggests that a phenomenon is occurring that is not captured by the 1-D models, and that standard 3-D models also do not capture the phenomenon [60], [61].

As discussed earlier, the 2-equation models are semi-empirical in nature and include many assumptions and simplifications to model complex flows and geometries with lower computational resources compared to a direct numerical simulation. One of the empirical constants with a major effect on the simulation results is the turbulent Pr number. As discussed in section 2.7, the standard values vary depending on the type of turbulent Pr and they are accepted as valid for “general flows”, of a wide range of applications and for a range of fluids.

To assess the impact of the turbulent Pr numbers in the RKE and SST models on SCW flow simulations, the experimental case shown in Figure 4-2 is used as a benchmark. As the NHT regime is easily captured with high accuracy, it is of interest to determine if the accuracy and the trends for the DHT regime can be improved, and if so, which turbulent Pr number has the greatest effect on the simulation results.

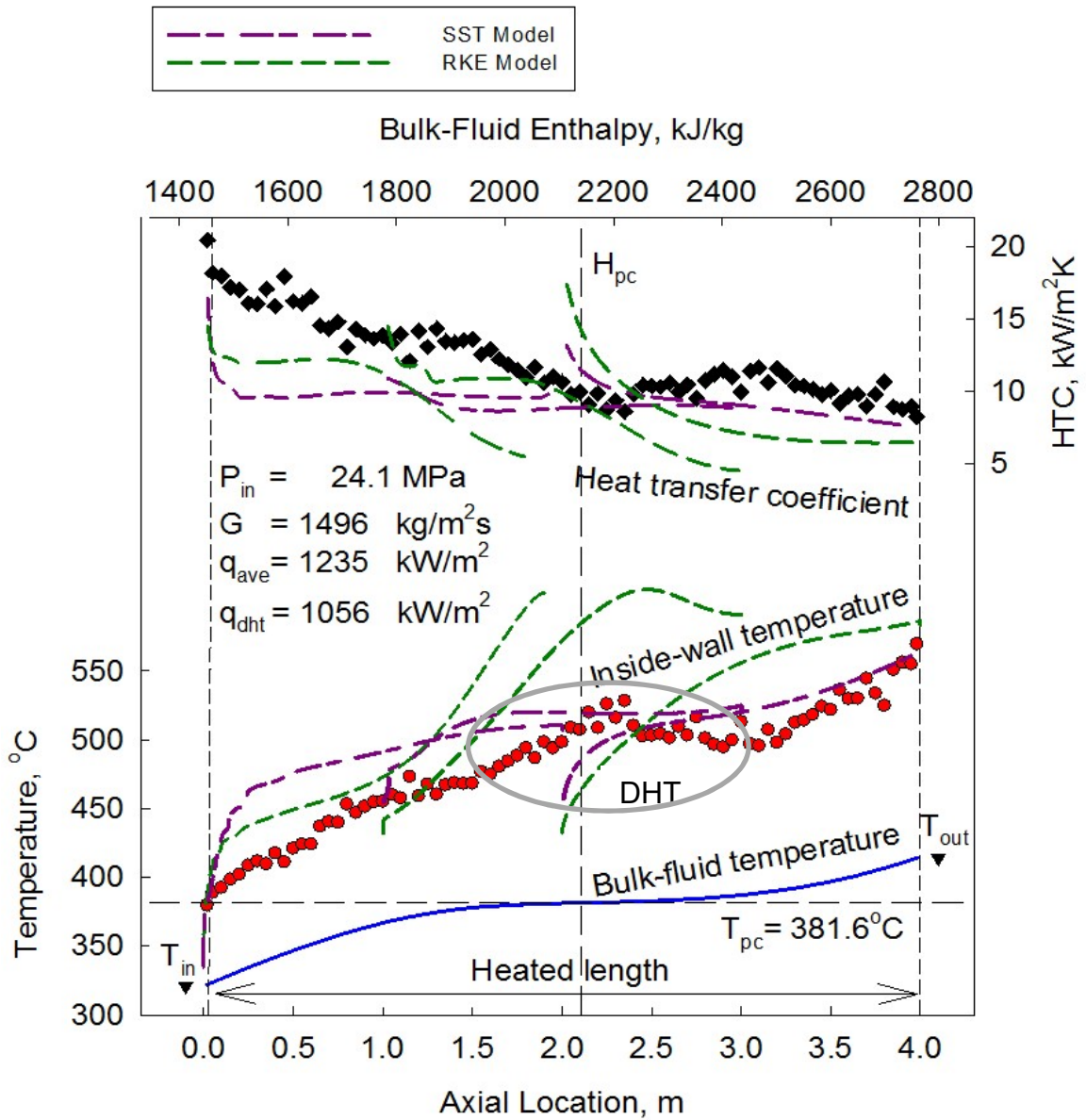


Figure 4-2: An experimental dataset sample from Kirillov et al. dataset [53] showing DHT, and the simulation result of RKE and SST models for wall temperatures and heat transfer coefficients

4.1 Assessment of Simple Tube 3D Flow and Thermal Distributions

To establish the viability of the mesh, and to explore the multidimensional effects of SCW flow, benchmark test runs are conducted for a normal heat transfer case, with no fluctuations in the data, and no apparent deterioration in heat transfer.

The chosen reference case is the vertical tube case No.38_06 in the Kirillov et al. experimental dataset [53]. It is shown in Figure 4-3 with a mass flux of 1002 kg/m²s, a heat flux of 391 kW/m² and pressure of 24 MPa. This case has the lowest heat flux to mass flux ratio (about 40%), thus representing the NHT regime. The DHT regime is represented by case No.49_12, with 1496 kg/m²s, 1235 kW/m² and 24.1 MPa. This case has a heat to mass flux ratio of about 80%. Both RKE and SST models were used as shown in the test matrix in Table 3-4. Since the mesh is 2 meters in length and the test section is 4 meters in length, three simulations were used, from 0-2, 1-3 and 2-4 meters of heated length, to cover the entire range of the test section. This allowed for more optimal use of the computer memory. The results of the simulations are analyzed and compared to each other.

4.1.1 NHT Regime Results

The simulations using the SST and RKE models show results with a good agreement with experimental results, with a maximum deviation of 3%.

As mentioned earlier, the simulations for each experimental case is conducted over 3 distances, and from the temperature profiles shown in Figure 4-3, the accuracy and the continuance between the 3 simulations under the NHT regime are observed. It is of interest now to analyze the flow and thermal distributions in the flow which correspond to the phenomenon of NHT which is characterized by good heat transfer from the heated wall to the bulk fluid.

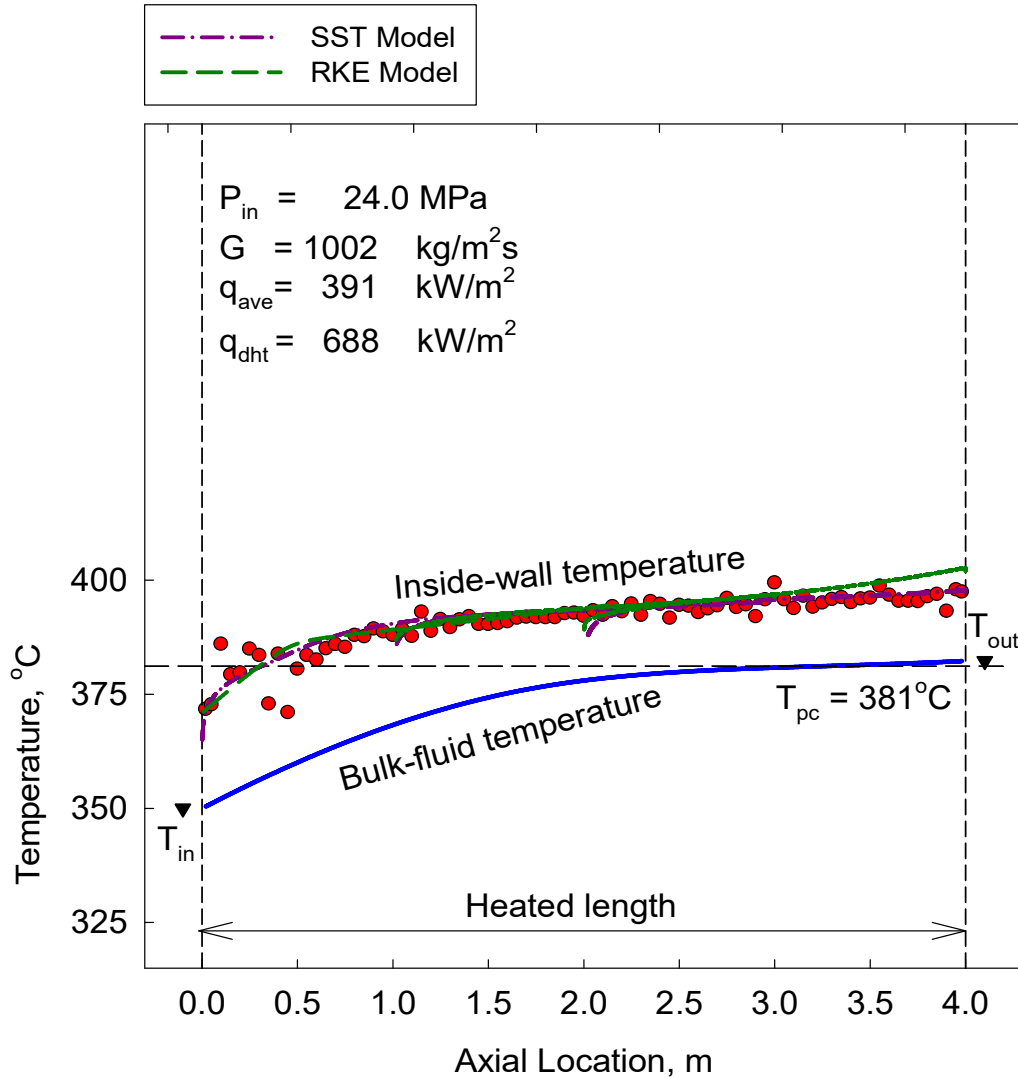


Figure 4-3: Reference case from Kirillov et al. dataset [53] for the 3D mesh of a simple tube geometry

The following plots (Figure 4-4 to Figure 4-8) show the property fields for the 1-3 m section of the heated length, using the SST turbulence model.

Figure 4-4 shows the 3D distribution of temperature in the tube, in the center plane (YZ plane, in the 3D cutout above the figure). This method allows the property variations to be shown both axially and radially. The temperature profile shows the unheated entrance region, after which the wall temperature rises rapidly with the introduction of the heat flux at the wall, while the rest of the fluid (from ~20-

30 microns to the center) doesn't change as rapidly. This is an example of the normal heat transfer regime (NHT) where CFD predicts the experimental wall temperature profiles within 3% accuracy.

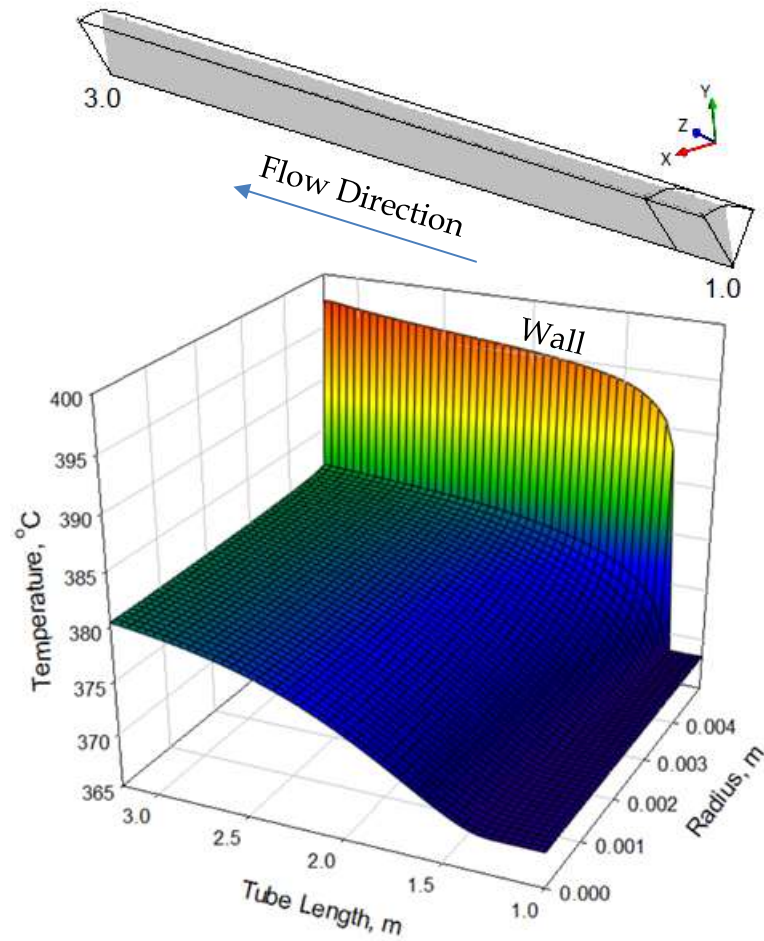


Figure 4-4: 3D Fluid temperature plot for a case with: $P = 24$ MPa, $G = 1002$ kg/m²s, and $q = 391$ kW/m², using the SST model (NHT)

The corresponding property profiles are plotted for density, viscosity, specific heat and turbulent kinetic energy in Figure 4-5 to Figure 4-8.

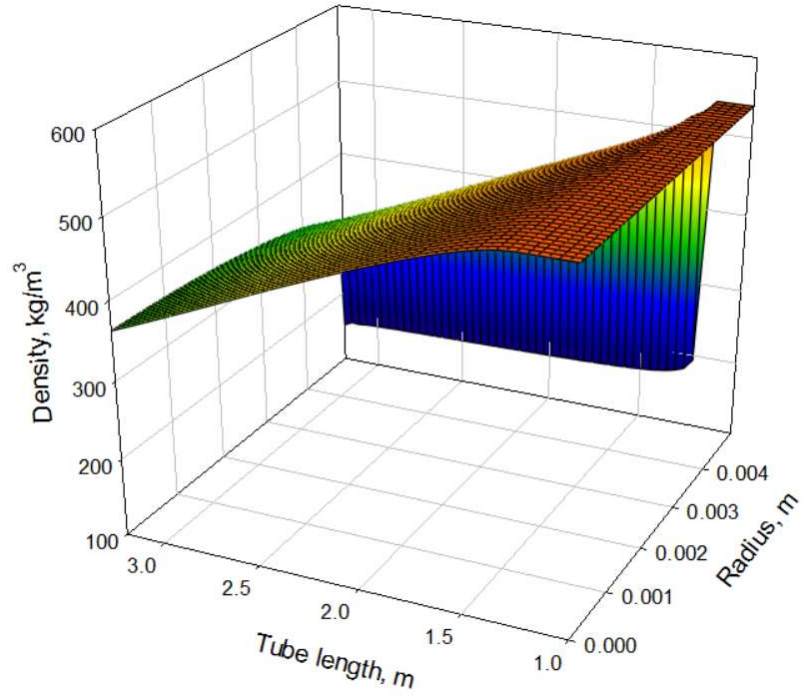


Figure 4-5: 3D density plot for a case with: $P = 24$ MPa, $G = 1002$ kg/m²s, and $q = 391$ kW/m², using the SST model

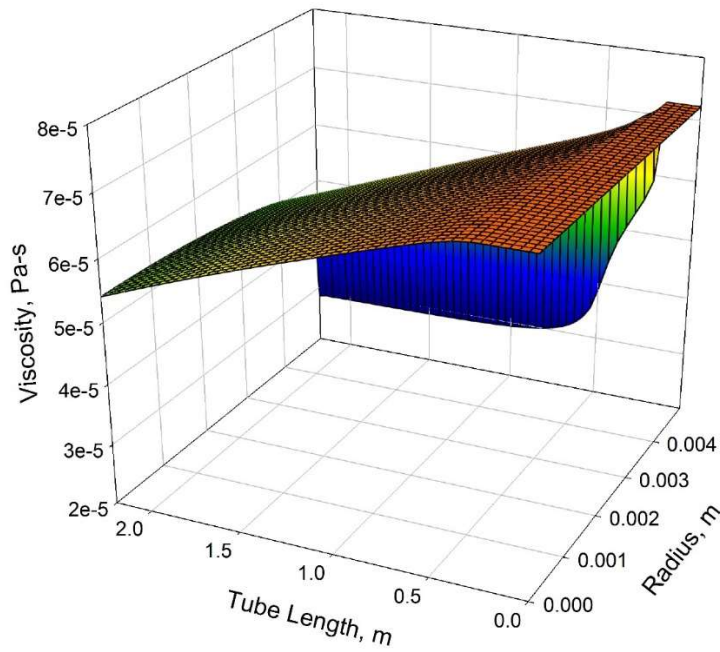


Figure 4-6: 3D viscosity plot for a case with $P = 24$ MPa, $G = 1002$ kg/m²s, and $q = 391$ kW/m², using the SST model

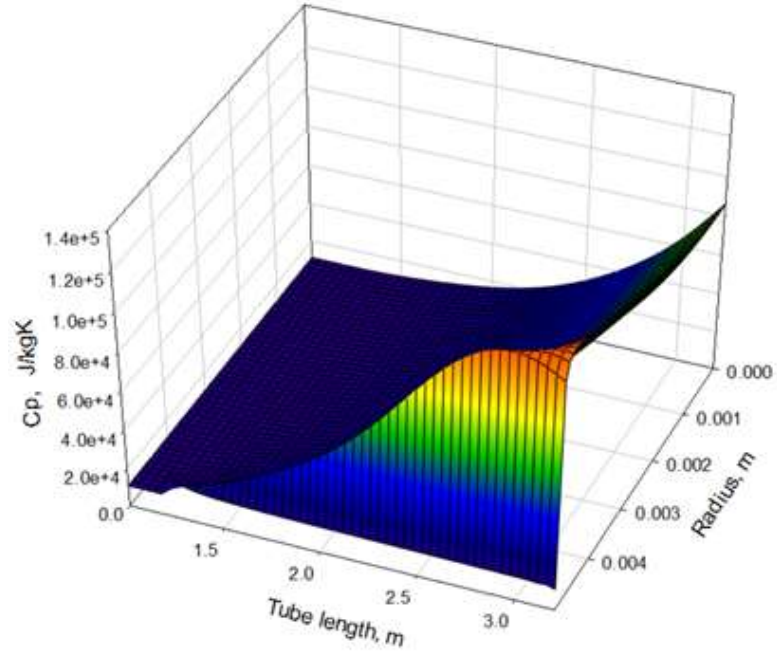


Figure 4-7: 3D specific heat plot for a case with: $P = 24 \text{ MPa}$, $G = 1002 \text{ kg/m}^2\text{s}$, and $q = 391 \text{ kW/m}^2$, using the SST model

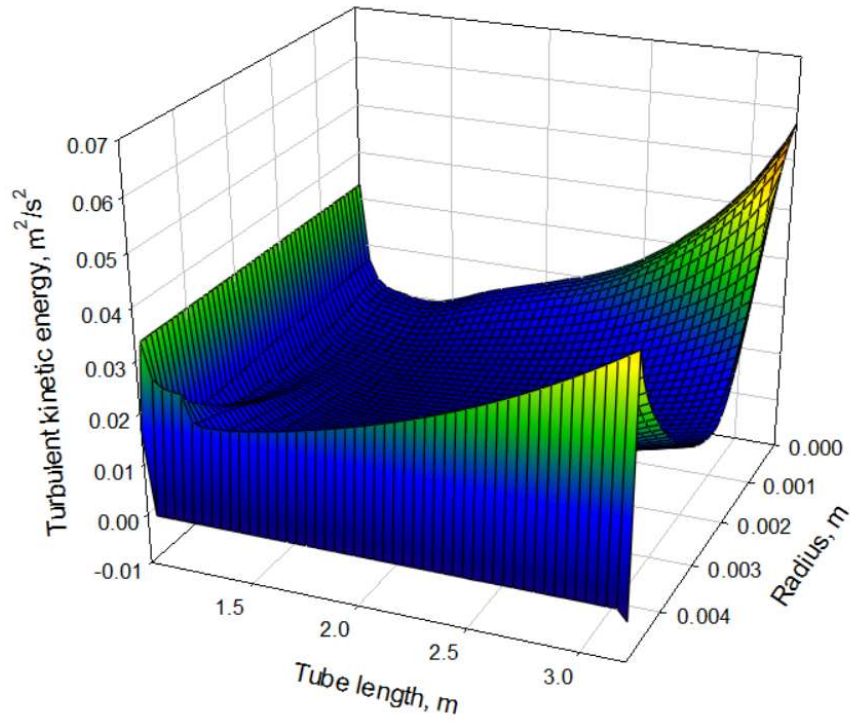


Figure 4-8: 3D turbulent kinetic energy plot for a case with $P = 24 \text{ MPa}$, $G = 1002 \text{ kg/m}^2\text{s}$, and $q = 391 \text{ kW/m}^2$, using the SST model

The variations shown in the figures above represent the expected trends in transferring the energy from a heated wall to a moving fluid. The temperature at the heated wall increases ahead of the rest of the fluid, and the density plot helps to showcase the relative magnitude of change between the wall and the center, and the inlet and outlet of the water.

The viscosity plot shows in a similar manner the change throughout the flow field, and using the mass flux and the hydraulic equivalent diameter, the Reynolds number range can be calculated in the range of 2×10^5 to 5×10^5 .

The specific heat peak occurs at these conditions at 381°C , and has a value of ~ 115 kJ/kg \cdot K. C_p only reaches such high values near the outlet and the effect of the peak does not disturb the heat transfer in the tube, as shown by the steady rise in temperature profiles.

The turbulent kinetic contour shows the driving force for heat transfer by creating energy difference between the radial segments of the fluids. The bigger the difference, the better the heat transfer in theory.

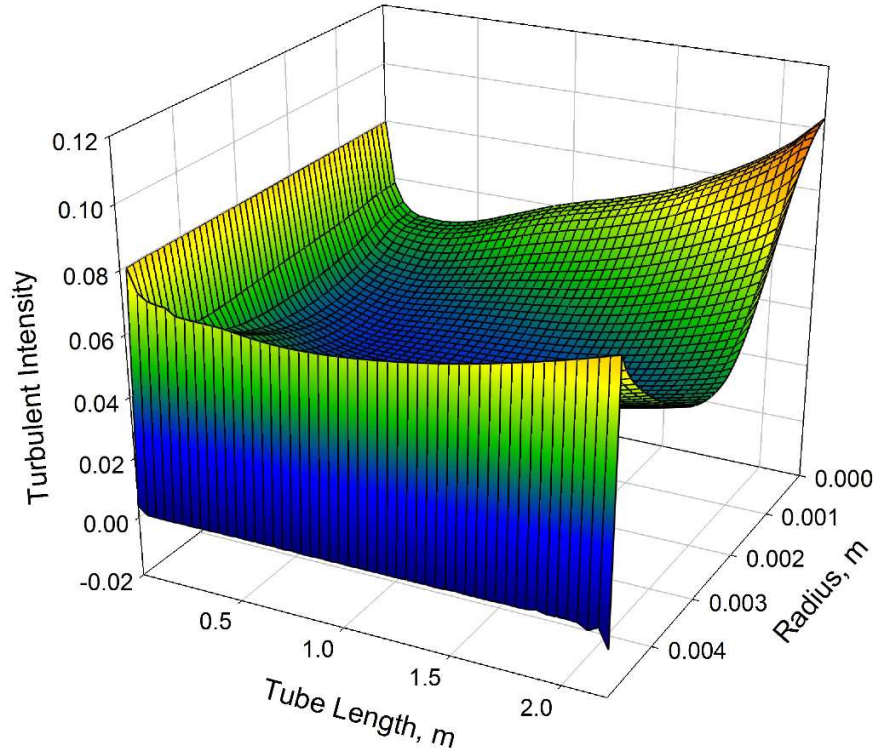


Figure 4-9: 3D turbulence intensity plot for a case with: $P = 24$ MPa, $G = 1002$ kg/m²s, and $q = 391$ kW/m², using the SST model

The turbulence intensity (also known as turbulence level) is defined as [28]:

$$I \equiv \frac{u'}{U} \quad [4-1]$$

Where u' is the root-mean-square of the turbulent velocity fluctuations and U is the mean flow velocity. The turbulence level can be also related to the turbulent kinetic energy as:

$$u' \equiv \sqrt{\frac{1}{3}(u_x'^2 + u_y'^2 + u_z'^2)} = \sqrt{\frac{2}{3}k} \quad [4-2]$$

$$k = \frac{3}{2}(UI)^2 \quad [4-3]$$

The turbulence levels in the flow can be divided into categories:

1. High-turbulence case: High-speed flow inside complex geometries like heat-exchangers and flow inside rotating machinery (turbines and compressors). Typically the turbulence intensity is between 5% and 20%
2. Medium-turbulence case: Flow in not-so-complex devices like large pipes, ventilation flows etc. or low speed flows (low Reynolds number). Typically the turbulence intensity is between 1% and 5%
3. Low-turbulence case: Flow originating from a fluid that stands still, like external flow across cars, submarines and aircrafts. Very high-quality wind-tunnels can also reach really low turbulence levels. Typically the turbulence intensity is very low, well below 1%.

The intensity plotted in Figure 4-9 reaches a maximum of roughly 10%, while the mean flow intensity is closer to 4-5%. This is an indication of the medium/high turbulence level in the flow under NHT conditions.

The results for the RKE model are broadly similar to the SST model for the NHT regime, and they are shown in Appendix B for reference.

4.1.2 DHT Regime Results

For the DHT case analysis, Figure 4-10 shows the temperature profiles predicted by the SST and RKE models. The property distributions are studied and compared to the NHT results, the variation in turbulent Pr results, and later in the chapter to the subcritical flow results.

The RKE and SST model results for the 1-3 meters of heated length are shown in the form of 3D plots for the central axial plane in the mesh. The property fields are shown in the axial and radial directions. Figure 4-11 and Figure 4-12 show the temperature profiles for the RKE and SST models respectively, where in addition to the wall temperatures displayed in Figure 4-10, the fluid temperatures all the way to the axis of the tube can be visualized as well.

The corresponding density plots are shown in Figure 4-13 and Figure 4-14, in which the change in density can be seen to be steeper than that in the NHT case, as it transitions from the liquid-like region to the gas-like region. The lowest density achieved by the fluid is naturally lower than that in the NHT regime. Another point observed in these plots, is the trend of the density at the center of the tube, where it can be seen that due to the over-prediction of DHT using the RKE model, the heat is not transferred well to the center of the flow and the density is higher compared to the SST model which does not show the DHT trend and shows a better transfer of heat to the fluid.

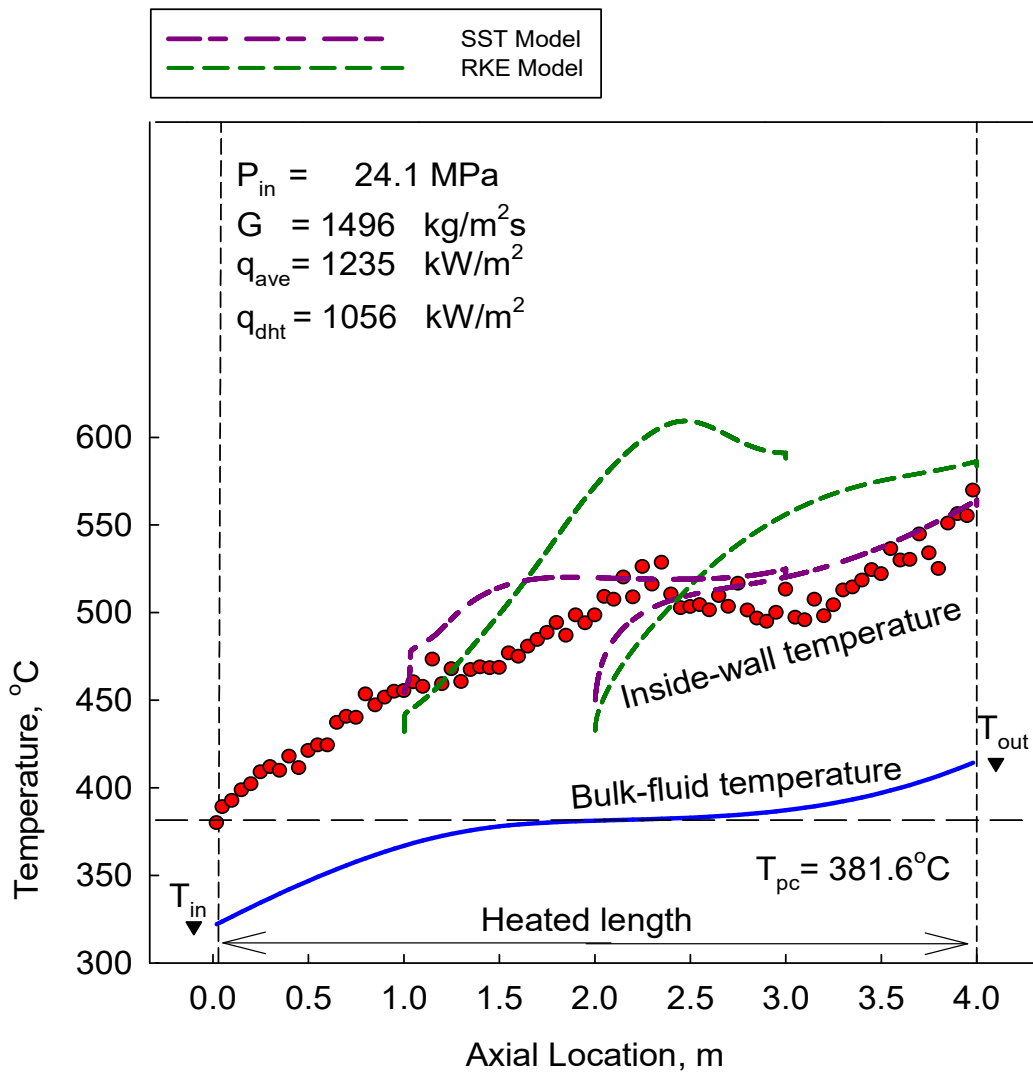


Figure 4-10: DHT case for the 3D mesh of a simple tube geometry

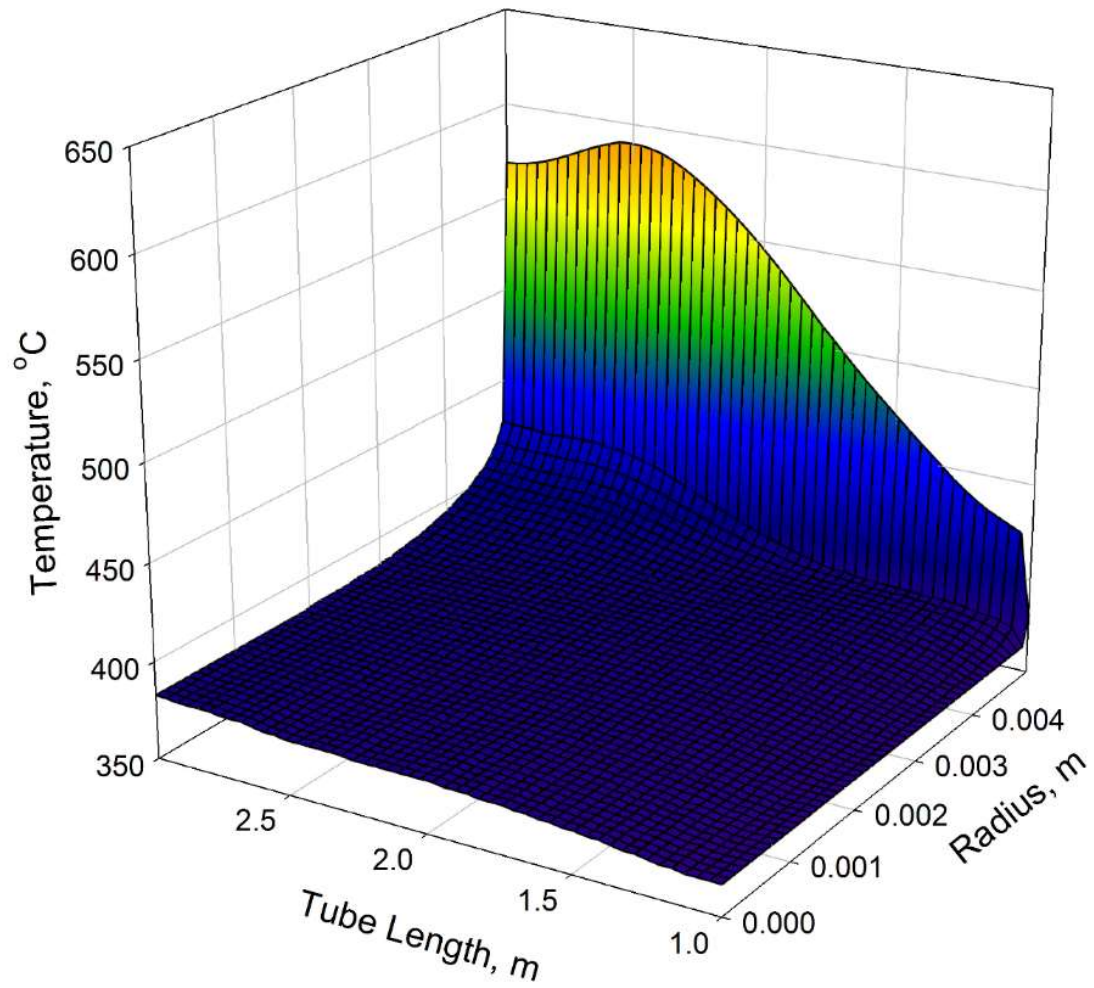


Figure 4-11: 3D Temperature plot for a case with: $P = 24.1$ MPa, $G = 1496$ kg/m²s, and $q = 1235$ kW/m², using the RKE model (DHT)

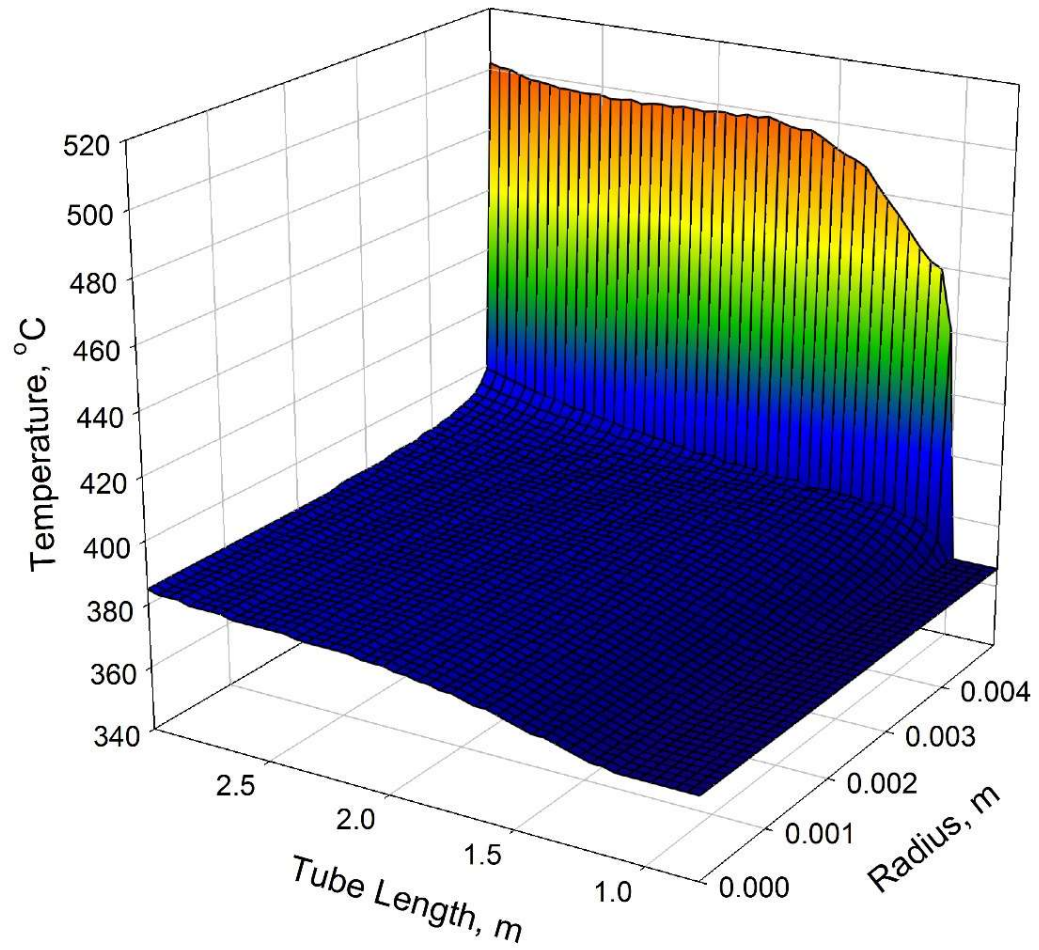


Figure 4-12: 3D Temperature plot for a case with: $P = 24.1$ MPa, $G = 1496$ kg/m²s, and $q = 1235$ kW/m², using the SST model (DHT)

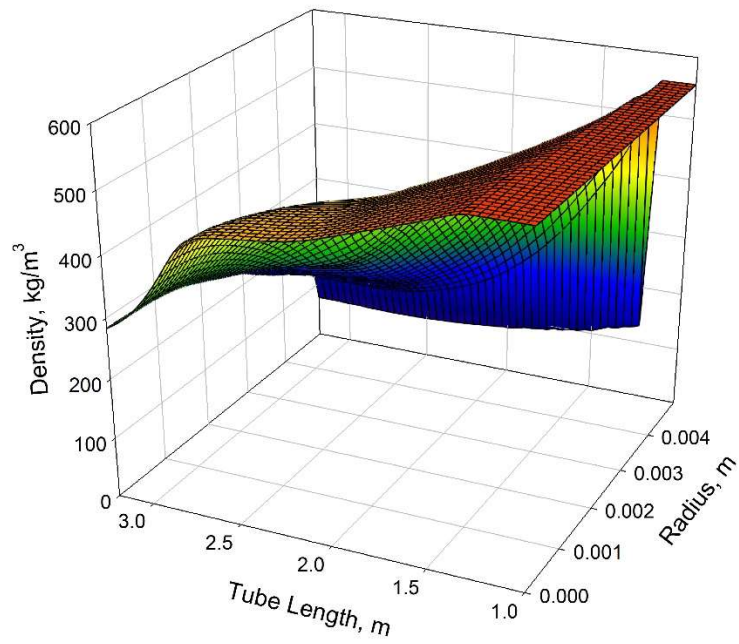


Figure 4-13: 3D Density plot for a case with: $P = 24.1$ MPa, $G = 1496$ kg/m²s, and $q = 1235$ kW/m², using the RKE model

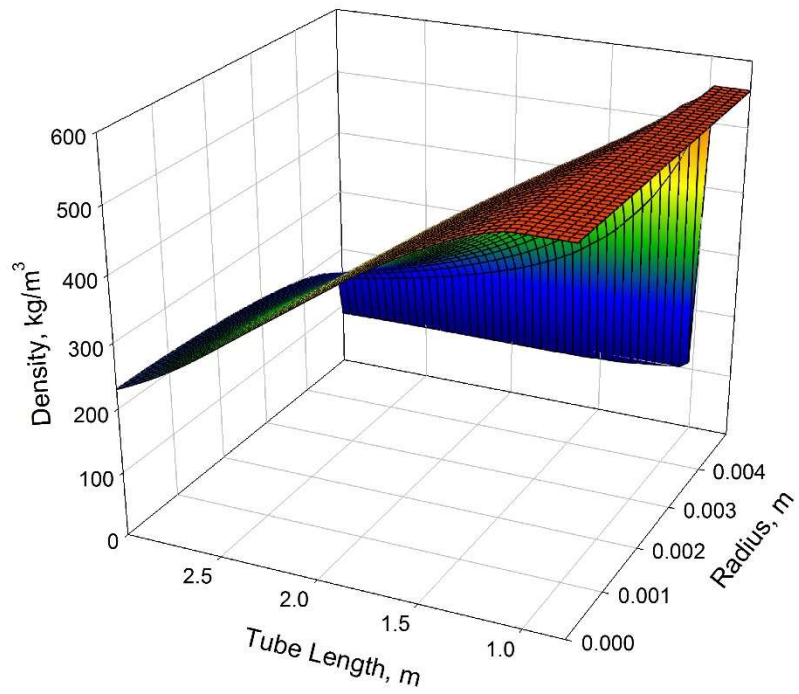


Figure 4-14: 3D Density plot for a case with: $P = 24.1$ MPa, $G = 1496$ kg/m²s, and $q = 1235$ kW/m², using the SST model

Figure 4-15 and Figure 4-16 represent the viscosity of the fluid throughout the flow region (RKE and SST respectively), and using the mass flux and the hydraulic diameter, the Reynolds number can be calculated to be in the order of 10^5 (between 2.5×10^5 and 5×10^5).

The figure (and axis) orientations differ depending on the graph, to show the property fields correctly. For example, the velocity contours in Figure 4-17 and Figure 4-18 are shown with the X and Y axis reversed, to show the development of the velocity from the wall outwards. The RKE model shows an increase in the velocity of the fluid near the end of the heated length, as the flow recovers from the deterioration in heat transfer and fluid near the center gains more heat from the wall. This leads to the drop in density observed earlier, as well as the acceleration in the flow near the center. The same does not occur in the SST model case, where the heat transfer is more uniform throughout and there's no signs of DHT and recovery phases.

Similarly, the specific heat plots in Figure 4-19 and Figure 4-20 are rotated to show the peak reached by the fluid as it passes the pseudocritical point. As expected, the fluid at the wall passes through it first, and as the heat is transferred to the bulk fluid, the temperature rises and the pseudocritical temperature is reached incrementally away from the wall, along the axial direction of the flow. As the pseudocritical point moves away from the wall however, there is a disturbance in the fluid's thermal conductivity (shown in Figure 4-21, Figure 4-22 and earlier in the thermos-physical properties of water in Figure 2-1). That increase in thermal conductivity means the heat transfers better throughout the fluid in that temperature range. This leads to the rapid change in C_p at approximately the 2-meter mark in the heated length, as the bulk fluid passes the pseudocritical point (shown also in Figure 4-10).

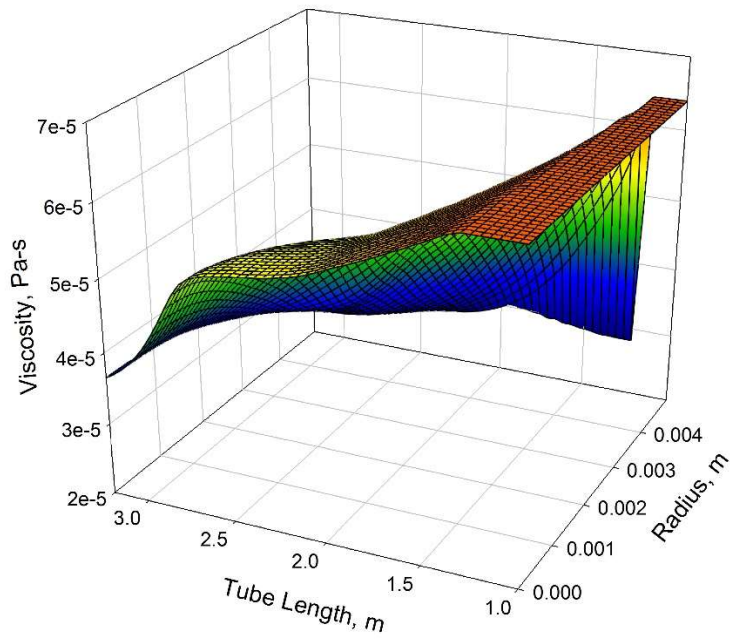


Figure 4-15: 3D Viscosity plot for a case with: $P = 24.1$ MPa, $G = 1496$ kg/m²s, and $q = 1235$ kW/m², using the RKE model

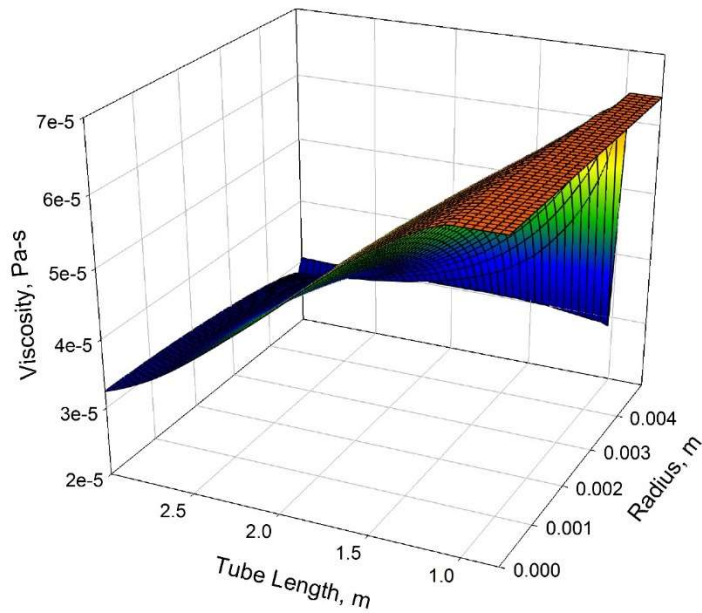


Figure 4-16: 3D Viscosity plot for a case with: $P = 24.1$ MPa, $G = 1496$ kg/m²s, and $q = 1235$ kW/m², using the SST model

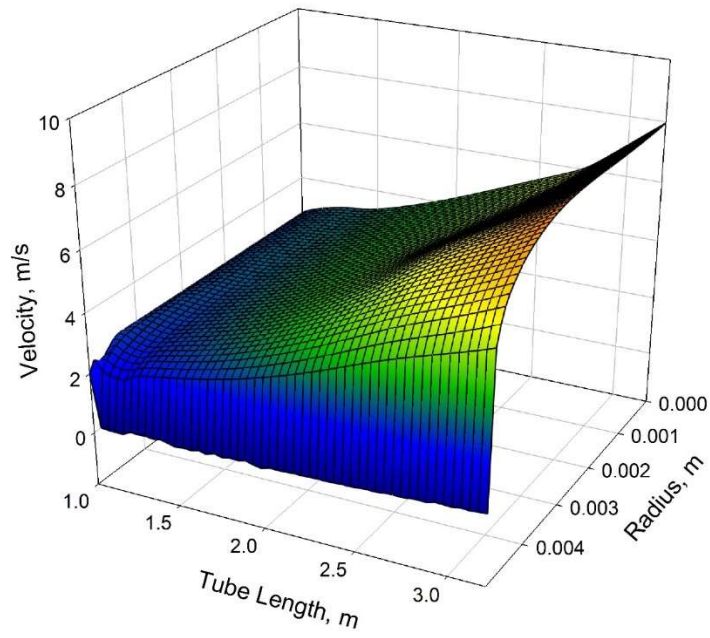


Figure 4-17: 3D Velocity plot for a case with: $P = 24.1$ MPa, $G = 1496$ kg/m²s, and $q = 1235$ kW/m², using the RKE model

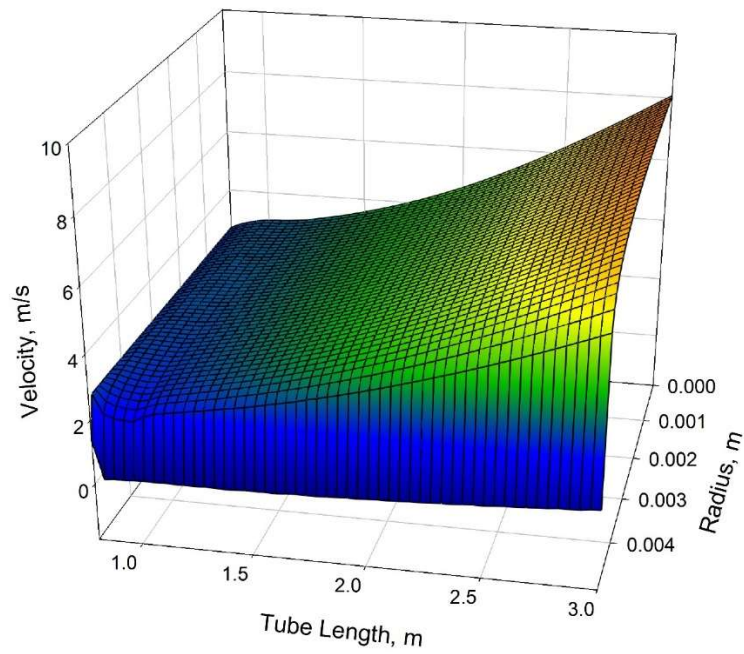


Figure 4-18: 3D Velocity plot for a case with: $P = 24.1$ MPa, $G = 1496$ kg/m²s, and $q = 1235$ kW/m², using the SST model

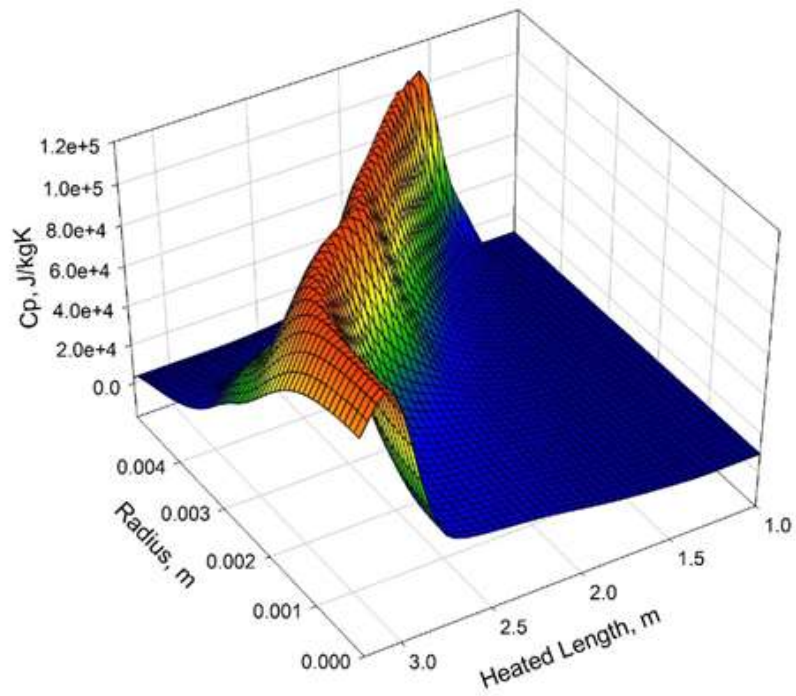


Figure 4-19: 3D Specific heat plot for a case with: $P = 24.1$ MPa, $G = 1496$ kg/m²s, and $q = 1235$ kW/m², using the RKE model

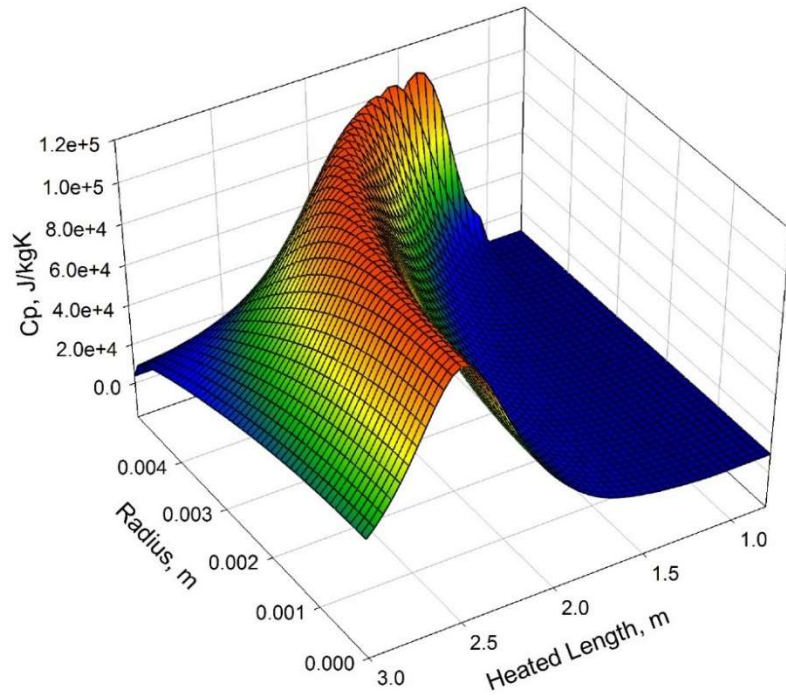


Figure 4-20: 3D Specific heat plot for a case with: $P = 24.1$ MPa, $G = 1496$ kg/m²s, and $q = 1235$ kW/m², using the SST model

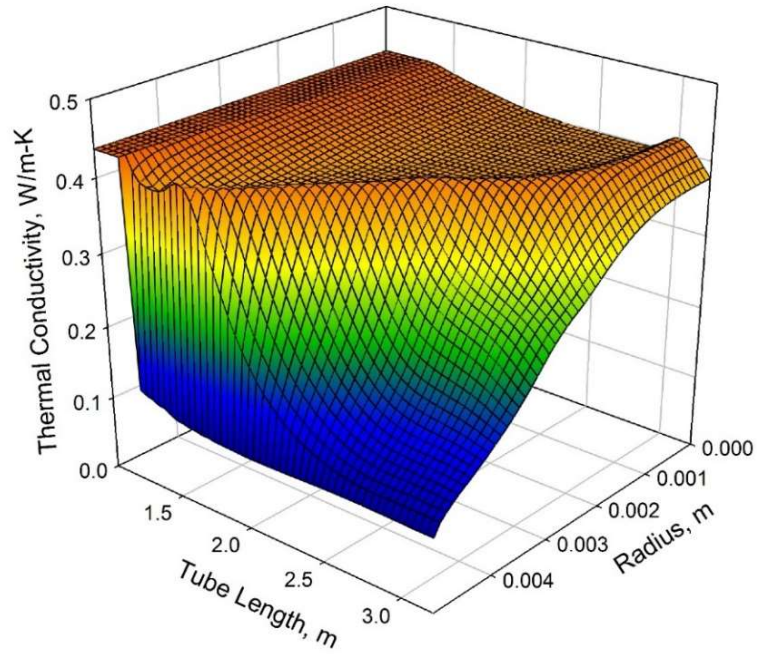


Figure 4-21: 3D Thermal conductivity plot for a case with: $P = 24.1$ MPa, $G = 1496$ kg/m²s, and $q = 1235$ kW/m², using the RKE model

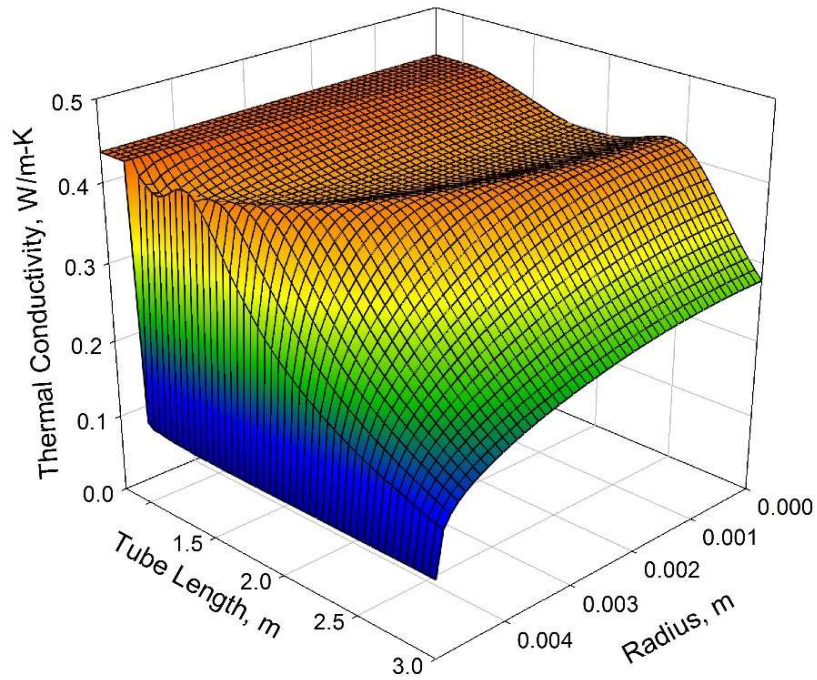


Figure 4-22: 3D Thermal conductivity plot for a case with: $P = 24.1$ MPa, $G = 1496$ kg/m²s, and $q = 1235$ kW/m², using the SST model

Figure 4-23 and Figure 4-24 show the RKE turbulent kinetic energy and the turbulence intensity levels in the flow, while Figure 4-25 and Figure 4-26 show the corresponding SST trends. The highest levels are reached near the wall region, where the inertial forces overcome the viscosity forces and eddies form. When comparing the levels and trends of turbulence to the NHT cases, the behavior shows a suppression of turbulence at the start of the computational domain, where there's no variance radially in the turbulence levels. This leads to the increase in wall temperature in experimental and computational results. The recovery in heat transfer and the reduction in wall temperature is marked by a significant increase in turbulence levels near the wall, creating a driving force for heat transfer at the end of the 2 meter length.

These results show the prediction of the RKE and SST models without modifying the turbulent Pr number, and as such, the turbulence is suppressed more than in the experimental data, and the calculated wall temperature (for the RKE model) is over 50°C higher than the experimental points at the peak of the DHT region.

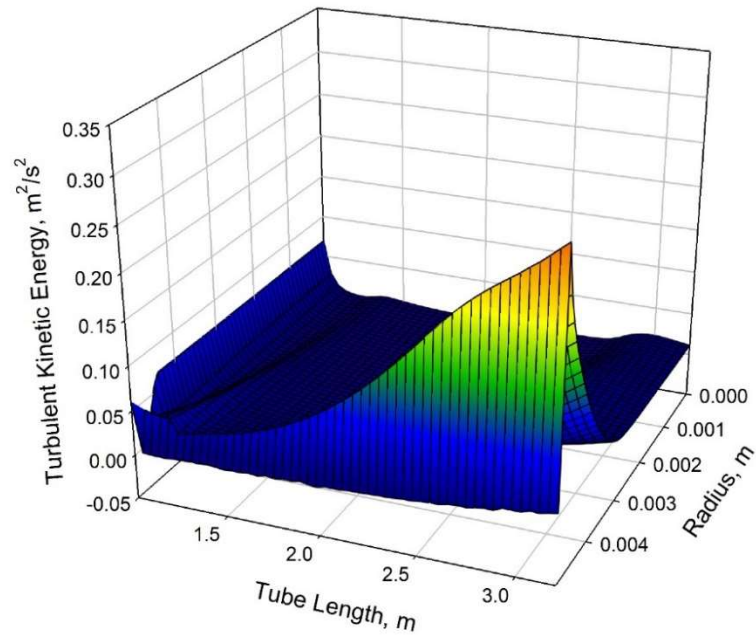


Figure 4-23: 3D Turbulent kinetic energy plot for a case with: $P = 24.1$ MPa, $G = 1496$ kg/m²s, and $q = 1235$ kW/m², using the RKE model

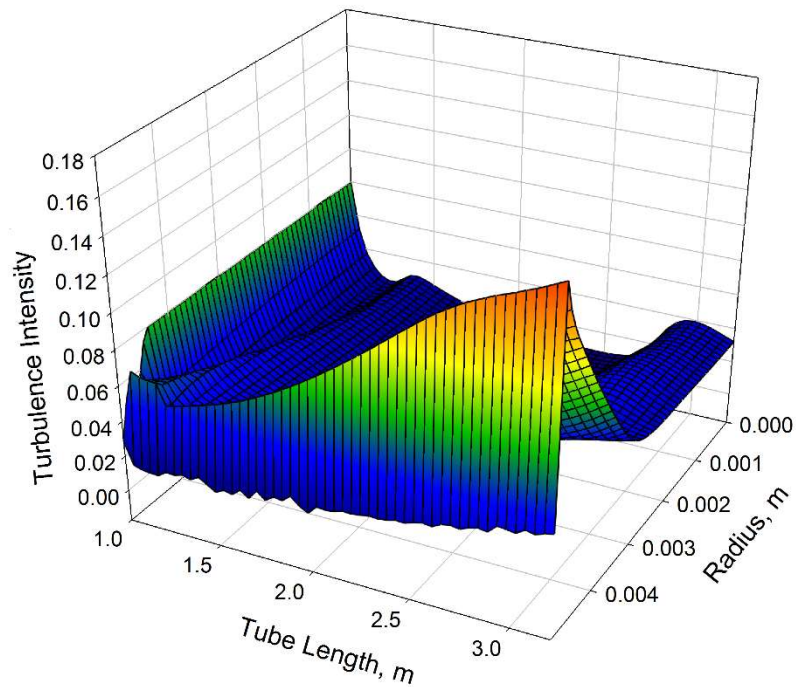


Figure 4-24: 3D Turbulent intensity plot for a case with: $P = 24.1$ MPa, $G = 1496$ kg/m²s, and $q = 1235$ kW/m², using the RKE model

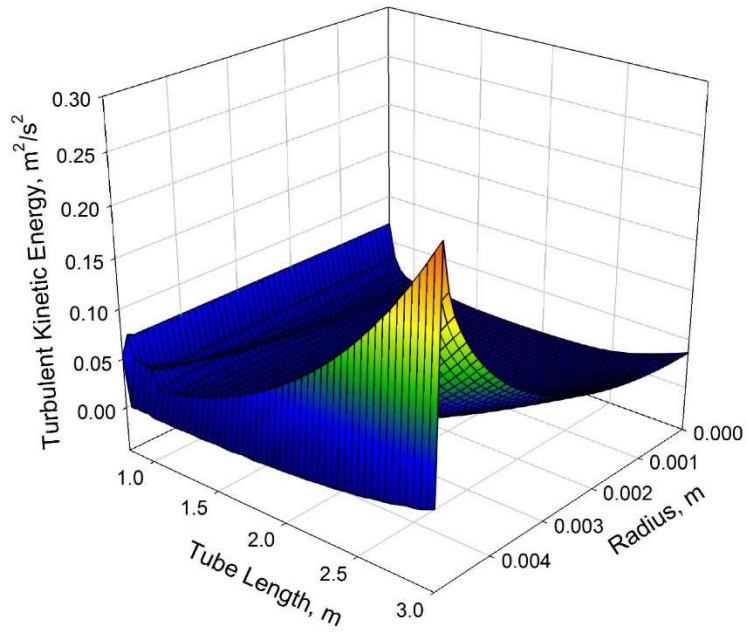


Figure 4-25: 3D Turbulent kinetic energy plot for a case with: $P = 24.1 \text{ MPa}$, $G = 1496 \text{ kg/m}^2\text{s}$, and $q = 1235 \text{ kW/m}^2$, using the SST model

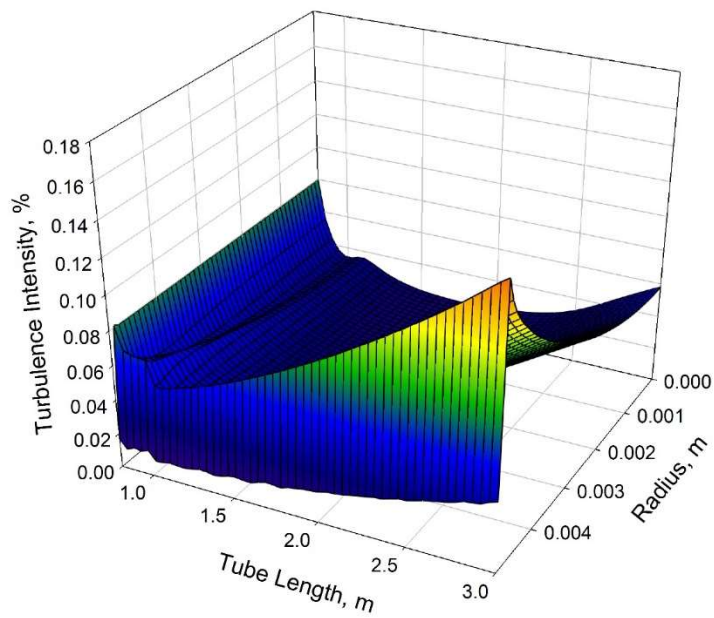


Figure 4-26: 3D Turbulence intensity plot for a case with: $P = 24.1 \text{ MPa}$, $G = 1496 \text{ kg/m}^2\text{s}$, and $q = 1235 \text{ kW/m}^2$, using the SST model

4.1.3 Subcritical Flow Results

A subcritical flow case with a pressure of 1 MPa, mass flow rate of 1496 kg/m²s, and a heat flux of 1235 kW/m² was simulated in the same geometry to analyze the differences between a liquid subcritical flow and the abovementioned supercritical cases. The inlet and outlet temperatures of the bulk fluid were specified as 25 and 100°C respectively. This is a hypothetical case with no experimental data, however, the FLUENT code has been extensively tested and verified for subcritical flow conditions [62].

The temperature profile in Figure 4-27 shows the linear increase in temperature at the same rate for the fluid at the wall and away from the wall. When compared to the NHT in a supercritical flow case (Figure 4-4), the effect of the property variation in supercritical fluids is apparent, even before crossing the pseudocritical line. The wall temperature increases steadily while the rest of the fluid's temperature rises slowly as the density drops closer to the pseudocritical point. While the density of the subcritical liquid, Figure 4-28, drops from ~1000 to 960 kg/m³ (~4% drop), the supercritical fluid drops from 600 to 350 for the bulk fluid and down to less than 200 kg/m³ at the wall (over 60% drop). This change affects the turbulence production and the acceleration of the flow as it gains more heat.

Similar trends are observed for other fluid properties, such as the viscosity in Figure 4-29 which is an order of magnitude higher than that of the supercritical fluid, and the specific heat in Figure 4-30 which does not undergo the significant change that defines the pseudocritical point, but rather increases by less than 2% throughout the flow region.

The turbulent kinetic energy in Figure 4-31 and the turbulence intensity in Figure 4-32 show the steady rise in turbulence for the fluid away from the wall, and the continuous difference radially drives the heat away from the heated walls, resulting in a good dissipation of heat in the fluid as shown in the temperature profile.

Finally, the velocity profile is shown in Figure 4-33, and while the velocity of the flow is lower than that of the supercritical fluid (under the same mass and heat flux), it appears to develop a similar profile axially and radially. The difference appears to be in the velocity gradient which creates the difference in the turbulence production (turbulent kinetic energy in equation 2-24).

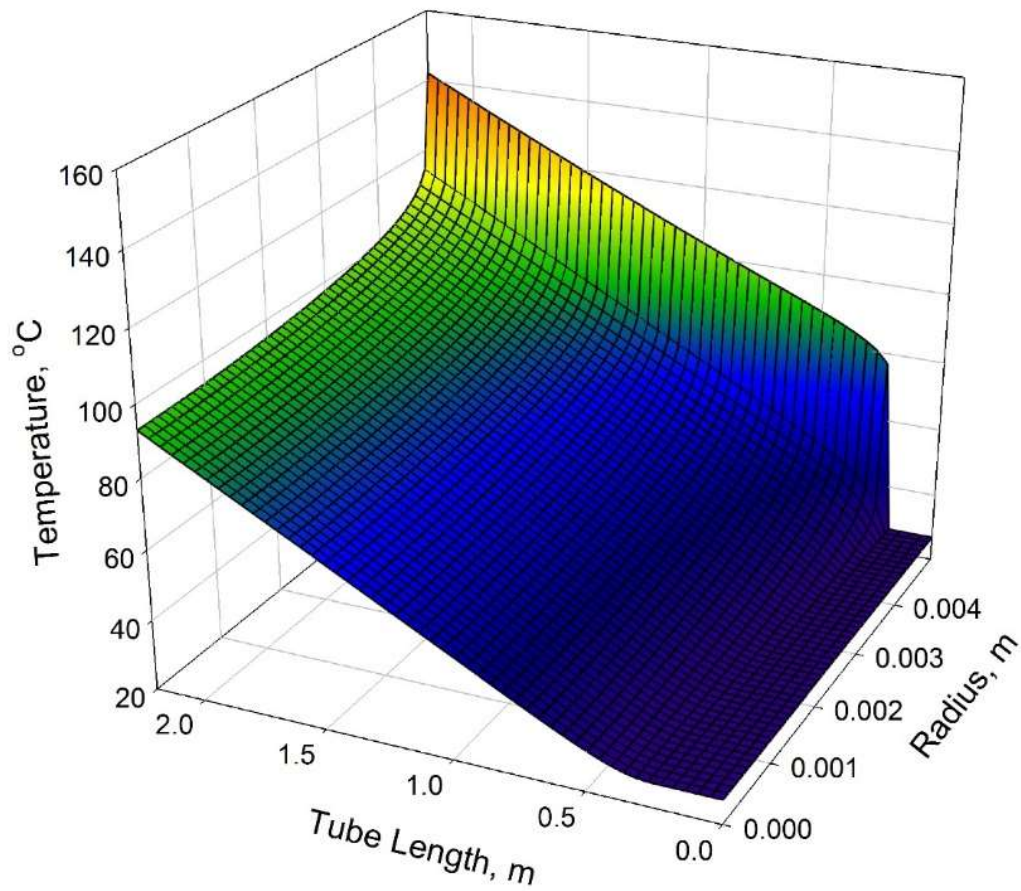


Figure 4-27: 3D Temperature plot for a case with: $P = 1 \text{ MPa}$, $G = 1496 \text{ kg/m}^2\text{s}$, and $q = 1235 \text{ kW/m}^2$, using the SST model

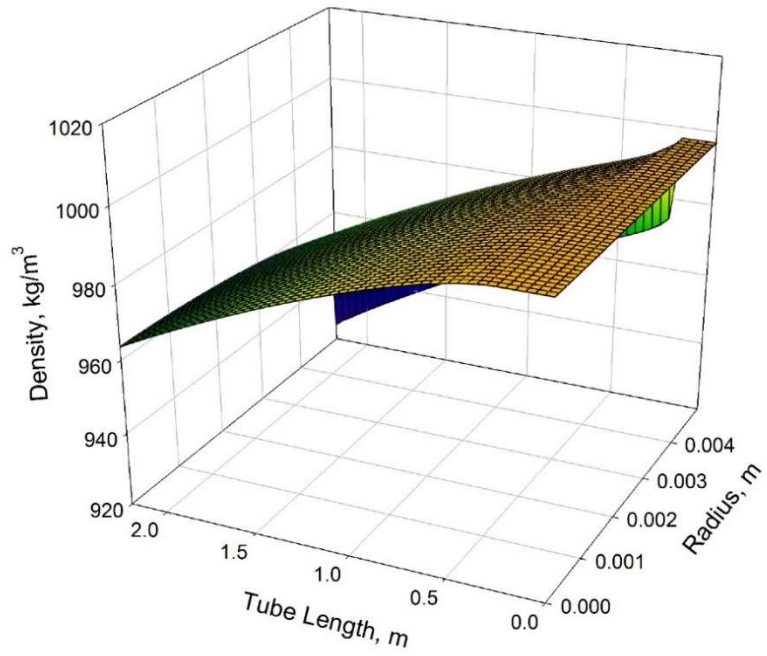


Figure 4-28: 3D Density plot for a case with: $P = 1 \text{ MPa}$, $G = 1496 \text{ kg/m}^2\text{s}$, and $q = 1235 \text{ kW/m}^2$, using the SST model

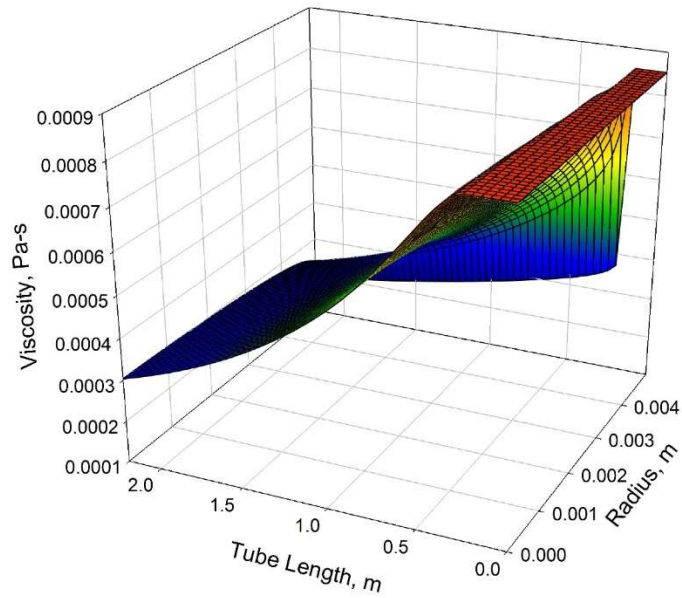


Figure 4-29: 3D Viscosity plot for a case with: $P = 1 \text{ MPa}$, $G = 1496 \text{ kg/m}^2\text{s}$, and $q = 1235 \text{ kW/m}^2$, using the SST model

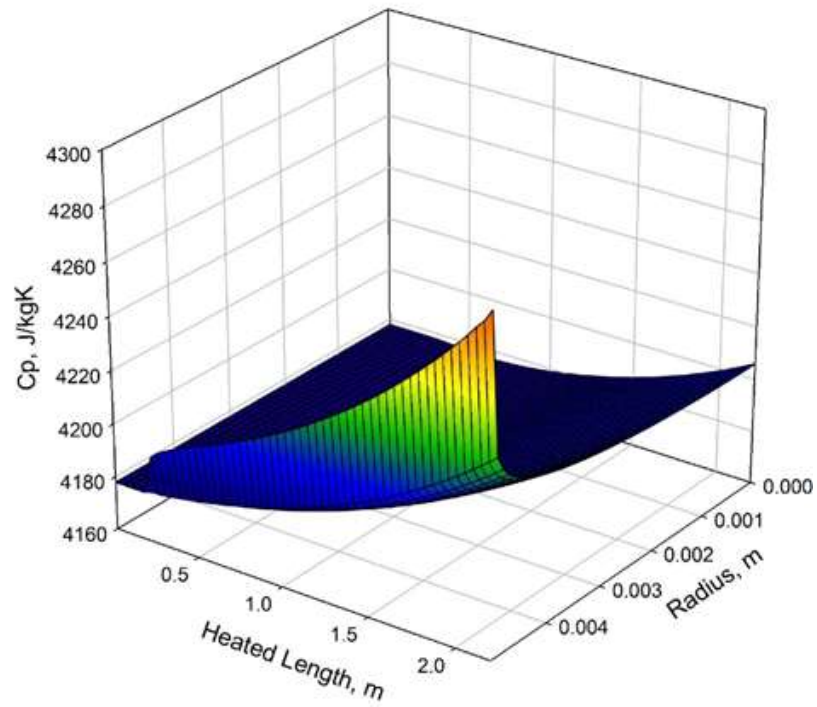


Figure 4-30: 3D Specific heat plot for a case with: $P = 1 \text{ MPa}$, $G = 1496 \text{ kg/m}^2\text{s}$, and $q = 1235 \text{ kW/m}^2$, using the SST model

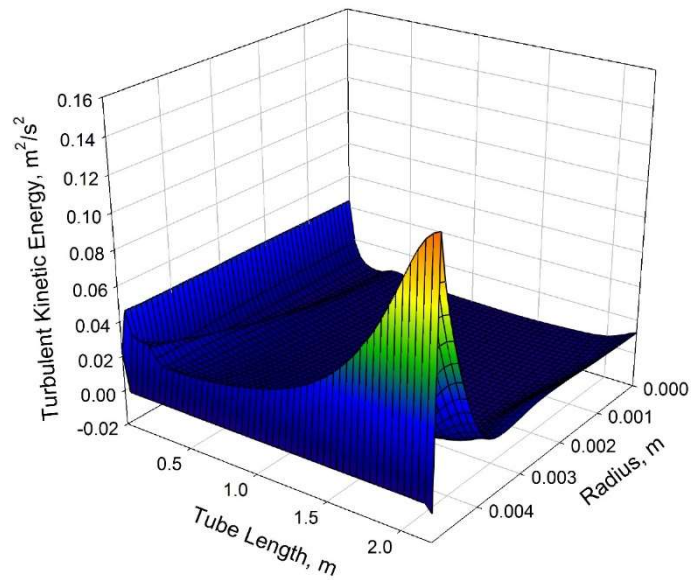


Figure 4-31: 3D Turbulent kinetic energy plot for a case with: $P = 1 \text{ MPa}$, $G = 1496 \text{ kg/m}^2\text{s}$, and $q = 1235 \text{ kW/m}^2$, using the SST model

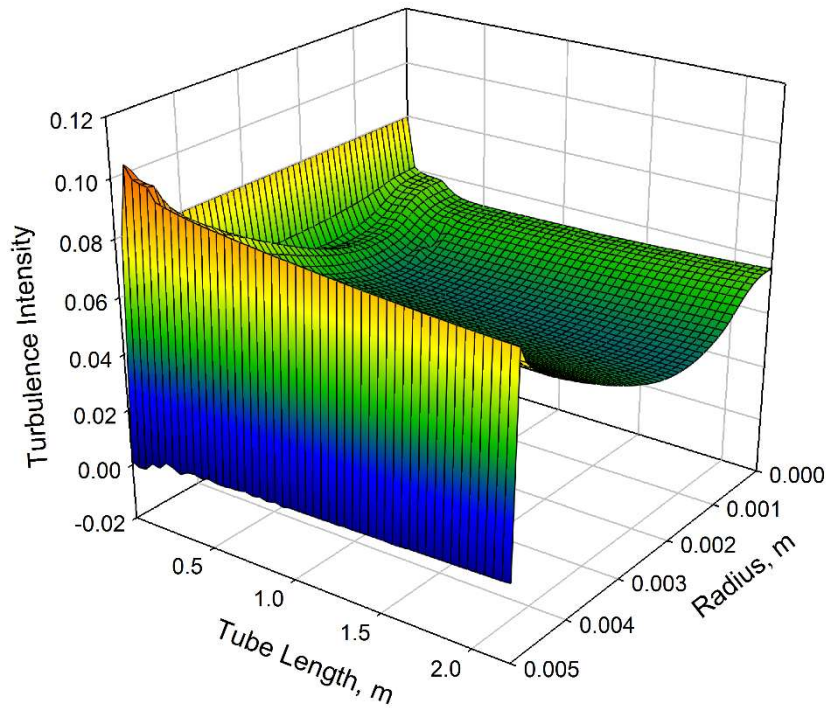


Figure 4-32: 3D Turbulence intensity plot for a case with: $P = 1 \text{ MPa}$, $G = 1496 \text{ kg/m}^2\text{s}$, and $q = 1235 \text{ kW/m}^2$, using the SST model

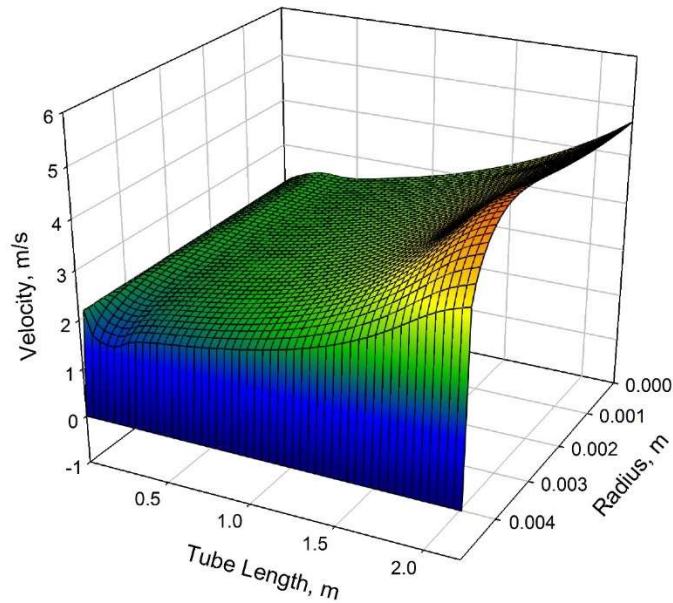


Figure 4-33: 3D Velocity plot for a case with: $P = 1 \text{ MPa}$, $G = 1496 \text{ kg/m}^2\text{s}$, and $q = 1235 \text{ kW/m}^2$, using the SST model

4.2 Turbulent Prandtl Number Variations Results

To understand the effects of turbulent Prandtl number on the CFD results, multiple simulations were run while varying the turbulent Prandtl number for each equation from its standard model constant. The temperature profiles for the original model and the modified runs are shown in Figure 4-34 and Figure 4-35. The figures show only the wall temperatures from 1-3 meters of the heated length (the region where heat transfer deteriorates).

As for the temperature profiles, the unmodified RKE model shows an overestimation of the experimental values for the wall temperature in the DHT region. As the various turbulent Pr numbers are modified, the temperature profiles deviate significantly from the original model. The SST model shows a closer estimation of the wall temperatures for the standard model and much less deviation than the RKE model with the modifications to the turbulent Pr numbers.

The turbulent Pr number is the ratio of turbulent diffusivity of momentum to the turbulent diffusivity of heat. As such, the expected behaviour for increasing its value is to decrease the effect of turbulent heat diffusion in the respective equation. Decreasing it will in turn increase the turbulent heat diffusion effect.

The turbulent Pr number however does not carry the same value for all equations in which it is present. The values adopted in the numerical models are derived empirically to fit experimental data in a wide range of operation for various fluids. The variations shown in the tables are the turbulent kinetic energy and its (specific) dissipation rate equations, as well as for the energy production equation and temperature calculation at the wall. The SST model has additional values for the turbulent kinetic energy and the specific dissipation rate as it uses different equations for the inner and outer wall regions.

As addressed earlier, the values for the turbulent Pr number vary between different models and different equations in the same model. The SST model which divides the flow into near-wall (inner) and outer regions has different values for turbulent Pr number which shows the extent of the difference between the effects of turbulent diffusion of momentum and heat in these regions. In the inner region, the values for the turbulent kinetic energy and its dissipation rates are higher than the outer region, reflecting the higher impact of the momentum diffusion, which is to be expected in the boundary layer region.

Turbulent Pr number variations

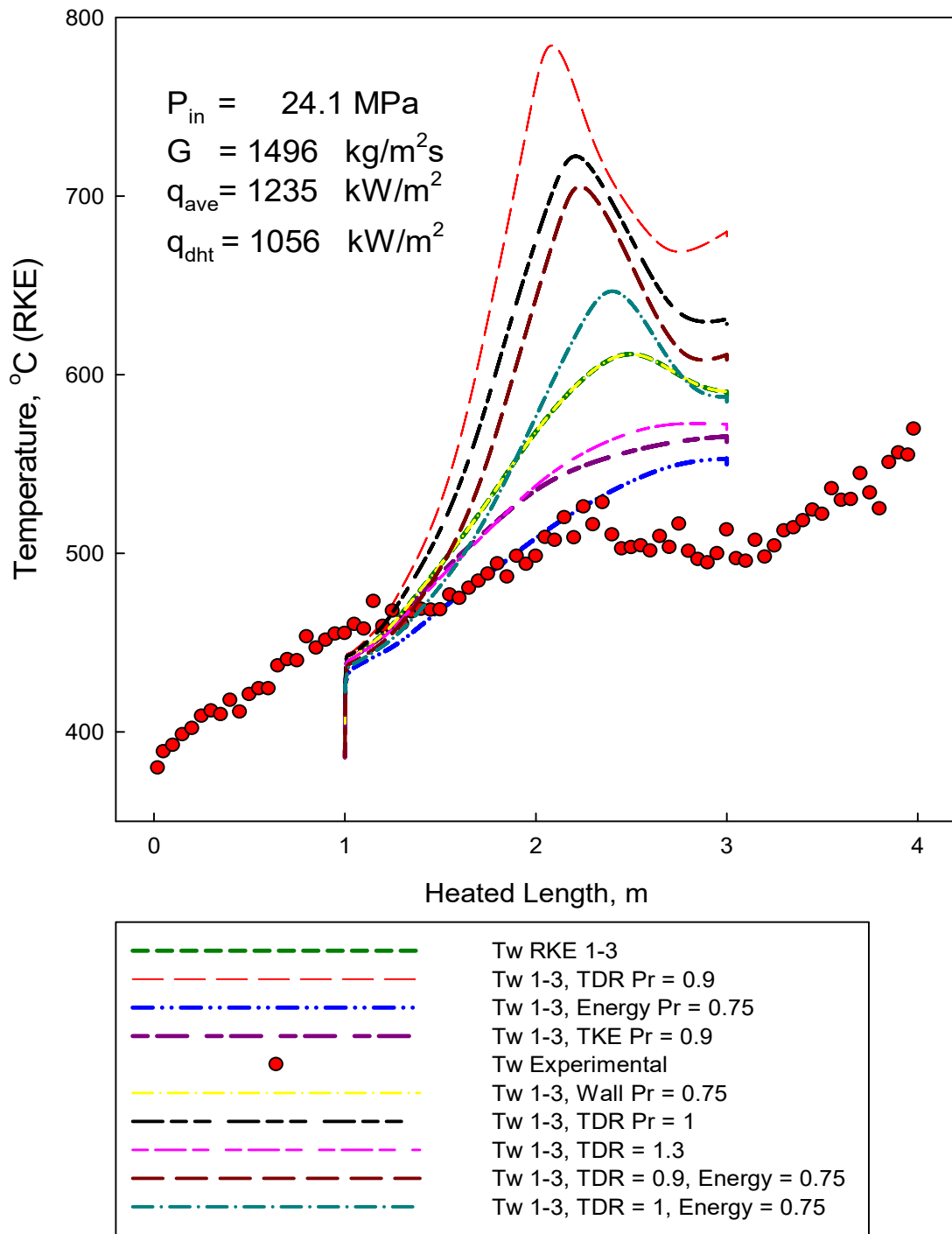


Figure 4-34: Effect of turbulent Pr number on wall temperature profiles, RKE model

Turbulent Pr number variations

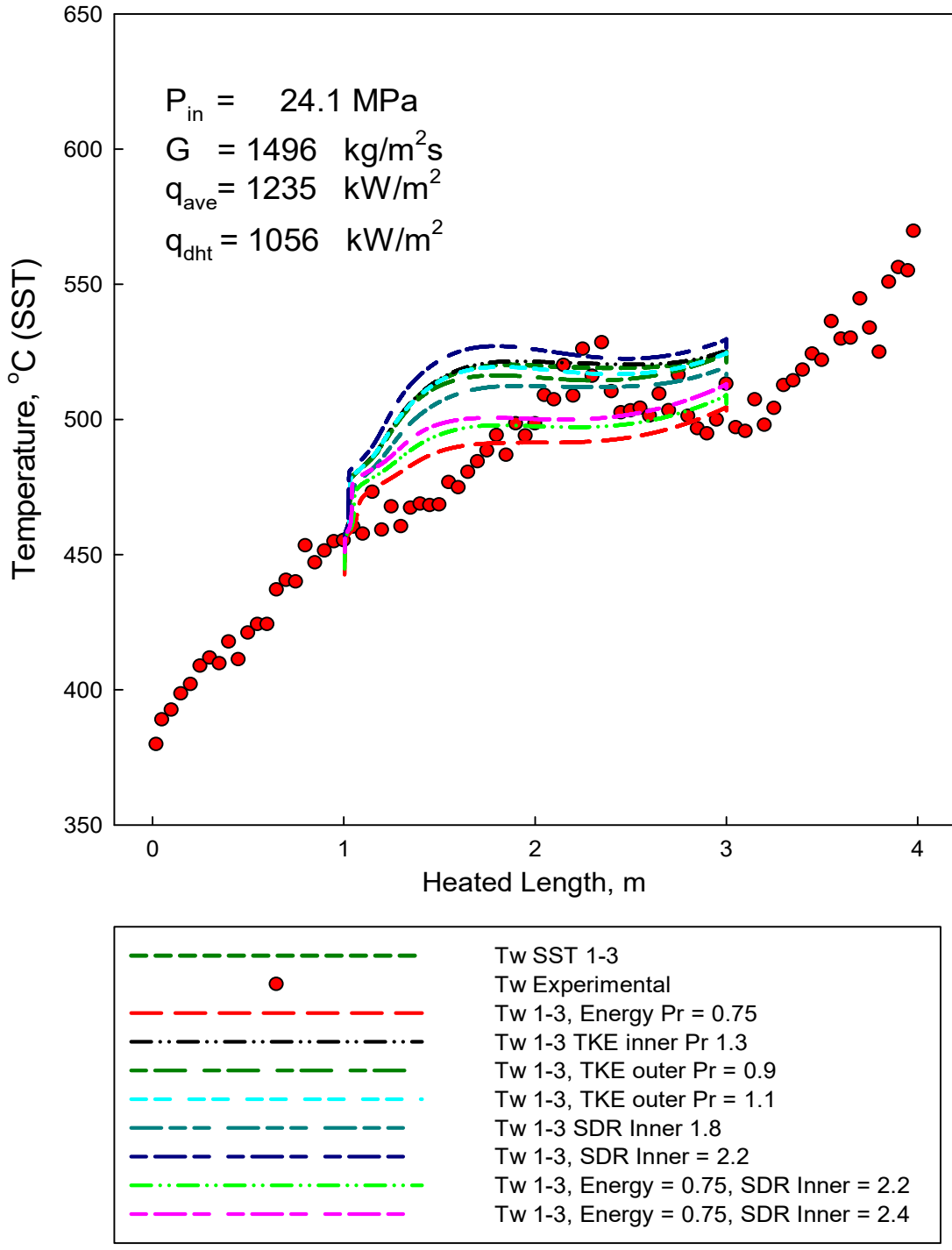


Figure 4-35: Effect of turbulent Pr number on temperature profiles, for SST model

Figure 4-34 and Figure 4-35 above show a sample of the results obtained for each model. Appendix A includes figures with the simulation results of further variations.

What is apparent in the simulation results is the relative sensitivity of the models to the change in the turbulent Pr numbers. The RKE model response in predicting temperature profiles is much larger than that of the SST model.

In terms of predicting the general trends of heat transfer deterioration, the RKE model tends to show the correct temperature behavior, by suppressing the heat transfer to the fluid and increasing the wall temperature as a result, which resembles the trends exhibited by the experimental results. The SST model on the other hand shows little in the way of heat transfer suppression, and overall minimal over-prediction of wall temperature.

Figure 4-36 and Figure 4-37 show the deviation from experimental data for each of the Pr_t variations.

Error Analysis for RKE Turbulent Pr Variations

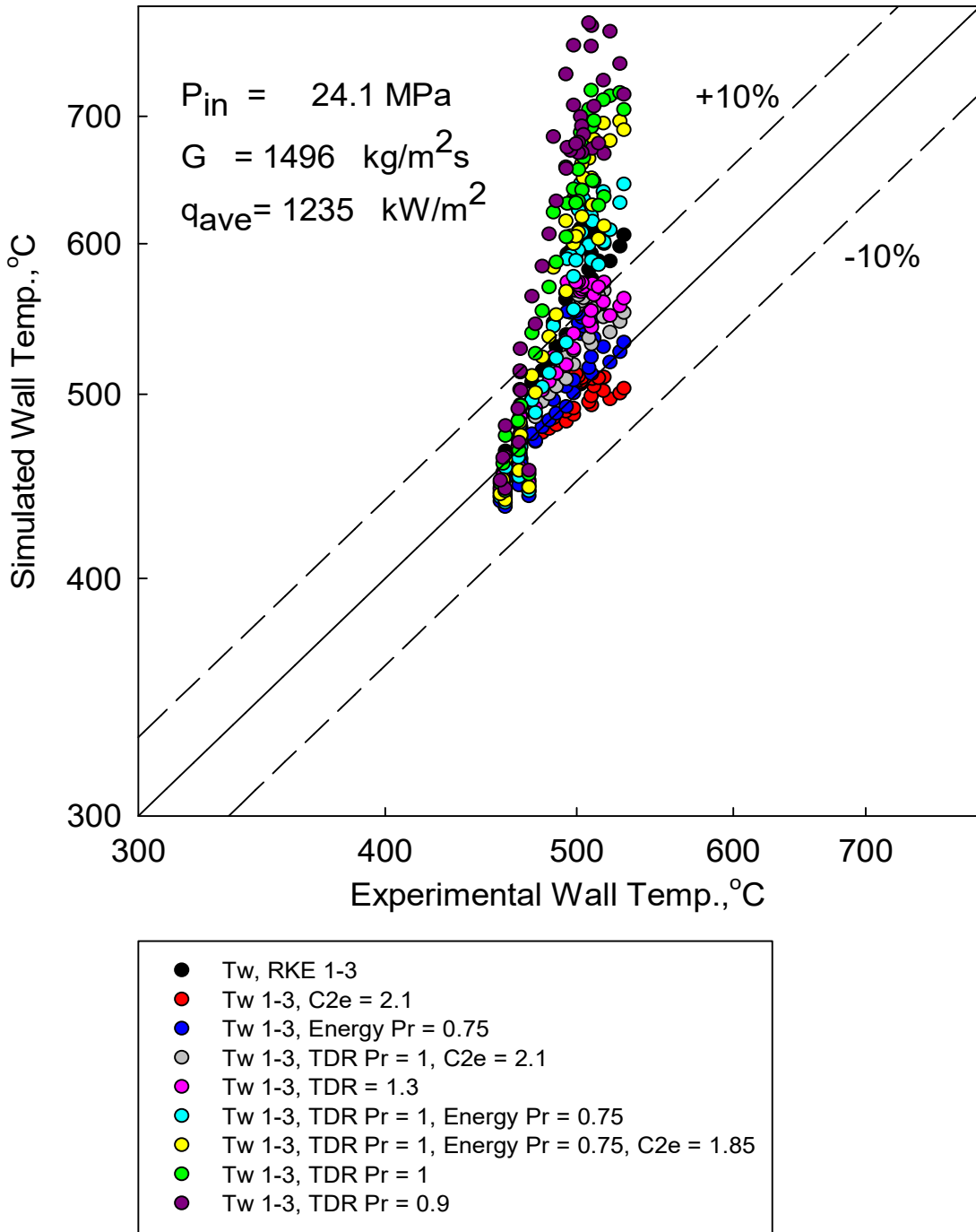


Figure 4-36: Errors in Simulated Wall Temperatures for RKE Model

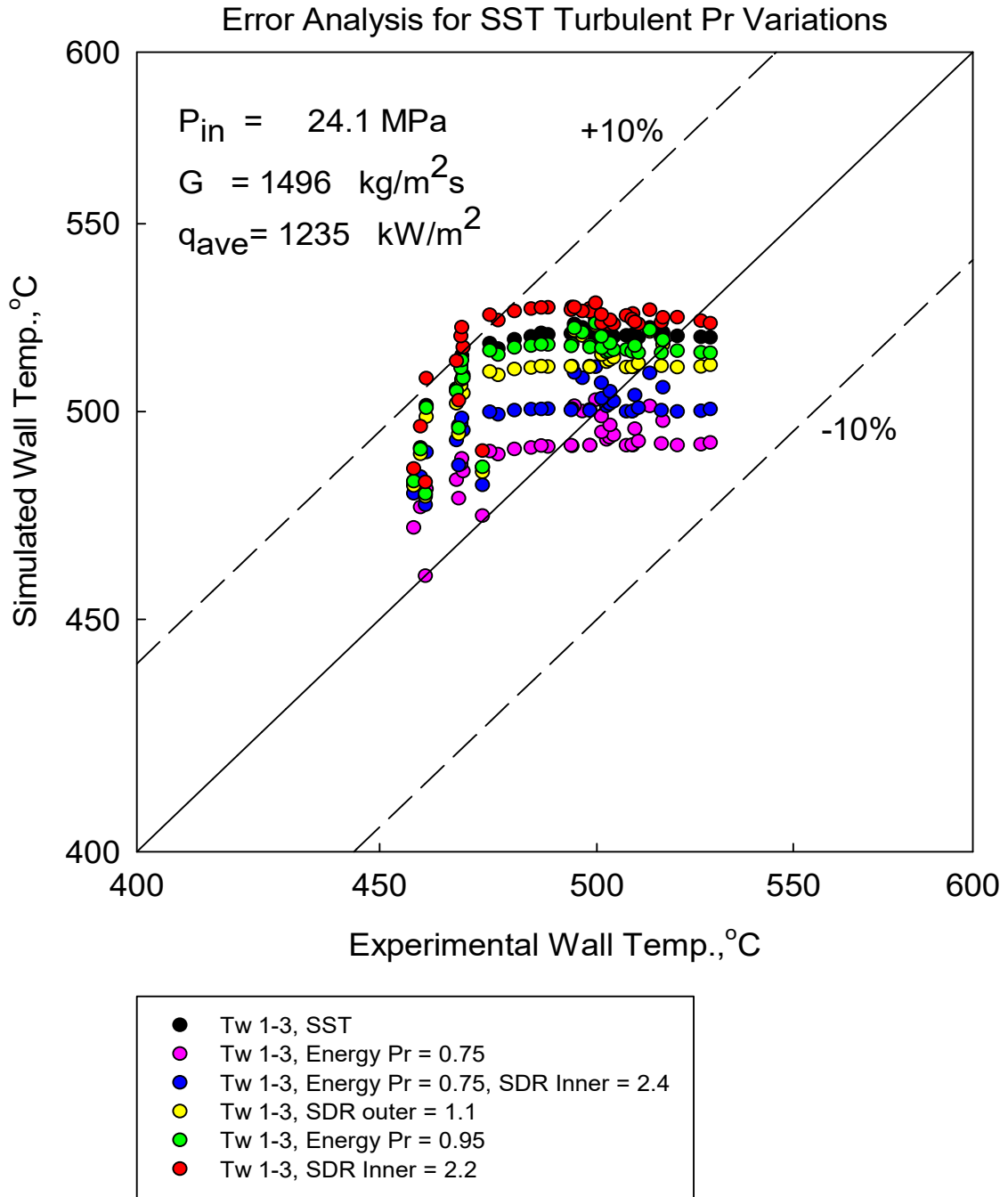


Figure 4-37: Errors in Simulated Wall Temperatures for SST Model

This type of error analysis is beneficial as it shows the deviation from experimental data as well as the trends for the wall temperatures. The closer the points are to the 45° line, the better the trend estimation. As such, it can be seen that the RKE model, especially in the simulations with Energy $Pr_t = 0.75$, and TDR $Pr_t = 1.3$, shows a much better trend than the SST model, even though both models can predict within $\pm 10\%$.

The SST model with all variations in turbulent Pr , shows the same trends of a somewhat flattened temperature profile, compared to the RKE model. As in the case of the RKE model, the Energy Pr_t shows the most significant effect and brings the temperature closest to the experimental values, within the smallest error margin.

Overall, the effect of the Pr_t change is generally on the magnitude of the simulated temperature but not necessarily the trends exhibited by the models. If the model does not predict an adequate trend for the heat transfer phenomena, the change in the turbulent Pr might reduce the error between the results and the experimental data, but it will not change the resulting temperature profile.

The heat transfer from the wall to the fluid is affected by the amount of turbulent kinetic energy in the fluid, and the different between the values radially drives the turbulence and hence the transfer of heat.

The energy Pr_t , which has the largest impact on the simulation results, and shows the best approximation for both models when altered, appears in the production terms due to buoyancy, which are modeled as:

$$G_{ij} = \beta \frac{\mu_t}{Pr_t} \left(g_i \frac{\partial T}{\partial x_j} + g_j \frac{\partial T}{\partial x_i} \right) \quad (4-4)$$

Where Pr_t is the turbulent Prandtl number for energy, and g_i is the component of the gravitational vector in the i -th direction, and β is the coefficient of thermal expansion.

The production terms appear in the transport equation for the turbulent kinetic energy and its dissipation rate. For the turbulent kinetic energy, that equation is:

$$\frac{\partial}{\partial t}(\rho k) + \frac{\partial}{\partial x_j}(\rho k v_j) = \frac{\partial}{\partial x_j} \left[\left(\mu + \frac{\mu_t}{\sigma_k} \right) \frac{\partial k}{\partial x_j} \right] + G_k + G_b - \rho \epsilon - Y_M + S_k \quad (4-5)$$

Thus the turbulent kinetic energy is augmented when $G_b > 0$ and suppressed when $G_b < 0$. The buoyancy effects on the generation of the turbulent kinetic energy are relatively well understood for common flow conditions, while the effect on its dissipation rate are less clear. In FLUENT, by default, the buoyancy effects on the dissipation rate are neglected by setting the production term to zero in the transport equation for ϵ .

Multiple experimental studies have been conducted on upward and downward flows in supercritical fluids [63], [64], [65]. These studies have found that deterioration occurs in upward but not downward flows. Researchers have hypothesized that the major impact is from the turbulent shear stress being modified differently by buoyancy forces for downward and upward flows. For upward flow, the buoyancy forces act to reduce the turbulent shear stress, resulting in localized spikes in wall temperature. For downward flow, buoyancy forces act to enhance the turbulent shear stress, enhancing the heat transfer compared to cases with no influence of buoyancy.

As the earlier figures depict, using the standard values for the Pr_t in the turbulent models leads to an over-approximation of the experimental data (in DHT cases but not NHT), while reducing the energy Pr_t results in a closer match while maintaining the trend exhibited by the DHT regime. This behaviour is an indication of the buoyancy increase as the flow transitions into the deteriorated regime. It is not unexpected, as the fluid density drops through the pseudocritical region and the flow accelerates as a result. It is however, unaccounted for in the turbulence models, which consider the same constant Pr_t no matter the condition.

While this does not create significant abnormalities in subcritical flows, it appears to be of importance in supercritical conditions.

It is observed in the temperature profiles, that even with the better fit accomplished by reducing the energy Pr_t , the recovery of the wall temperature is still lacking. This may also be explained with the increase of buoyancy in the flow, which would result in an even lower Pr_t towards the end of the computational domain, and the solution would not be resolved adequately using the same constant Pr_t .

Determining the turbulent Prandtl number for a fluid experimentally is possible yet very difficult [66], [67], [68]. The latest published finding for an experimental determination study was in the early 1990s, and the studies mainly focus on low Reynolds number flows in subcritical conditions. While some studies have shown methods of numerically computing the Pr_t [29], [33], [37], there is no published data for experimental determination of its value in supercritical conditions.

To analyze the effects of reducing the energy Pr_t (to 0.75) on the flow properties, the results are plotted in the 3D space. The temperature distribution in Figure 4-38 shows the lower wall temperature compared to the unmodified model, which also corresponds to a slightly higher temperature at the center of the tube, to maintain the total bulk-fluid temperature profile, as it is solved by the conservation of energy. Figure 4-39 shows a plot of the difference between the temperature profile of the unmodified model and with the Pr_t of 0.75. The red mesh plane marks the zero difference. This figure helps to show the heat being transferred to the bulk of the fluid more when the energy Pr_t is reduced.

The corresponding properties such as density (in Figure 4-40), specific heat (in Figure 4-41), thermal conductivity (Figure 4-42) and viscosity (Figure 4-43), all show similar trends to the unmodified model, with the exception of being closer in value to the true properties shown in the experimental data.

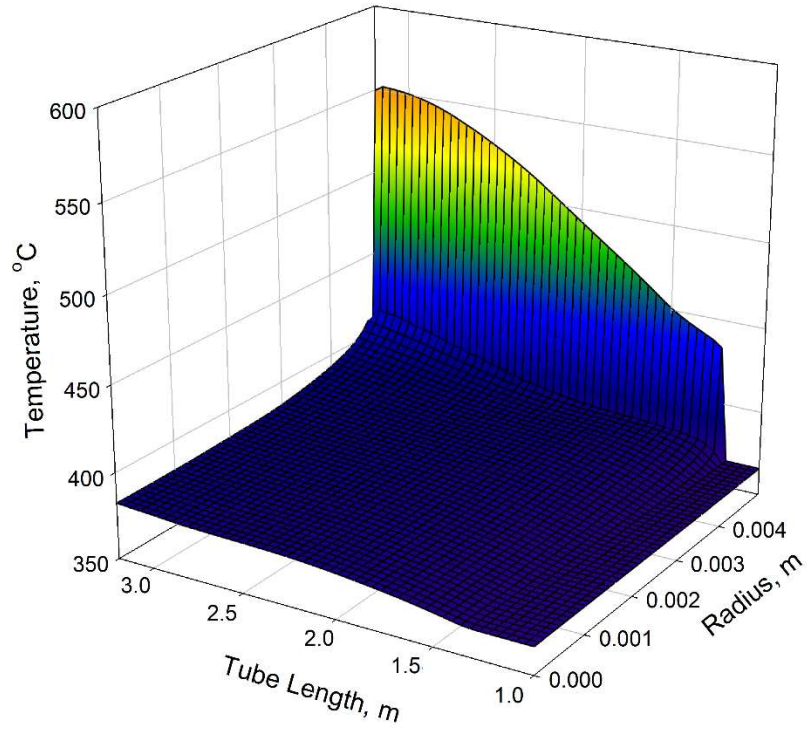


Figure 4-38: 3D Temperature plot for a case with: $P = 24.1 \text{ MPa}$, $G = 1496 \text{ kg/m}^2\text{s}$, and $q = 1235 \text{ kW/m}^2$, using the RKE model and Energy $Pr_t = 0.75$

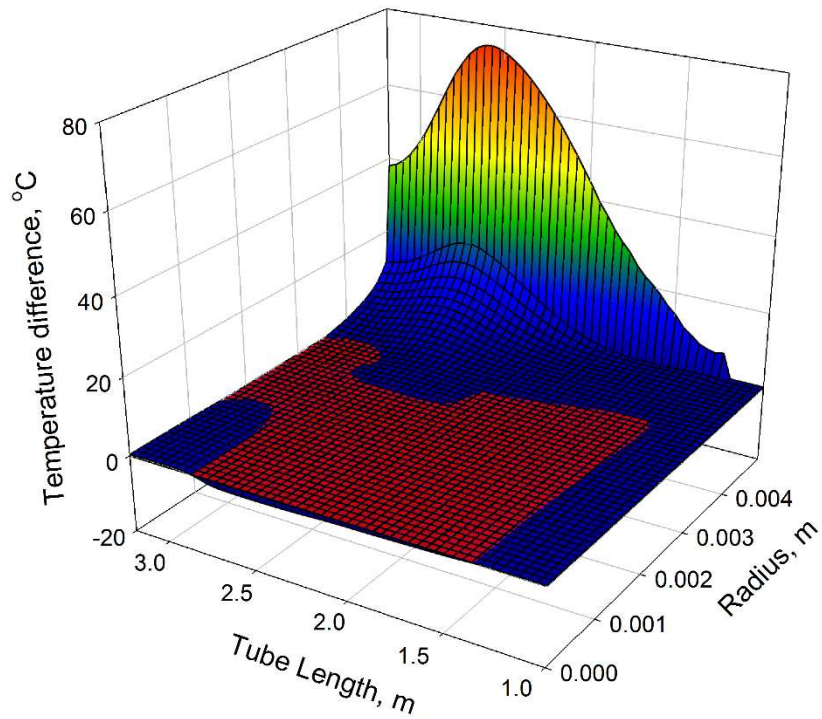


Figure 4-39: 3D Temperature difference plot (Energy $Pr_t = 0.85 - 0.75$) for a case with: $P = 24.1 \text{ MPa}$, $G = 1496 \text{ kg/m}^2\text{s}$, and $q = 1235 \text{ kW/m}^2$, using the RKE model

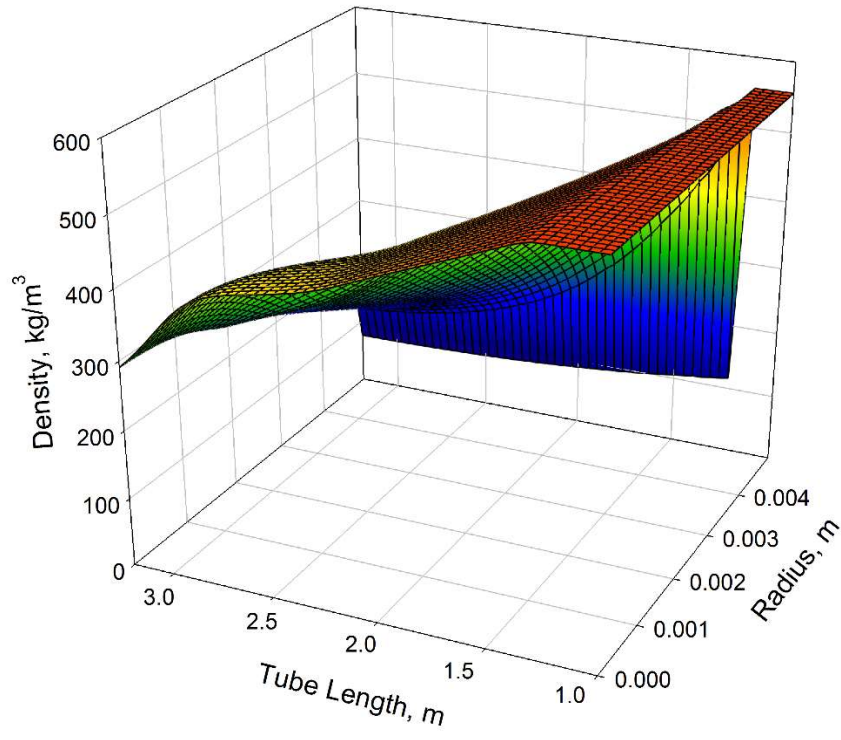


Figure 4-40: 3D Density plot for a case with: $P = 24.1$ MPa, $G = 1496$ kg/m²s, and $q = 1235$ kW/m², using the RKE model and Energy $Pr_t = 0.75$

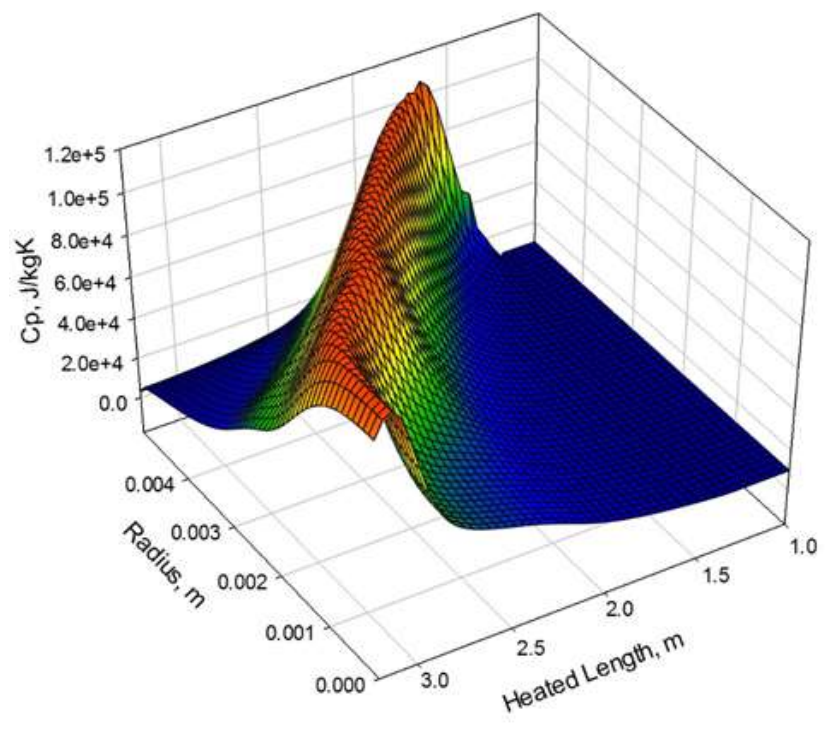


Figure 4-41: 3D Specific heat plot for a case with: $P = 24.1$ MPa, $G = 1496$ kg/m²s, and $q = 1235$ kW/m², using the RKE model and Energy $Pr_t = 0.75$

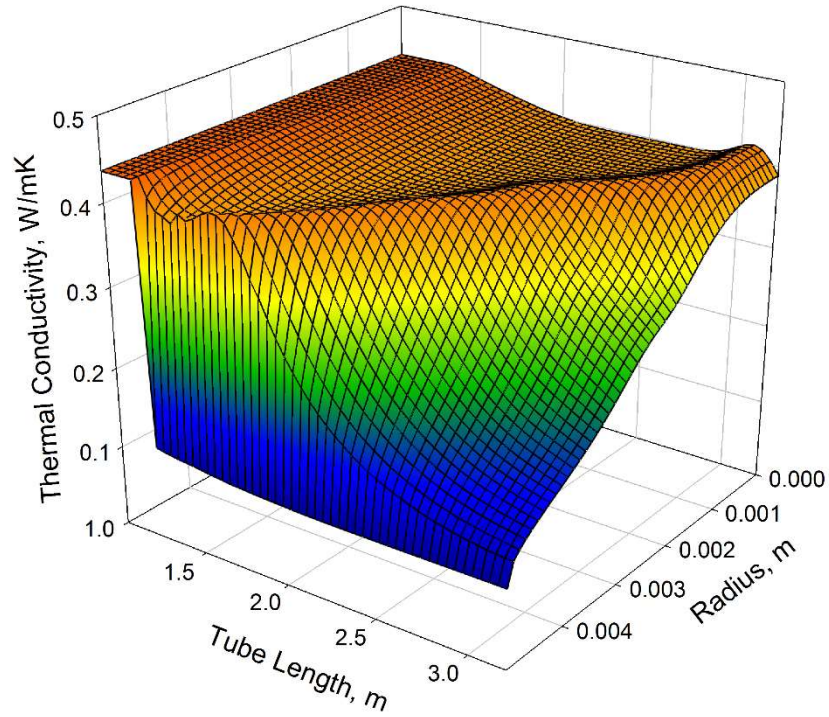


Figure 4-42: 3D Thermal conductivity plot for a case with: $P = 24.1$ MPa, $G = 1496$ kg/m²s, and $q = 1235$ kW/m², using the RKE model and Energy $Pr_t = 0.75$

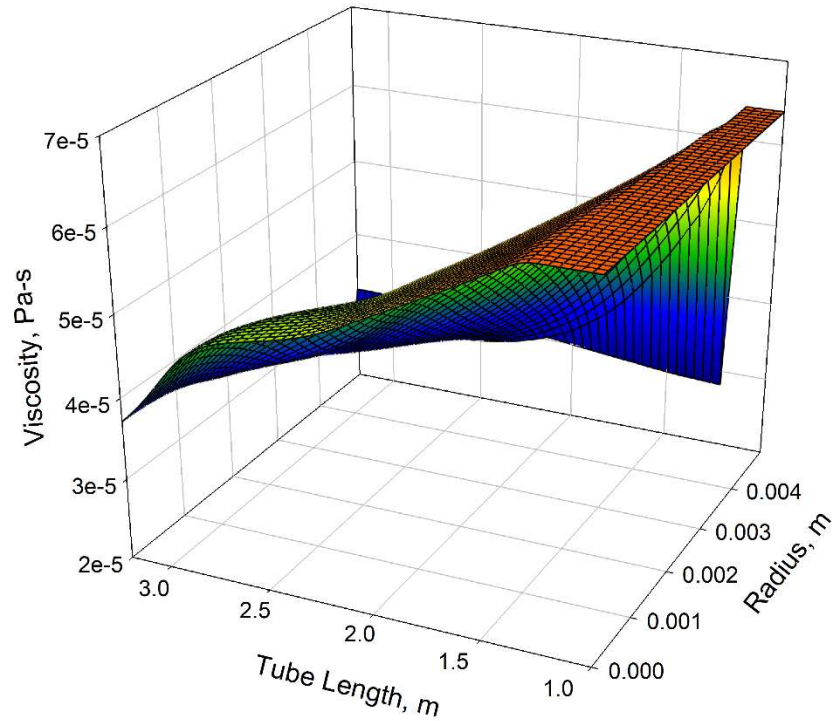


Figure 4-43: 3D Viscosity plot for a case with: $P = 24.1$ MPa, $G = 1496$ kg/m²s, and $q = 1235$ kW/m², using the RKE model and Energy $Pr_t = 0.75$

The effect on turbulent kinetic energy (Figure 4-44) and turbulence intensity (Figure 4-45) is of importance here, to show the effect of buoyancy on turbulence and heat transfer in the DHT regime. Figure 4-46 and Figure 4-47 depict the differences in turbulent kinetic energy and turbulence intensity between the unmodified model and the reduced Pr_t . The red plane in each graph shows a zero difference between the variables.

The results reflect the profile shown in the temperature difference, where in the first meter of heated length, the buoyancy effect is shown to be higher, leading to a lower wall temperature for the reduced Pr_t . The last half meter is where the unmodified model shows a higher level of turbulence, driving the recovery in the wall temperature that's not observed in the reduced Pr_t .

Figure 4-48 shows the simulations results for the reduced Pr_t RKE model at 0.5-2.5, 1-3 and 2-4 meters axially. The simulation from 0.5 to 2.5 meters shows a very high accuracy in matching the trend and the magnitude of the experimental data, signifying that the buoyancy increase starts quite early in the case of DHT. The lack of accurate recovery in temperature profile at 1-3 meters indicates further changes in the Pr_t which cannot be accounted for by using a constant value. Similarly, the 2-4 meter length test shows the Pr_t returns to 0.75 for the last meter section of the tube.

This is numerical evidence of the variability of the Pr_t in SCW under DHT conditions, which in turn is evidence of buoyancy effect variability as well.

Figure 4-49 shows the original and modified RKE model results for the 1-3 and 2-4 meter sections of the heated length, clearly marking the difference in prediction accuracy, while also showcasing a discontinuity demonstrating the variability of the Pr_t in this region.

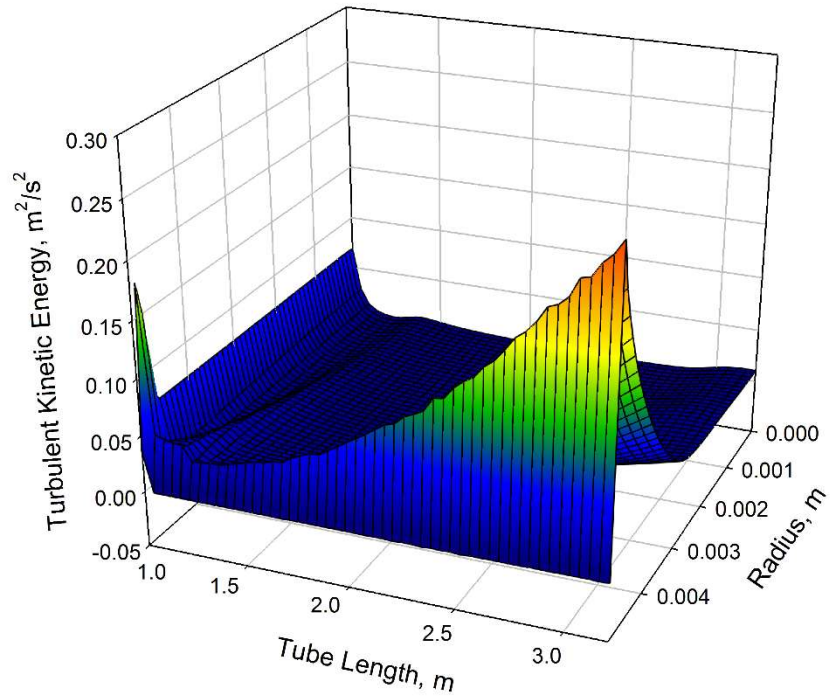


Figure 4-44: 3D Turbulent kinetic energy plot for a case with: $P = 24.1$ MPa, $G = 1496$ kg/m²s, and $q = 1235$ kW/m², using the RKE model and Energy $Pr_t = 0.75$

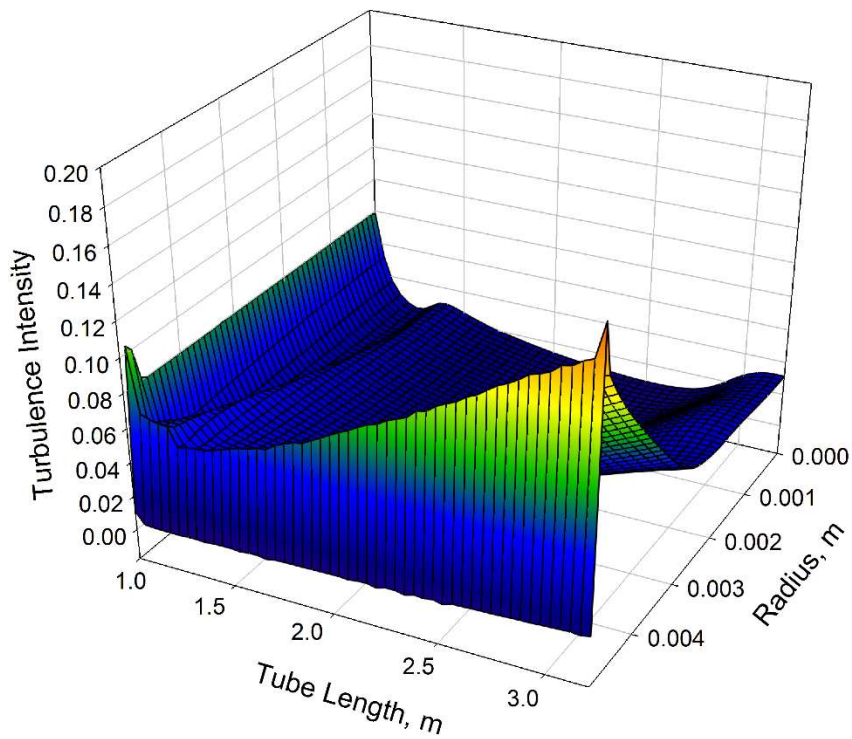


Figure 4-45: 3D Turbulence intensity plot for a case with: $P = 24.1$ MPa, $G = 1496$ kg/m²s, and $q = 1235$ kW/m², using the RKE model and Energy $Pr_t = 0.75$

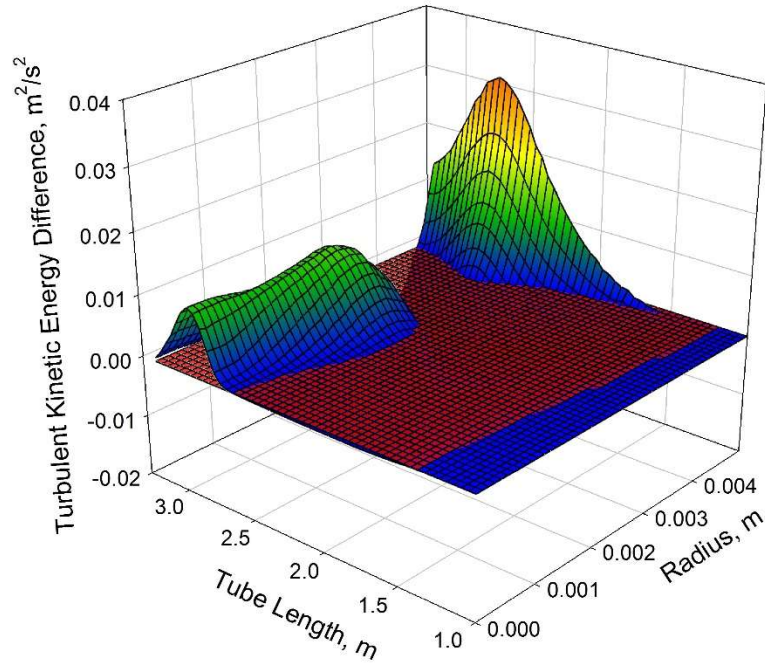


Figure 4-46: 3D Turbulent kinetic energy difference (Energy Pr_t 0.85 - 0.75) for a case with: $P = 24.1$ MPa, $G = 1496$ $\text{kg}/\text{m}^2\text{s}$, and $q = 1235$ kW/m^2 , using the RKE model

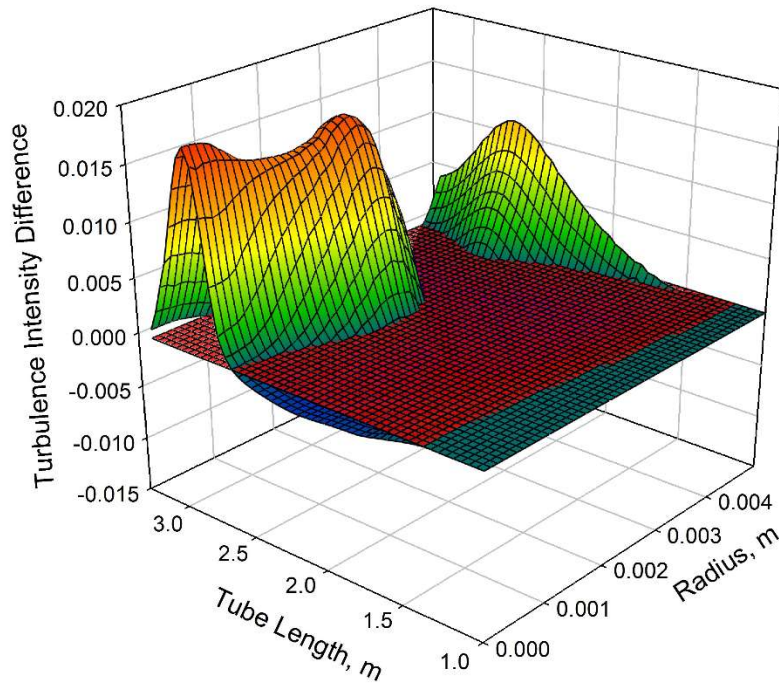


Figure 4-47: 3D Turbulence intensity difference (Energy Pr_t 0.85 - 0.75) for a case with: $P = 24.1$ MPa, $G = 1496$ $\text{kg}/\text{m}^2\text{s}$, and $q = 1235$ kW/m^2 , using the RKE model

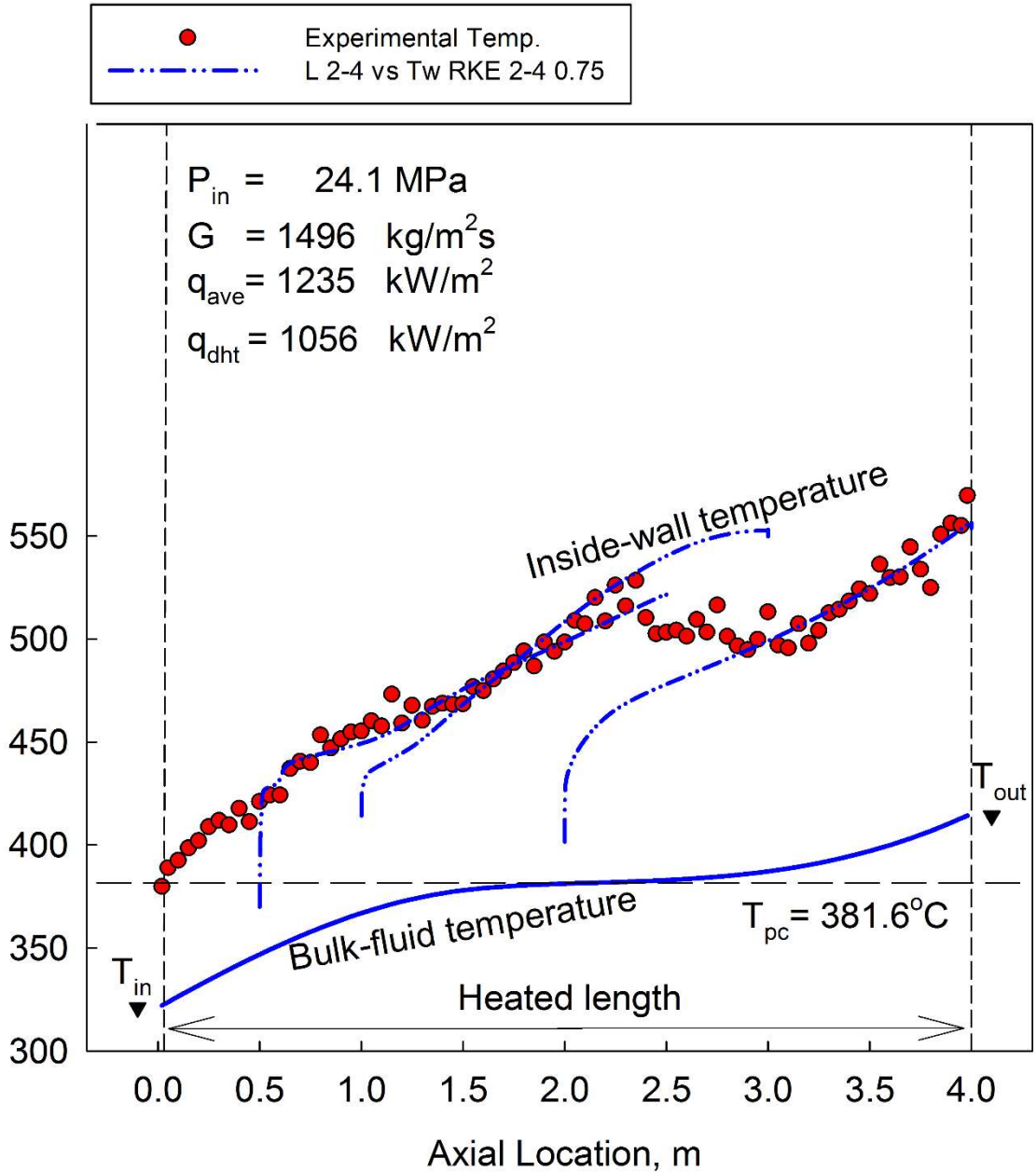


Figure 4-48: Temperature profiles for a case with: 24.1 MPa, $G = 1496 \text{ kg/m}^2\text{s}$, and $q = 1235 \text{ kW/m}^2$, $P =$ using the RKE model with Energy $Pr_t = 0.75$

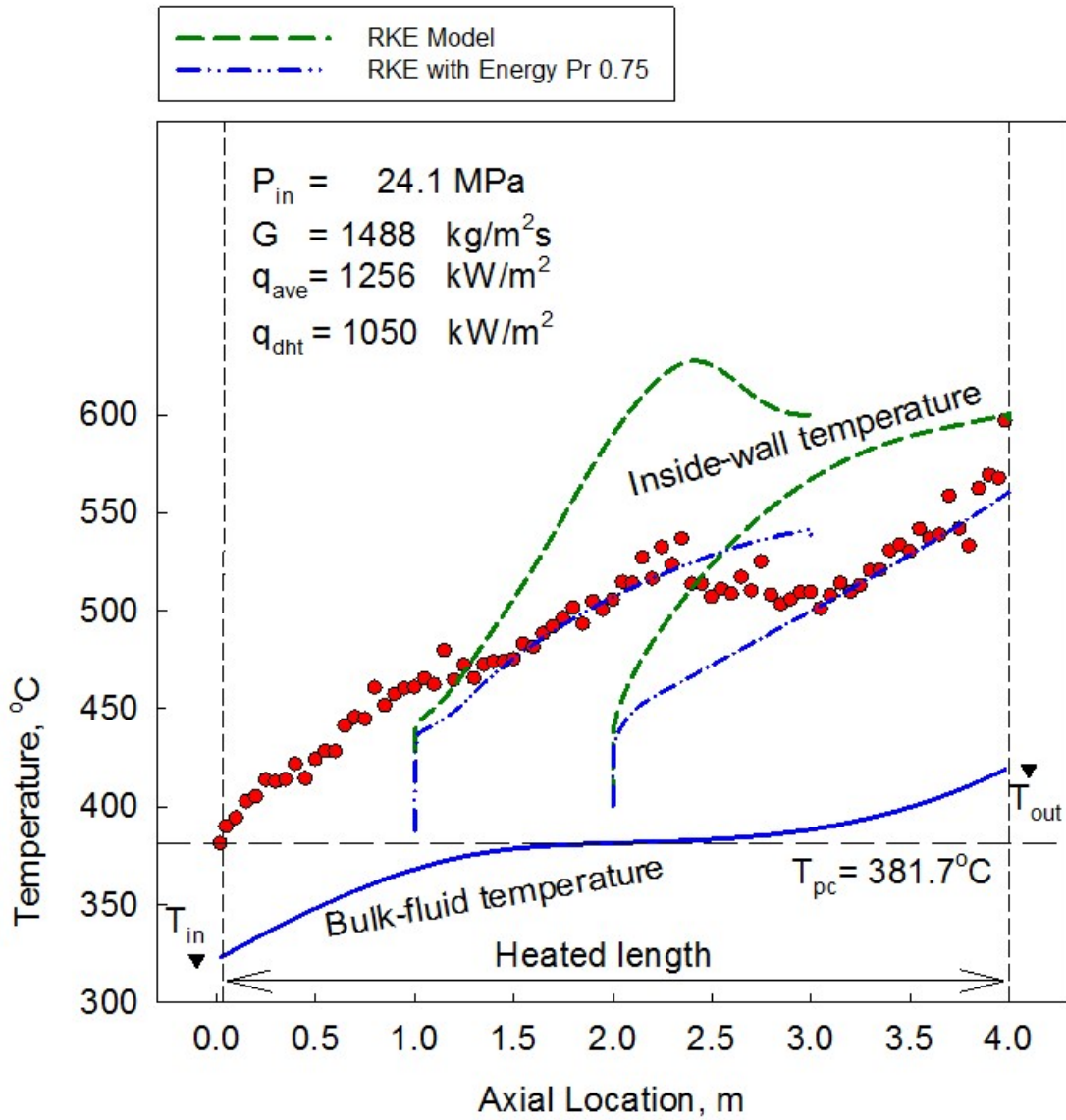


Figure 4-49: Temperature profiles for a case with: $P = 24.1 \text{ MPa}$, $G = 1488 \text{ kg/m}^2\text{s}$, and $q = 1256 \text{ kW/m}^2$, using the unmodified RKE model and with Energy $Pr_t = 0.75$

4.3 Downward flow results

The discussion on buoyancy effects brings attention to the potential differences between upward and downward flow. The analysis above has all been conducted in upward flow against gravity. A simulation with the same operating conditions as the DHT case with a mass flux of $1496 \text{ kg/m}^2\text{s}$ and a heat flux of 1235 kW/m^2 is conducted with the sole difference of reversing the gravity force direction, effectively making the flow downwards. This is a hypothetical case with no experimental data, and is done to illustrate the difference created by the buoyancy force acting against the flow under supercritical conditions.

The temperature profile in Figure 4-50 shows an axial and radial development that resembles that of the NHT results shown earlier in the chapter. The temperature at the wall rises steadily as the heat is transferred to the rest of the fluid quite efficiently. This trend is supported by the density behaviour in Figure 4-51 and especially in the specific heat in Figure 4-52 which shows the pseudocritical point moving through the fluid radially very rapidly as opposed to the slow propagation in the upwards flow (Figure 4-41 for example).

This is an example of the improved mixing in the flow as the flow properties away from the wall do not vary significantly at each axial location. This phenomenon is replicated again in the viscosity in Figure 4-53 and thermal conductivity in Figure 4-54.

All of this mixing comes from the high turbulence levels in the flow, as shown in the turbulence intensity in Figure 4-55 and the turbulence kinetic energy in Figure 4-56. The levels are much higher than those in the upwards flow, and remain consistently high throughout the entire flow. To get an idea of magnitude difference, Figure 4-57 shows a plot of the difference between the downwards and upwards flow turbulence intensity.

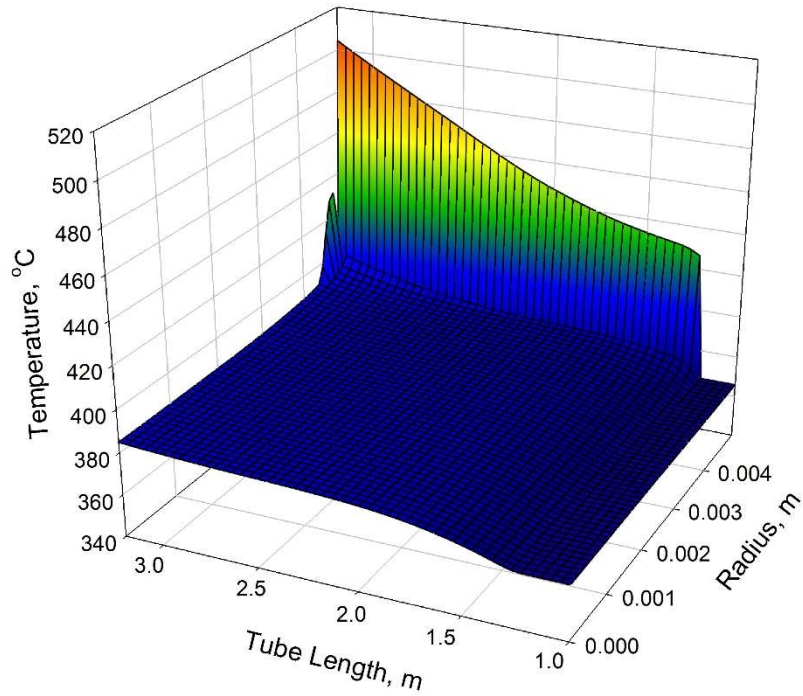


Figure 4-50: 3D Temperature plot for a case with: $P = 24.1$ MPa, $G = 1496$ kg/m²s, and $q = 1235$ kW/m², flowing downwards, using the RKE model and Energy $Pr_t = 0.75$

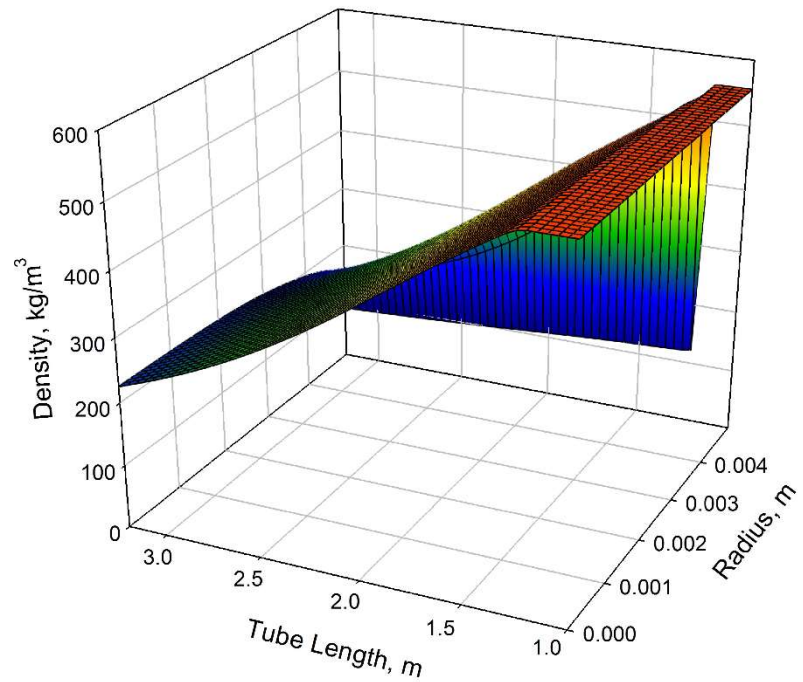


Figure 4-51: 3D Density plot for a case with: $P = 24.1$ MPa, $G = 1496$ kg/m²s, and $q = 1235$ kW/m², flowing downwards, using the RKE model and Energy $Pr_t = 0.75$

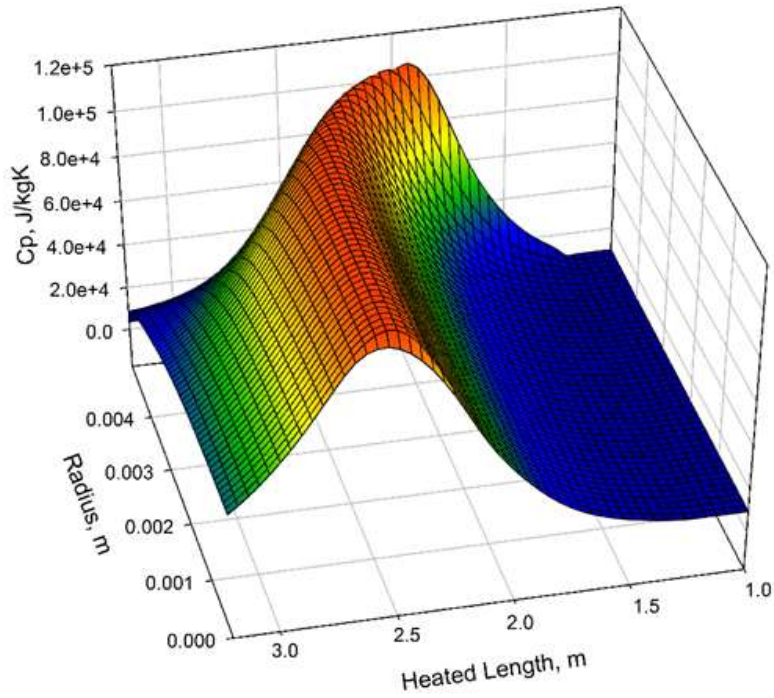


Figure 4-52: 3D Specific heat plot for a case with: $P = 24.1$ MPa, $G = 1496$ kg/m²s, and $q = 1235$ kW/m², flowing downwards, using the RKE model and Energy $Pr_t = 0.75$

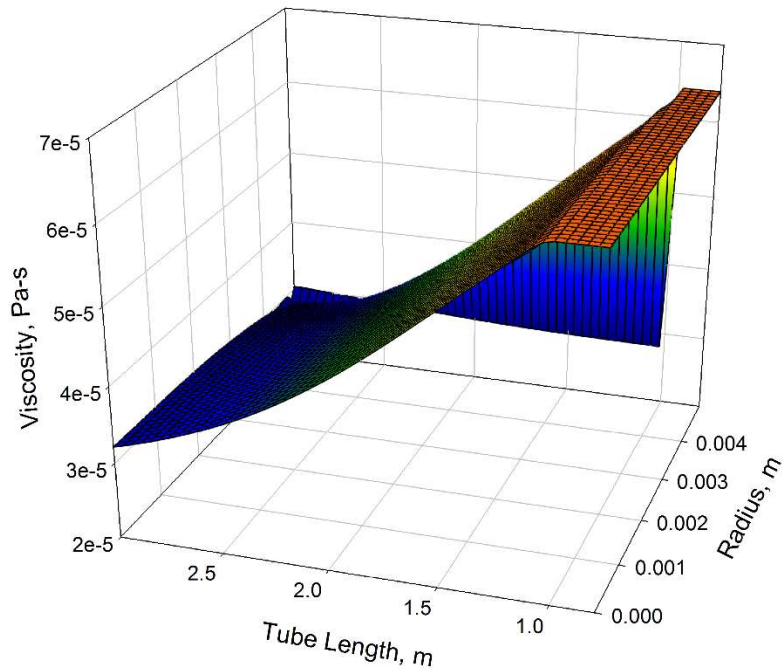


Figure 4-53: 3D Viscosity plot for a case with: $P = 24.1$ MPa, $G = 1496$ kg/m²s, and $q = 1235$ kW/m², flowing downwards, using the RKE model and Energy $Pr_t = 0.75$

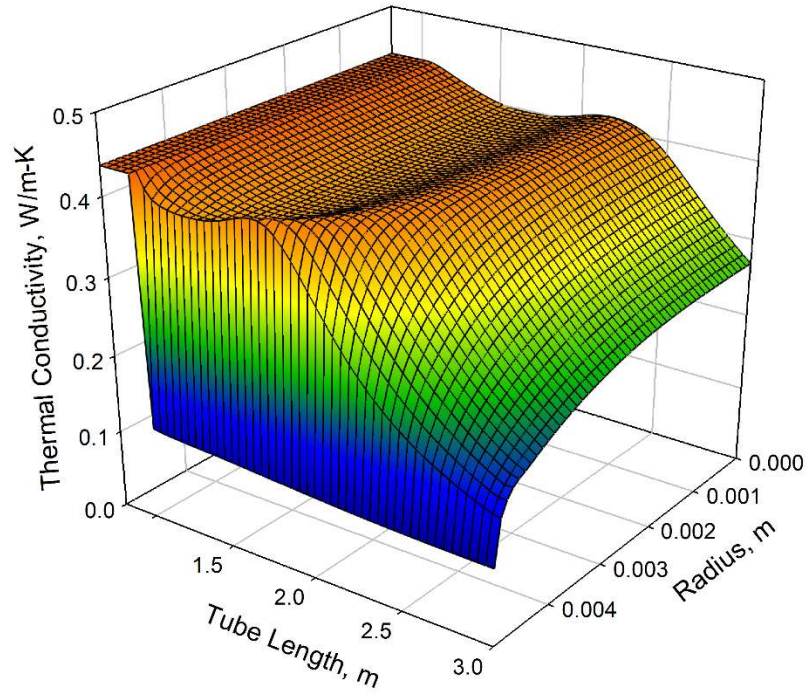


Figure 4-54: 3D Thermal conductivity plot for a case with: $P = 24.1$ MPa, $G = 1496$ kg/m²s, $q = 1235$ kW/m², flowing downwards, using the RKE and Energy $Pr_t = 0.75$

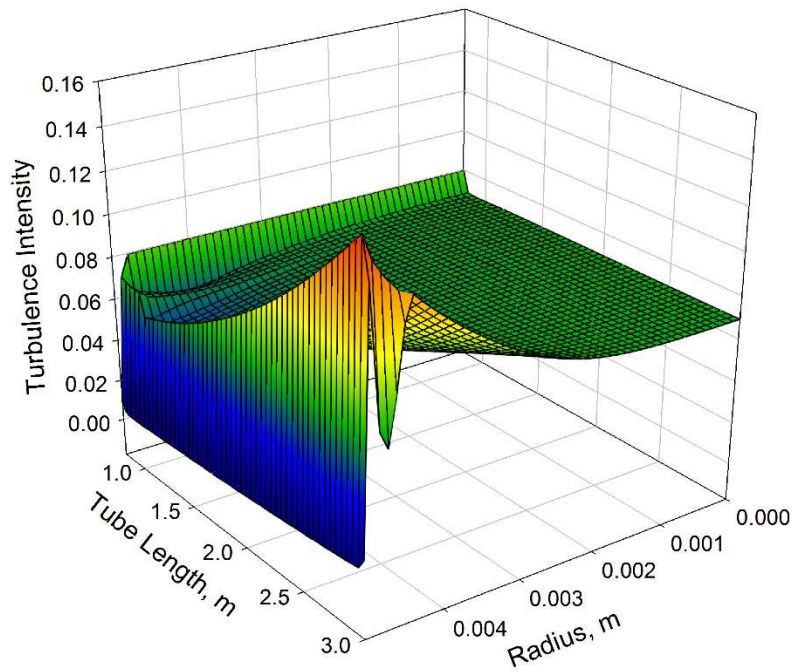


Figure 4-55: 3D Turbulence intensity plot for a case with: $P = 24.1$ MPa, $G = 1496$ kg/m²s, $q = 1235$ kW/m², flowing downwards, using the RKE and Energy $Pr_t = 0.75$

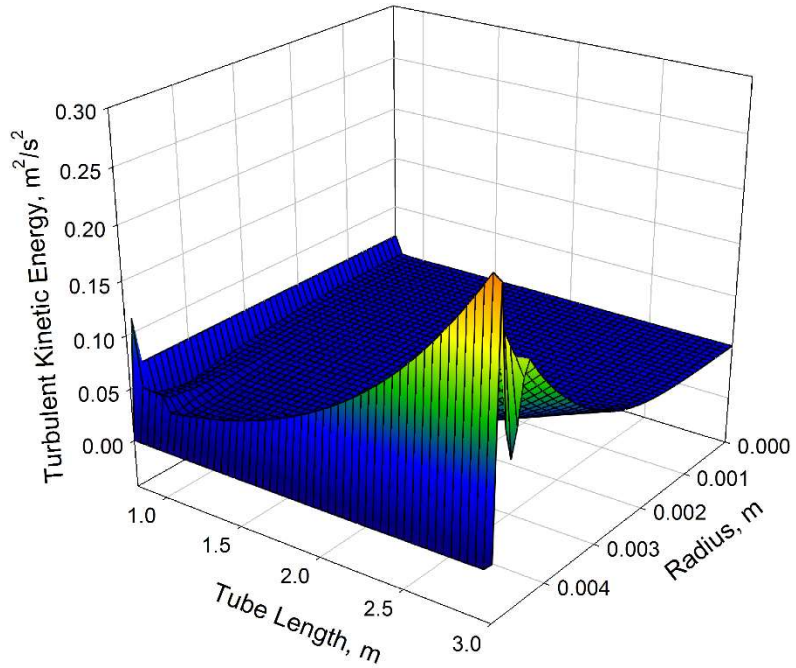


Figure 4-56: 3D Turbulence kinetic energy plot for a case with: $P = 24.1$ MPa, $G = 1496$ kg/m²s, and $q = 1235$ kW/m², flowing downwards, RKE model with Energy $Pr_t = 0.75$

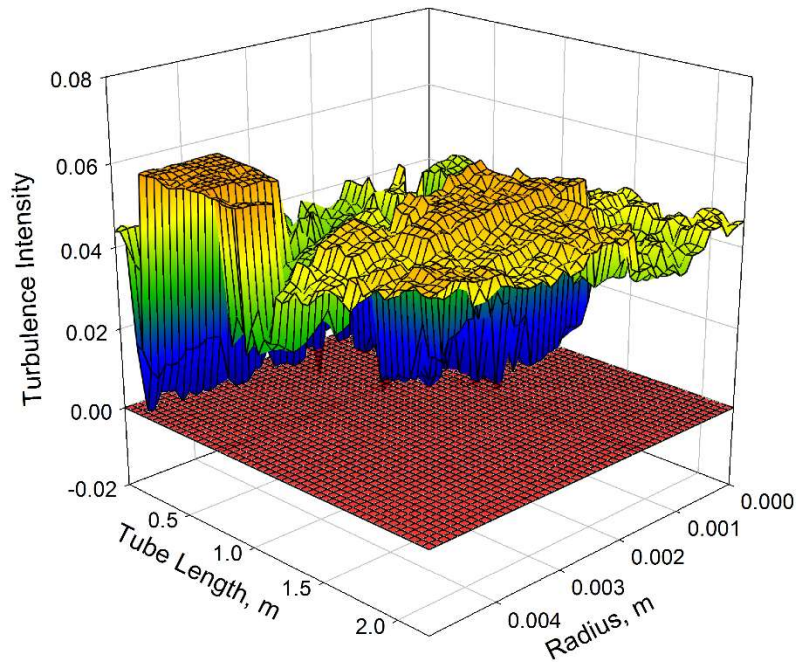


Figure 4-57: 3D Turbulence intensity difference (Downwards - upwards) for a case with: $P = 24.1$ MPa, $G = 1496$ kg/m²s, and $q = 1235$ kW/m², RKE with Energy $Pr_t = 0.75$

4.4 Summary

In this section, the work conducted on a simple tube geometry is used to characterize supercritical water flow in the normal and deteriorated heat transfer regimes, by studying the property variation in the 3D space. As the CFD models suffer in predicting the deterioration in heat transfer, the effect of the turbulent Pr number on CFD simulation results is determined and characterized. The major contributor to increasing the model's accuracy in predicting the DHT phenomenon comes from accounting for the buoyancy force influence on generating turbulence in the flow.

As the flow transitions from normal to deteriorated heat transfer regimes, the increase in buoyancy accelerates the flow through the center of the flow, creating effectively a separation in the flow at the wall and away from the wall. As a result, the wall temperature rises quickly, while the fluid is unable to transfer the heat generated at the wall away towards the center.

To further confirm the effects of buoyancy on heat transfer, the downward flow numerical results confirm the effects of buoyancy force (when reversed) as it works to increase the turbulence levels in the flow and enhance the mixing, thus mitigating the deterioration phenomenon under the same flow conditions with upwards flow.

Chapter 5: Annular Channel with Helical Fins

As part of the analysis to meet the second objective of this thesis - to analyze the geometrical effects on SCW flow – a study is done on an annular flow channel with a helically-ribbed heated inner tube.

The experimental data used for this geometry share the same pressure of 22.6 MPa and mass flux of 2000 kg/m²s, while varying the inlet temperatures (205 - 210°C) and the heat flux (1.543 - 2.547 MW/m²). The resultant dataset operating parameters are different from the bare tube dataset, with lower pressure, lower inlet temperature, higher mass flux, and higher heat flux. Nevertheless, when comparison is needed, it can be based on the operating regimes, which are identified as normal and deteriorated heat transfer regimes. The cases with their operating conditions are listed in Table 5-1.

Table 5-1: Operating Parameters for Annular Channel with Helical Fins Experiments

Case #	Pressure, MPa	G, kg/m ² s	q _{ave} , MW/m ²	T _{in} , °C	Regime
1	22.6	2000	1.543	205	NHT
2	22.6	2000	1.758	207	NHT
3	22.6	2000	2.033	208	NHT
4	22.6	2000	2.547	214	DHT

As mentioned in the methodology section, the wall temperatures were measured using thermocouples engraved in copper plugs inside the inner tube, and the temperatures were averaged for each cross section. This presents a source of uncertainty for the true wall temperature of the fluid (reported by the authors as $\pm 3.2\%$ [56]), as the existence of the helical fins adds a variable thickness to the wall, and the calculated values for the fluid temperatures at the wall will not in fact be uniform. The fundamental role of the fins is to increase the heat transfer area and remove more heat compared to a bare wall. In addition, due to the heat generation

in the solid structure, and the angles between the fins and the tube surface, the heat flux distribution will not be uniform (radially or axially) and there will be areas of higher heat flux to the fluid, causing higher temperatures, which may not be reflected in the experimental data.

To distinguish the different surfaces in the following results, Figure 5-1 shows the naming convention used throughout this chapter to refer to the base and fins. The base of the channel is divided into 4 sections by the fins, and they are referred to as Flow ID 1, 2, 3, and 4. The fins are denoted by 2 sides and a top.

The figure also illustrates a thermocouple engraved in a copper plug, of the same diameter as the inside diameter of the annulus. The exact location of each of the thermocouples relative to the fin is not known, due to the helicity of the geometry (Cut planes illustrating the locations of the thermocouples is shown in Figure D-1 in Appendix D).

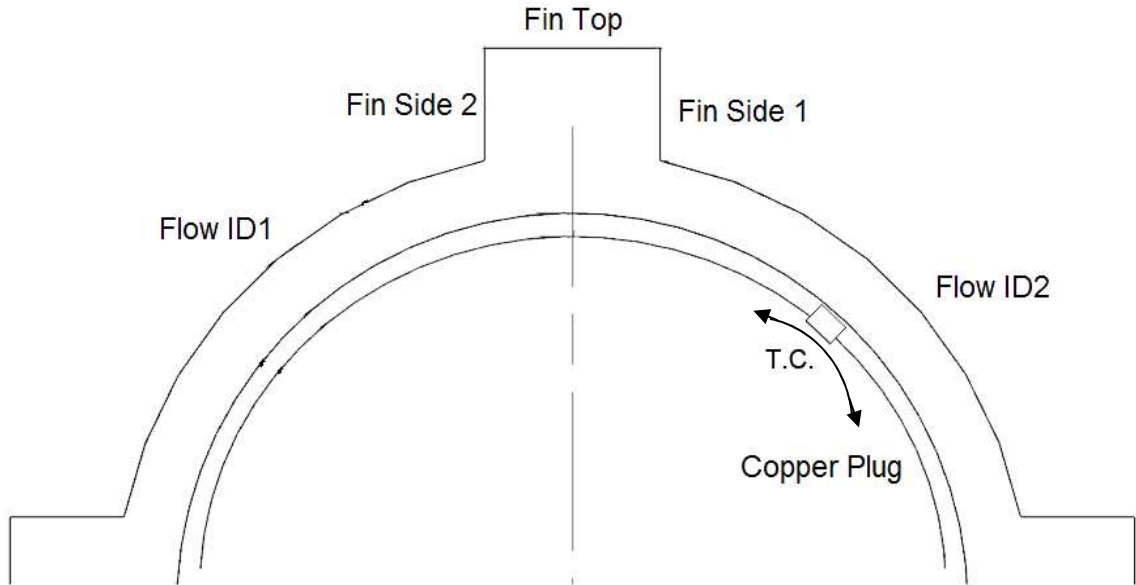


Figure 5-1: Illustration of the finned rod surfaces names

5.1 Case 1 - SST Model, Free Mesh, Heated Fins

By analyzing the first case, with the lowest heat flux of 1.543 MW/m^2 , the experimental data showcases a normal heat transfer regime, with a steady rise in wall and bulk-fluid temperatures. The heat flux is below the deteriorated heat flux for $2000 \text{ kg/m}^2\text{s}$, and the highest temperatures do not cross the pseudocritical point, which means the fluid is entirely in the compressed liquid region.

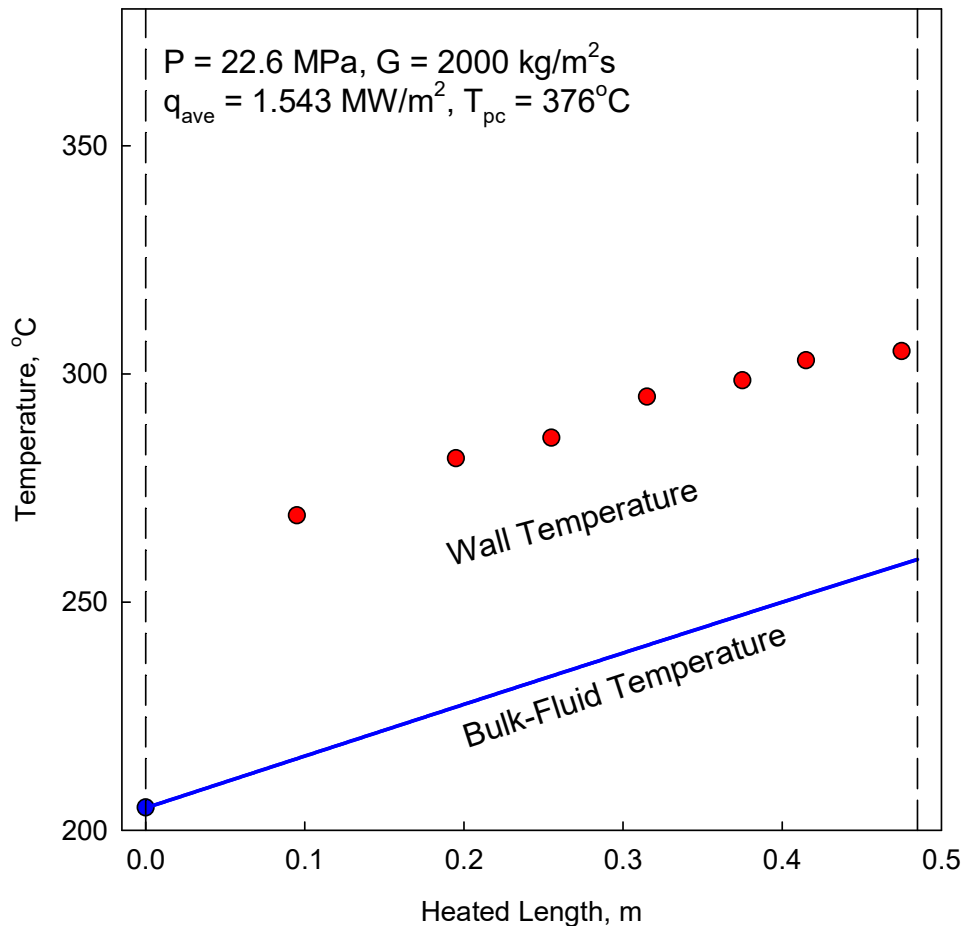


Figure 5-2: Sample Experimental Run for the Annular Channel with Helical Fins, with bulk-fluid and wall temperatures [56]

The results of the first simulation using the SST model and the free mesh (from the 2D blocking) are shown in the next set of graphs. Due to the number of heated walls, the helicity of the geometry, and the angles created by the fins, the fluid

temperatures at the walls create a spread over around 50°C (as opposed to the uniform profile in a bare tube for example).

Figure 5-3 shows the temperature contours at the walls (as well as the inlet and outlet surfaces). The unheated inlet section is at a uniform temperature of 205°C, before entering the heated channel where the temperature rises steadily until the outlet. The temperature distribution shows more clearly the regions of low and high temperature. The highest temperatures in each cross section are achieved where the fins meet the base, where the heat flux from both walls raises the temperature of the fluid beyond that of the inner tube alone.

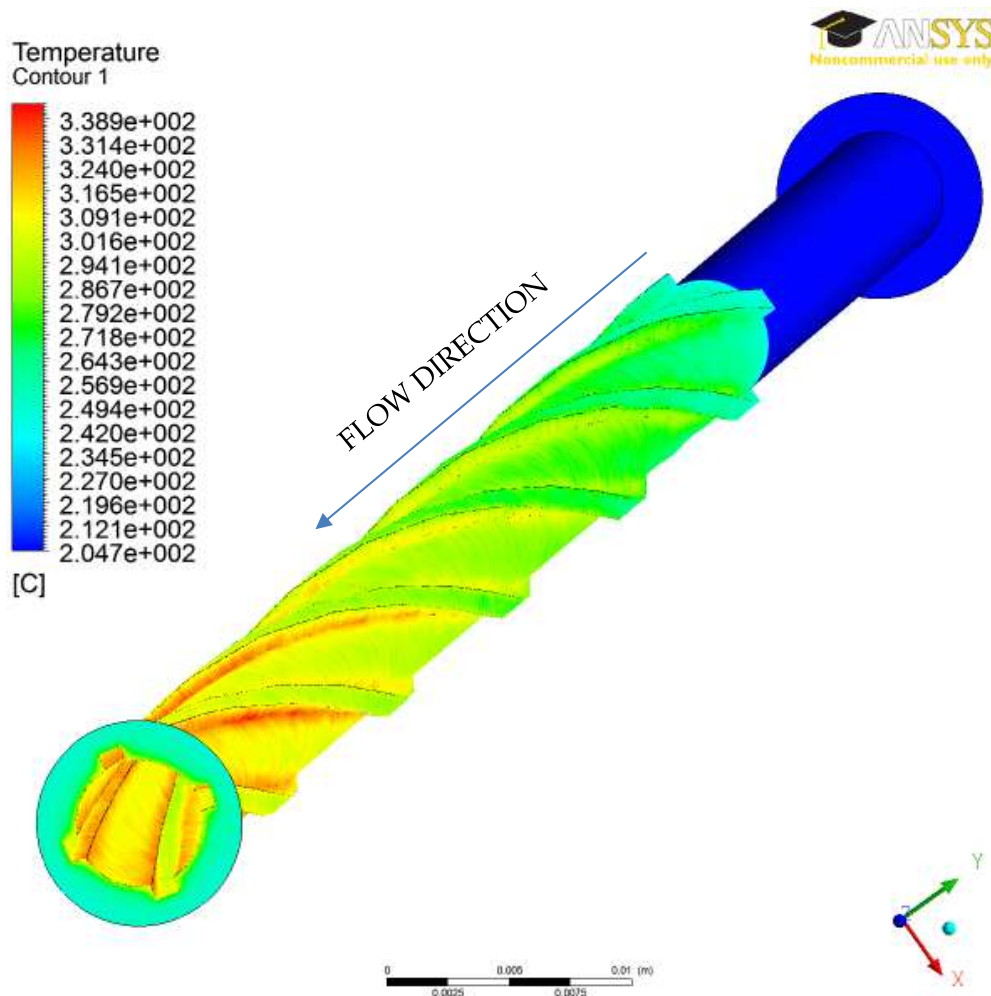


Figure 5-3: Temperature Contour for the Fluid at the Walls of the Annular Channel Using the SST Model ($P = 22.6 \text{ MPa}$, $G = 2000 \text{ kg/m}^2\text{s}$, $q = 1.543 \text{ MW/m}^2$)

Figure 5-4 shows a close up of the temperature contour, where it can be seen that the temperature difference can reach around 50-60°C at the same cross section. However, when averaging the temperatures, the average will be closer to the lower end, as the number of cells away from where the fin meets the base is higher than that area.

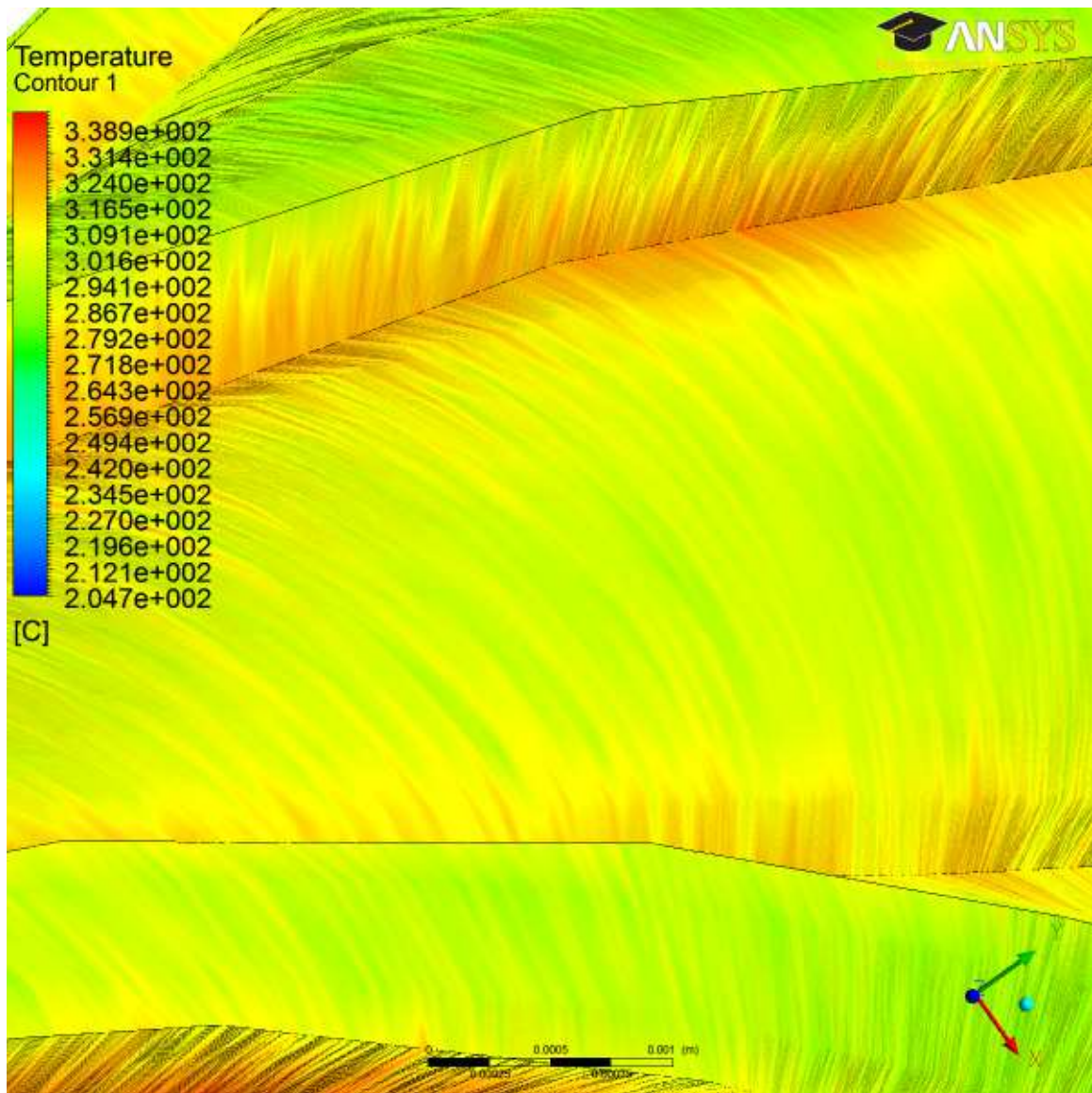


Figure 5-4: Close-up of Temperature Contour for the Fluid at the Walls of the Annular Channel Using the SST Model ($P = 22.6 \text{ MPa}$, $G = 2000 \text{ kg/m}^2\text{s}$, $q = 1.543 \text{ MW/m}^2$)

Figure 5-5 shows the wall temperatures for the fluid at the inner flow tube base (without the fins). The inner tube is divided by the fins into 4 regions, and for visual reasons, 3 of those are plotted in the figure. The 4th wall (Flow_ID 4) temperatures are not plotted as they mask most of the rest, due to the similarity in values (the values are used in the calculations for averaging the temperature profile however).

The spread shows the lowest and highest temperatures at each cross section throughout the flow region. It can be seen from the relative density of the temperature points that most of the nodes capture a slightly lower temperature (denser band at lower temperatures), while less points are at higher temperatures (near the fin walls). However, due to the nature of the free mesh, the number of nodes at each cross section (same Z value) is different. This will be addressed further when discussing the averaging of the temperatures.

Figure 5-6 and Figure 5-7 show the wall temperatures for two of the helical fins. It is apparent that they share the same profiles and exhibit the same trends (as do the other two fins, the graphs of which were omitted due to their similarities). It is also noticeable that the fin sides are generally at a higher temperature than the fin top. This fact is to be expected, as the fin top is in contact with cooler fluid (closer to the bulk-fluid temperature) and has one wall as a source of heat, as opposed to two adjacent walls in the case of the fin sides.

To visualize the temperature and property distributions better, CFD Post software is used to create contours, which helps showcase the distributed properties, as well as the relative differences in different regions of the flow.

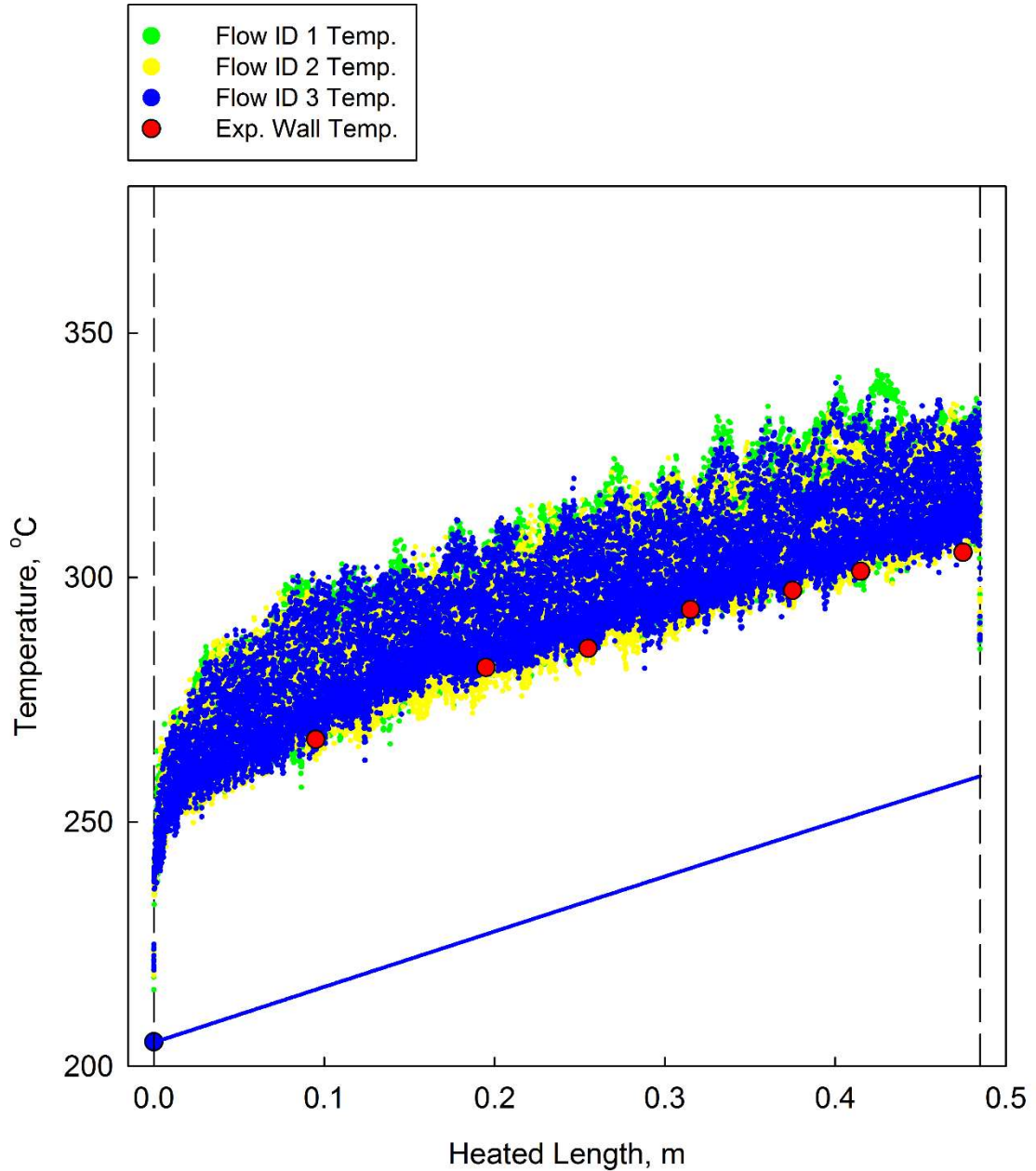


Figure 5-5: Simulated Temperatures for the Fluid at Three Walls of the Inner Tube of the Flow Channel Using the SST Model ($P = 22.6$ MPa, $G = 2000$ kg/m²s, $q = 1.543$ MW/m²)

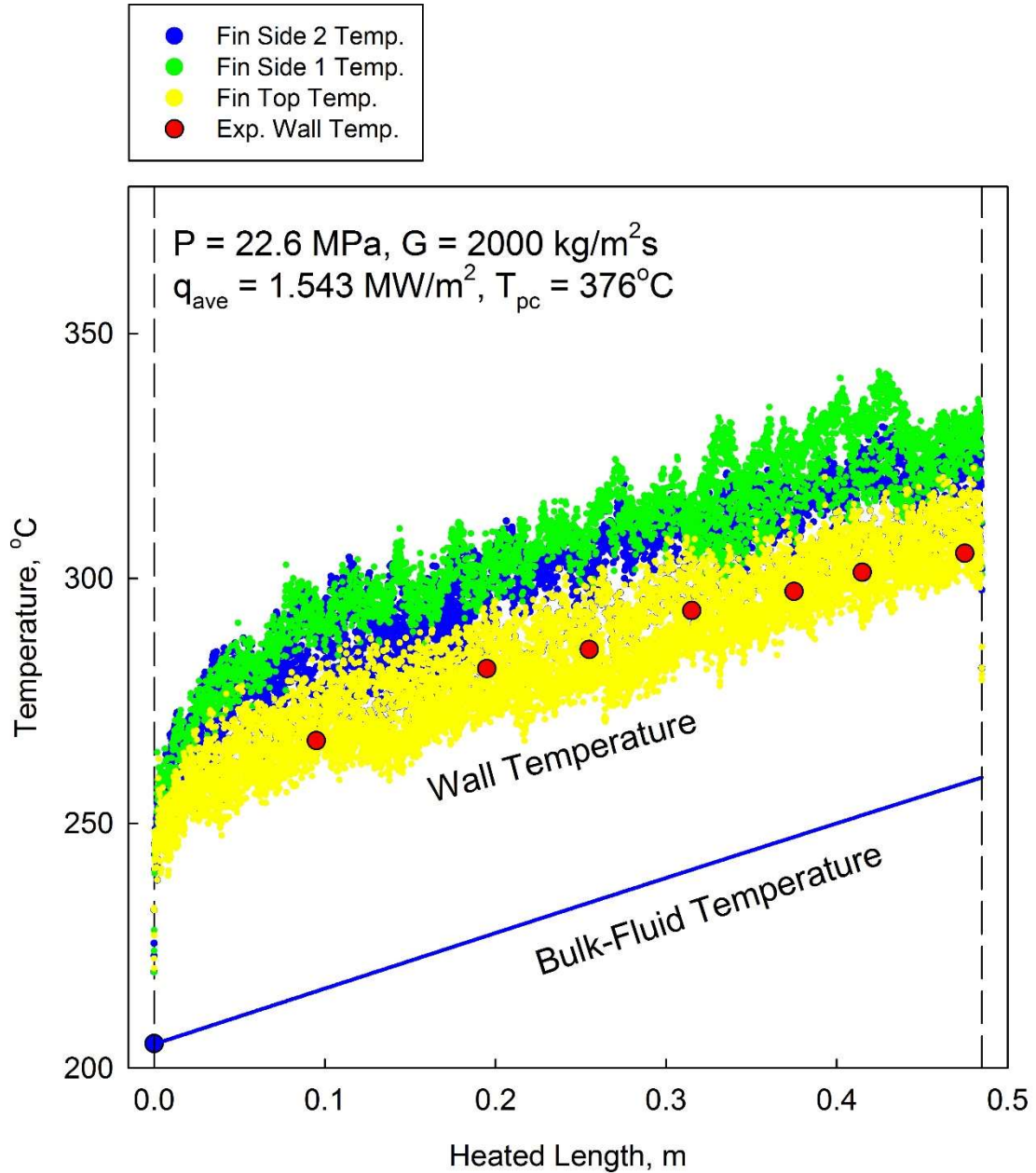


Figure 5-6: Simulated Temperatures for the Fluid at the Three Walls of a Helical Fin (Fin 1) Using the SST Model ($P = 22.6 \text{ MPa}$, $G = 2000 \text{ kg/m}^2\text{s}$, $q = 1.543 \text{ MW/m}^2$)

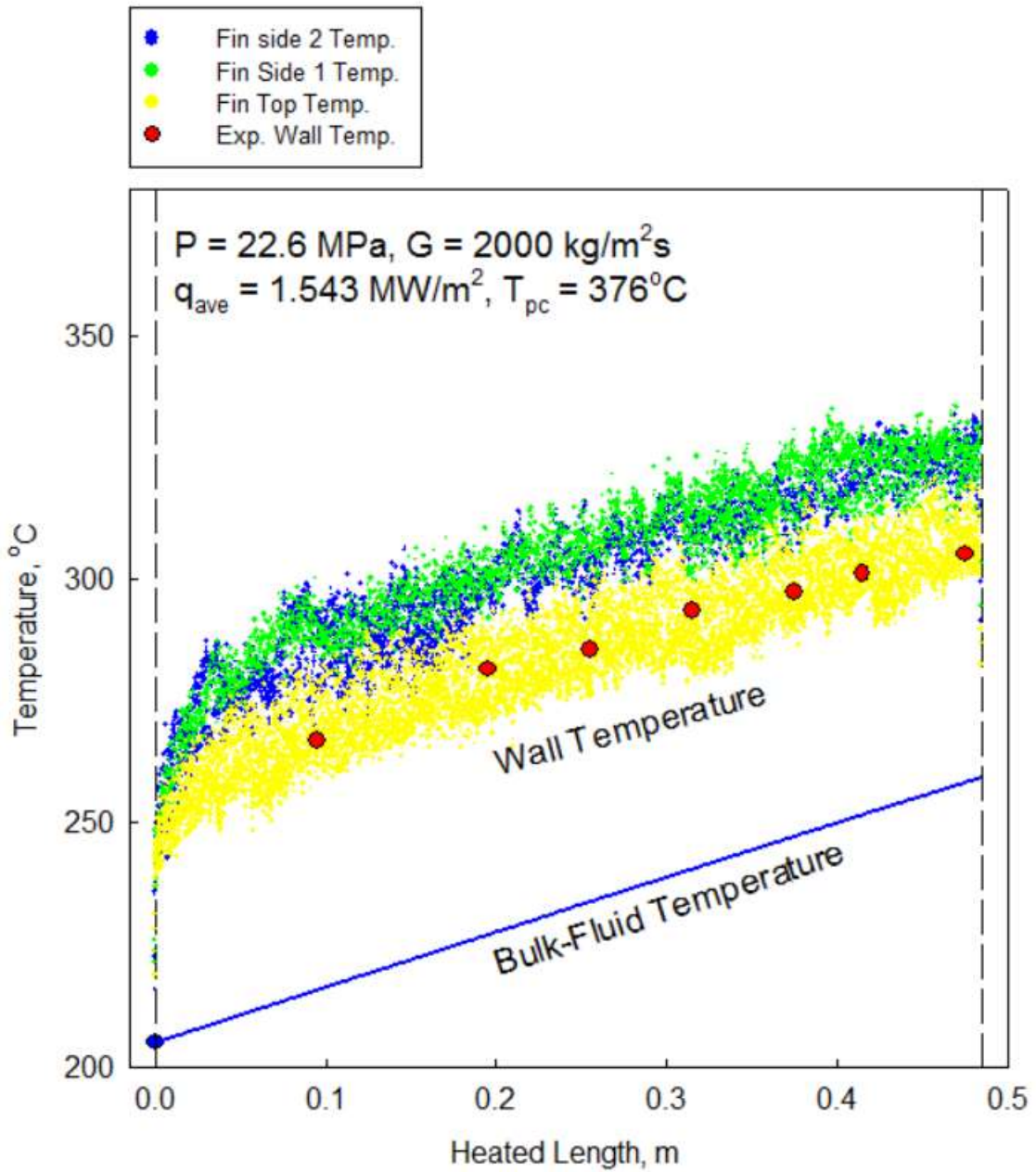


Figure 5-7: Simulated Temperatures for the Fluid at the Three Walls of a Helical Fin (Fin 2) Using the SST Model ($P = 22.6 \text{ MPa}$, $G = 2000 \text{ kg/m}^2\text{s}$, $q = 1.543 \text{ MW/m}^2$)

In order to compare the simulated wall temperatures to the experimental measurements, the temperature bands have to be averaged across each cross section. However, due to the random nature of the axial position of the mesh nodes (no nodes share the exact same Z value in their coordinates), the averaging process cannot be done satisfactorily using a simple algorithm of averaging the temperatures that share the same axial distance. Such a method, implemented using a MATLAB code, resulted in narrow bands that still had a spread over minimum and maximum values, as shown in Figure 5-8.

Thus a regression algorithm was used to create a best fit line for the entire collection of the simulated wall-fluid data (145,000 points). The simulated temperatures for the entire heated wall are shown in Figure 5-9 alongside a regression line that shows the best fit curve for the data.

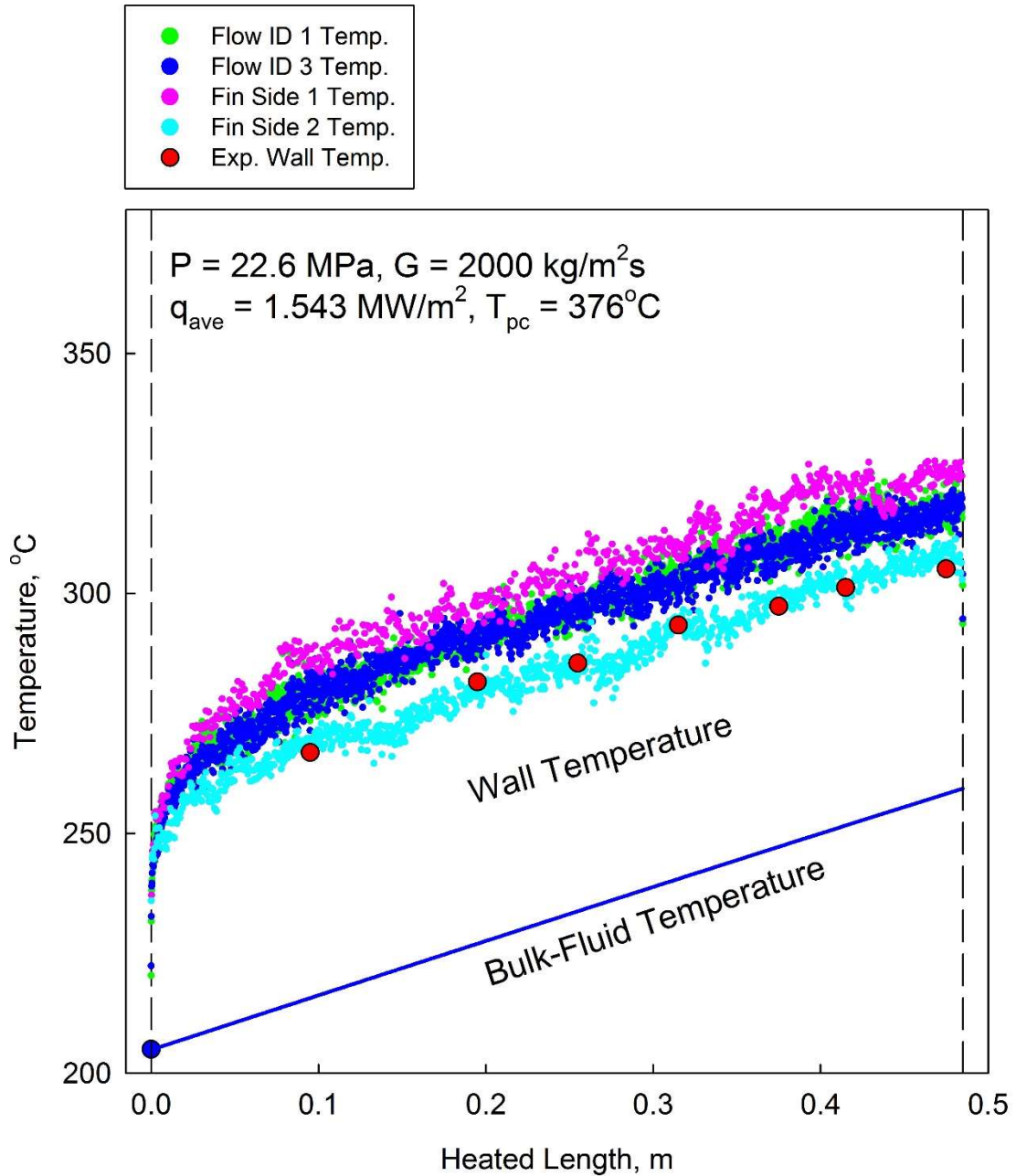


Figure 5-8: Simulated Temperatures for the Fluid at Two Walls of the Inner Flow Tube, and Two Helical Fin Walls (Side and Top) Using the SST Model (P = 22.6 MPa, G = 2000 kg/m²s, q = 1.543 MW/m²)

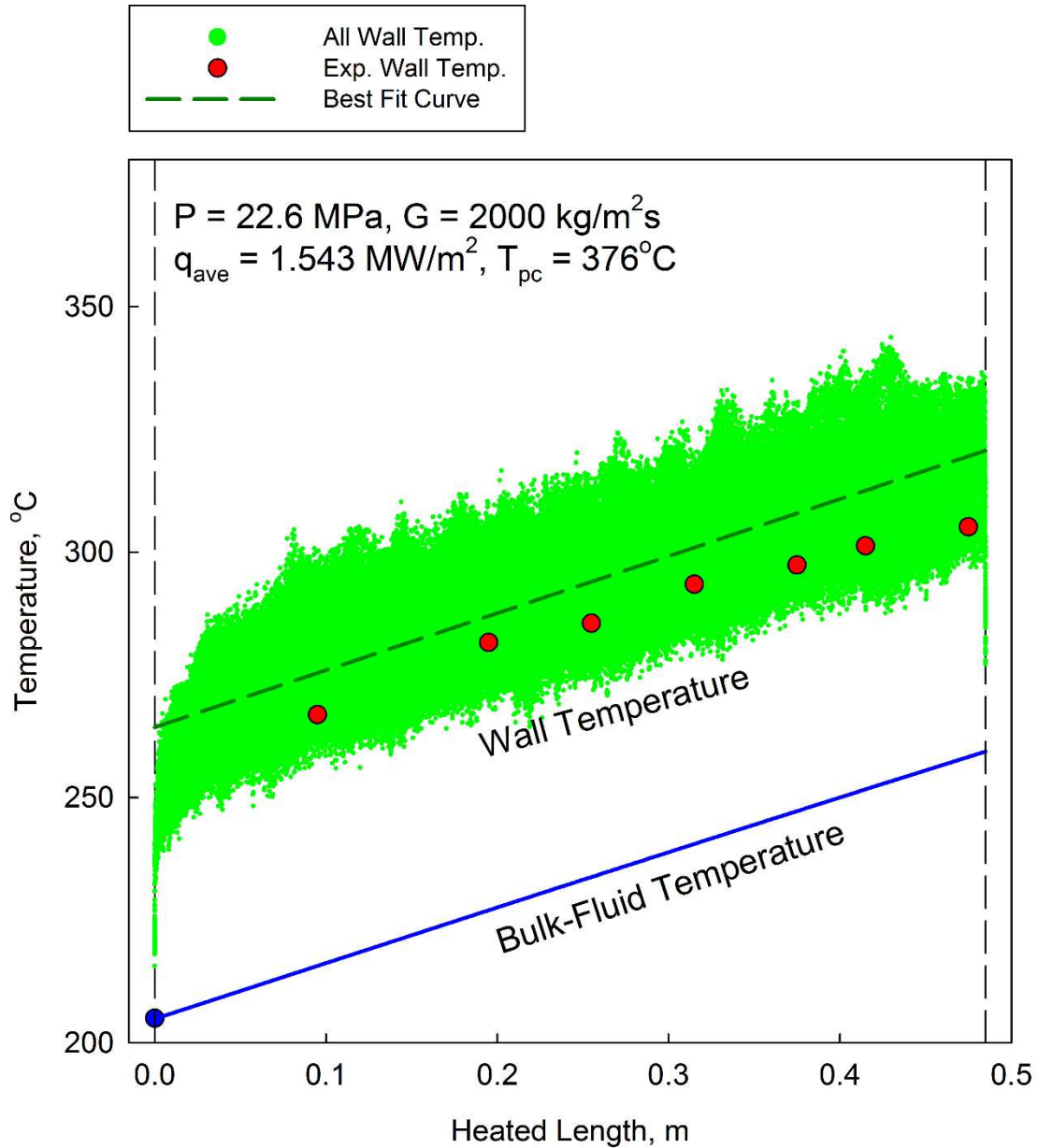


Figure 5-9: Simulated Temperatures for the Fluid at All Heated Walls of the Annular Channel (SST Model, $P = 22.6 \text{ MPa}$, $G = 2000 \text{ kg/m}^2\text{s}$, $q = 1.543 \text{ MW/m}^2$), and the Average Temperature Profile Using Curve Fitting

The curve fit algorithm is used to create a regression line for the data, preserving the overall trend, as well as capturing the relative density of the temperature points. As the surface of the inner heated wall accounts for a larger percentage of the total heated surface than the helical fins, the average temperature will be skewed towards the value at these walls.

The average temperature line slightly over predicts the experimental wall temperatures, by an average of 4%. It must be noted again, however, that the comparison is done to values calculated using an equation to calculate temperature difference in a cylindrical wall (using only the thermal conductivity of the steel), with a uniformly distributed heat generation source and without the fin effect. Due to the uncertainties these factors create, and even with the close proximity of the simulated results to the “experimental” points, the true value of the temperature at the wall is likely to be different to that shown in the graphs. Nevertheless, the profile and trends exhibited by these points shall be considered as the main point of comparison for the purposes of this study.

As the simulation results show a good fit for the data, the post processing tool can be utilized to explore the 3D effects in much more detail than what is available in the current experimental capabilities. In addition to the wall temperature contour shown earlier in Figure 5-3, a look at the radial distribution of temperature can be seen in Figure 5-10, with close-up views in Figure 5-11 and Figure 5-12. Figure 5-13 and Figure 5-14 show close-up views of a radial cross section contour with the mesh lines. These figures show the radial rate of change for the fluid temperature from the heated wall to the outer, unheated wall, as well as the areas of highest wall temperature.

As in the case of the simple bare tube, the temperature change is most significant within ~50 microns from the wall, after which the temperature blends in to the bulk fluid temperature. This effect can be explained by studying the turbulence kinetic energy in the fluid, and its rate of change, as well as the turbulence intensity.

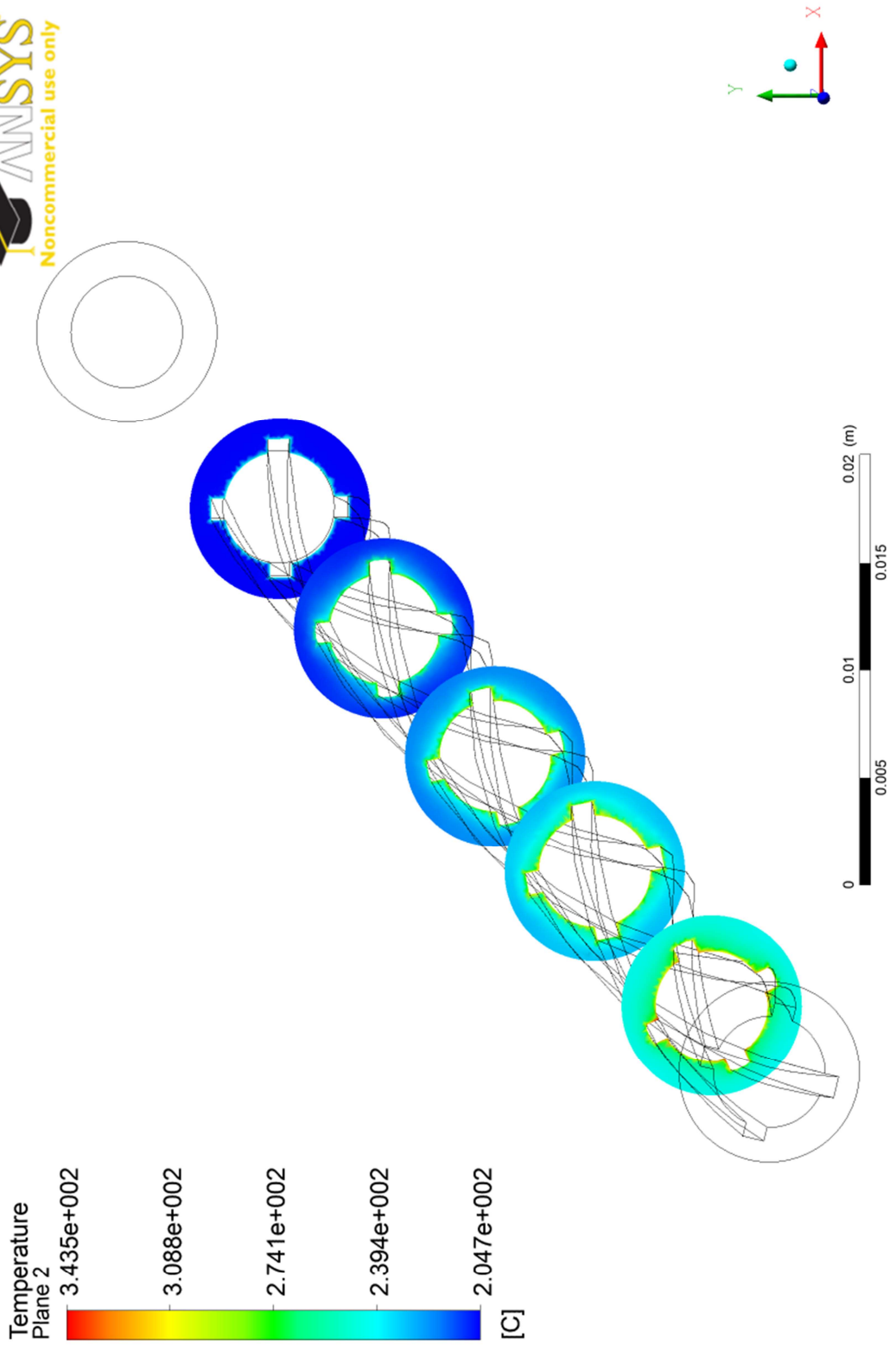


Figure 5-10: Temperature Contour for the Fluid at Various Cross Sections in the Annular Channel (SST Model, $P = 22.6 \text{ MPa}$, $G = 2000 \text{ kg/m}^2\text{s}$, $q = 1.543 \text{ MW/m}^2$)

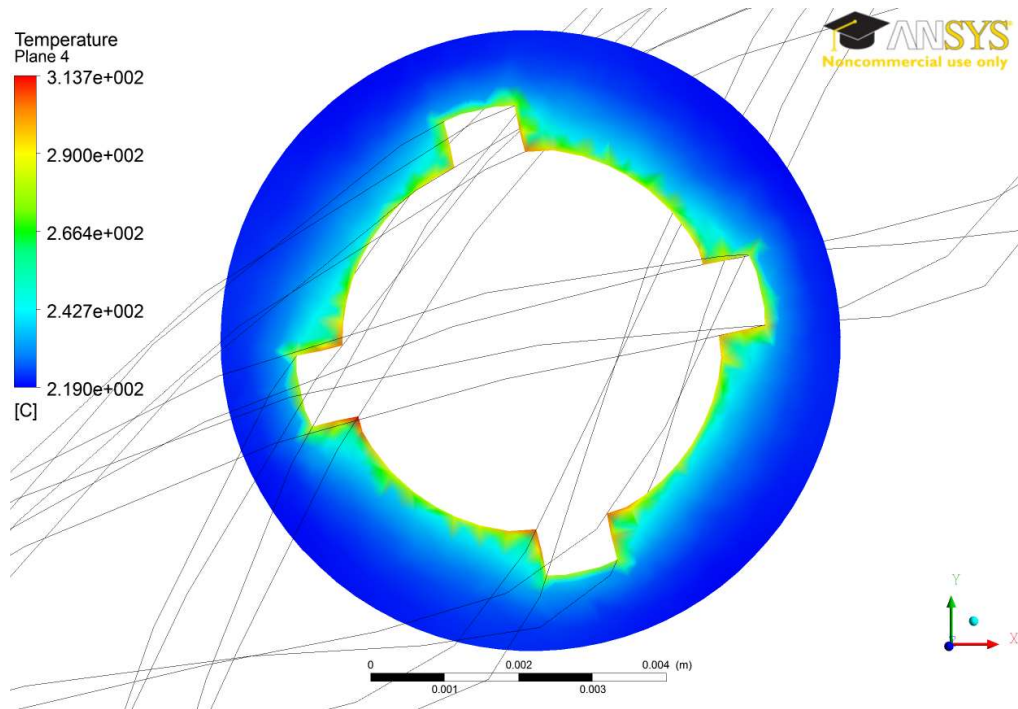


Figure 5-11: Close-up of Temperature Contour for the Fluid at a Radial Cross Section in the Annular Channel (SST Model, $P = 22.6$ MPa, $G = 2000$ kg/m²s, $q = 1.543$ MW/m²)

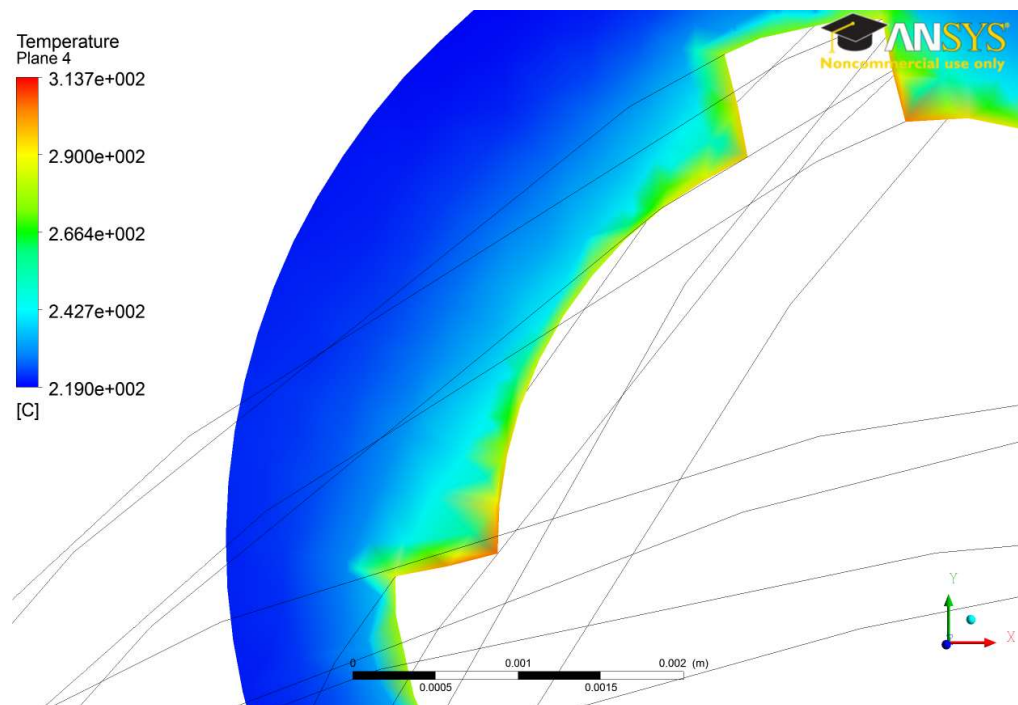


Figure 5-12: Close-up of Temperature Contour for the Fluid at a Radial Cross Section in the Annular Channel (SST Model, $P = 22.6$ MPa, $G = 2000$ kg/m²s, $q = 1.543$ MW/m²)

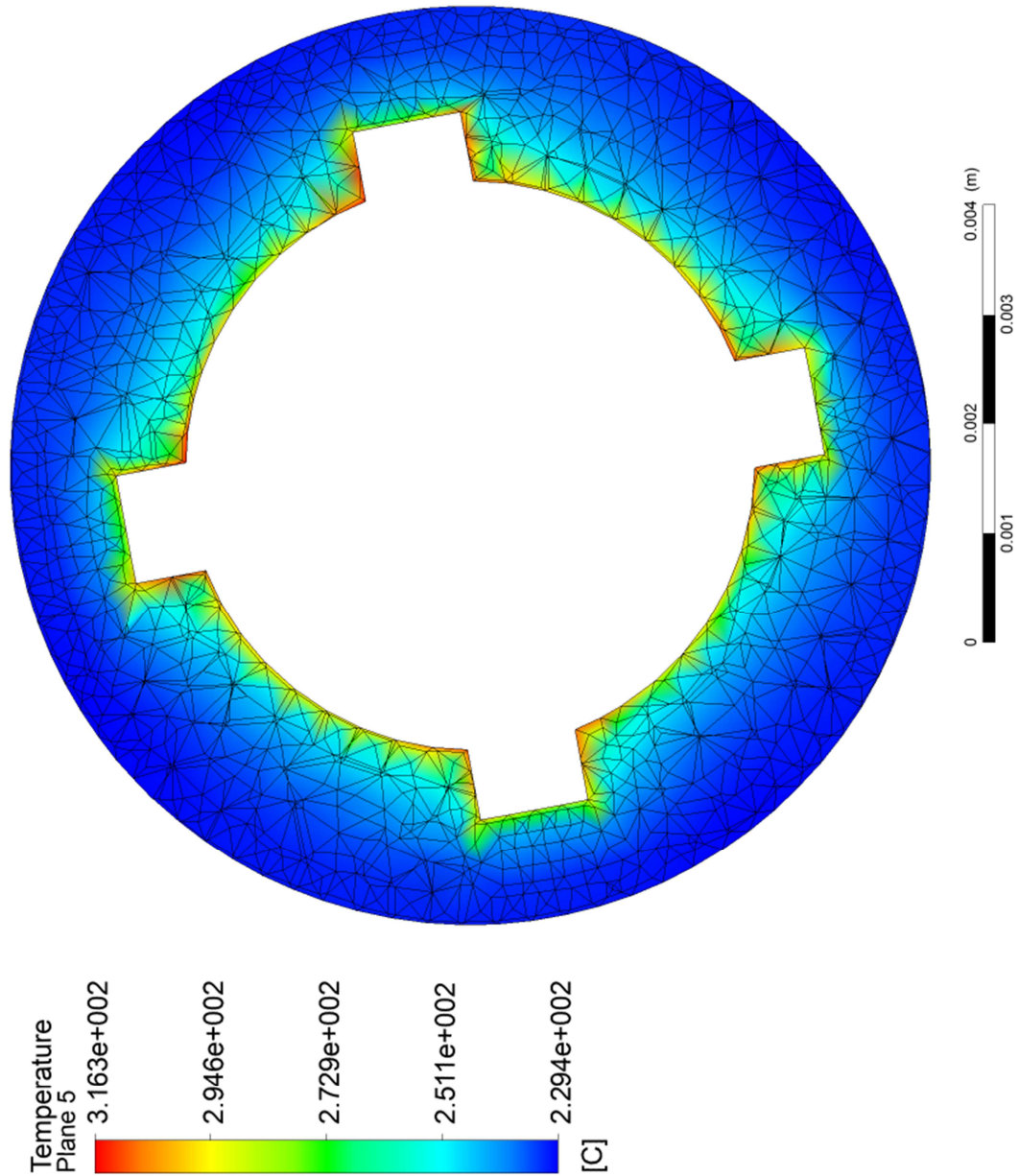
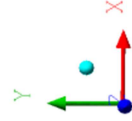


Figure 5-13: Close-up of Temperature Contour and Mesh at a Radial Cross Section in the Annular Channel (SST Model, $P = 22.6 \text{ MPa}$, $G = 2000 \text{ kg/m}^2\text{s}$, $q = 1.543 \text{ MW/m}^2$)

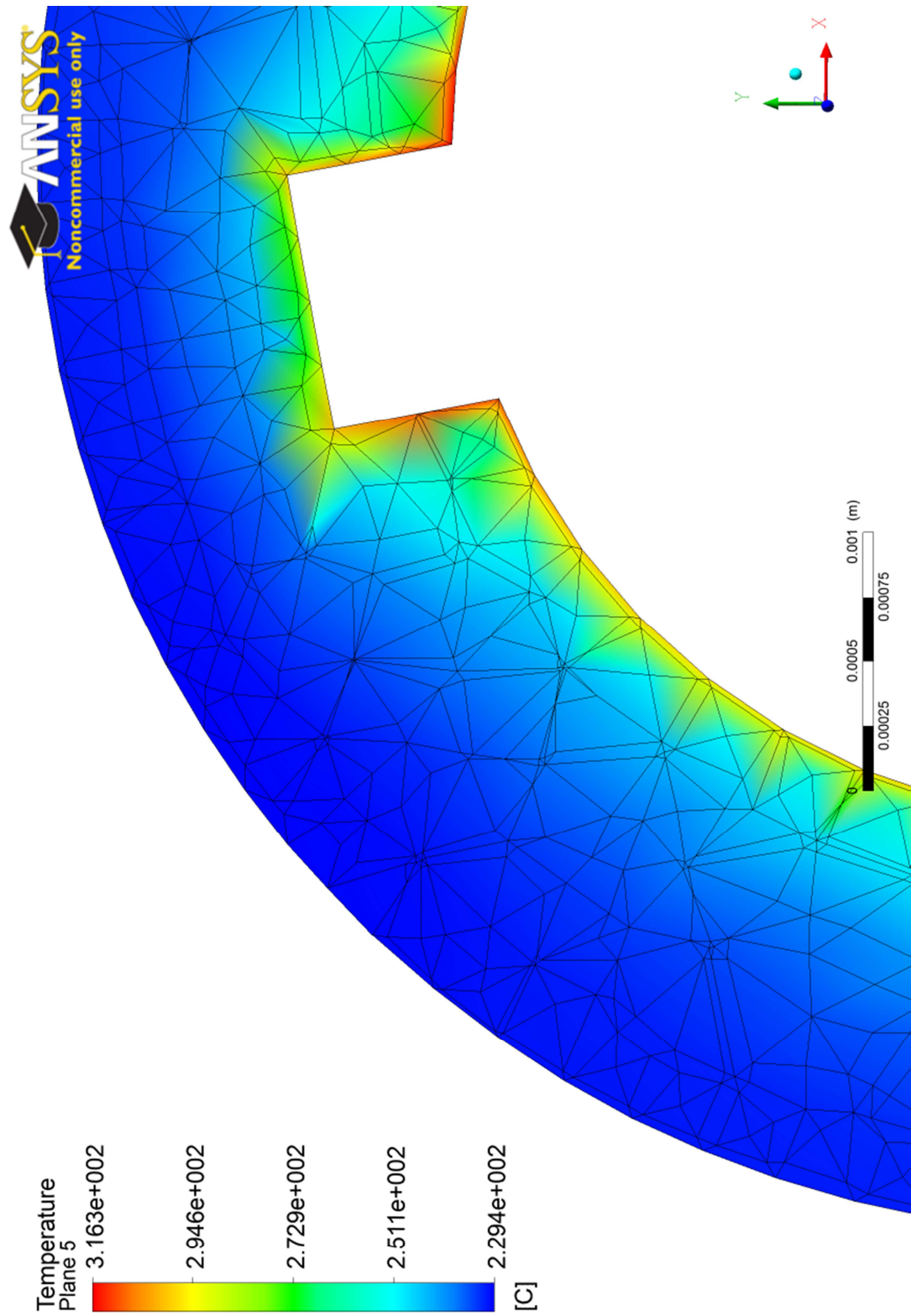


Figure 5-14: Close-up of Temperature Contour and Mesh at a Radial Cross Section in the Annular Channel (SST Model, $P = 22.6 \text{ MPa}$, $G = 2000 \text{ kg/m}^2\text{s}$, $q = 1.543 \text{ MW/m}^2$)

Figure 5-15 shows a longitudinal cross section of the turbulence kinetic energy contour. The scale is global for all values in the solution, and the maximum is shown to be achieved only at the interface between the unheated entrance region and the beginning of the finned region. This is due to the flow disturbance the introduction of the fins produces. After that however, the turbulence energy in the flow is reduced throughout the heated region. Figure 5-16 shows the radial cross sections with local scales for the values. This scale shows the maximum values only within the contour, and it is obvious that the turbulence kinetic energy levels are relatively low, and match those of the flow in a bare tube under NHT regime (such as Figure 4-8 for example). This is one indication that the helical fins do not induce much turbulence in the supercritical fluid flow compared to a bare tube under similar conditions.

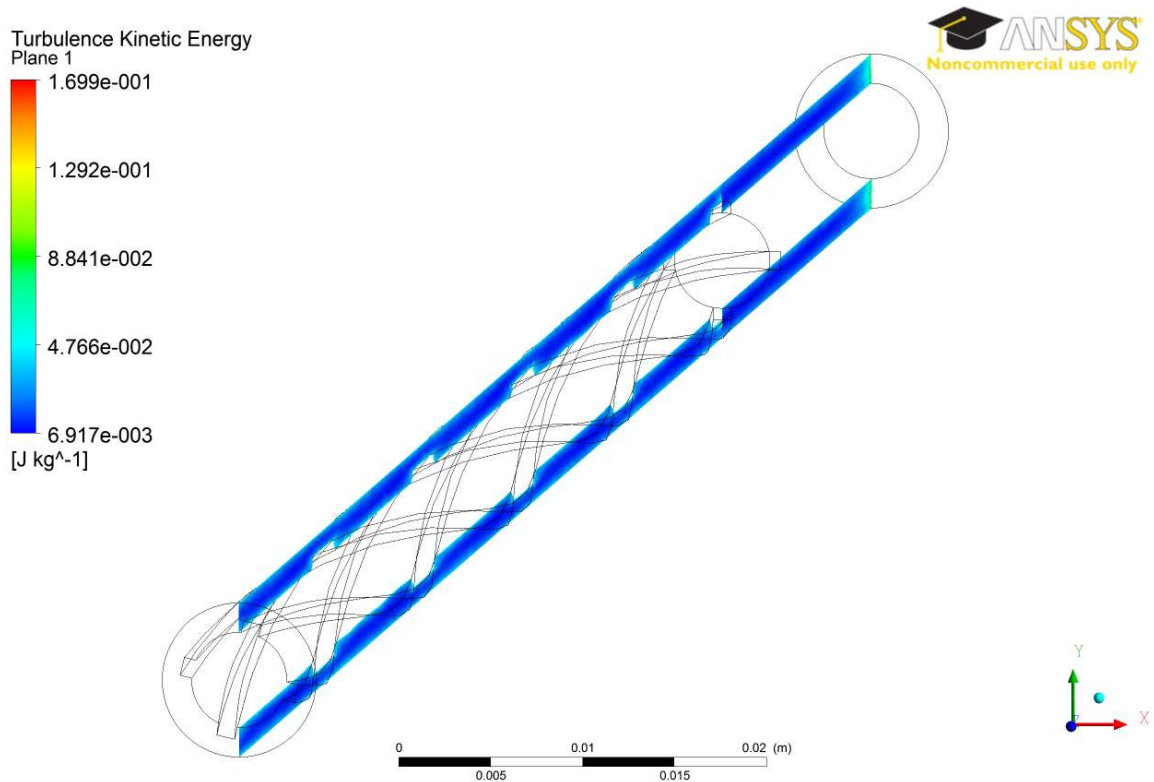


Figure 5-15: Turbulence Kinetic Energy Contour for the Fluid at a longitudinal Cross Section (SST Model, $P = 22.6 \text{ MPa}$, $G = 2000 \text{ kg/m}^2\text{s}$, $q = 1.543 \text{ MW/m}^2$)

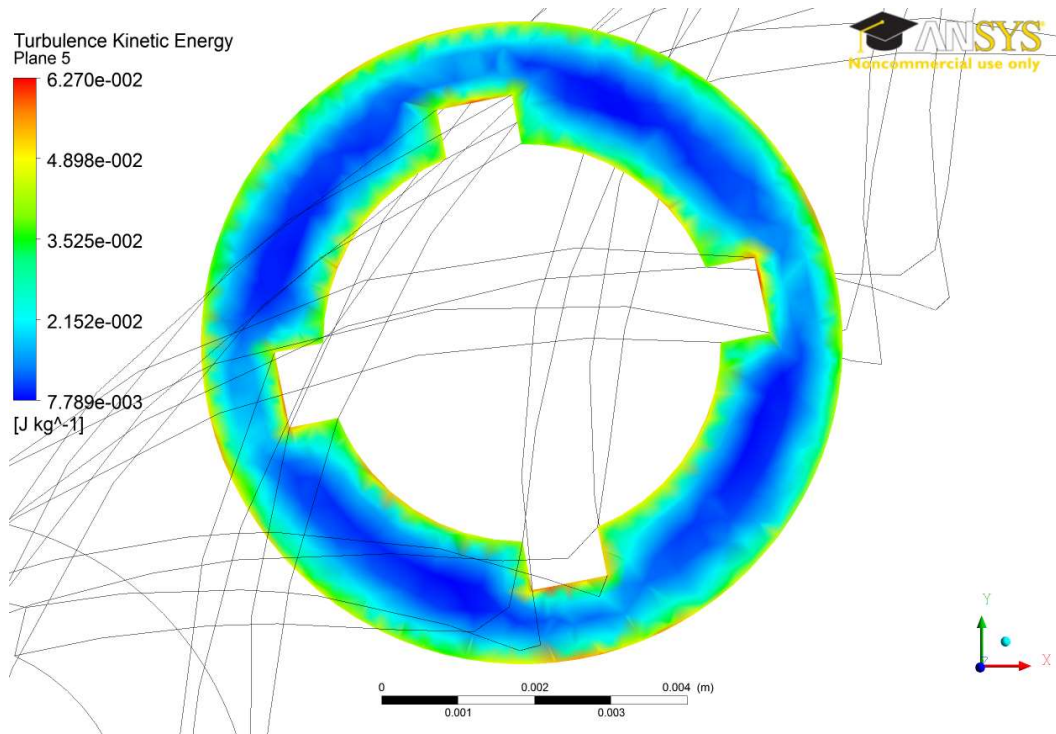


Figure 5-16: Close-up of Turbulence Kinetic Energy Contour for the Fluid at a Radial Cross Section (SST Model, $P = 22.6$ MPa, $G = 2000$ kg/m²s, $q = 1.543$ MW/m²)

Figure 5-17 shows the turbulence intensity radial contours, using local scales for each contour. The minimum and maximum limits are roughly 3.3 and 7.5%, with the majority of the flow in the lower end of that range. It is generally lower than that of the bare tube with NHT (4 - 10% in Figure 4-9), and actually closer to the DHT simulations (2 - 6% for the bulk fluid, Figure 4-26). It is apparent at this stage, that the helical fins do not induce turbulence in the flow compared to a simple tube. This result is not surprising as the fins do not impede the flow or disturb it (there is no change in flow area), rather they work to redirect it helically around the flow area. To confirm this observation, the velocity contours and velocity streams are needed.

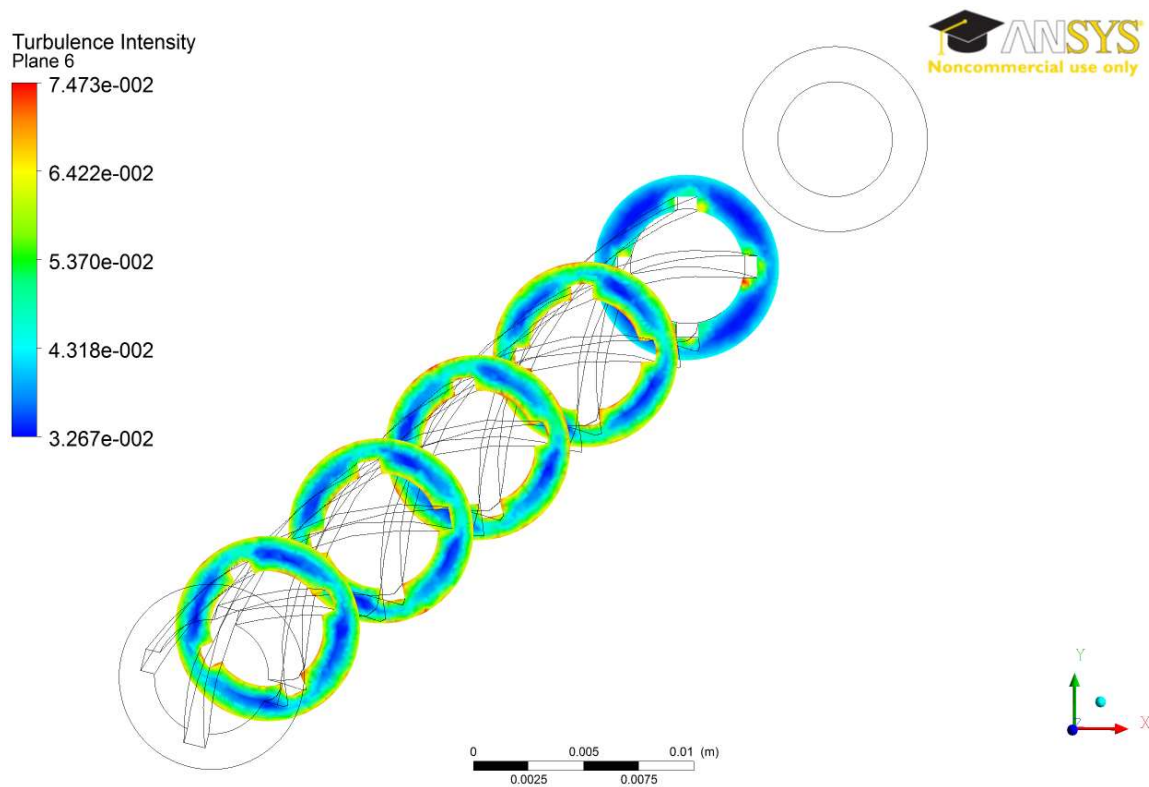


Figure 5-17: Turbulence Intensity Contour for the Fluid at Various Radial Cross Sections (SST Model, $P = 22.6$ MPa, $G = 2000$ kg/m²s, $q = 1.543$ MW/m²)

The longitudinal contour of velocity in the flow domain is shown in Figure 5-18. This contour shows the global scale of the velocity, with a minimum value of zero at the walls (no slip) and a maximum of around 3.1 m/s in the mean flow. Figure 5-19 shows a close up of a contour to show the details of the velocity profile in a radial cross section.

Figure 5-20 shows the velocity streams in the flow domain, where it can be seen that the helicity of the geometry drives the fluid to flow in “channels” created by the fins. And since the fins do not create an obstruction or disturbance in the flow (such as an area change would), the turbulence levels remain relatively low, and the radial component of the velocity remain at two orders of magnitude lower than that of the axial component, as shown in Figure 5-21.

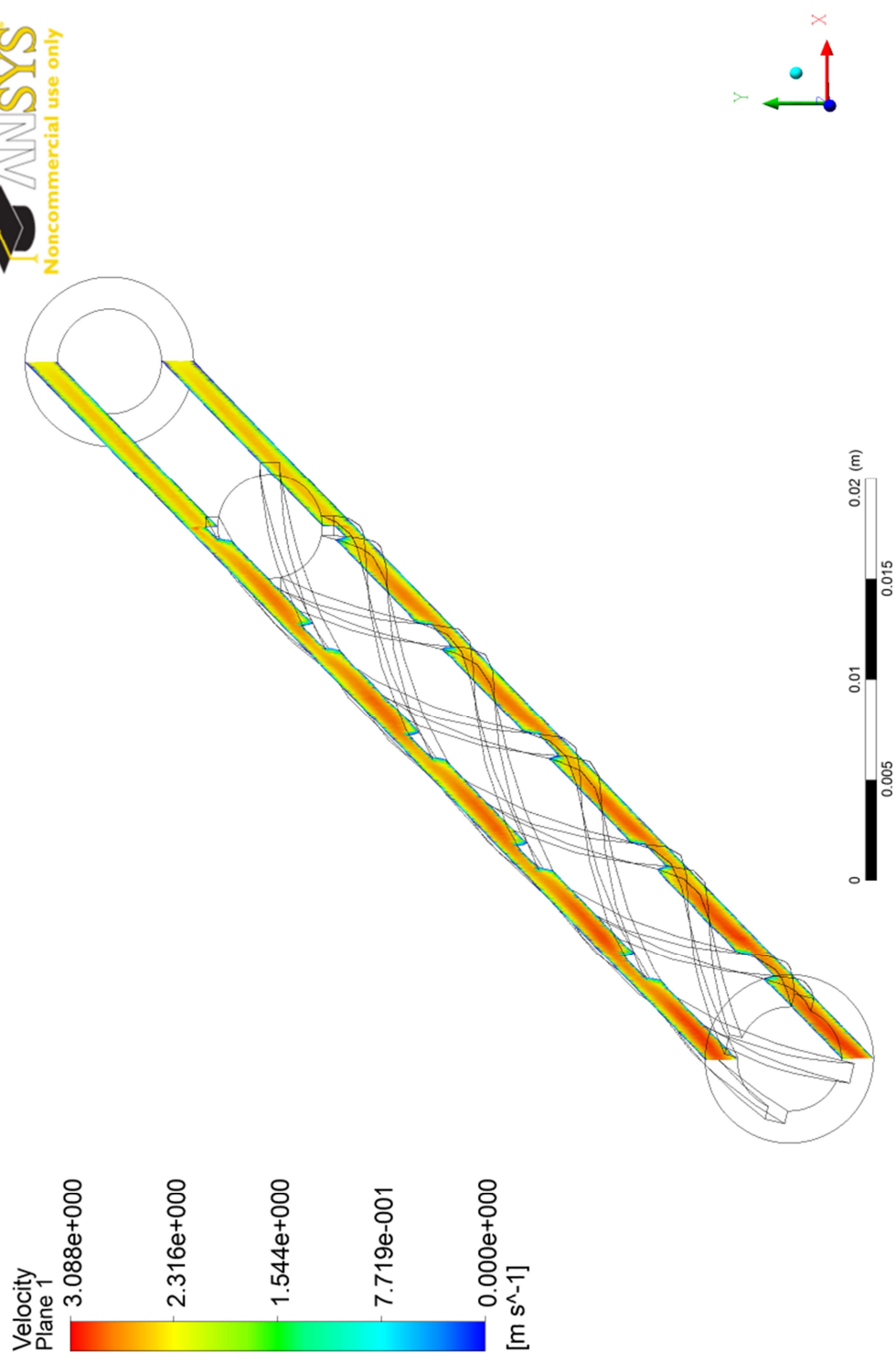


Figure 5-18: Velocity Contour for the Fluid at a longitudinal Cross Section (SST Model, $P = 22.6 \text{ MPa}$, $G = 2000 \text{ kg/m}^2\text{s}$, $q = 1.543 \text{ MW/m}^2$)

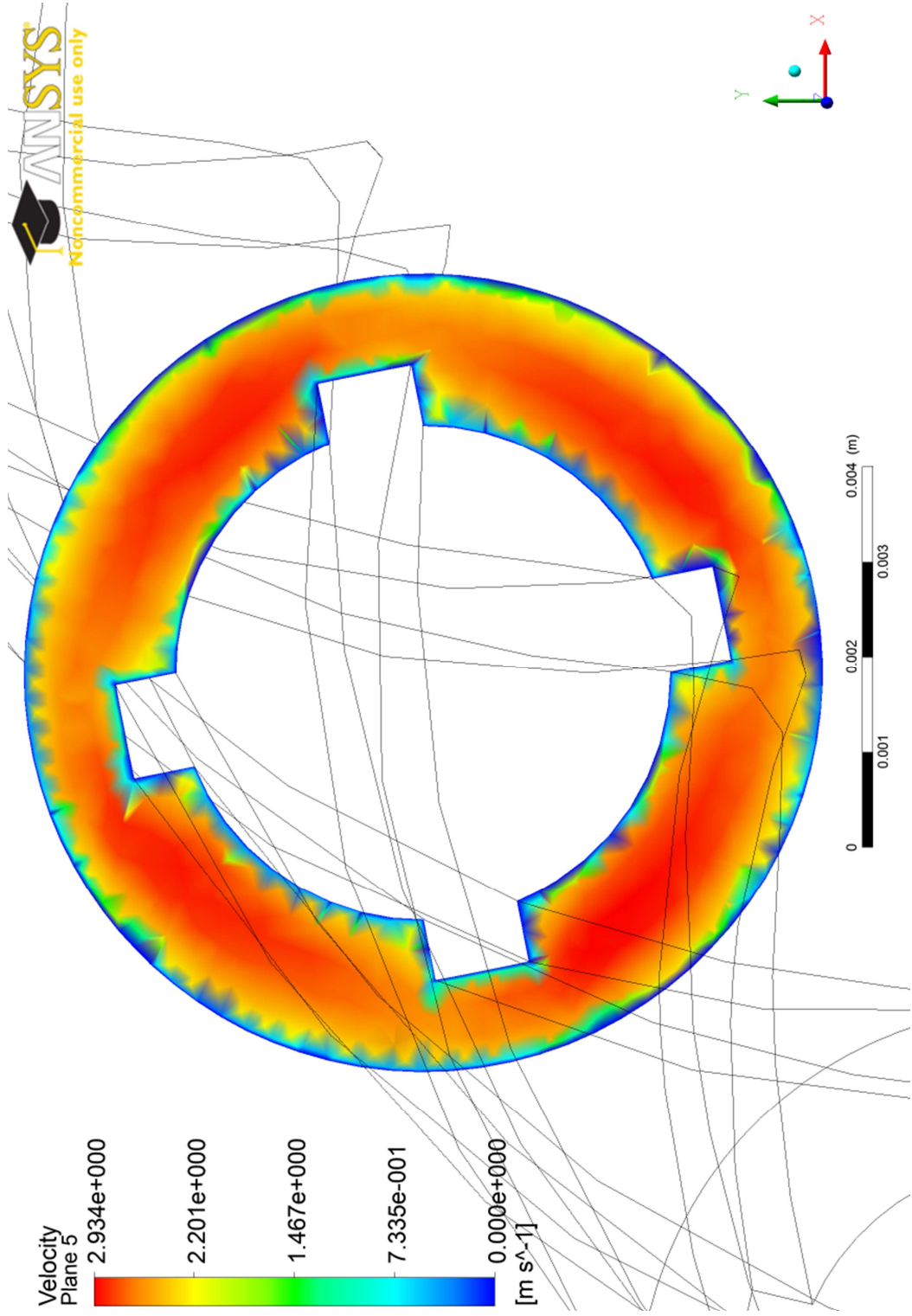


Figure 5-19: Velocity Contour for the Fluid at a Radial Cross Section (SST Model, $P = 22.6 \text{ MPa}$, $G = 2000 \text{ kg/m}^2\text{s}$, $q = 1.543 \text{ MW/m}^2$)

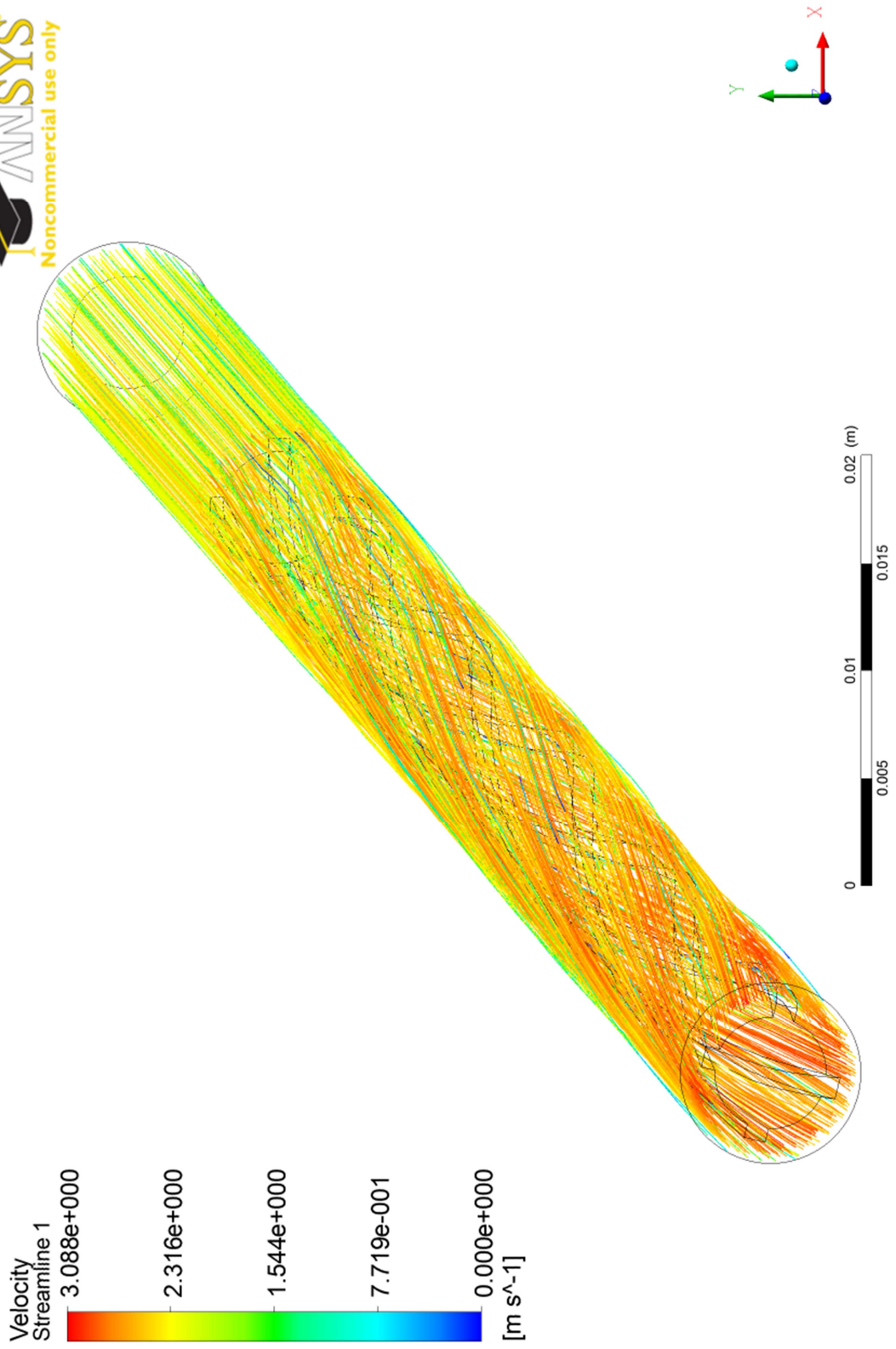


Figure 5-20: Velocity Streamlines for the Fluid in the Flow Domain (SST Model, P = 22.6 MPa, G = 2000 kg/m²s, q = 1.543 MW/m²)

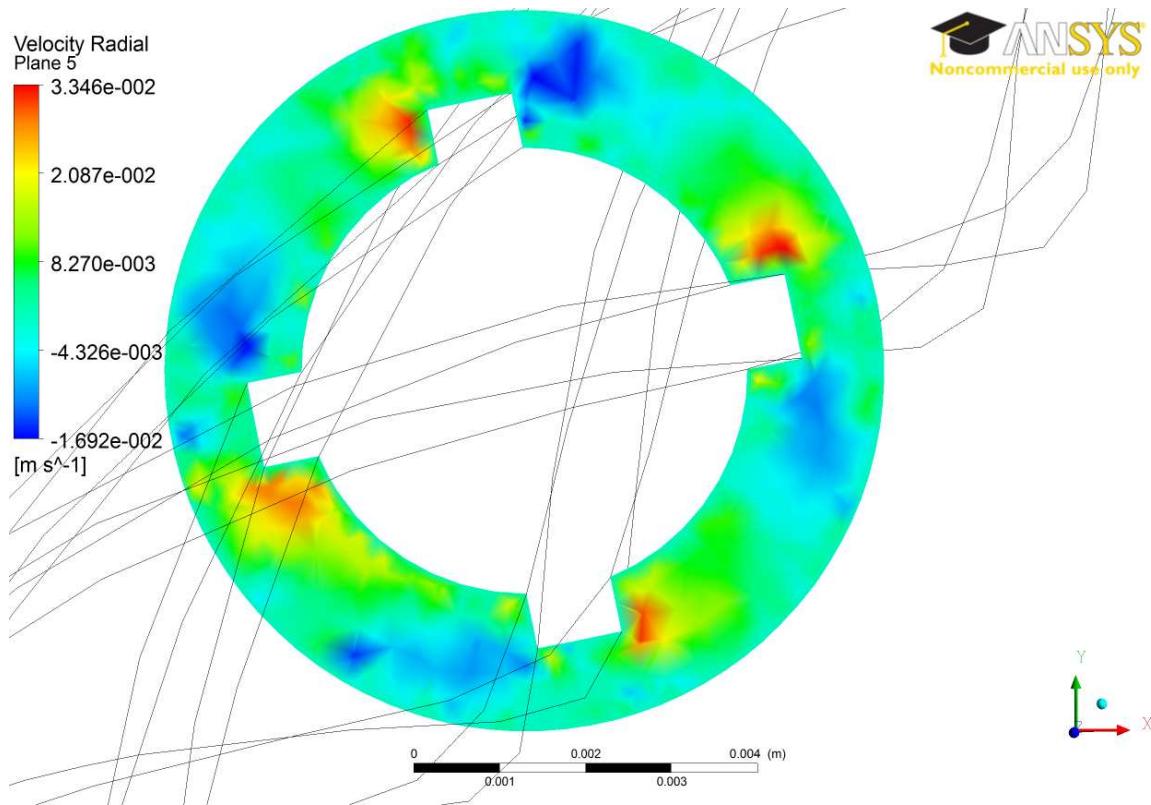


Figure 5-21: Radial Velocity Component Contour for the Fluid at a Radial Cross Section (SST Model, $P = 22.6$ MPa, $G = 2000$ kg/m²s, $q = 1.543$ MW/m²)

The density of the fluid and its change throughout the flow region can be plotted using contours as shown in Figure 5-22. The figure shows the density of the fluid at the wall from the inlet to the outlet. It can be seen that the density changes from a maximum of roughly 870 kg/m³ to a low of 730 kg/m³. Using these values, and knowing the temperature and the pressure of the fluid in the flow region, it can further be established that the fluid is in the compressed liquid region of properties, and does not incur a significant density change in the heated length. Alternate views of the density contour are shown in Figure 5-24 and Figure 5-23, illustrating the radial changes as well. The specific heat of the fluid also remains within the same order of magnitude and does not reach its peak near the pseudocritical point, as shown in Figure 5-25 and Figure 5-26. This is believed to be one of the main reasons for the fluid behaving in the NHT regime and exhibiting no deterioration in heat transfer.

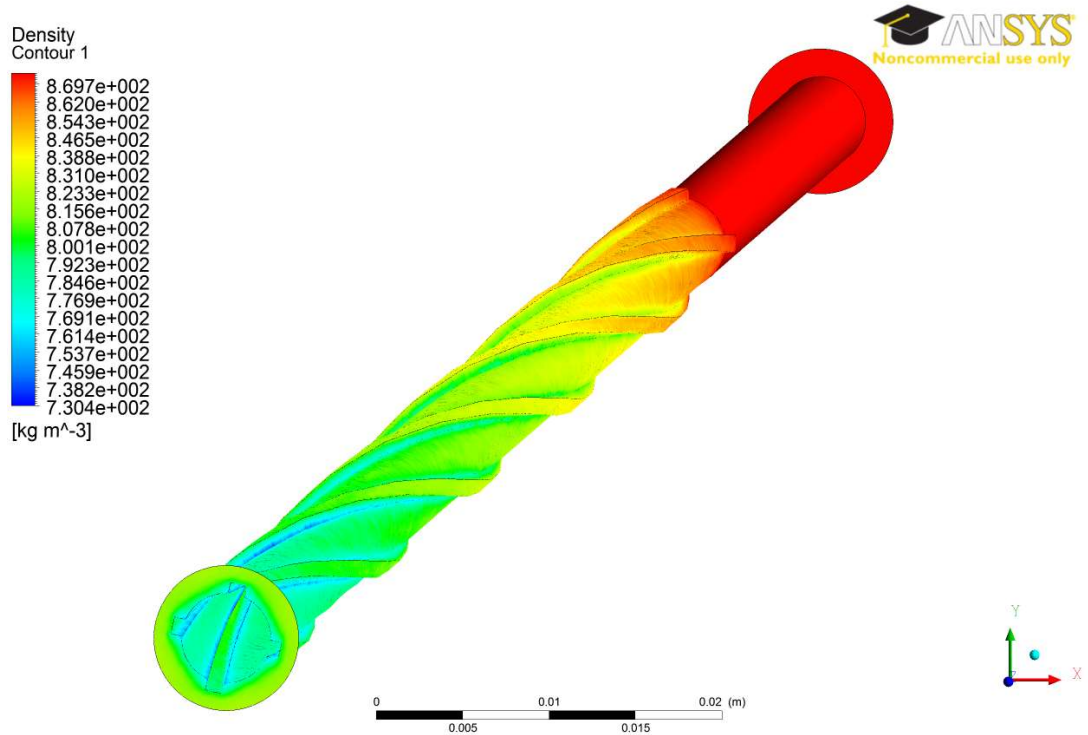


Figure 5-22: Density Contour for the Fluid at the Walls of the Annular Channel (SST Model, $P = 22.6$ MPa, $G = 2000$ kg/m²s, $q = 1.543$ MW/m²)

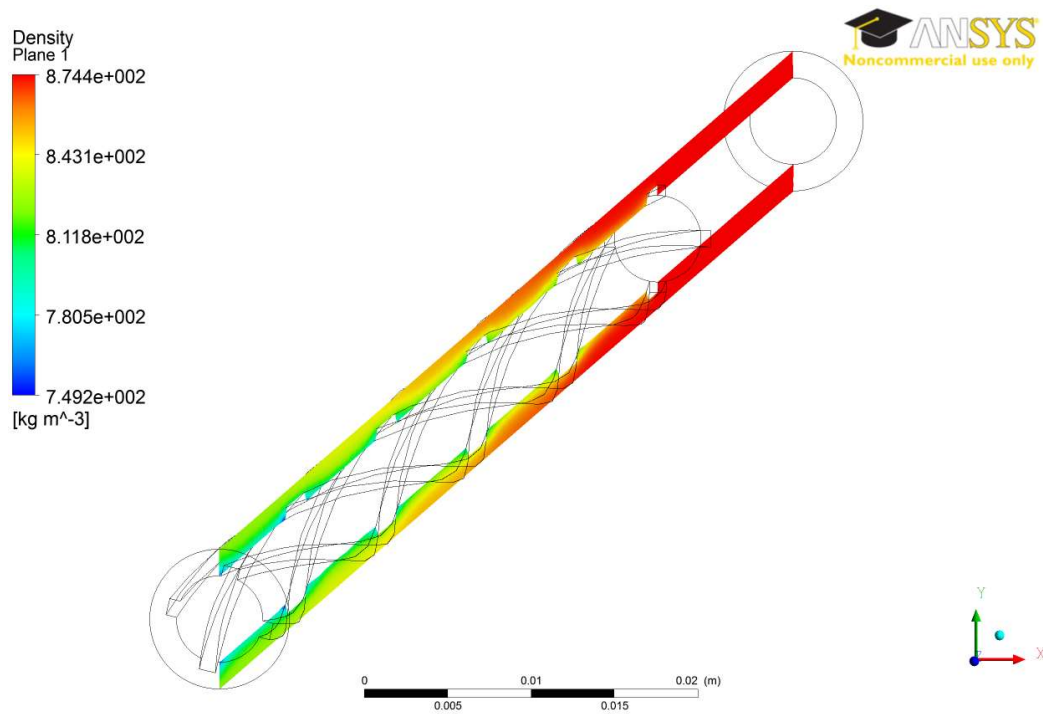


Figure 5-23: Density Contour for the Fluid at a longitudinal Cross Section in the Annular Channel (SST Model, $P = 22.6$ MPa, $G = 2000$ kg/m²s, $q = 1.543$ MW/m²)

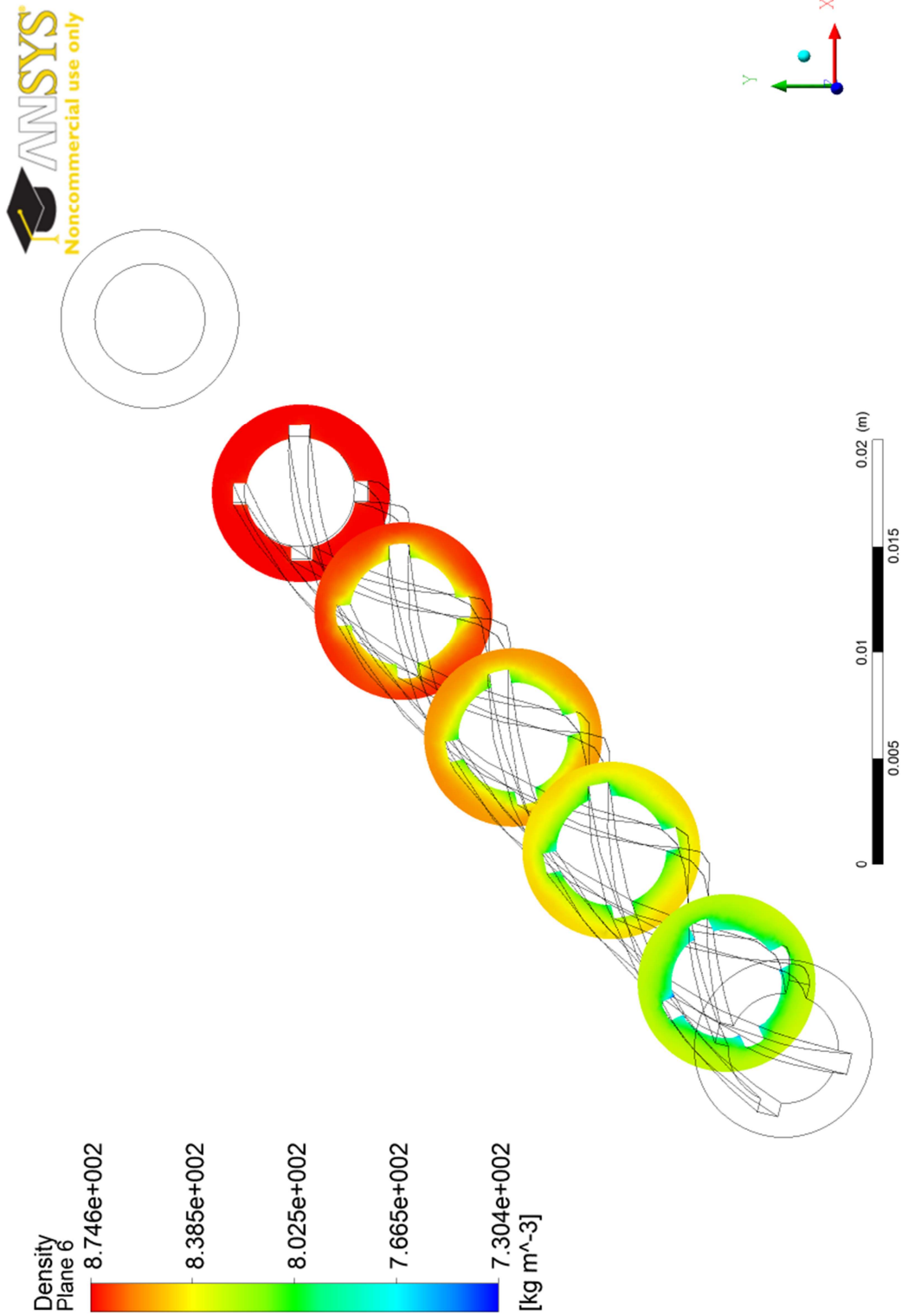


Figure 5-24: Density Contour for the Fluid at Various Cross Sections in the Annular Channel (SST Model, $P = 22.6$ MPa, $G = 2000$ kg/m²s, $q = 1.543$ MW/m²)

Specific Heat Capacity At Constant Pressure
Contour 1

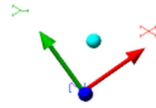
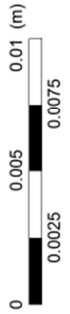
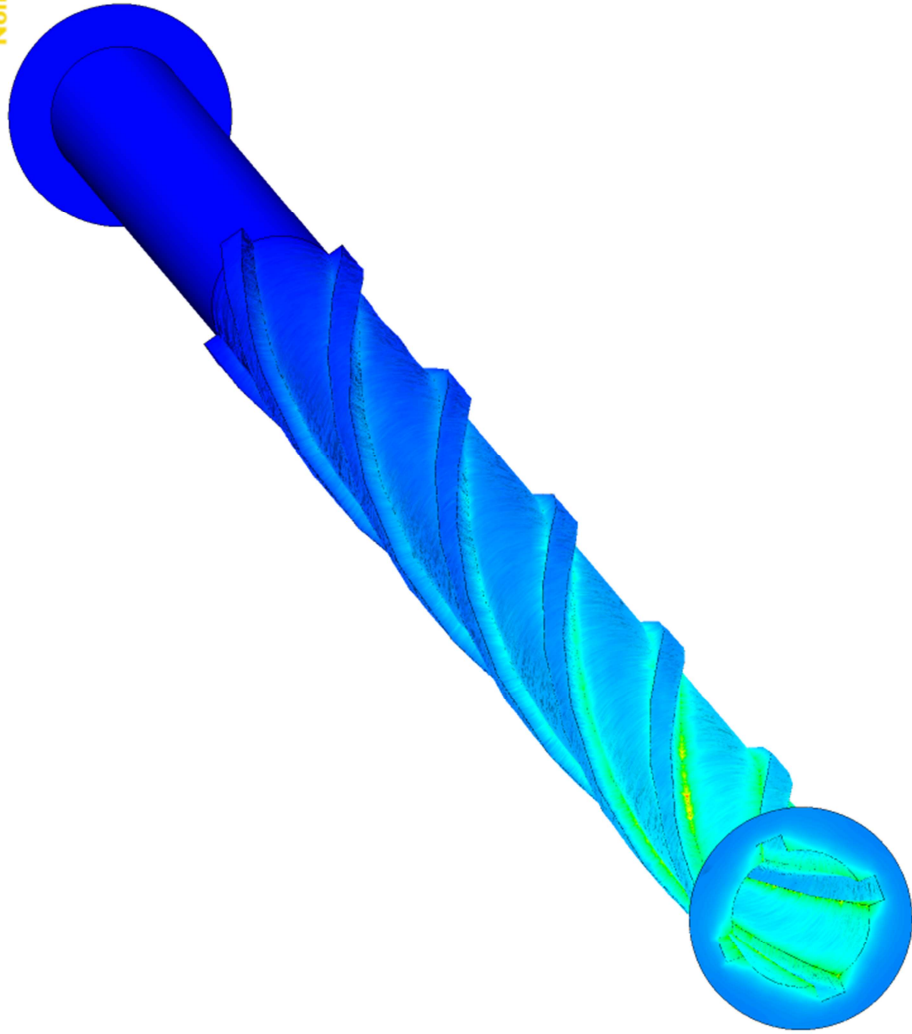
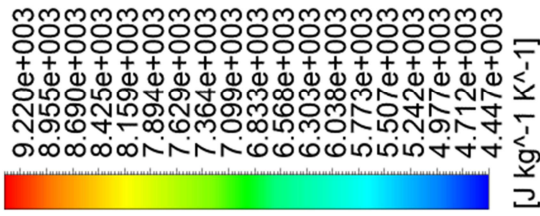


Figure 5-25: Specific Heat Contour for the Fluid at the Walls of the Annular Channel (SST Model, $P = 22.6 \text{ MPa}$, $G = 2000 \text{ kg/m}^2\text{s}$, $q = 1.543 \text{ MW/m}^2$)

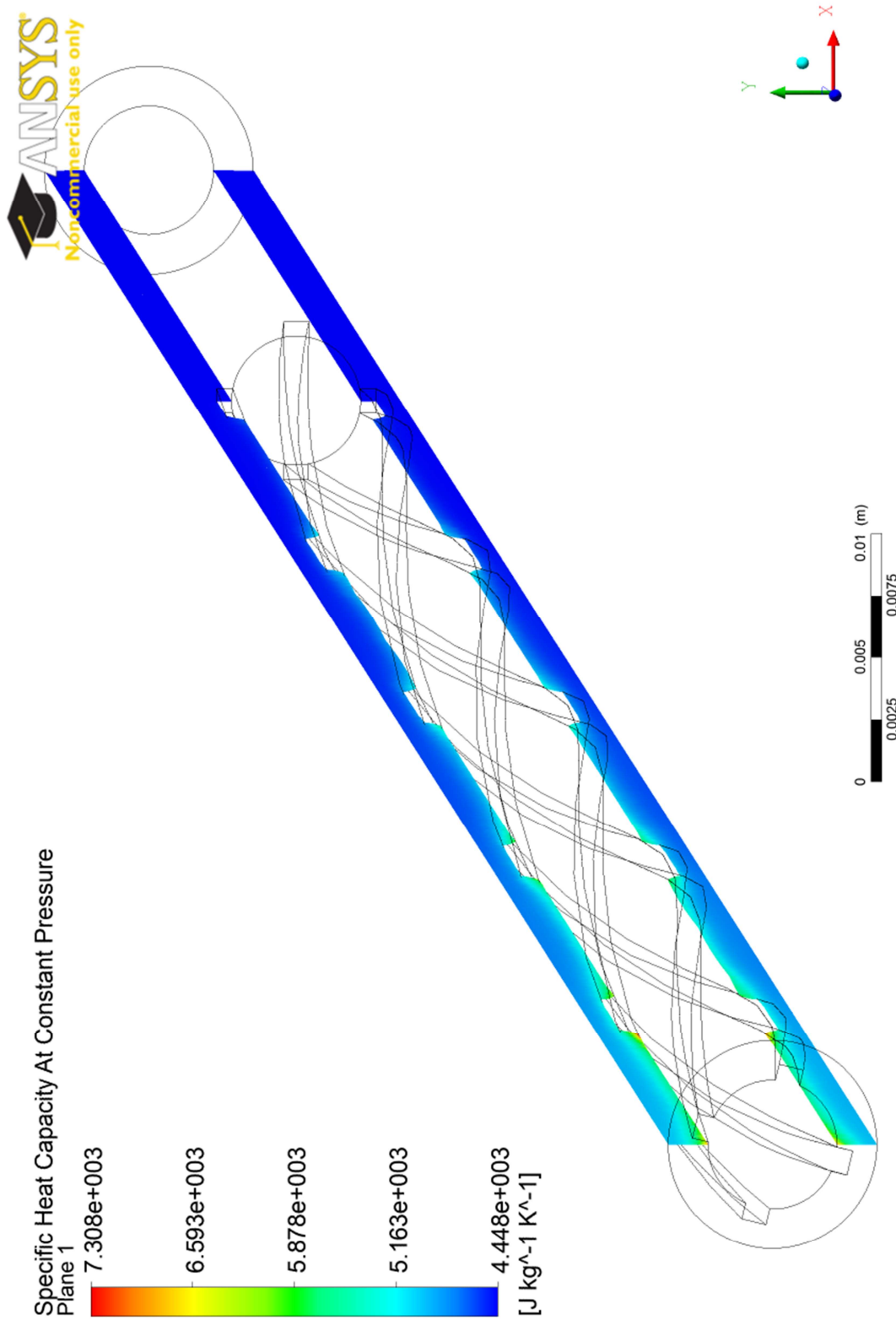


Figure 5-26: Specific Heat Contour for the Fluid at a Longitudinal Cross Section (SST Model, $P = 22.6 \text{ MPa}$, $G = 2000 \text{ kg/m}^2\text{s}$, $q = 1.543 \text{ MW/m}^2$)

5.2 Case 1 - SST Model, 3D Blocking Mesh

As mentioned earlier in the methodology section, the free mesh had to be used for the analysis of the annular channel with helical fins, due to the complexity of the geometry that resulted in a bad quality mesh when using 3D blocking techniques to generate a mesh for the flow domain. The quality of the mesh, influenced by the helicity of the geometry and the difficulty of creating small cells close to the heated surfaces, meant further complications in the FLUENT solver.

The issues with the mesh (through the mesh check in FLUENT) are the existence of negative volume cells, left handed cells, and high aspect ratio cells (creating problems in wall distance calculations). In the solver, there are options to further repair the geometry, and attempt to fix the cells with high skewness or the Y^+ values that may cause convergence issues. However, often these algorithms do not result in a good quality mesh, and the best option is to solve the issue from the mesh generator itself.

These issues caused convergence problems, where the solutions would not converge to the desired residual values of 10^{-4} and did not, in many cases, even reach 10^{-2} . The result of that convergence level is unrealistic profiles for the temperature at the walls, as shown in Figure 5-27. The simulations, for both the SST and RKE models, and for all cases of varying heat fluxes, show oscillations in the wall temperatures as a result of poor convergence.

When looking at the radial contours in CFD Post, it was then apparent that the mesh was physically distorted as it was read by the solver (the distortions did not appear in ICEM CFD). Figure 5-28 and Figure 5-29 show the temperature contours radially in the flow domain, and Figure 5-30 and Figure 5-31 show close-ups of the contours with a mesh overlay, to show the distortion created by the helical lines that guide the 3D blocking to create the mesh.

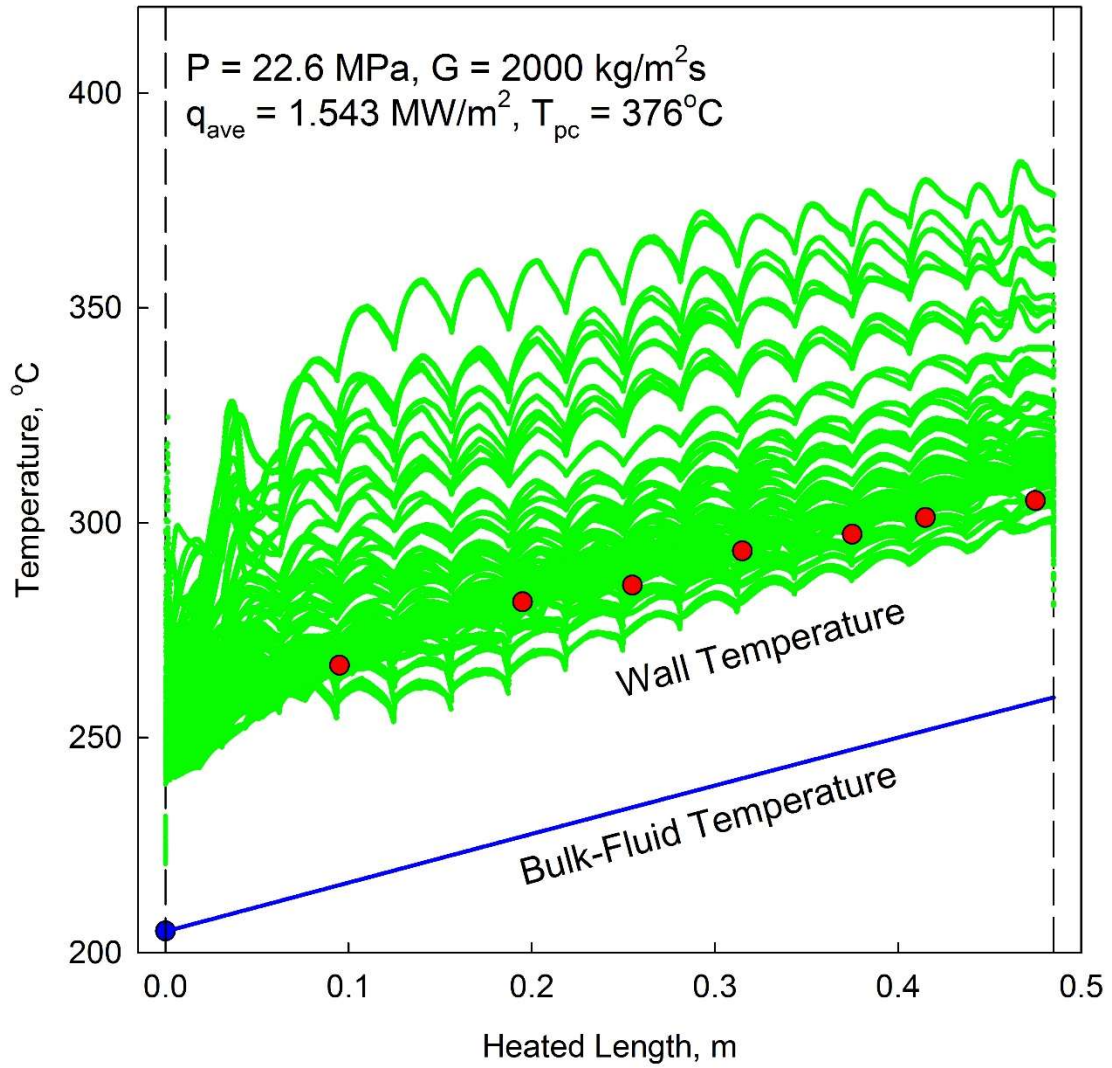


Figure 5-27: Simulated Temperatures for the Fluid at All Heated Walls of the Annular Channel (SST Model, 3D Blocking Mesh)

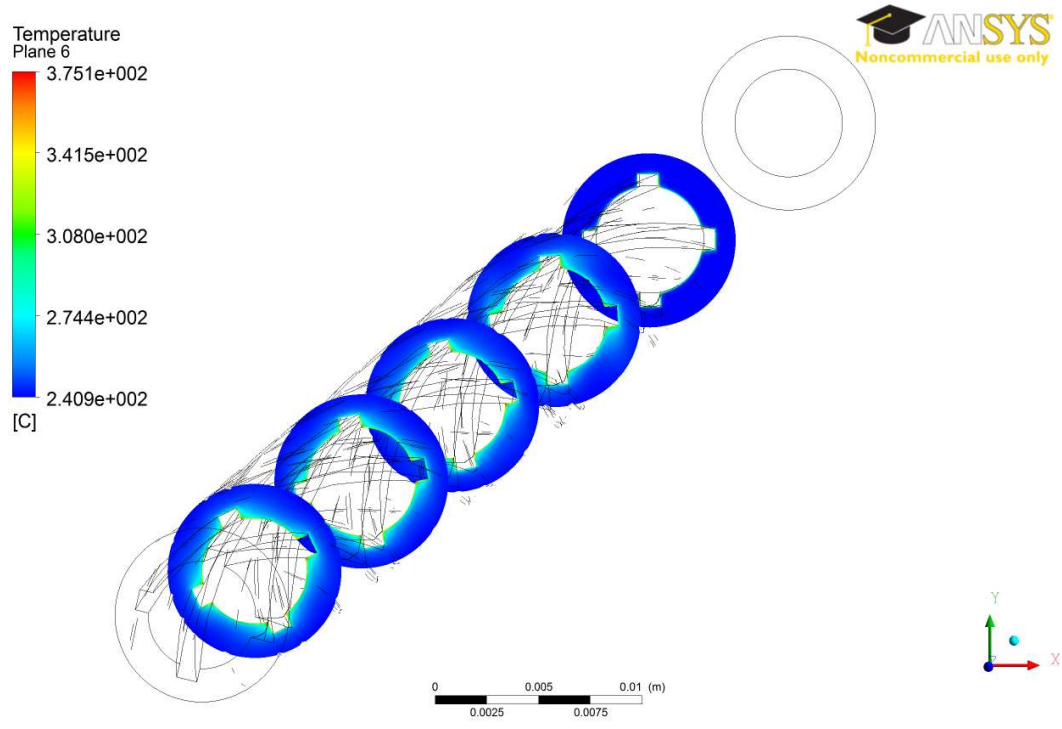


Figure 5-28: Temperature Contour for the Fluid at Various Cross Sections in the Annular Channel (SST Model, $P = 22.6$ MPa, $G = 2000$ kg/m²s, $q = 1.543$ MW/m²)

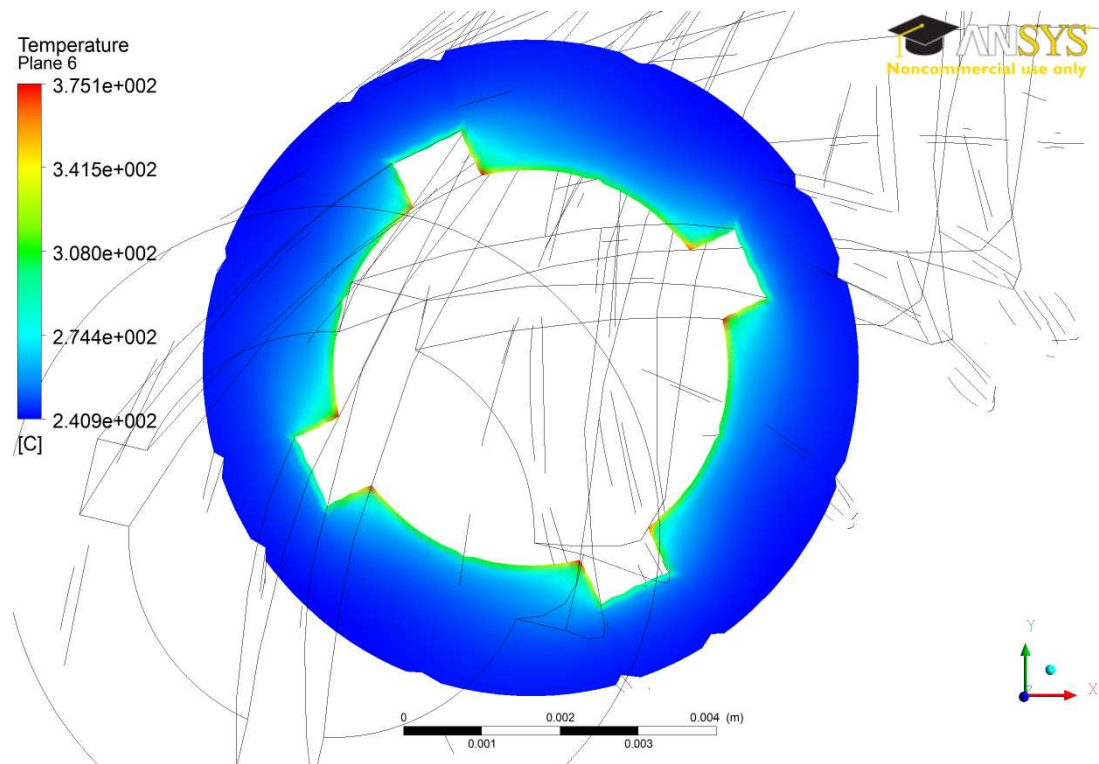


Figure 5-29: Temperature Contour for the Fluid at a Radial Cross Section in the Annular Channel (SST Model, $P = 22.6$ MPa, $G = 2000$ kg/m²s, $q = 1.543$ MW/m²)

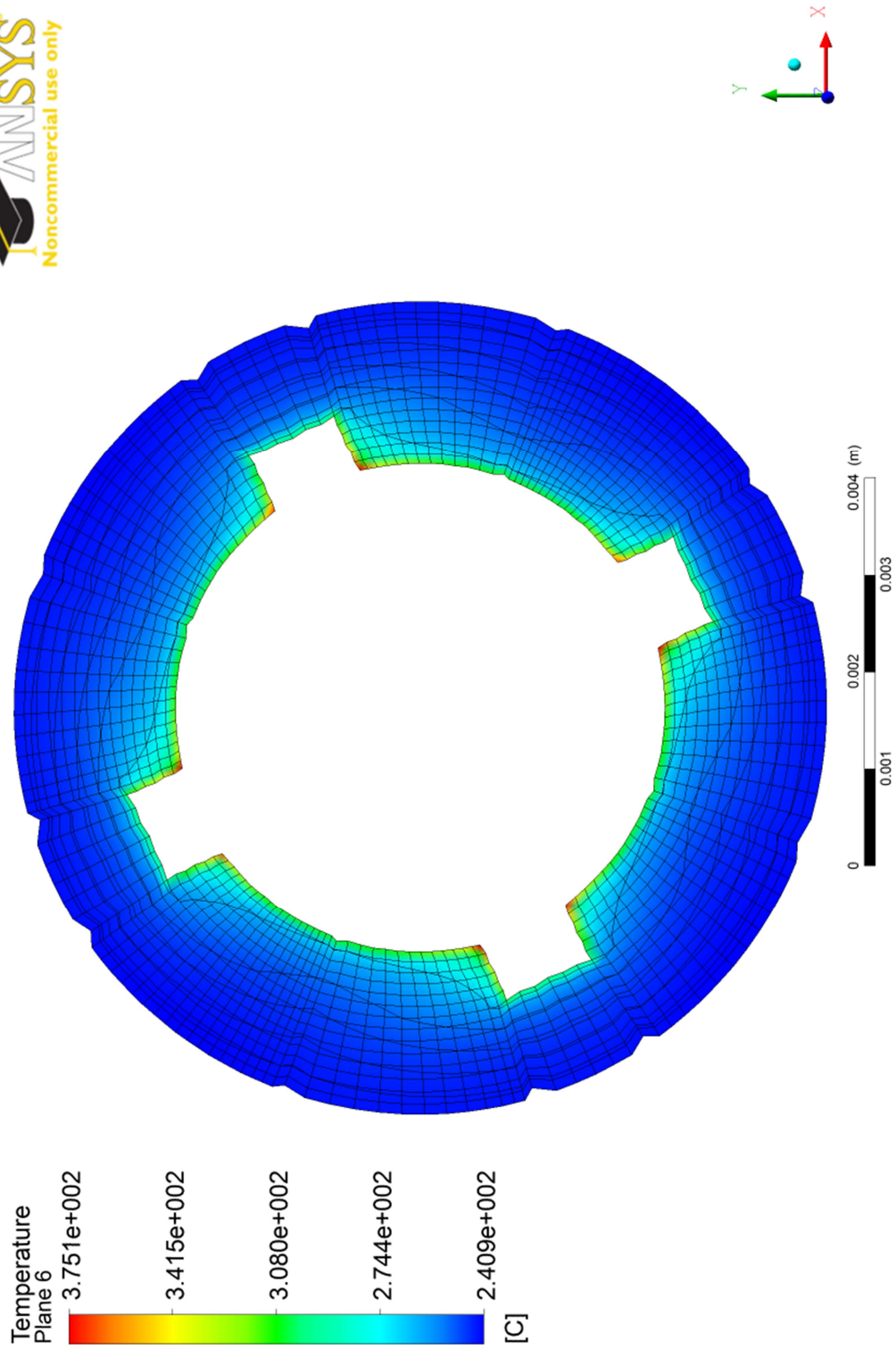


Figure 5-30: Temperature Contour for the Fluid at a Radial Cross Section in the Annular Channel (SST Model, $P = 22.6$ MPa, $G = 2000$ kg/m²s, $q = 1.543$ MW/m²)

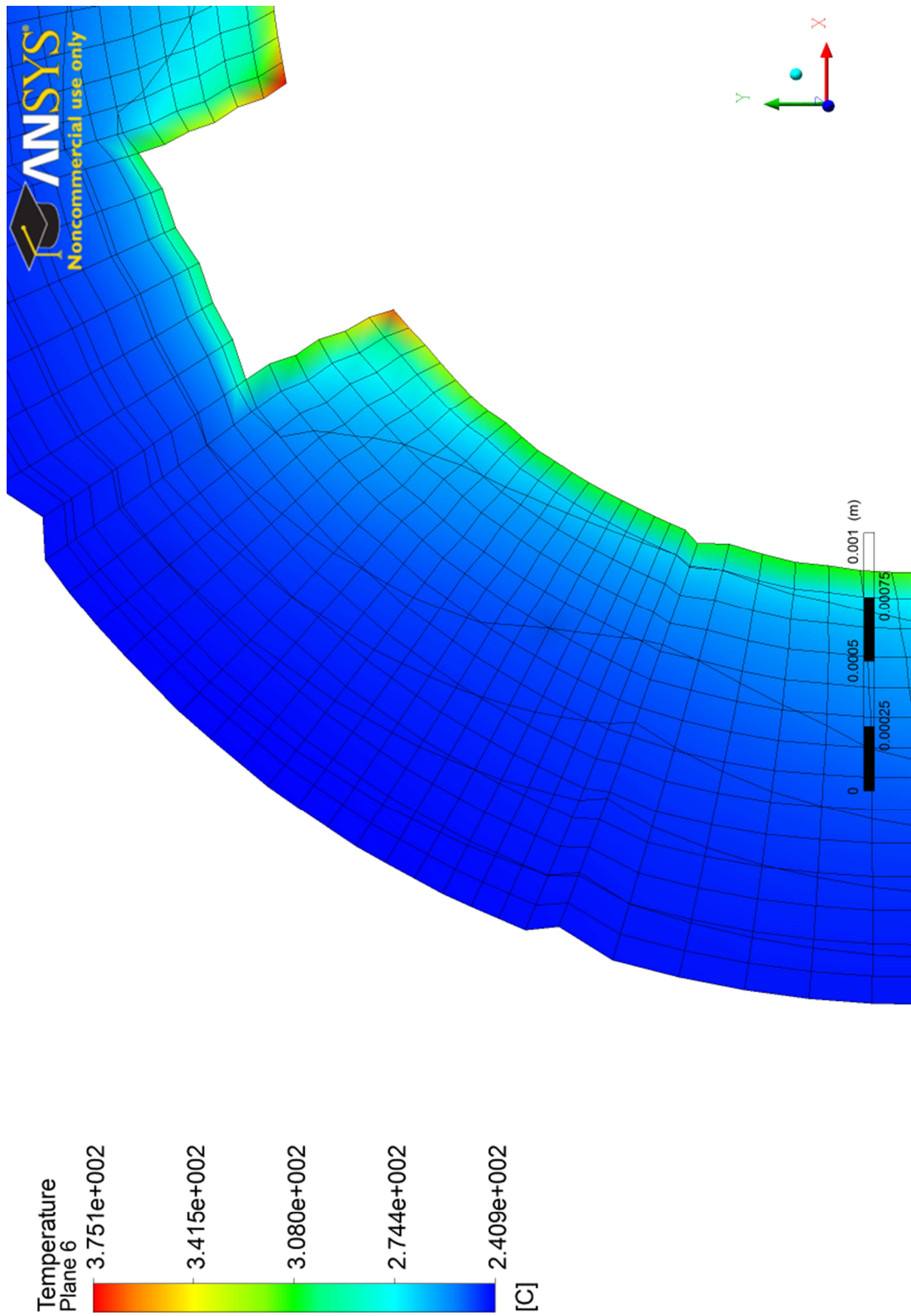


Figure 5-31: Close-up of Temperature Contour for the Fluid at a Radial Cross Section in the Annular Channel (SST Model, $P = 22.6$ MPa, $G = 2000$ kg/m²s, $q = 1.543$ MW/m²)

5.3 Case 1 - RKE Model, Free Mesh

The same case is simulated again using the RKE model, and the free mesh. The results are comparable to those of the SST model, with the exception of a slightly higher wall temperature prediction. However the trends and the temperature spread is similar to the SST model results as shown in Figure 5-32. The average simulated temperature is higher than the experimental wall temperature by about 10%, which is higher than the SST model prediction. The highest temperature predicted by the RKE model is $\sim 35^{\circ}\text{C}$ (11%) higher than that of the SST model, shown by the contours in Figure 5-33 and Figure 5-34. Conversely, the bulk fluid temperature is lower due to the reduction in the heat transfer from the wall. The radial temperature contours are shown with a mesh overlay in Figure 5-35 and a close-up contour in Figure 5-36.

The turbulent kinetic energy contours are shown in Figure 5-37 and Figure 5-38, where it can be seen that the turbulent energy is predicted to be much lower than that by the SST model. The energy dissipates quickly away from the walls and reaches several orders of magnitude lower than the SST values for the bulk fluid. By examining the turbulence intensity in Figure 5-39, the same can be observed, where the majority of the fluid has turbulence levels 3 orders of magnitude lower than that predicted by the SST model. This effectively places the flow in the laminar region.

As the SST model behaves as a $k-\omega$ near the wall and as $k-\epsilon$ away from the wall region, it is in theory better suited for modelling this type of flow, especially when the mesh cannot be refined to resolve the near wall region, as in the case of the free mesh used for these simulations.

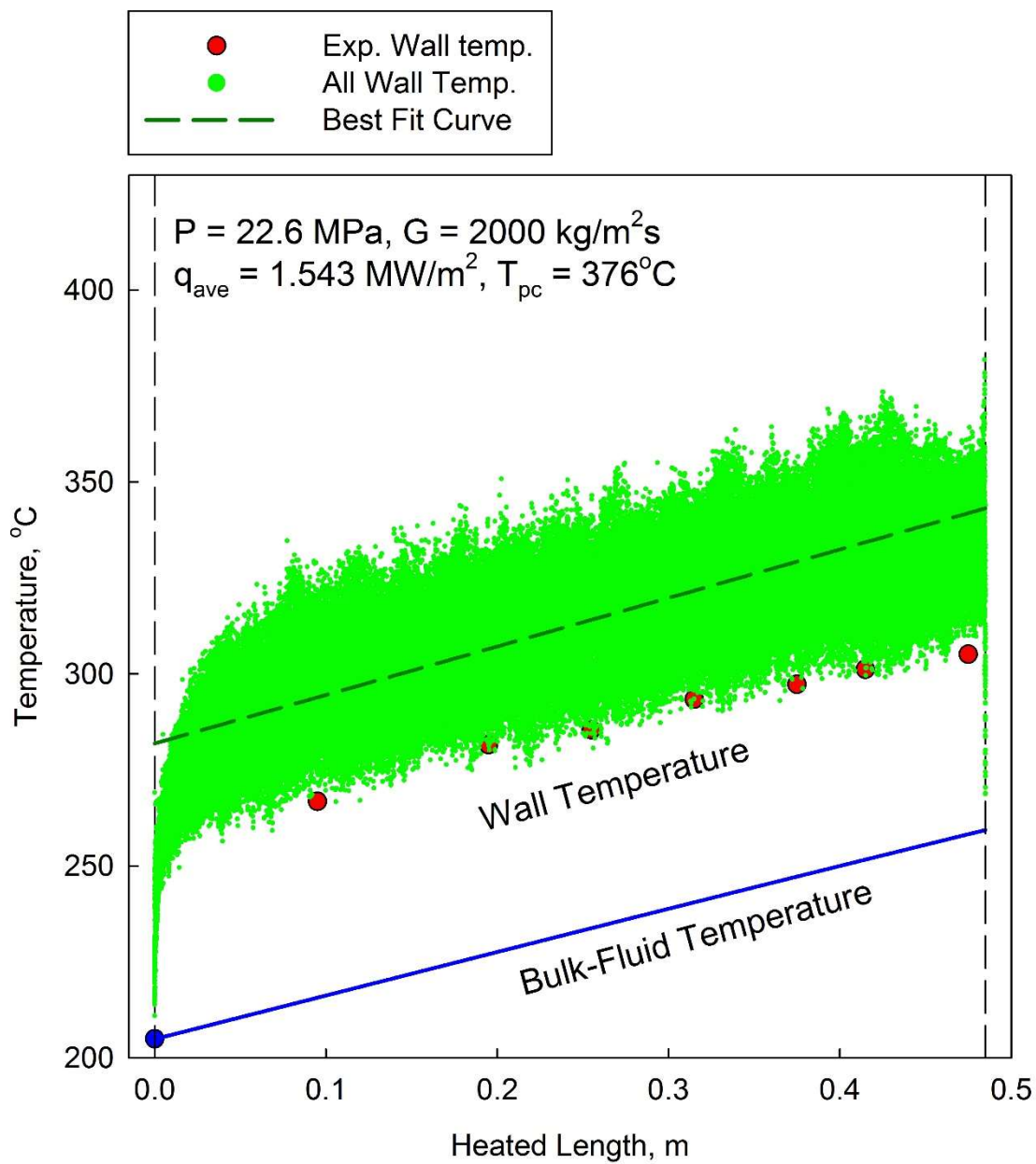


Figure 5-32: Simulated Temperatures for the Fluid at All Heated Walls of the Annular Channel (RKE Model), and the Average Temperature Profile Using Curve Fitting

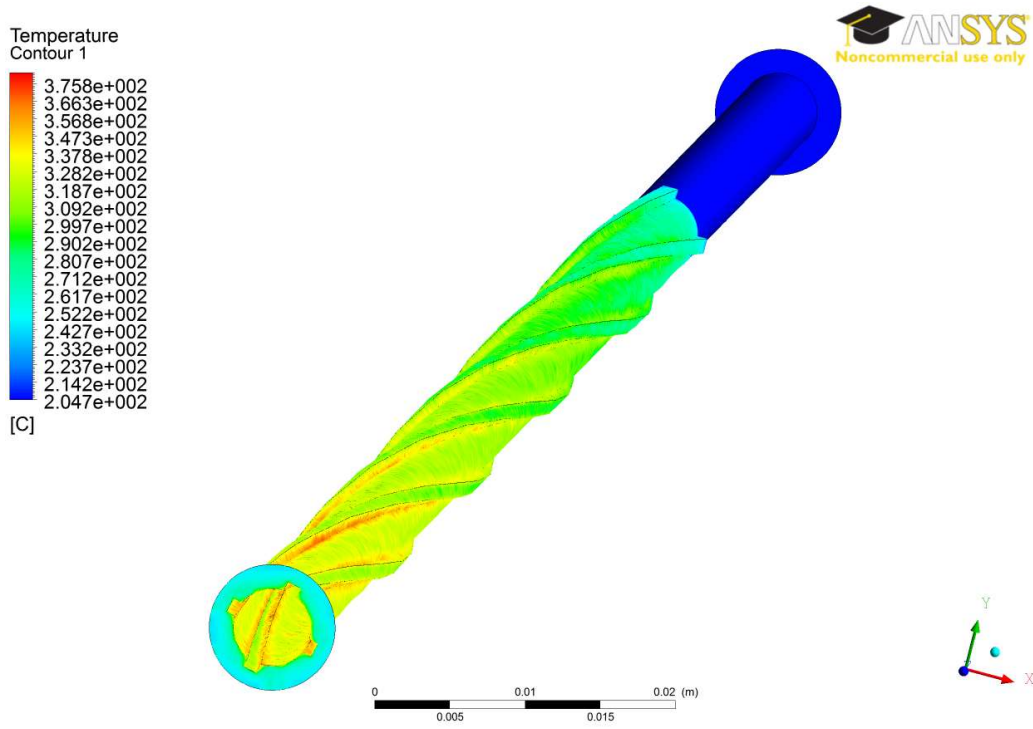


Figure 5-33: Temperature Contour for the Fluid at the Walls of the Annular Channel (RKE Model, $P = 22.6 \text{ MPa}$, $G = 2000 \text{ kg/m}^2\text{s}$, $q = 1.543 \text{ MW/m}^2$)

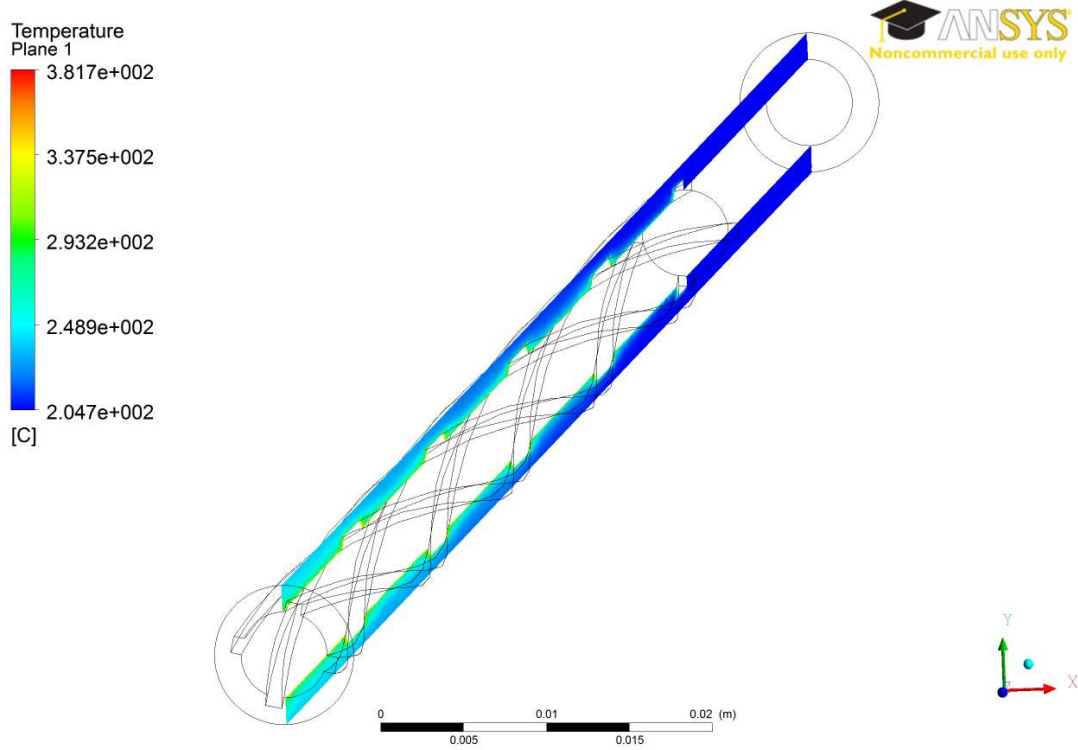


Figure 5-34: Temperature Contour for the Fluid at a Longitudinal Cross Section in the Annular Channel (RKE Model, $P = 22.6 \text{ MPa}$, $G = 2000 \text{ kg/m}^2\text{s}$, $q = 1.543 \text{ MW/m}^2$)

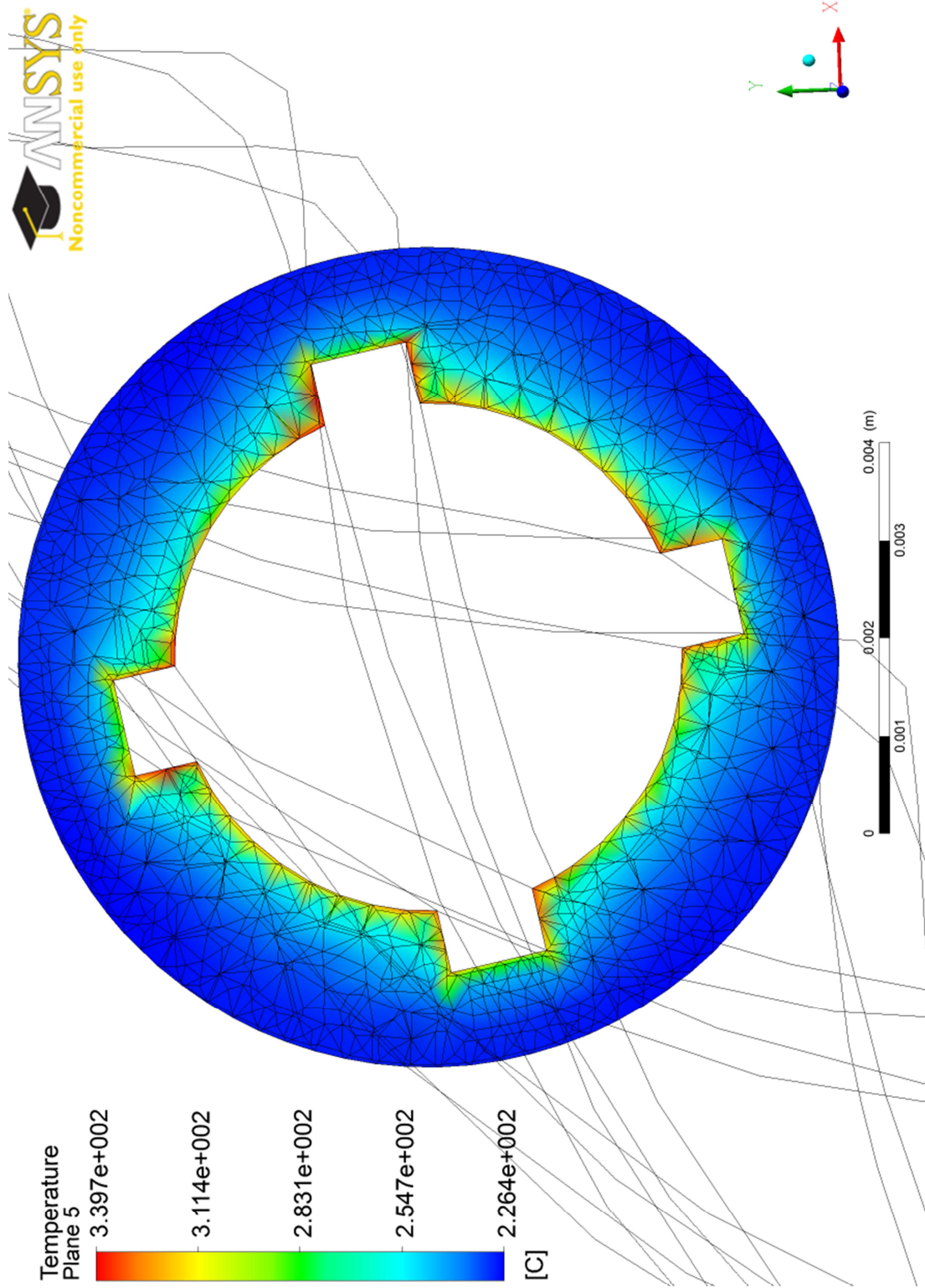


Figure 5-35: Temperature Contour with Mesh Lines at a Radial Cross Section in the Annular Channel (RKE Model, $P = 22.6 \text{ MPa}$, $G = 2000 \text{ kg/m}^2\text{s}$, $q = 1.543 \text{ MW/m}^2$)

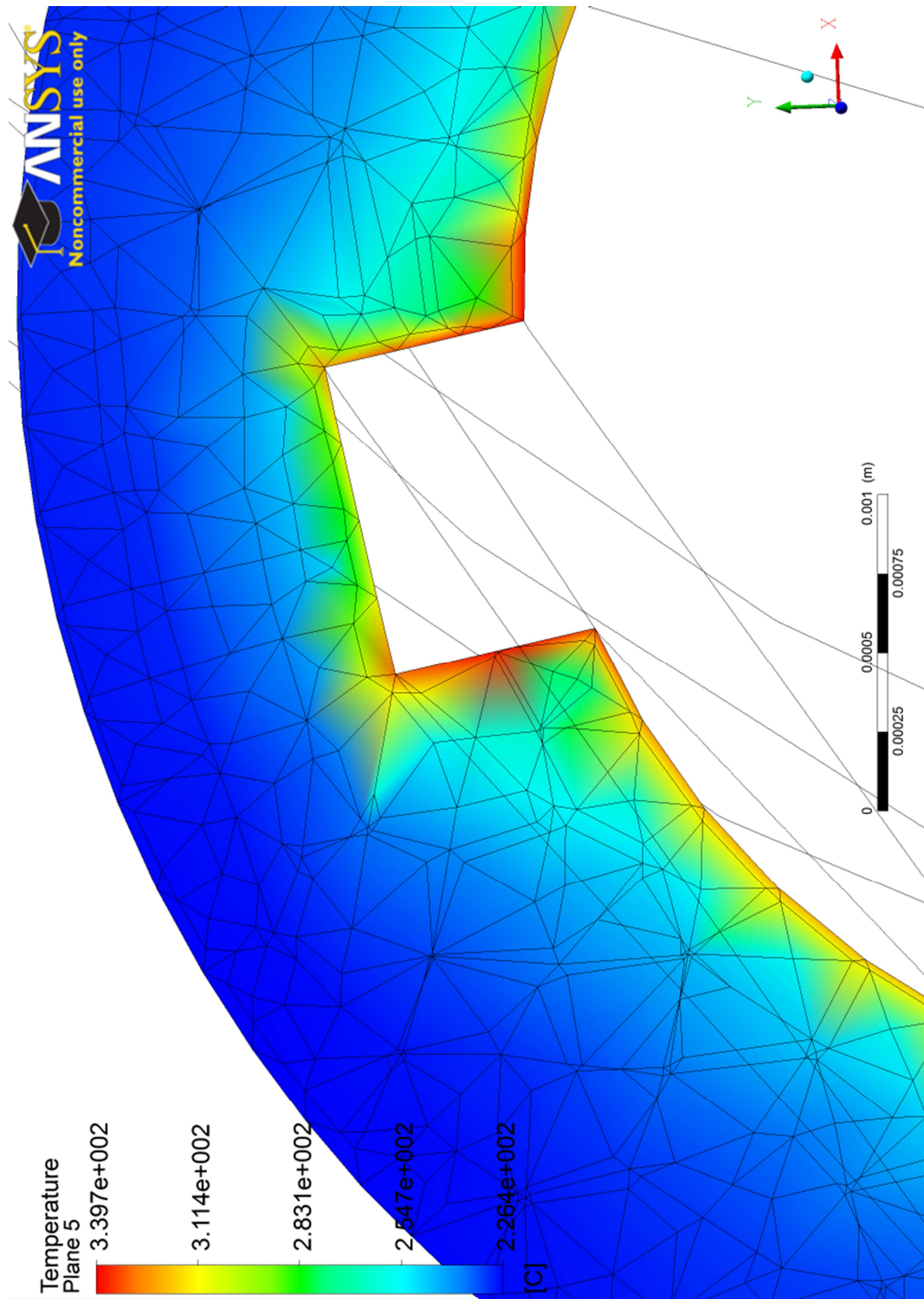


Figure 5-36: Close-up of Temperature Contour at a Radial Cross Section in the Annular Channel (RKE Model, $P = 22.6$ MPa, $G = 2000$ kg/m²s, $q = 1.543$ MW/m²)

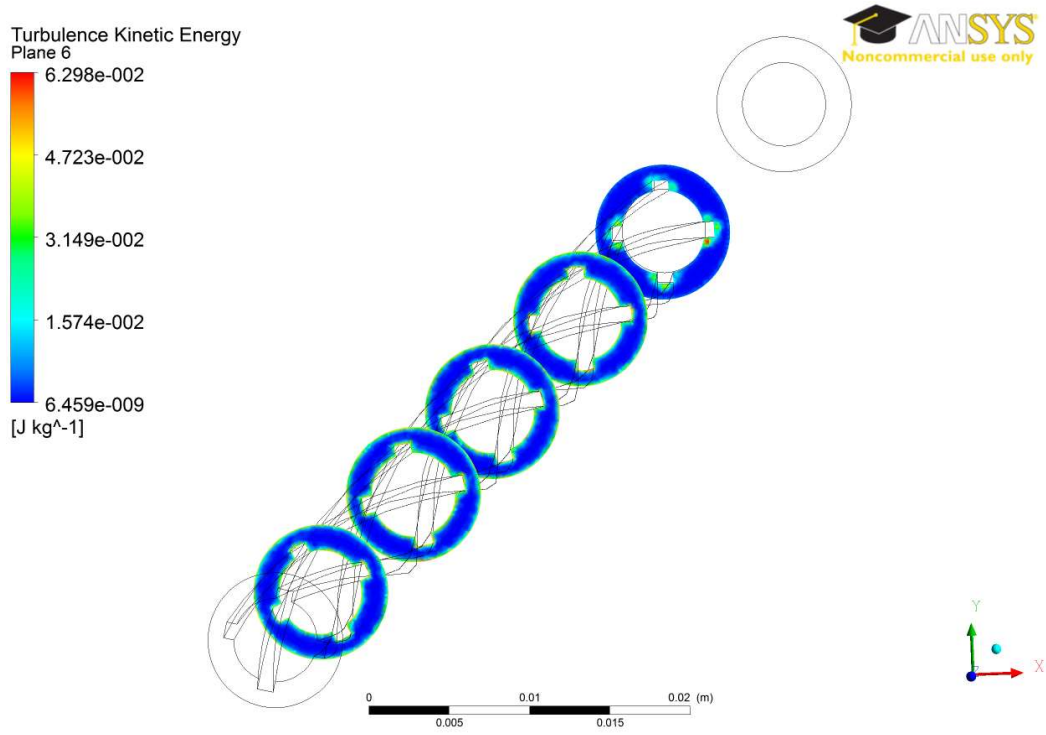


Figure 5-37: Turbulent Kinetic Energy Contour at Various Radial Cross Sections in the Annular Channel (RKE Model, $P = 22.6$ MPa, $G = 2000$ kg/m²s, $q = 1.543$ MW/m²)

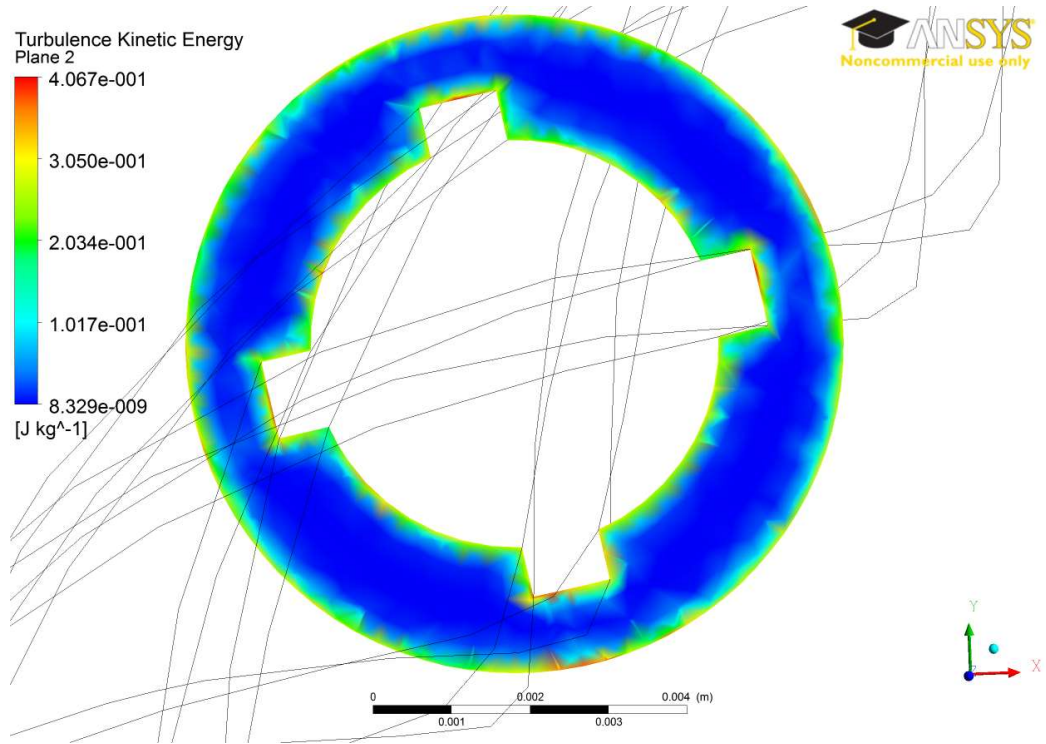


Figure 5-38: Turbulent Kinetic Energy Contour at a Radial Cross Section in the Annular Channel (RKE Model, $P = 22.6$ MPa, $G = 2000$ kg/m²s, $q = 1.543$ MW/m²)

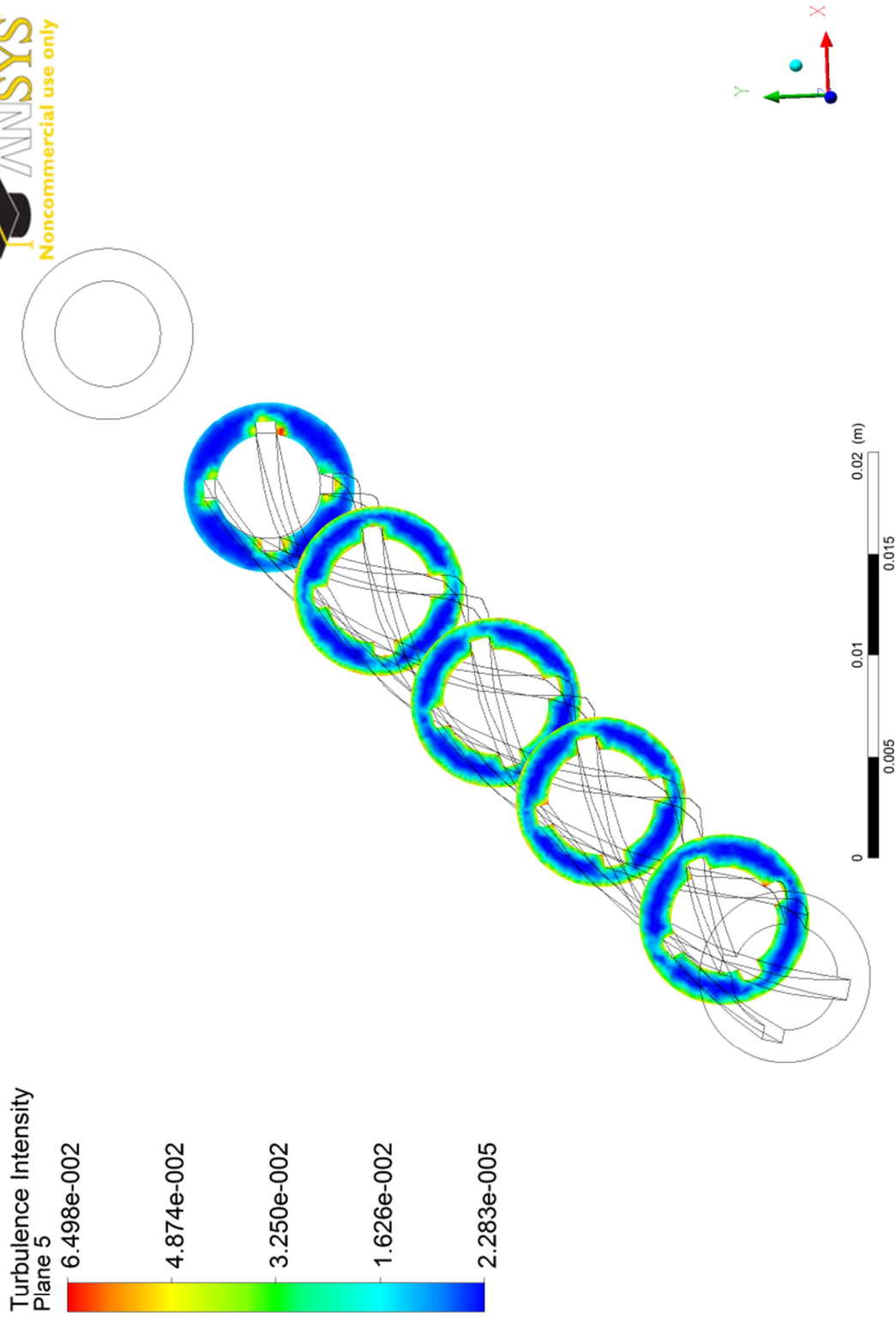


Figure 5-39: Turbulence Intensity Contour at Various Radial Cross Sections in the Annular Channel (RKE Model, $P = 22.6$ MPa, $G = 2000$ kg/m²s, $q = 1.543$ MW/m²)

Velocity profiles are shown in Figure 5-40 as a longitudinal contour, while Figure 5-41 shows the radial distribution, and Figure 5-42 represents the velocity streamlines throughout the flow domain.

The maximum velocity achievable by the flow in the RKE model is higher than that of the SST model, however, as the contours show (and most visible in the velocity streamlines), most of the fluid has a lower velocity, and overall lower than that of the SST model

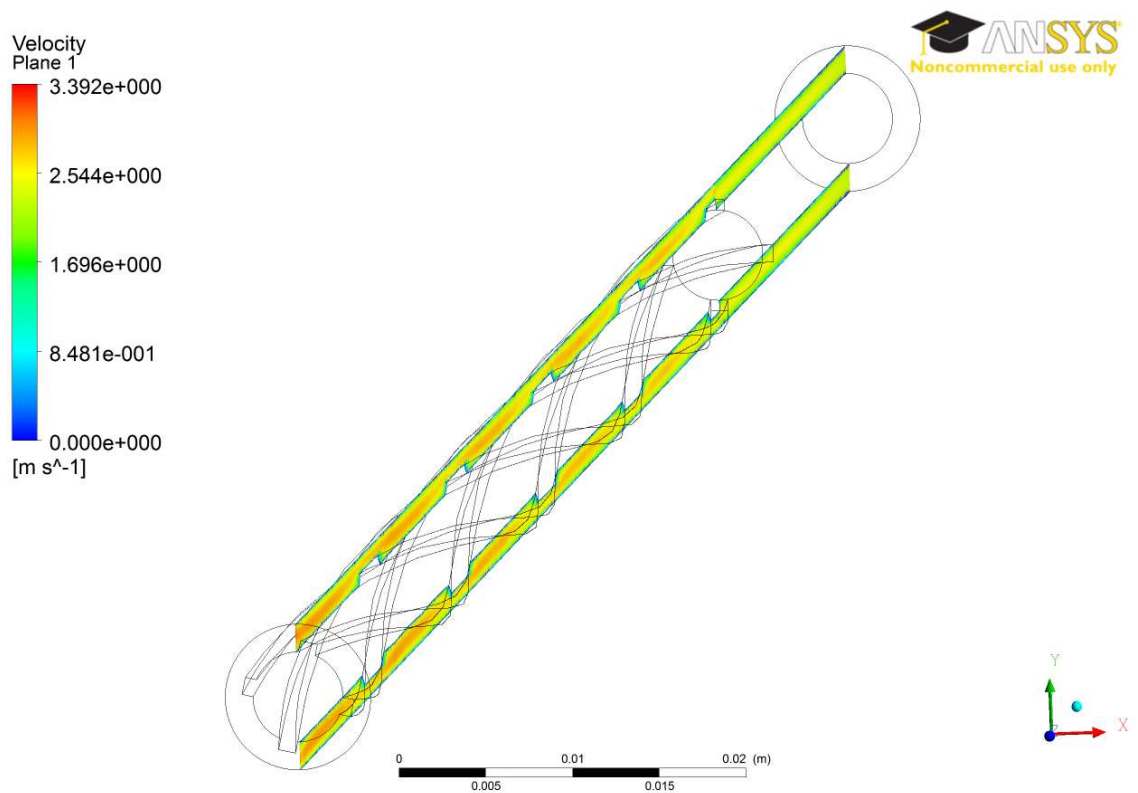


Figure 5-40: Velocity Contour at a Longitudinal Cross Sections in the Annular Channel (RKE Model, $P = 22.6$ MPa, $G = 2000$ kg/m²s, $q = 1.543$ MW/m²)

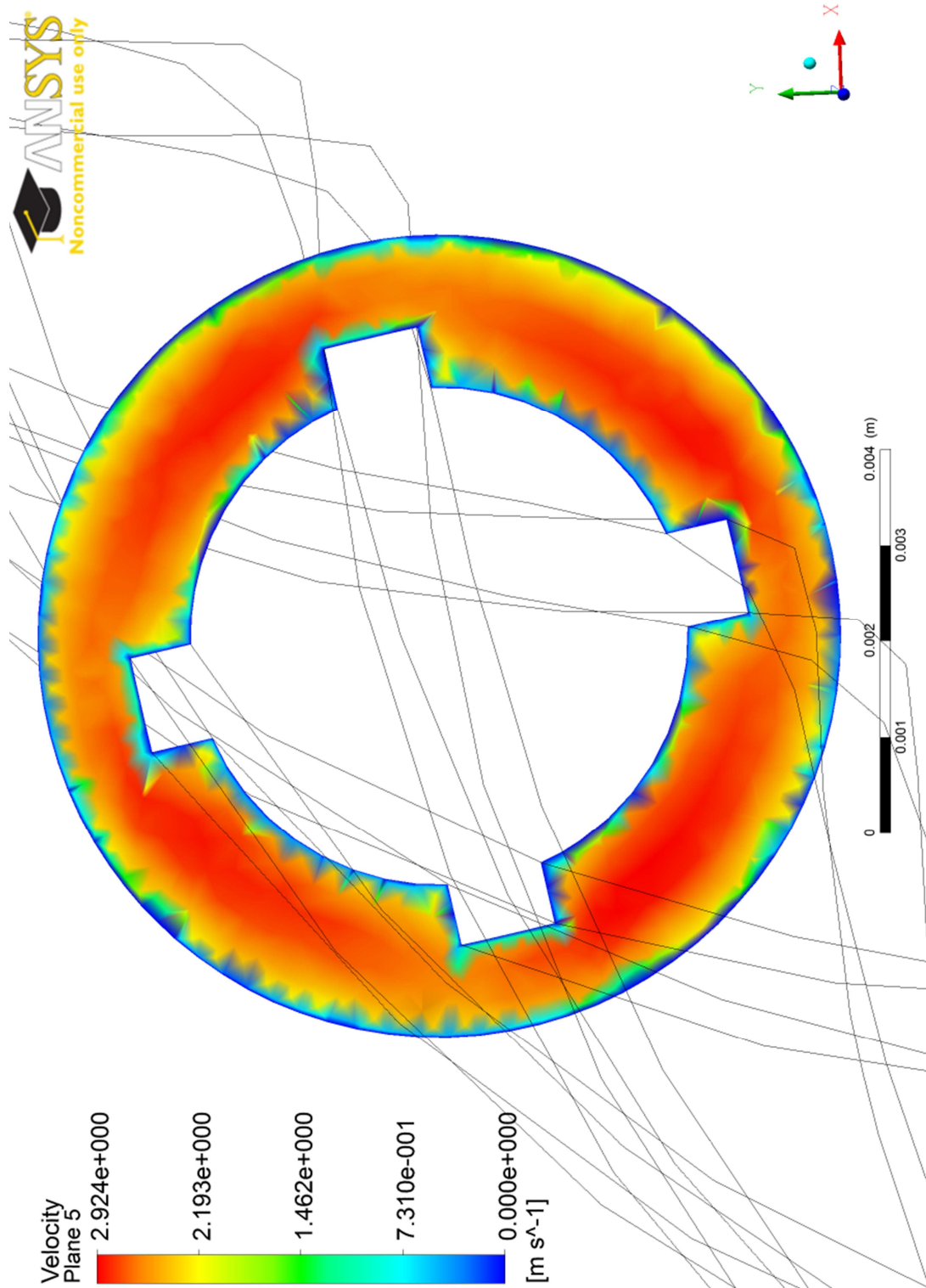


Figure 5-41: Velocity Contour at a Radial Cross Sections in the Annular Channel (RKE Model, $P = 22.6$ MPa, $G = 2000$ kg/m²s, $q = 1.543$ MW/m²)

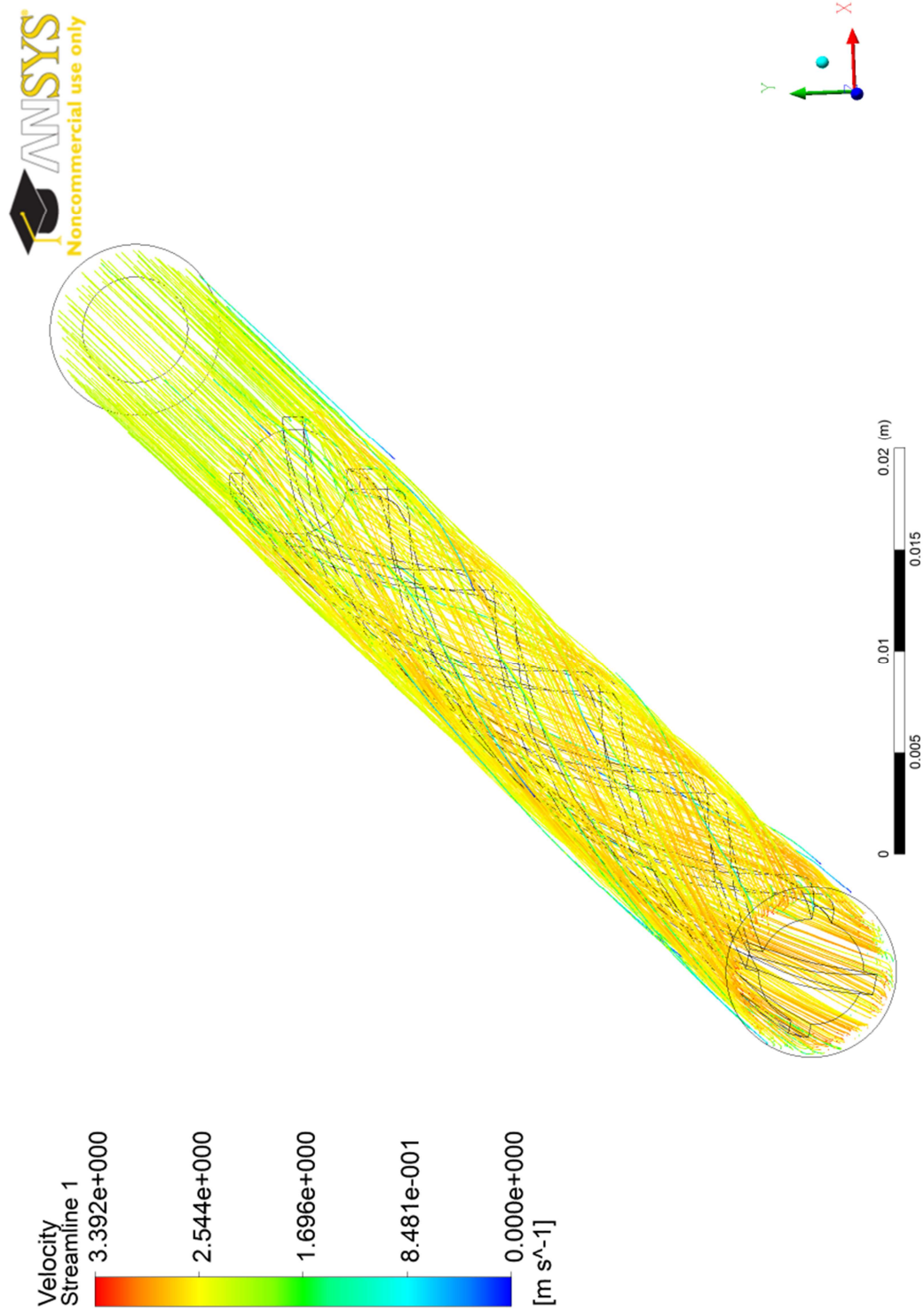


Figure 5-42: Velocity Streamlines for the Fluid in the Annular Channel (RKE Model, $P = 22.6 \text{ MPa}$, $G = 2000 \text{ kg/m}^2\text{s}$, $q = 1.543 \text{ MW/m}^2$)

5.4 Case 1 - Straight Fins, SST Model, Free Mesh

A case with straight fins instead of helical was simulated to study the impact of the helicity of the fins on the turbulence levels and the heat transfer in the fluid. The actual amount of energy imparted by the heating elements is roughly the same and the bulk fluid temperature rise is also quite similar. This is due to the fact that the heated length of the helical fins is only about half a millimeter more than the straight fins, as shown by the helix length equation (based on Pythagoras theorem):

$$L = N \times \sqrt{[P^2 + (\pi D)^2]} = 485.5 \text{ mm} \quad [5-1]$$

, where P is the pitch (400 mm), N is the number of turns (1.2125 turns in 485 mm) and D is the diameter of the helix (taken at the center of the fin, 5.8 mm).

The difference in heated length affects the total surface area of the base and the fins, however as shown in the calculation of the bulk-fluid temperature earlier in Table 3-8, the outlet temperature is only affected by 0.1-0.3°C in all cases.

As seen in Figure 5-43, the temperature distribution and the average temperature is nearly identical to that in the case with helical fins. Figure 5-44 and Figure 5-45 also show similar axial and radial distributions. Looking at the turbulent kinetic energy and the turbulence intensity in the fluid in Figure 5-46 and Figure 5-47, it is apparent that the helicity of the fins does not improve turbulence production and the range of turbulence intensity in both cases is ~3.3 - 7.5%.

Velocity contours in Figure 5-48 and streamlines in Figure 5-49 show an increase in velocity in the straight fins case by less than 1%, further confirming the similarities between the two geometries. These results were not surprising, as the helicity of the fins only drives in the fluid along a different path (shown by the velocity streams), and without a perturbation in the geometry (area changes along the heated length), there will be no additional turbulence introduced to the fluid.

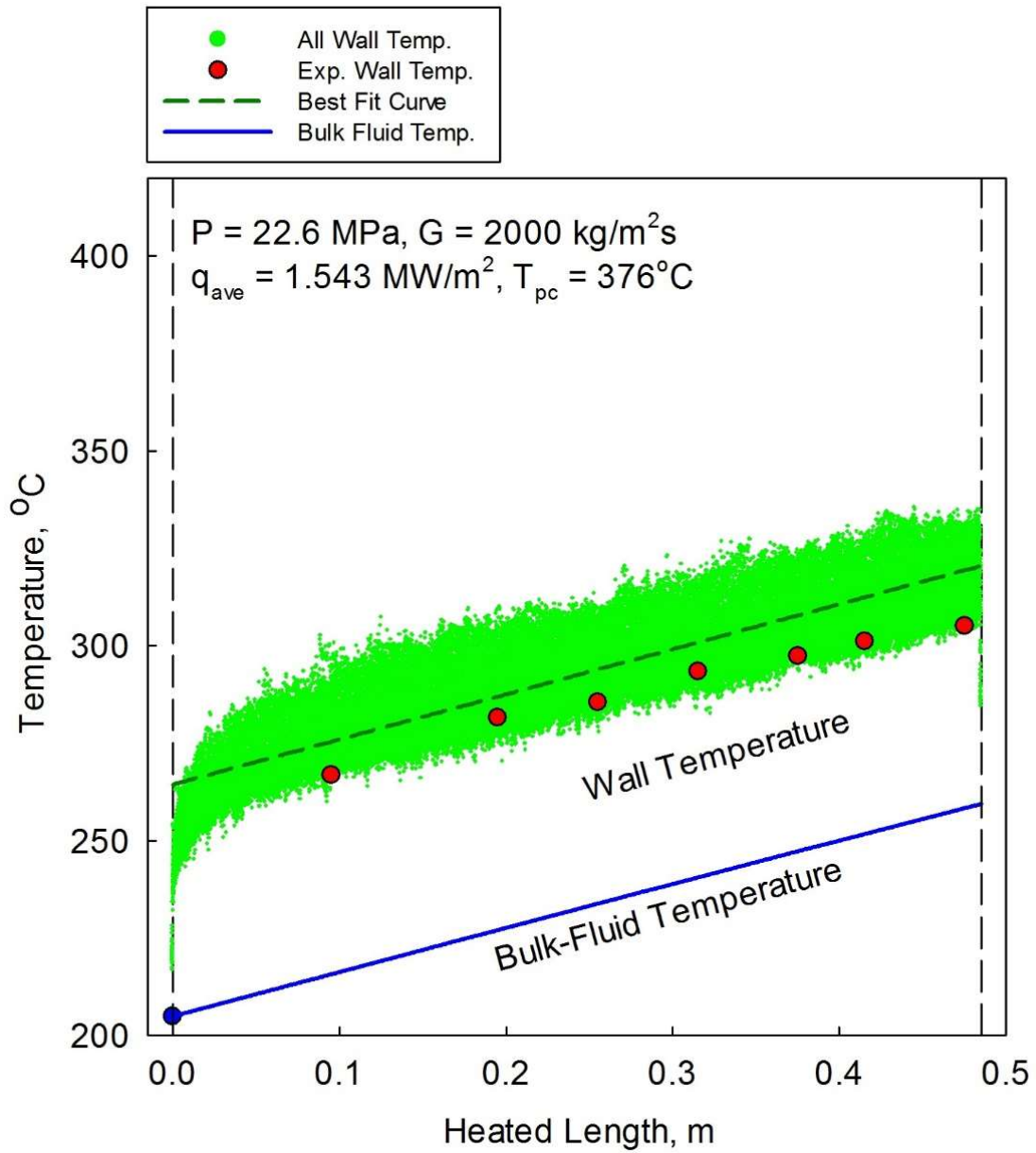


Figure 5-43: Simulated temperature for the fluid at all heated walls of the annular channel with straight fins (SST model), and the average temperature profile using curve fitting

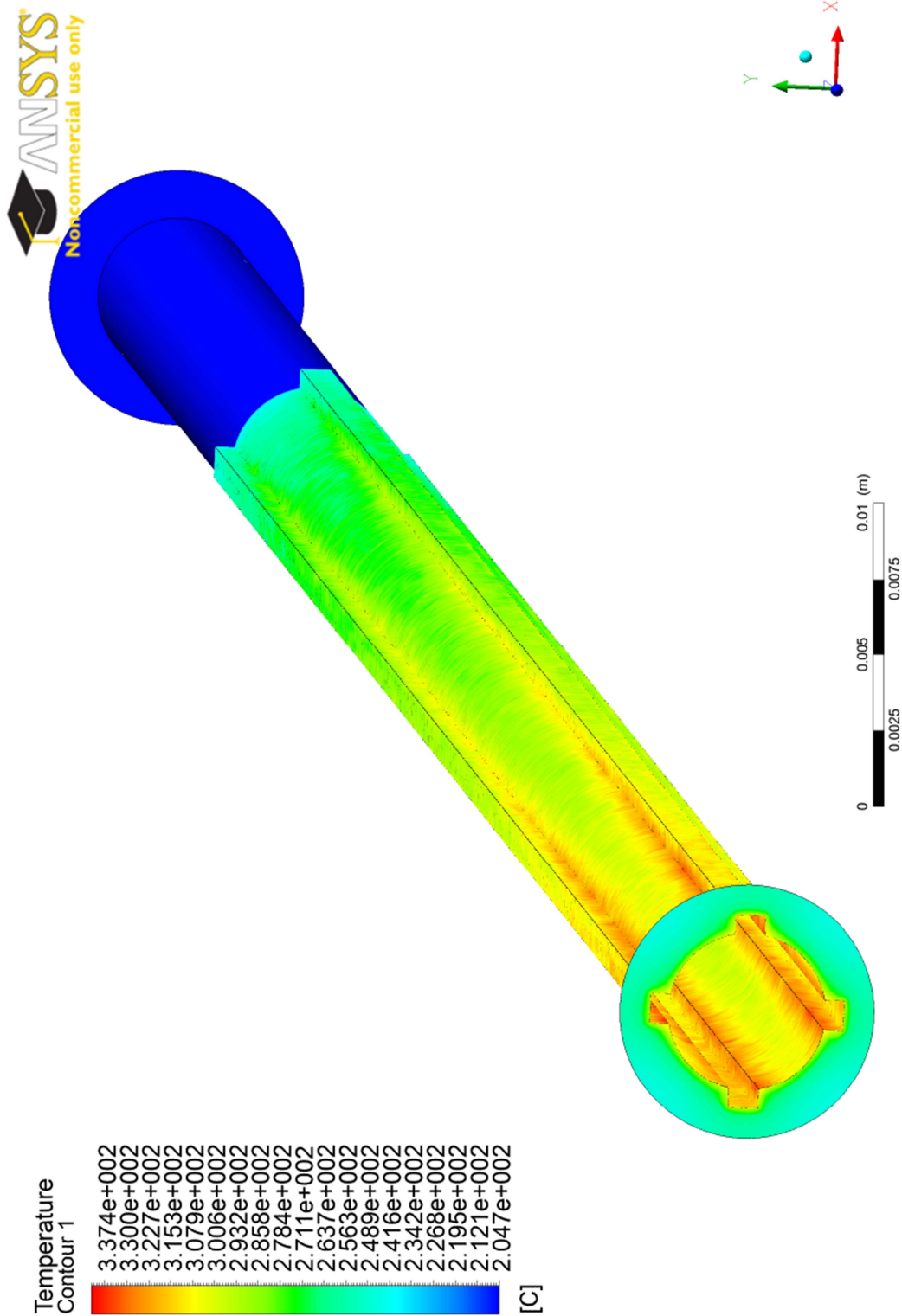


Figure 5-44: Temperature Contour for the Fluid at the Walls of the Annular Channel with Straight Fins (SST Model, $P = 22.6 \text{ MPa}$, $G = 2000 \text{ kg/m}^2\text{s}$, $q = 1.543 \text{ MW/m}^2$)

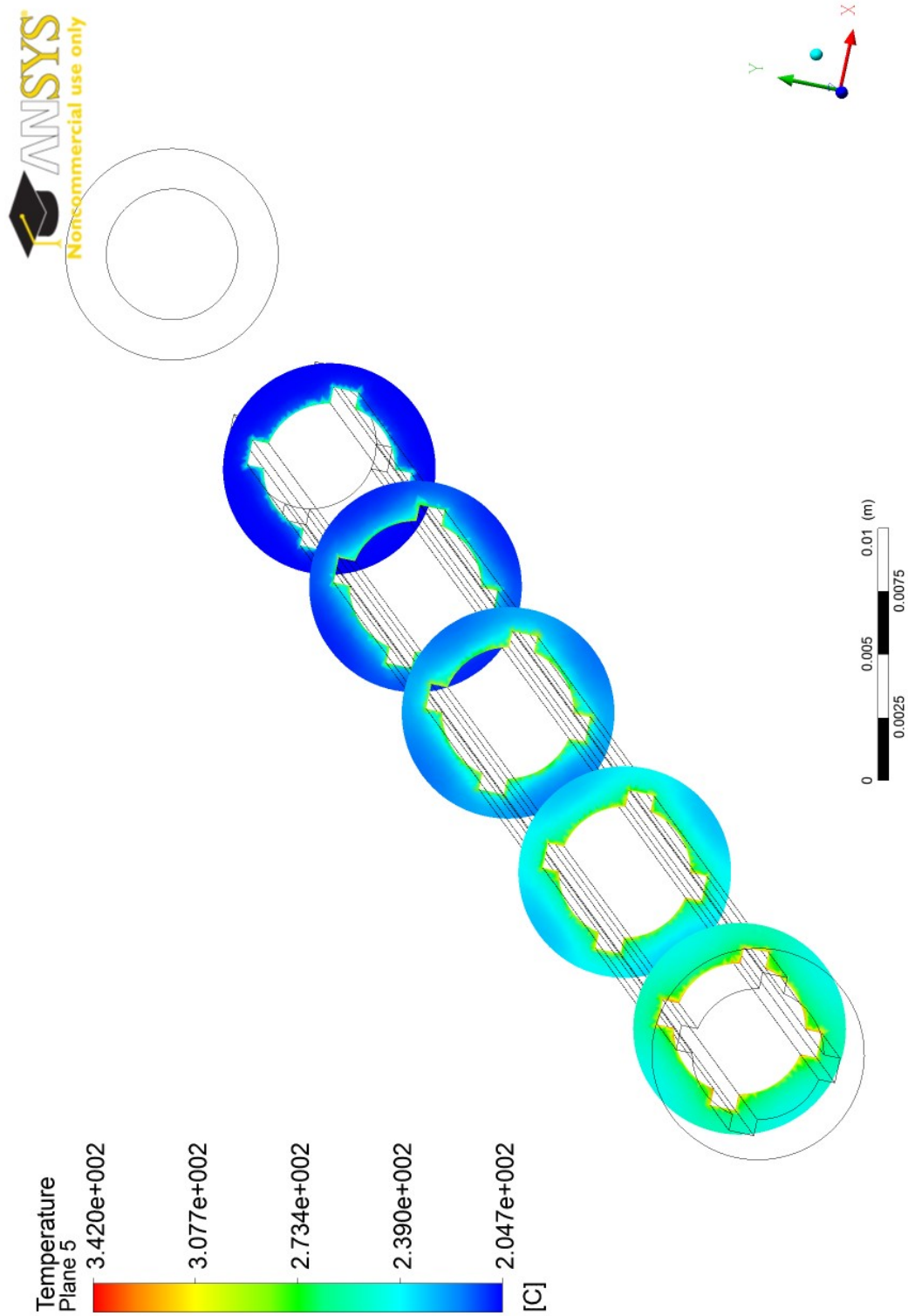


Figure 5-45: Temperature contours for the fluid at various cross sections in the annular channel with straight fins (SST model, $P = 22.6 \text{ MPa}$, $G = 2000 \text{ kg/m}^2\text{s}$, $q = 1.543 \text{ MW/m}^2$)

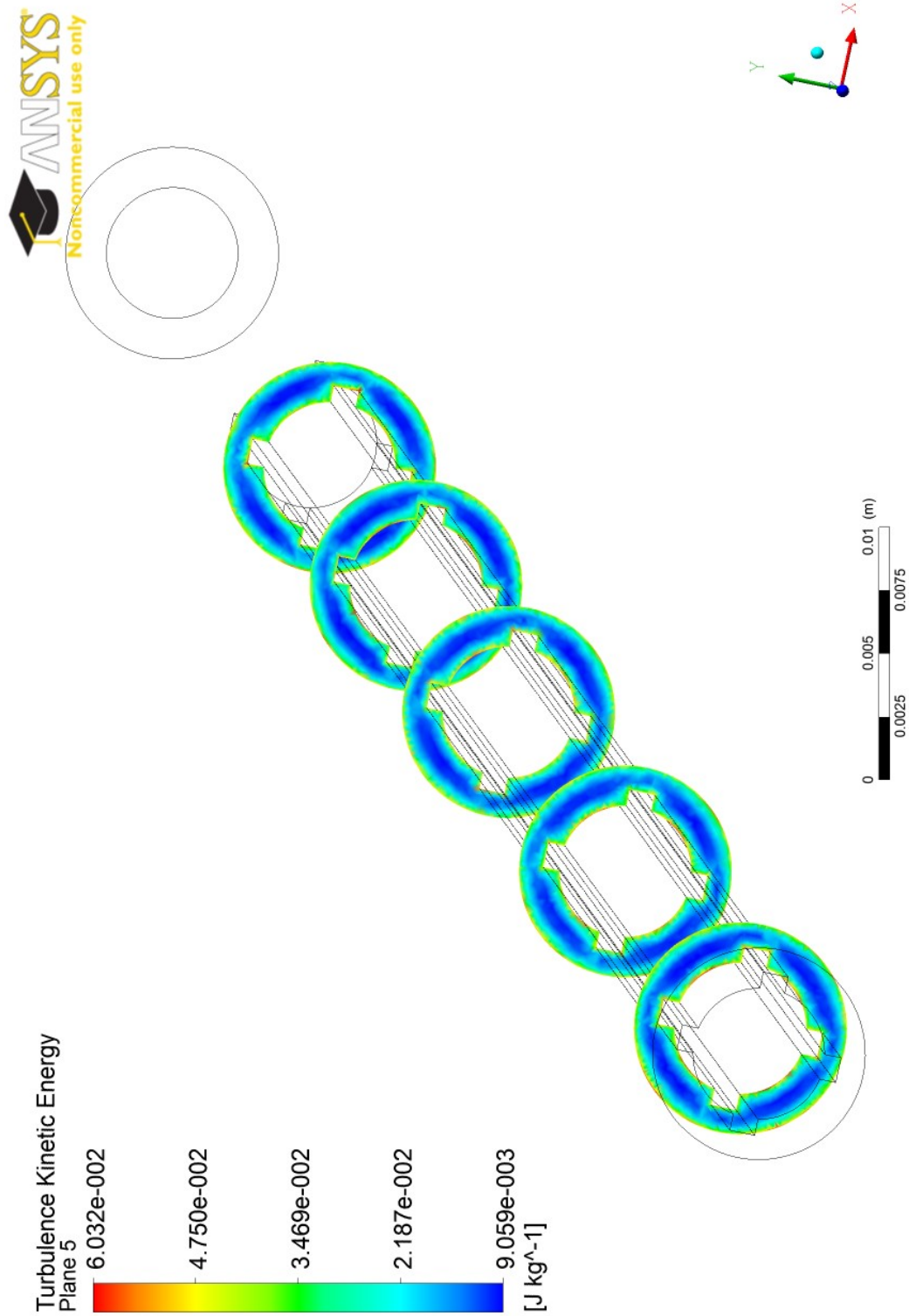


Figure 5-46: Turbulent kinetic energy contours for the fluid at various cross sections in the annular channel with straight fins (SST model, $P = 22.6 \text{ MPa}$, $G = 2000 \text{ kg/m}^2\text{s}$, $q = 1.543 \text{ MW/m}^2$)

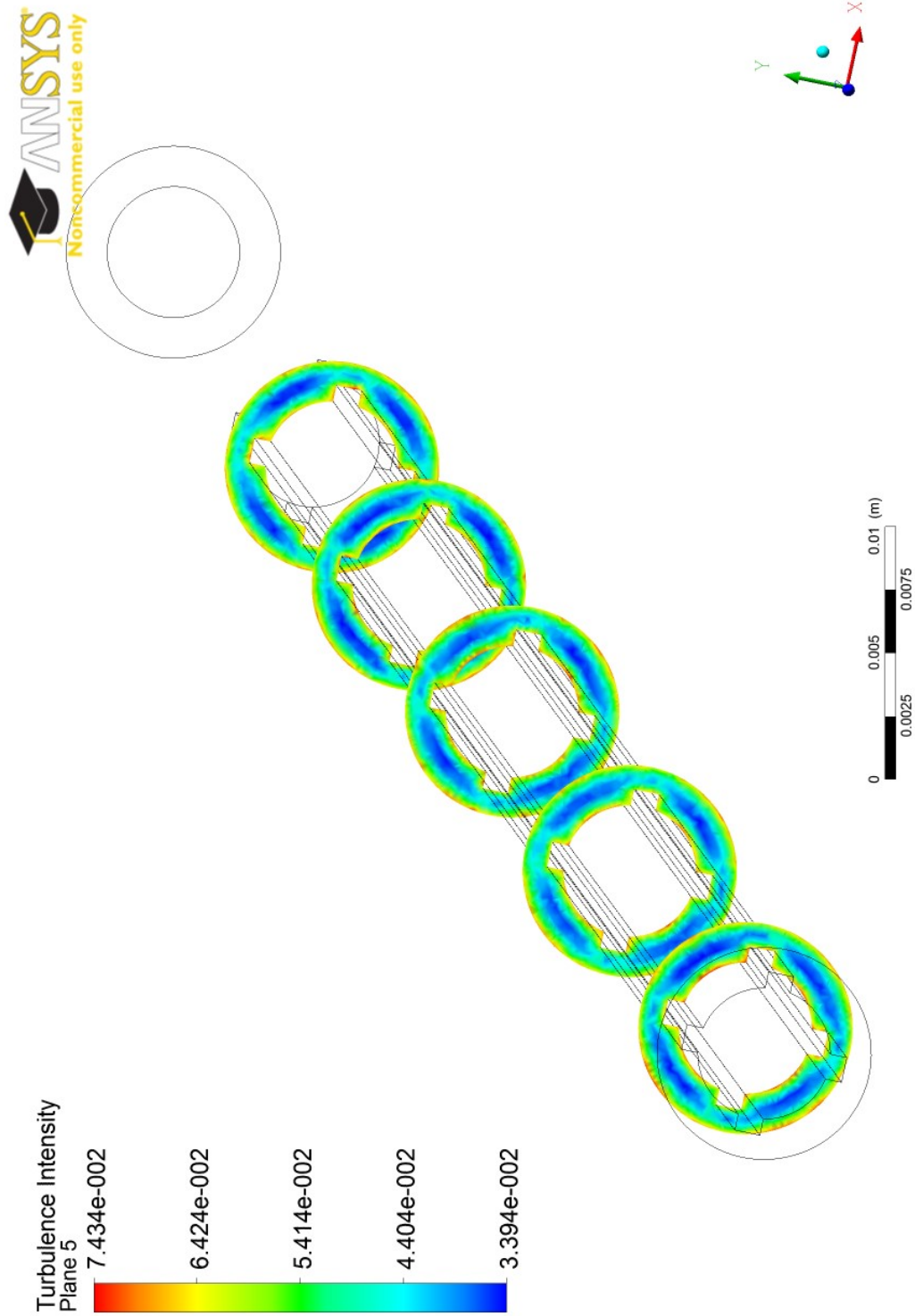


Figure 5-47: Turbulence intensity contours for the fluid at various cross sections in the annular channel with straight fins (SST model, $P = 22.6 \text{ MPa}$, $G = 2000 \text{ kg/m}^2\text{s}$, $q = 1.543 \text{ MW/m}^2$)

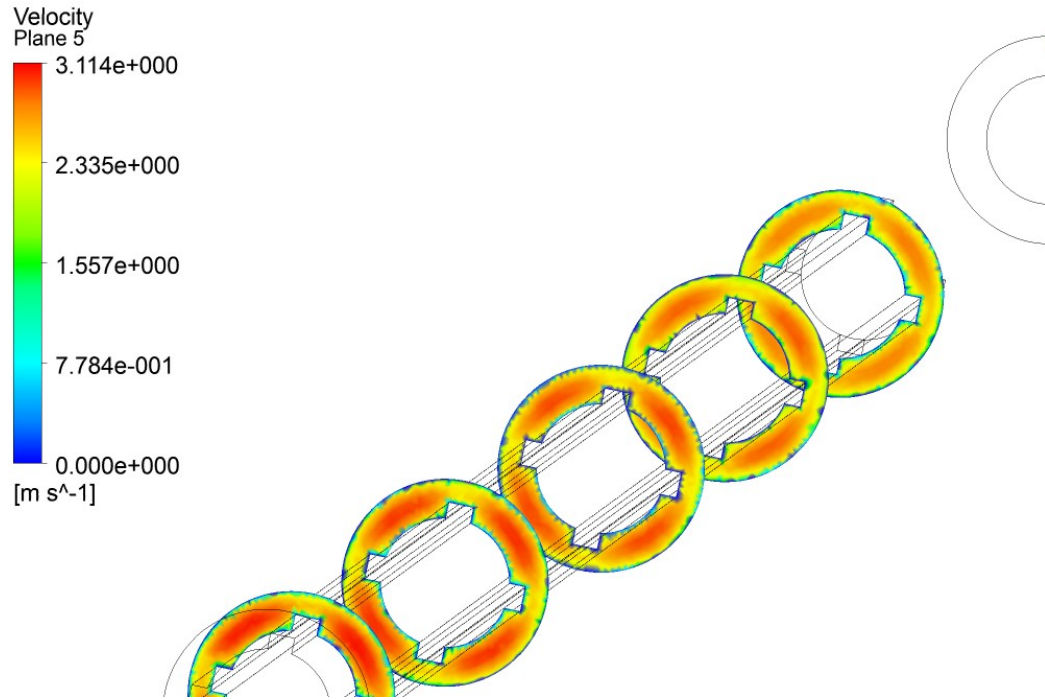


Figure 5-48: Velocity contours for the fluid at various cross sections in the annular channel with straight fins (SST model, $P = 22.6$ MPa, $G = 2000$ kg/m²s, $q = 1.543$ MW/m²)

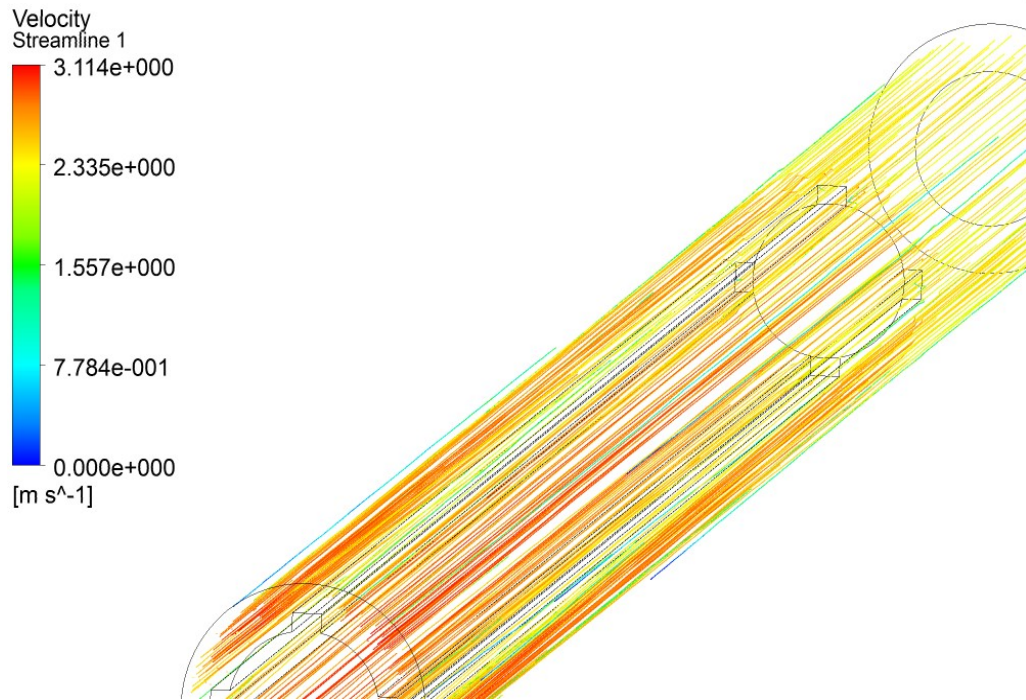


Figure 5-49: Velocity streamlines for the fluid in the annular channel with straight fins (SST model, $P = 22.6$ MPa, $G = 2000$ kg/m²s, $q = 1.543$ MW/m²)

5.5 Case 1 - No Fins, SST Model, Free Mesh

A number of simulations were conducted on an annular channel geometry with no fins, to further study the differences between the geometries and the effects the geometry change produces. By changing the geometry to remove the fins, multiple simulations are needed to cover the different scenarios created. From a geometrical point of view, there are three possible comparable geometries:

- Keeping the same inner and outer diameters of the annular channel, while removing the fins,
- Keeping the same inner diameter and changing the outer diameter to keep the same hydraulic equivalent diameter as the geometry with helical fins,
- Keeping the same inner diameter and changing the outer diameter to keep the same flow area as the geometry with helical fins.

By removing the fins from the geometry, there is less area for the heat to be released from, and as such, to keep the total amount of heat the same as in the case of the helical fins, the heat flux has to be increased to maintain the same power out of a smaller area. Thus cases are run for the same heat flux of 1.543 MW/m^2 and higher heat flux of 2 MW/m^2 to maintain a total power of 15.8 kW .

The first temperature results shown in Figure 5-50, Figure 5-51, and Figure 5-52 for the same ID and OD and heat flux of 1.543 MW/m^2 show an expected trend for a NHT regime case, with linearly increasing temperature throughout the heated region. The results of this simulation is in fact closer to the experimental points for the wall temperature, as shown by the average temperature profile. The uncertainty in this result could be due to the geometry dimensions/heat flux combination, an under-prediction by FLUENT, or the error in the calculation of the “experimental” wall temperature points. As the FLUENT models displayed a high accuracy in predicting the NHT regime in the bare tube cases, it is possible that the experimental points in the dataset do not reflect the true temperature of the walls in the helical fin geometry.

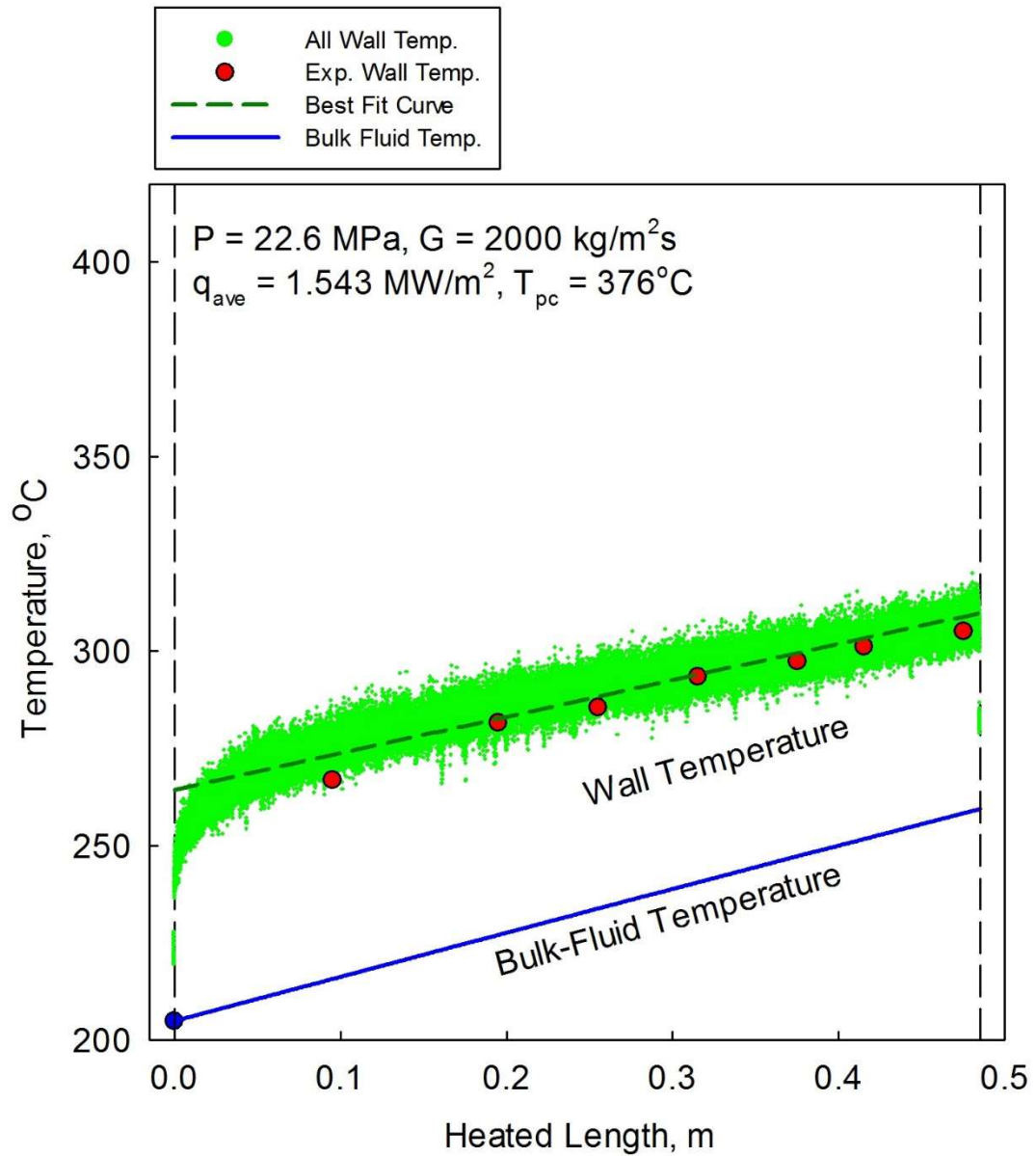


Figure 5-50: Simulated temperature for the fluid at the heated wall of the annular channel with no fins (SST model, same ID and OD of case with helical fins), and the average temperature profile using curve fitting

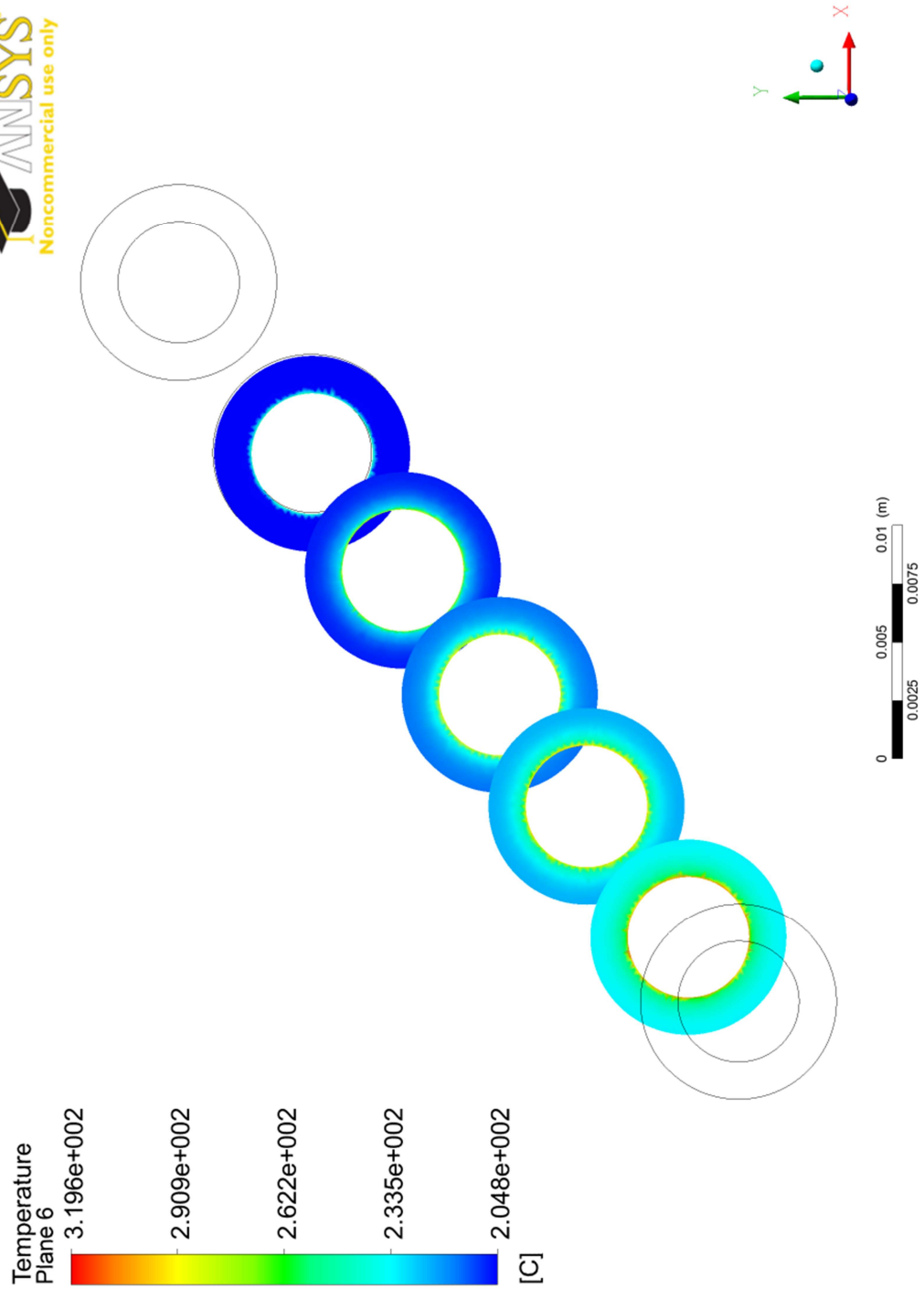


Figure 5-51: Temperature contours for the fluid at various cross sections in the annular channel with no fins (SST model, $P = 22.6$ MPa, $G = 2000$ kg/m²s, $q = 1.543$ MW/m²)

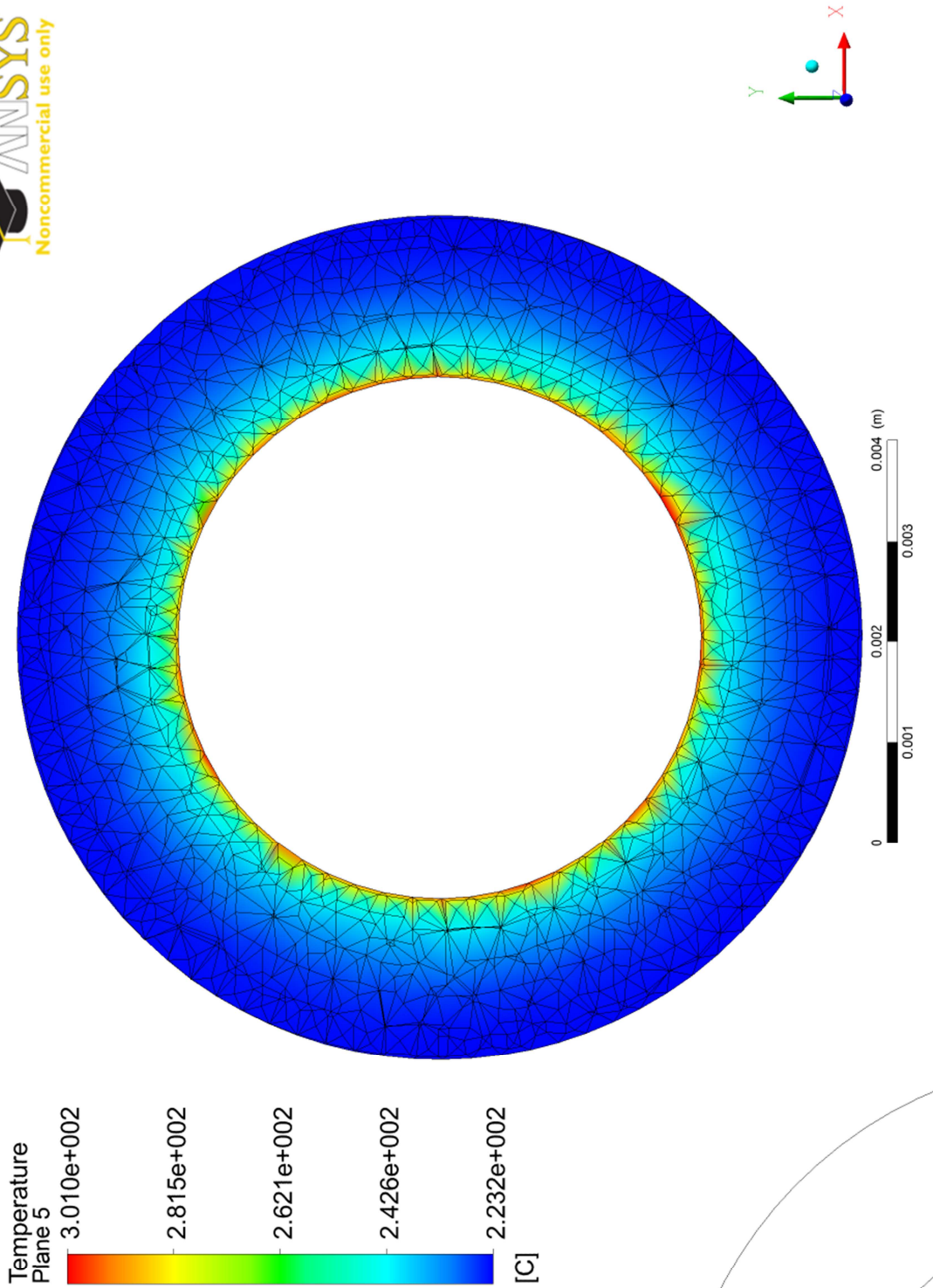


Figure 5-52: Temperature contour and mesh at a radial cross section in the annular channel with no fins (SST model, $P = 22.6$ MPa, $G = 2000$ kg/m²s, $q = 1.543$ MW/m²)

The next point of comparison is the turbulence production in the fluid, by studying the distributions in Figure 5-53, and Figure 5-54 for the turbulent kinetic energy and Figure 5-55, and Figure 5-56 for the turbulence intensity.

The turbulent kinetic energy axial contours show the highest value is at the inlet (set as a boundary condition) and quickly dissipates as the flow is resolved by the solver. The radial plots show the local ranges for the contours and when comparing these values to the same axial distance in the helical fins geometry (Figure 5-16 for example), the similarities are apparent between the two cases. Both cases show a turbulent kinetic energy in the same order of magnitude 7.3×10^{-3} – 4.77×10^{-2} for the annular channel with no fins, and 7.8×10^{-3} – 6.3×10^{-2} J/kg for the geometry with helical fins.

The same comparison is established for the turbulence intensity, with 3 – 6.6% for the no-fin geometry and 3.3 – 7.5% for the geometry with helical fins. The velocity contours in Figure 5-57 and Figure 5-58 show a lower velocity than the corresponding helical fins geometry case; 2.7 compared to 3.1 m/s. However this is attributed to the larger flow area in the no-fins geometry as it shares the same inner and outer diameters of the helical fins geometry but without the fins present.

Overall the differences are not significant between the two geometries and the introduction of the fins did not improve turbulence, nor did it improve the heat transfer; with both cases showing an average of 20 kW/m²K heat transfer coefficient.

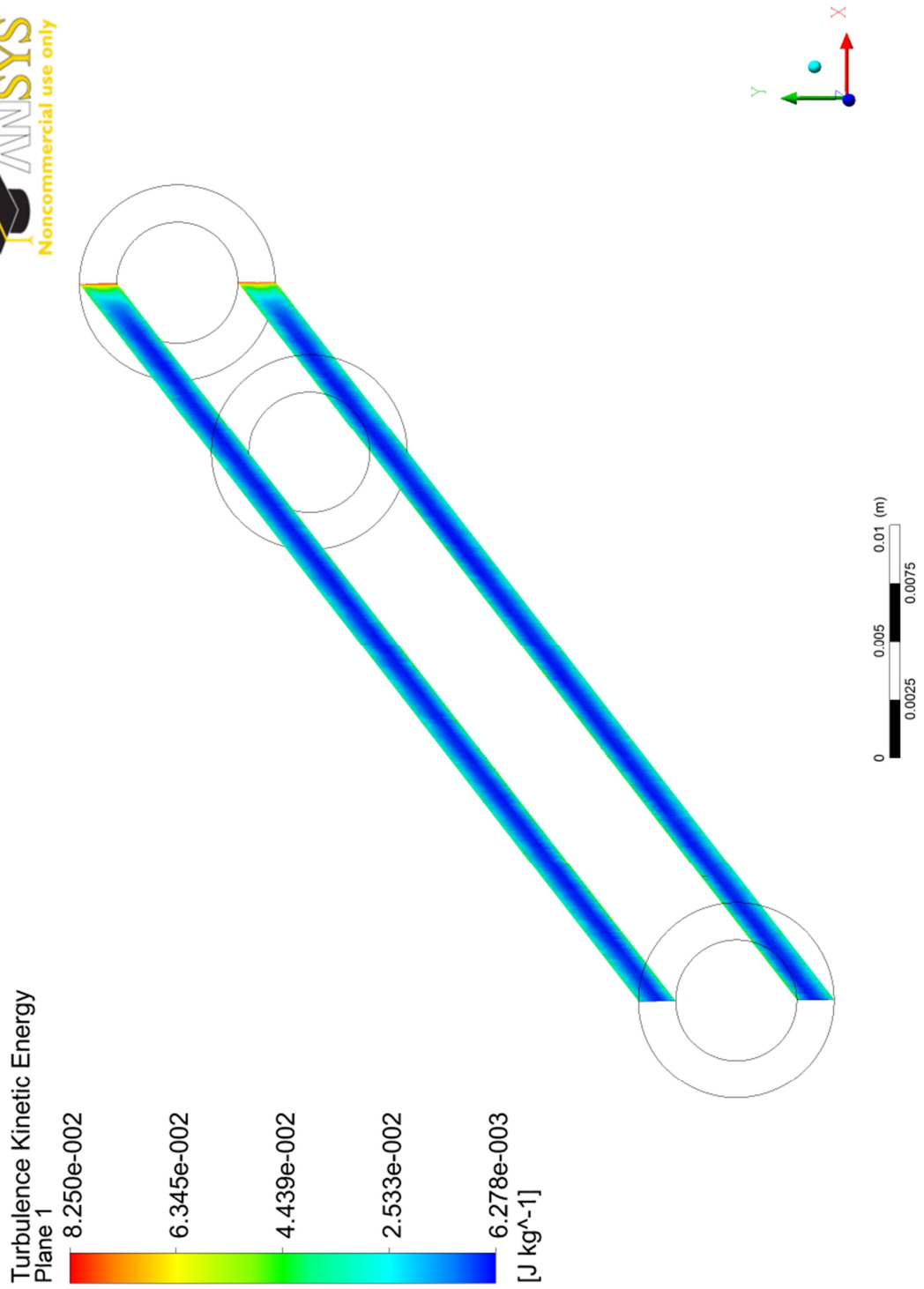


Figure 5-53: Turbulent kinetic energy contour at longitudinal cross section in the annular channel with no fins (SST model, $P = 22.6$ MPa, $G = 2000$ kg/m²s, $q = 1.543$ MW/m²)

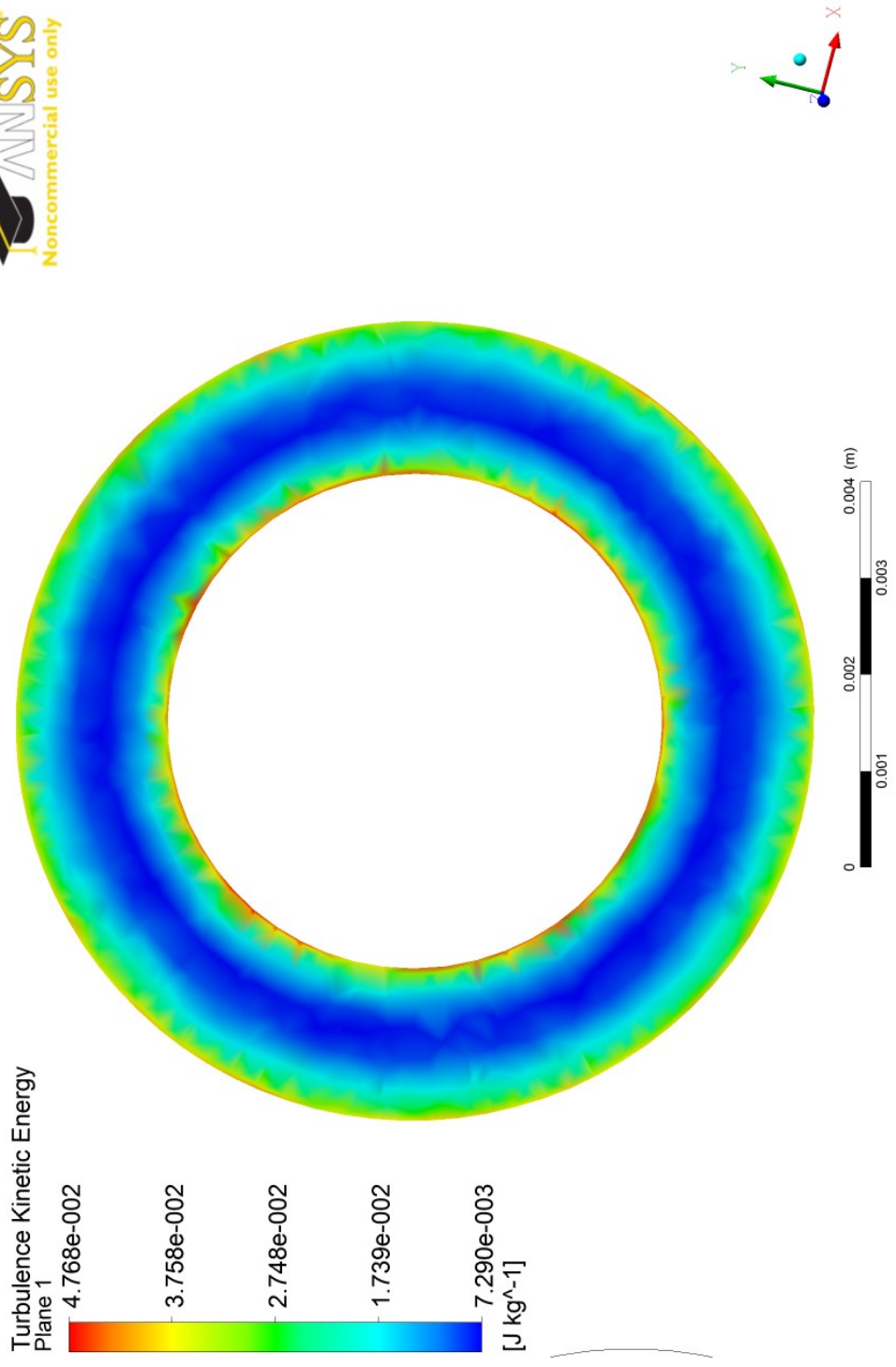


Figure 5-54: Turbulence kinetic energy contour at a radial cross section in the annular channel with no fins (SST model, $P = 22.6$ MPa, $G = 2000$ kg/m²s, $q = 1.543$ MW/m²)

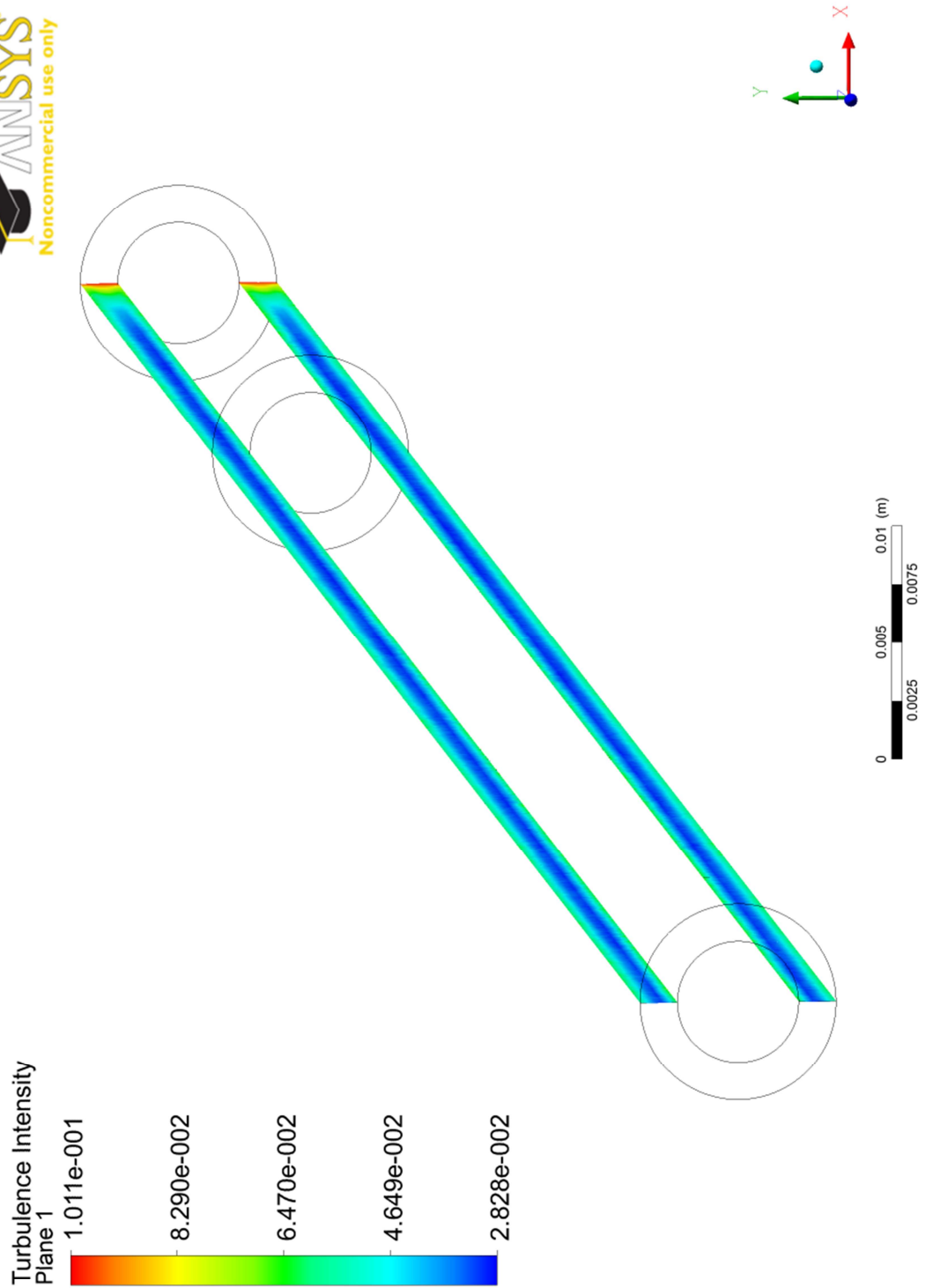


Figure 5-55: Turbulence intensity contours at a longitudinal cross section in the annular channel with no fins (SST model, $P = 22.6$ MPa, $G = 2000$ kg/m²s, $q = 1.543$ MW/m²)

Turbulence Intensity
Plane 1

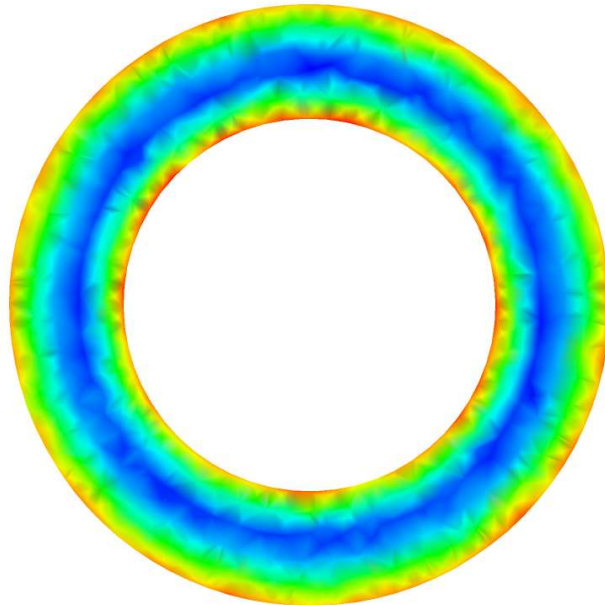
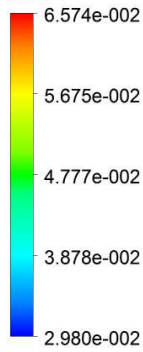


Figure 5-56: Turbulence intensity contour at a radial cross section in the annular channel with no fins (SST model, $P = 22.6 \text{ MPa}$, $G = 2000 \text{ kg/m}^2\text{s}$, $q = 1.543 \text{ MW/m}^2$)

Velocity
Plane 1

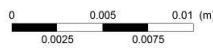
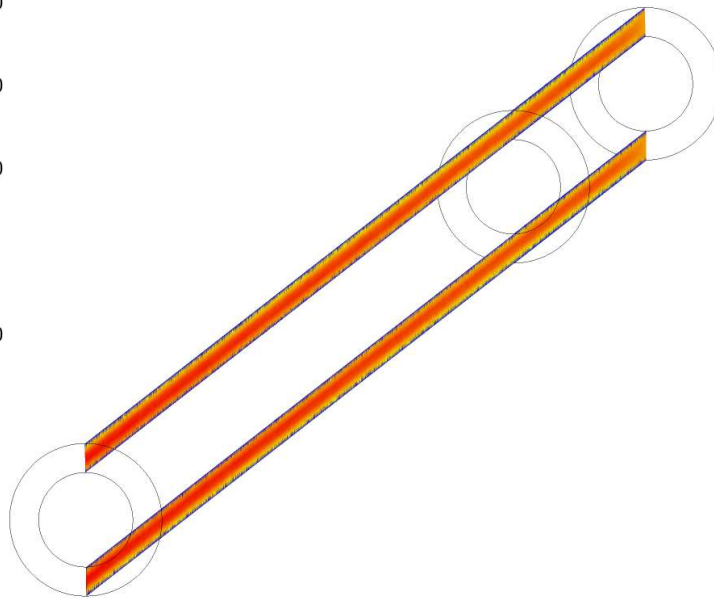
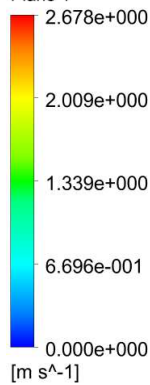


Figure 5-57: Velocity contour at a longitudinal cross section in the annular channel with no fins (SST model, $P = 22.6 \text{ MPa}$, $G = 2000 \text{ kg/m}^2\text{s}$, $q = 1.543 \text{ MW/m}^2$)

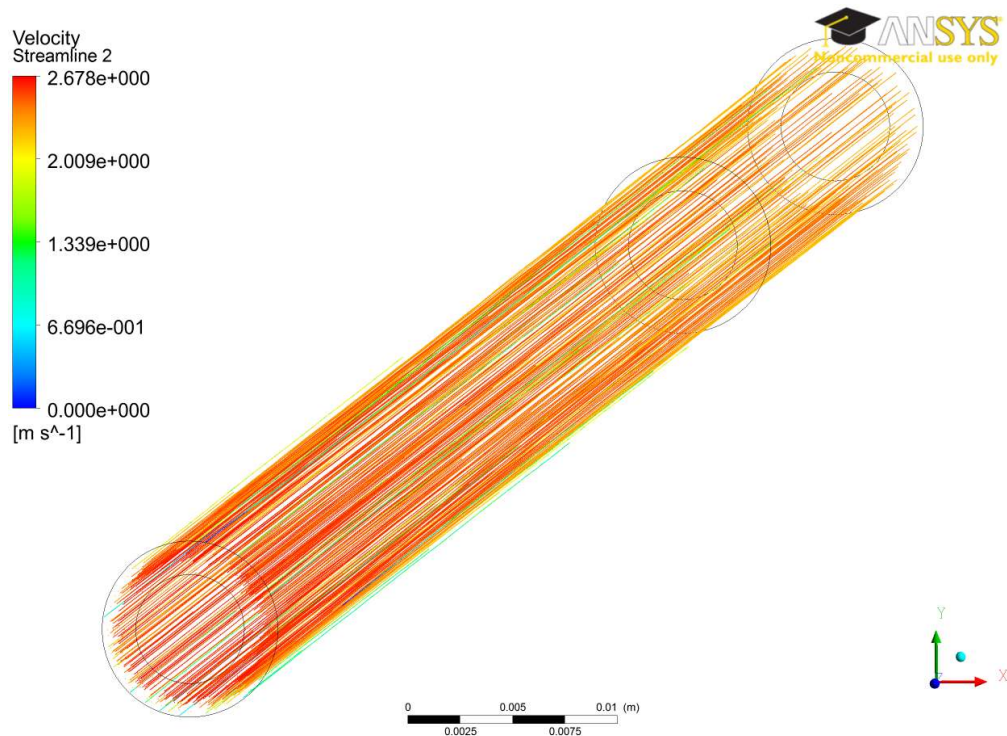


Figure 5-58: Velocity streams for the fluid in the annular channel with no fins (SST model, $P = 22.6$ MPa, $G = 2000$ kg/m²s, $q = 1.543$ MW/m²)

As mentioned earlier in the test matrix, multiple simulations were conducted for the annular channel with no fins, with a combination of geometry changes (hydraulic diameter and flow area) to match the original geometry and heat flux changes to match the original case total power. The following figures show the temperature profiles for these cases. The trends for the fluid properties follow the same trends as the first case with no fins discussed in this section.

Figure 5-59 represents the case with the same ID and OD as the helical fins but with a higher heat flux at the heated wall to account for the same total power to the fluid. The results, naturally, show a higher average wall temperature than the case with helical fins, showcasing the ability of the fins to lower the average temperature of the fluid by providing a larger surface area for the heat to dissipate from and contacting more of the colder fluid (at the top of the fins).

Figure 5-60 and Figure 5-61 show the temperature distributions for the geometry with the same hydraulic equivalent diameter as the helical fins geometry, with 1.543 and 2 MW/m² heat flux respectively. Finally Figure 5-62 and Figure 5-63 show the same results for the geometry with the same flow area as the helical fins geometry. The temperature trends and deviation from the experimental points are similar for cases with the same heat flux, regardless of the slight geometric change, as shown in the comparison of the average temperatures in Figure 5-64. The average wall temperature for the helical fins case is higher than the no-fin geometries with the same heat flux but much lower than those with 2 MW/m² (same total power to the fluid). As all cases are in the NHT, and comprise of linear wall temperature profiles below the pseudocritical point, the corresponding properties such as density, viscosity and specific heat all display linear trends as well. The changes in the properties are most significant within ± 25 degrees from the pseudocritical point, and the highest wall temperature reaches in these simulations is just outside that region (350°C compared to the pseudocritical point of 376°C).

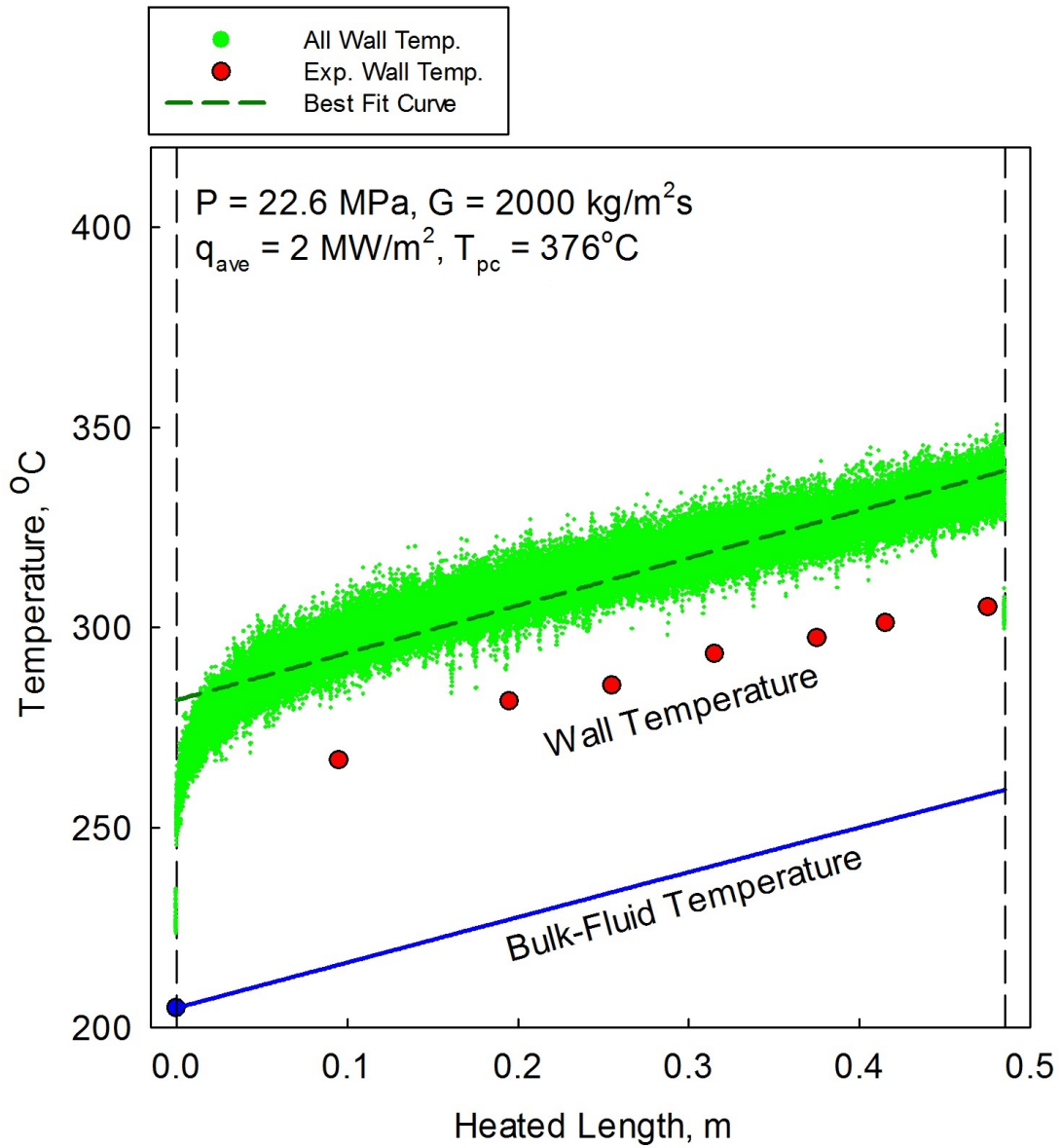


Figure 5-59: Simulated temperature for the fluid at the heated wall of the annular channel with no fins (SST model, equivalent power (2 MW/m²)), and the average temperature profile using curve fitting

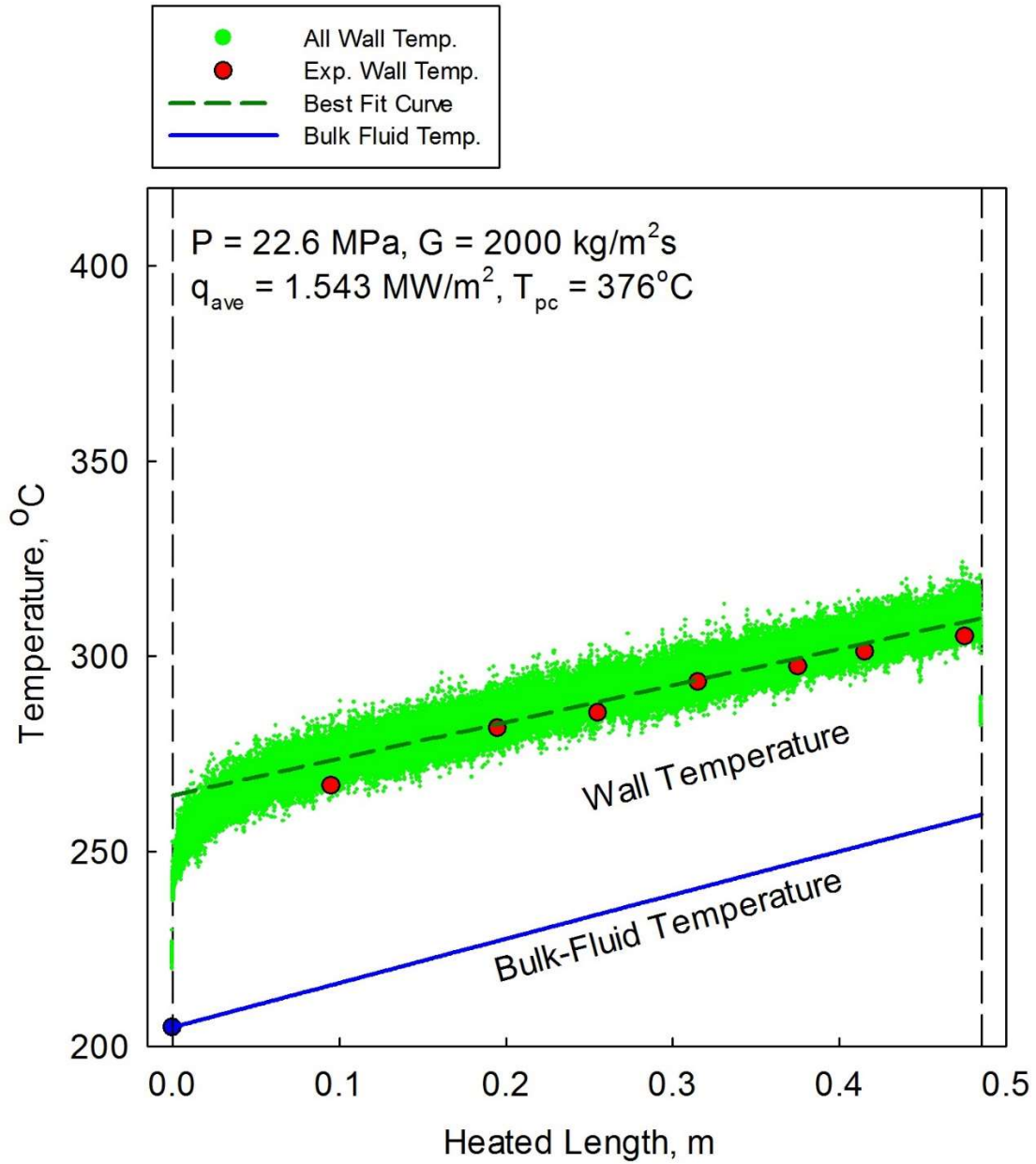


Figure 5-60: Simulated temperature for the fluid at the heated wall of the annular channel with no fins (SST model, same equivalent hydraulic diameter as the geometry with helical fins), and the average temperature profile using curve fitting

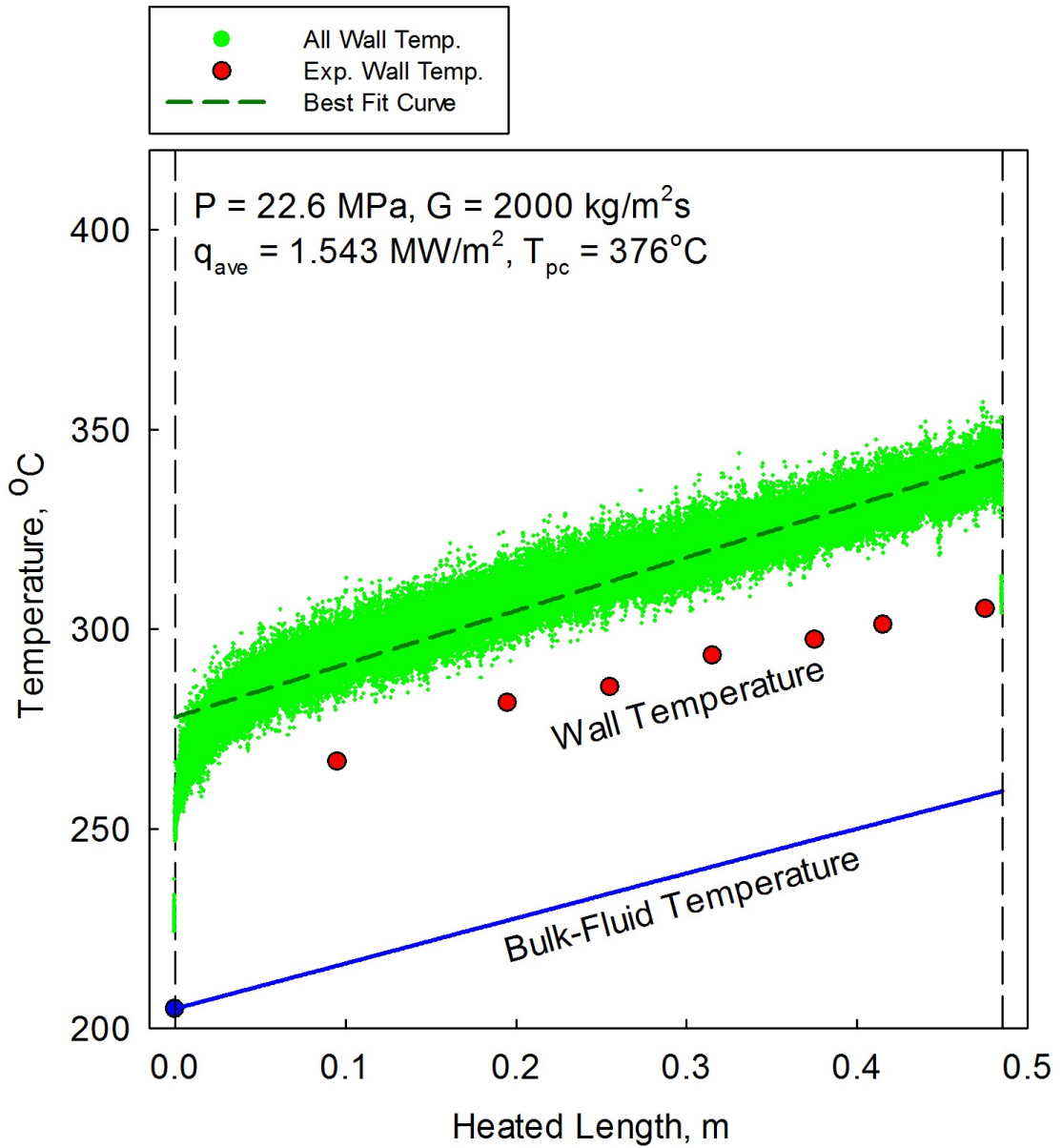


Figure 5-61: Simulated temperature for the fluid at the heated wall of the annular channel with no fins (SST model, same equivalent hydraulic diameter as the geometry with helical fins, equivalent power (2 MW/m^2)), and the average temperature profile using curve fitting

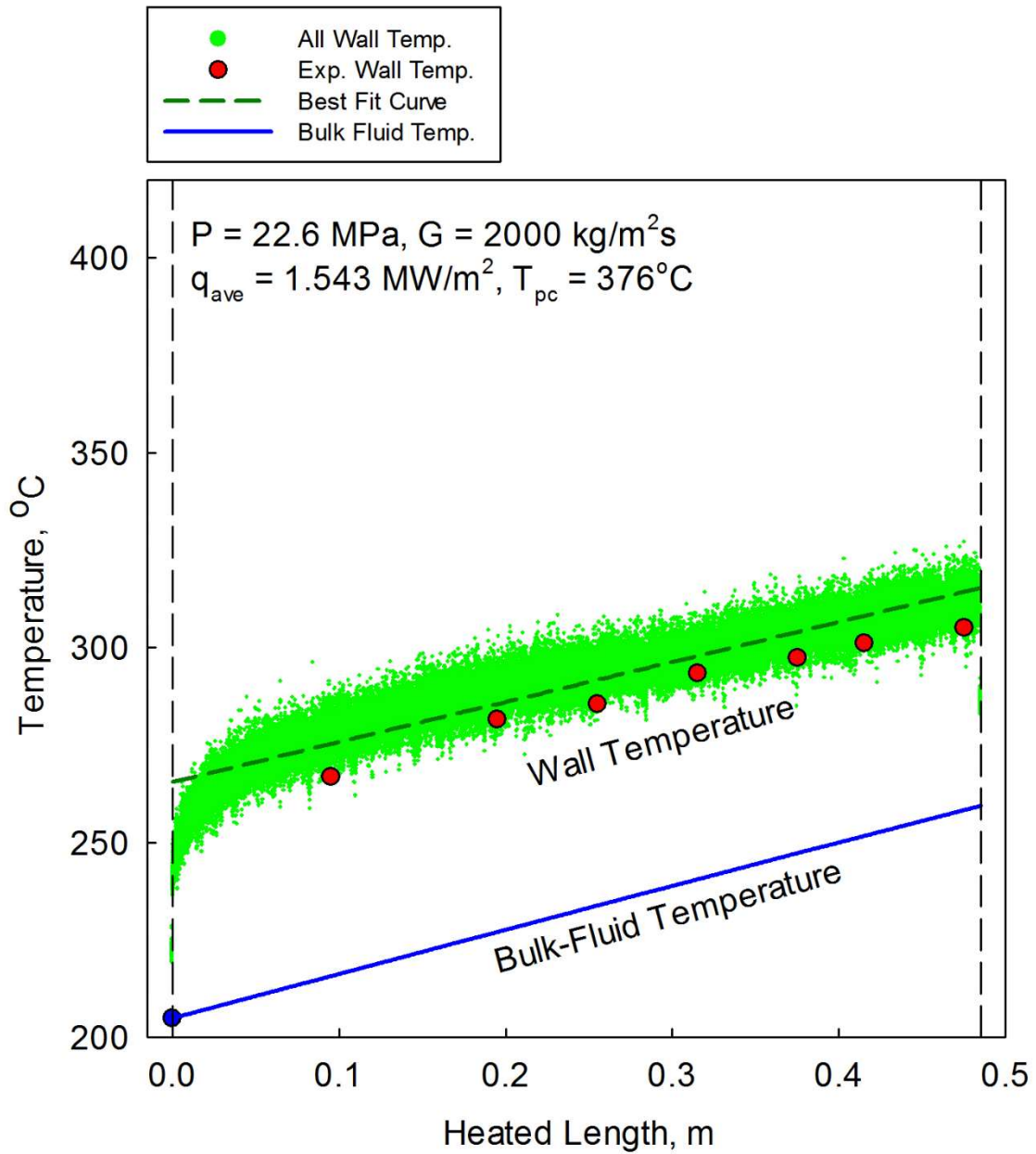


Figure 5-62: Simulated temperature for the fluid at the heated wall of the annular channel with no fins (SST model, same flow area as the geometry with helical fins), and the average temperature profile using curve fitting

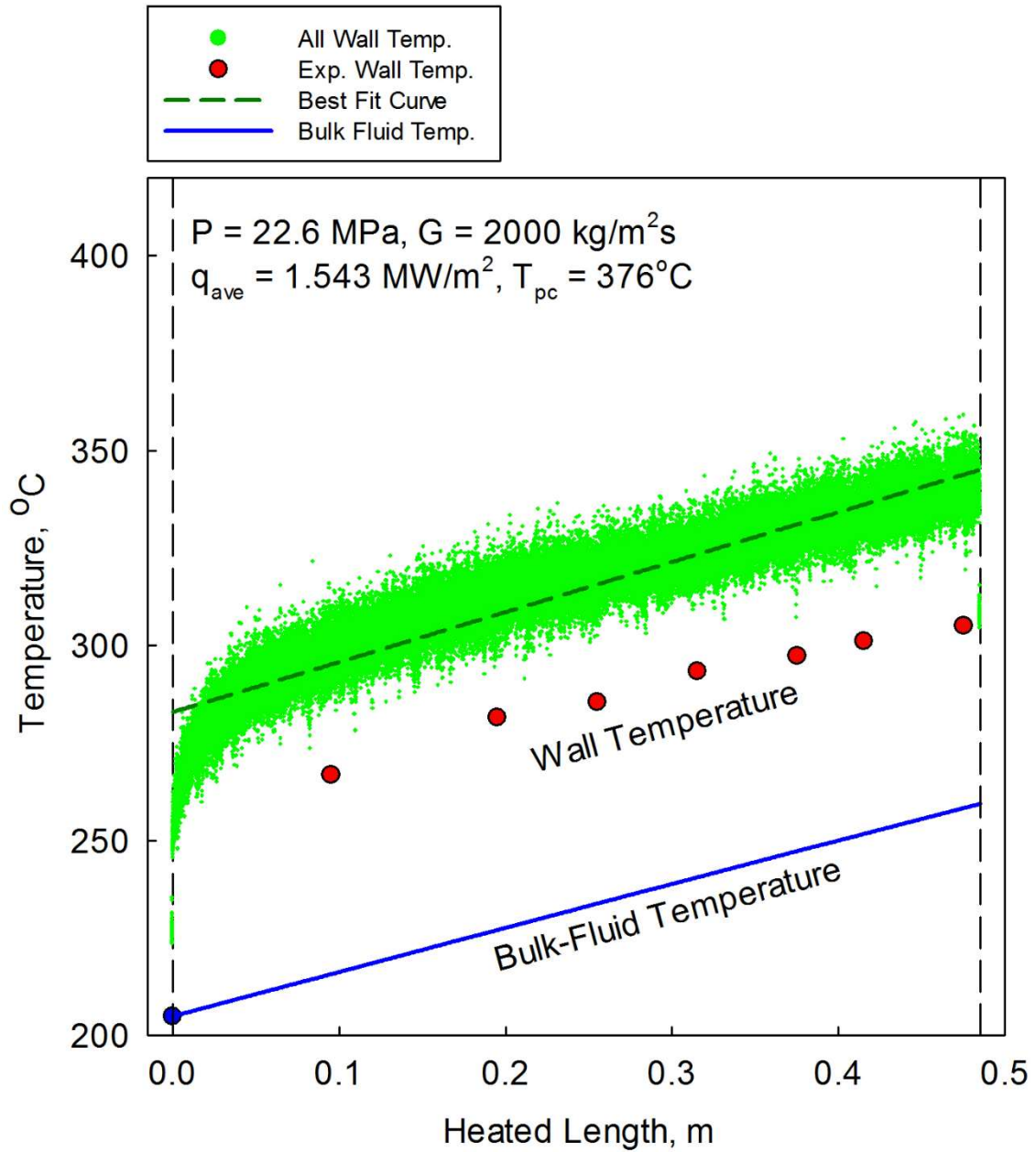


Figure 5-63: Simulated temperature for the fluid at the heated wall of the annular channel with no fins (SST model, same flow area as the geometry with helical fins, equivalent power (2 MW/m^2)), and the average temperature profile using curve fitting

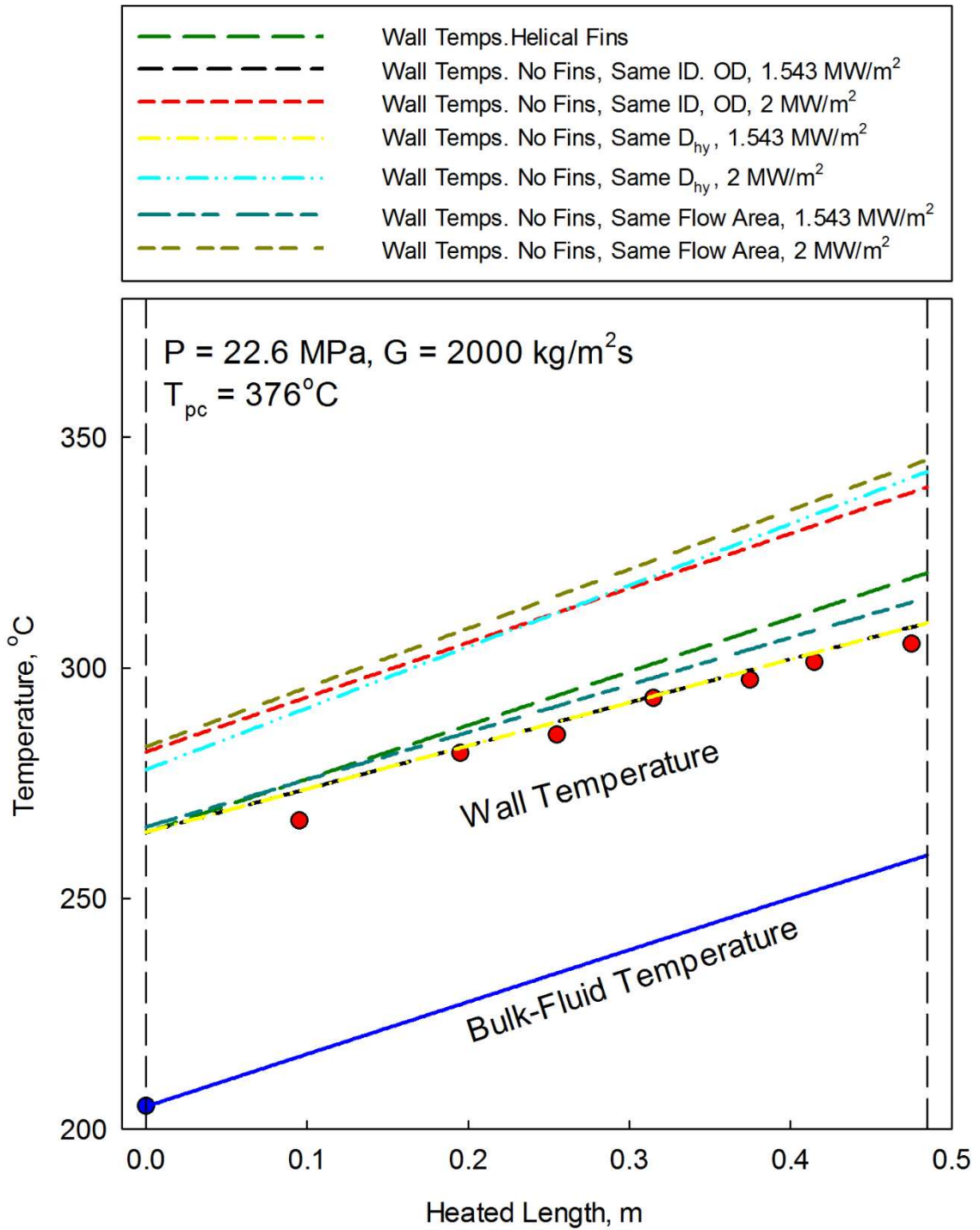


Figure 5-64: Comparison of average simulated temperatures for the fluid at the heated wall of the annular channel with helical fins and no fins (SST model)

5.6 Case 5 - SST Model, Free Mesh

To study the heat transfer deterioration in the annular channel geometry with helical fins, one experimental case provided with a heat flux of 2.547 MW/m^2 (1 MW/m^2 higher than the original case in the NHT). The experimental data points in Figure 5-65 depict a deterioration in the heat transfer as the fluid at the wall crosses the pseudocritical point. However, the prediction by the FLUENT models (SST and RKE) show a trend similar to that of the NHT regime. As the test matrix shows, simulations have been conducted with altered turbulent Prandtl numbers in both models, as it has been established earlier that they have an effect on the predicted temperature profile especially in the DHT regime. The results, however, show no difference in the prediction from the standard models, with no depiction of deterioration in the heat transfer.

As the wall temperature in the simulations crosses the pseudocritical point, there is no change to the rate of change of temperature and it continues to rise linearly as in the rest of the cases studied before.

Density profiles in Figure 5-66 and Figure 5-67 show similar trends to the NHT cases shown earlier as well, with the lowest value reaching about 570 kg/m^3 which remains within the region of high density supercritical fluid (does not reach the low density gas-like region). The turbulence intensity values in Figure 5-68 show a maximum reached at the interface between the unheated inlet region and the finned heated region where the flow is disturbed by the introduction of the fins. Otherwise, the highest turbulence intensity achieved in the heated region is on par with the predicted values for the NHT cases with a maximum of around 7-8%. The similarities extend further to the velocity profiles in Figure 5-69 and Figure 5-70 where the maximum velocity is about 3.2 m/s (higher temperatures and lower densities lead to higher peak velocities) with the same radial distribution and the same streamlines as discussed earlier.

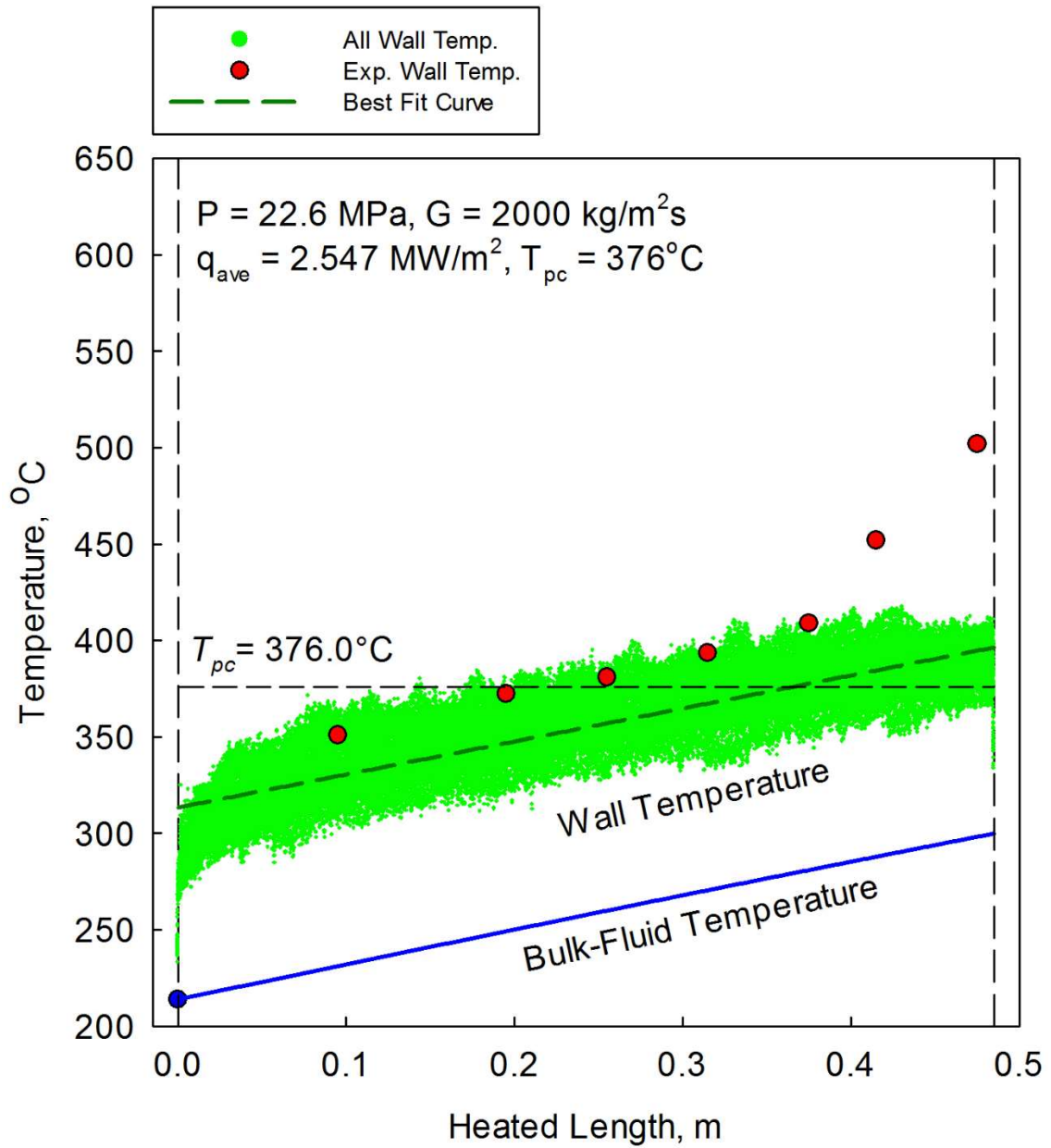


Figure 5-65: Simulated temperature for the fluid at all heated walls of the annular channel with straight fins (SST model), and the average temperature profile using curve fitting

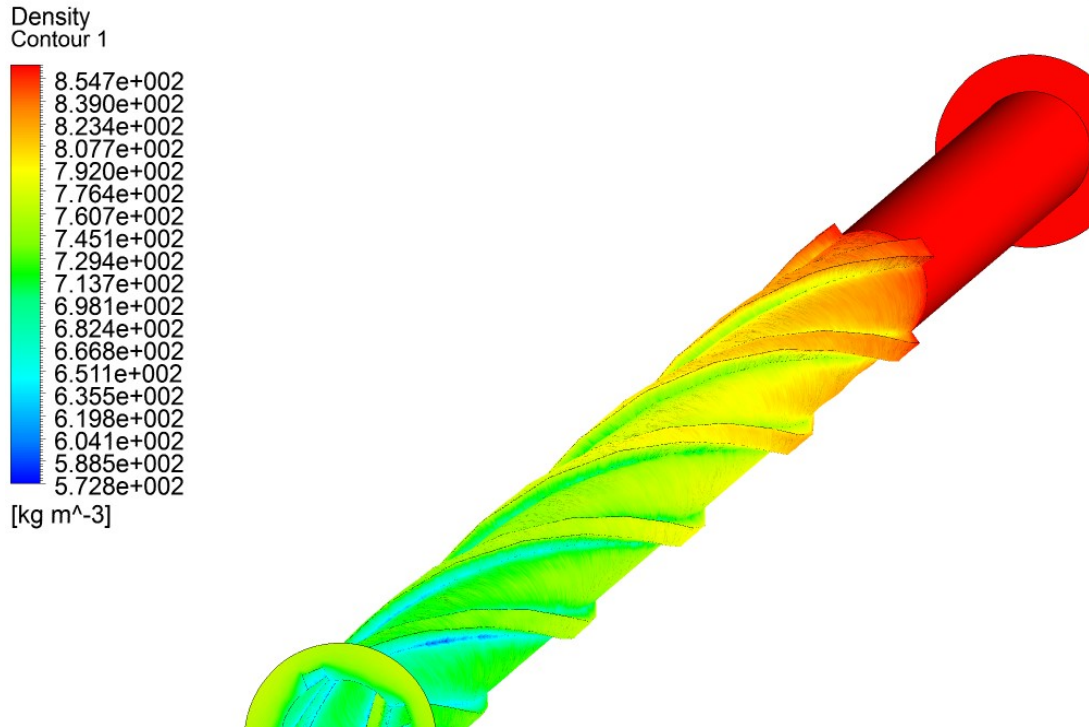


Figure 5-66: Density contours at the heated walls in the annular channel with helical fins (SST model, $P = 22.6$ MPa, $G = 2000$ kg/m²s, $q = 2.547$ MW/m²)

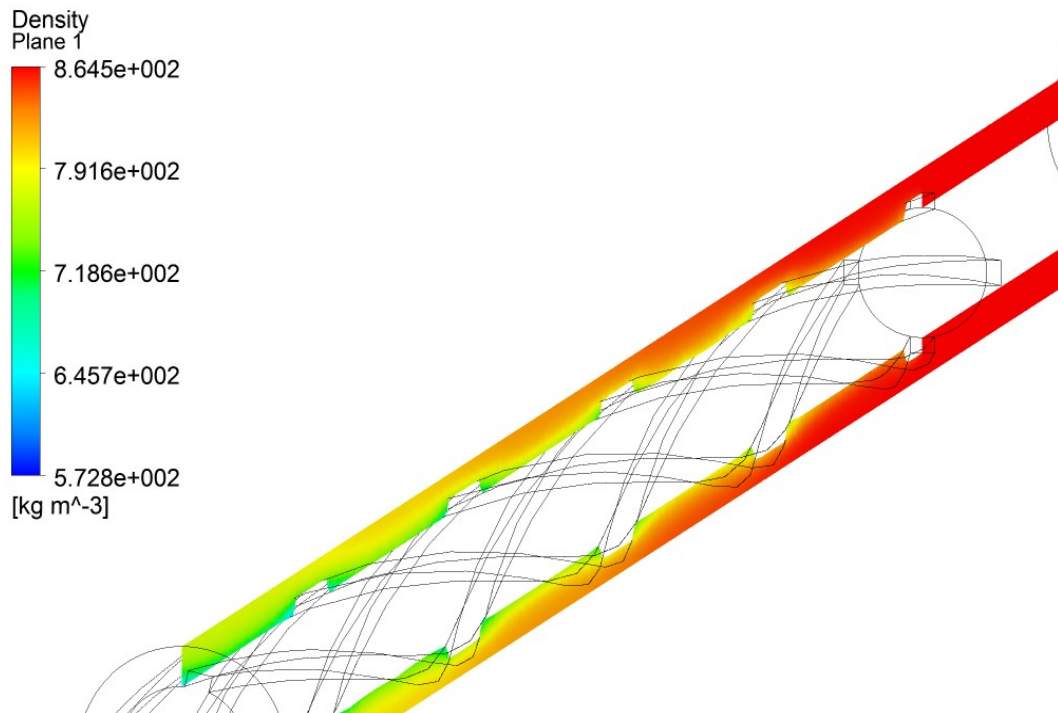


Figure 5-67: Density contours at a longitudinal cross section in the annular channel with helical fins (SST model, $P = 22.6$ MPa, $G = 2000$ kg/m²s, $q = 2.547$ MW/m²)

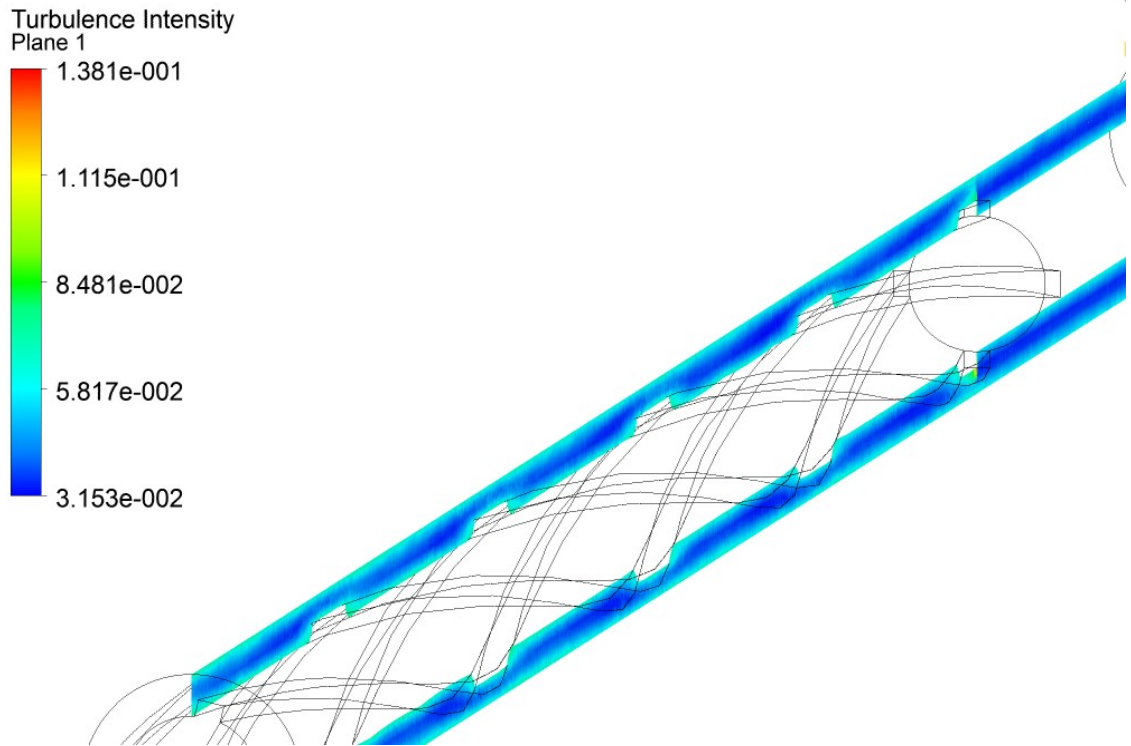


Figure 5-68: Turbulence intensity contours at a longitudinal cross section in the annular channel with helical fins (SST model, $P = 22.6$ MPa, $G = 2000$ kg/m²s, $q = 2.547$ MW/m²)

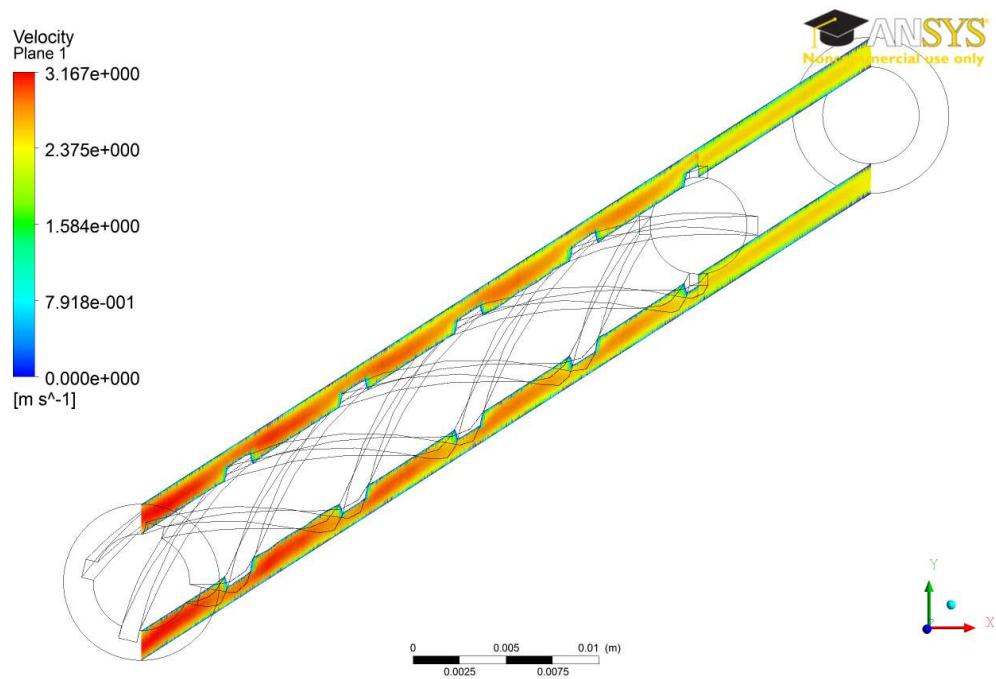


Figure 5-69: Velocity contours at a longitudinal cross section in the annular channel with helical fins (SST model, $P = 22.6$ MPa, $G = 2000$ kg/m²s, $q = 2.547$ MW/m²)

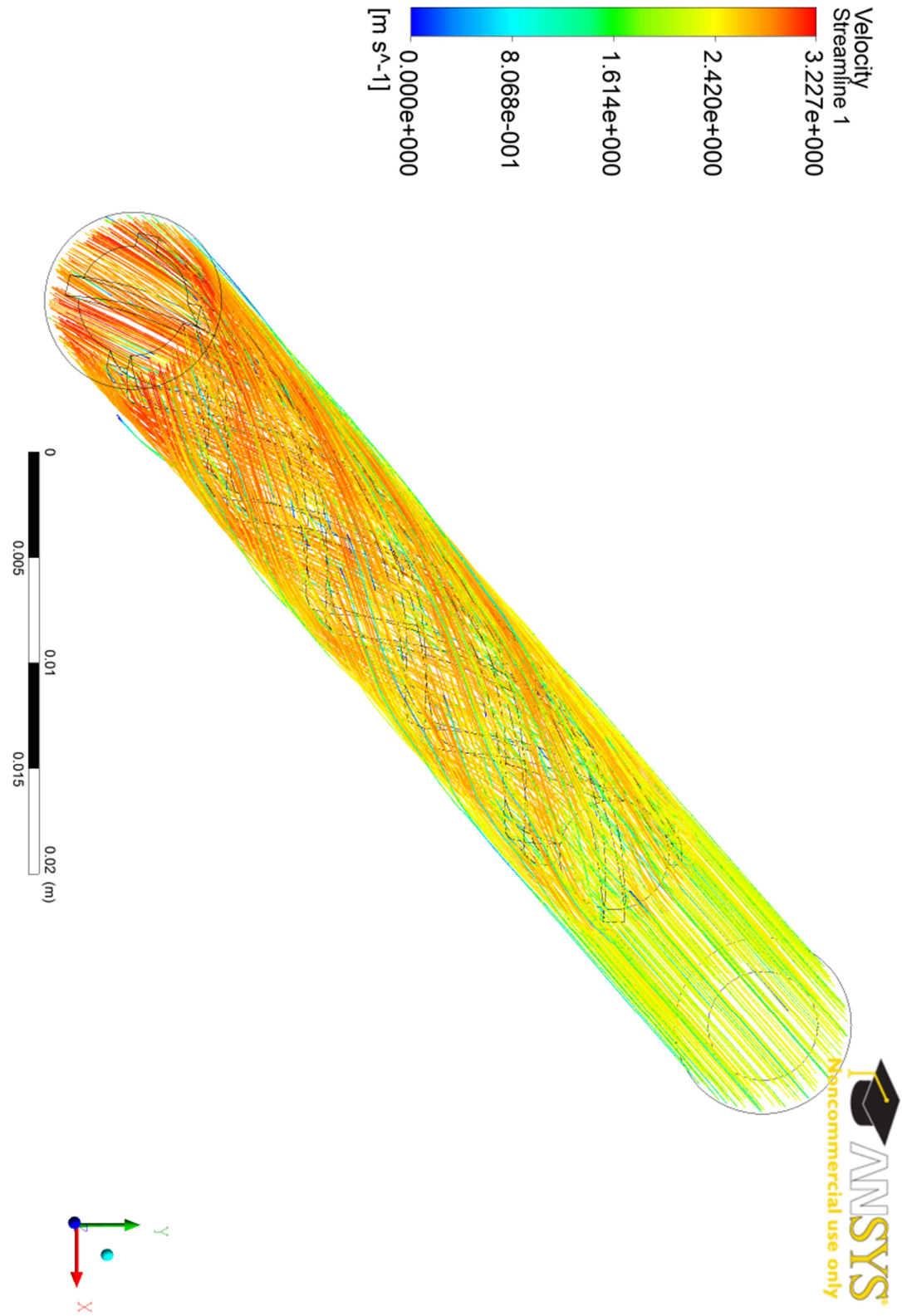


Figure 5-70: Velocity streams for the fluid in the annular channel with helical fins (SST model, $P = 22.6 \text{ MPa}$, $G = 2000 \text{ kg/m}^2\text{s}$, $q = 2.547 \text{ MW/m}^2$)

An interesting point to note in this DHT case, is the simulation results of the fluid specific heat, shown in Figure 5-71, Figure 5-72 and Figure 5-73. As the fluid crosses the pseudocritical point, the specific heat should reach a peak around 500 kJ/kg-K (as predicted by the property tables in NIST REFPROP). However, the simulation results, in which the wall fluid crosses the pseudocritical point, the specific heat values do not exceed 10 kJ/kg-K; 50 times lower than the peak value.

To understand this phenomenon, Table 5-2 shows the variation of specific heat as the temperature changes $\pm 1^\circ\text{C}$ at 22.6 MPa. Within the 1 degree space the specific heat changes by a full order of magnitude, and if the precise temperature is not captured by the solver, the peak will not appear as a result. As the mesh constructed for this geometry is somewhat coarse and unstructured, the temperature distribution field is also coarse and does not capture the fine changes as the fluid approaches and then crosses the pseudocritical point.

This effect appears to be the main reason for the FLUENT solver not predicting the deterioration in the heat transfer, as the high specific heat means the fluid would need a high amount of energy to raise its temperature (by 1°C for 1 kg) and without the presence of this peak in the simulation result, deterioration is unlikely to appear in the temperature profile.

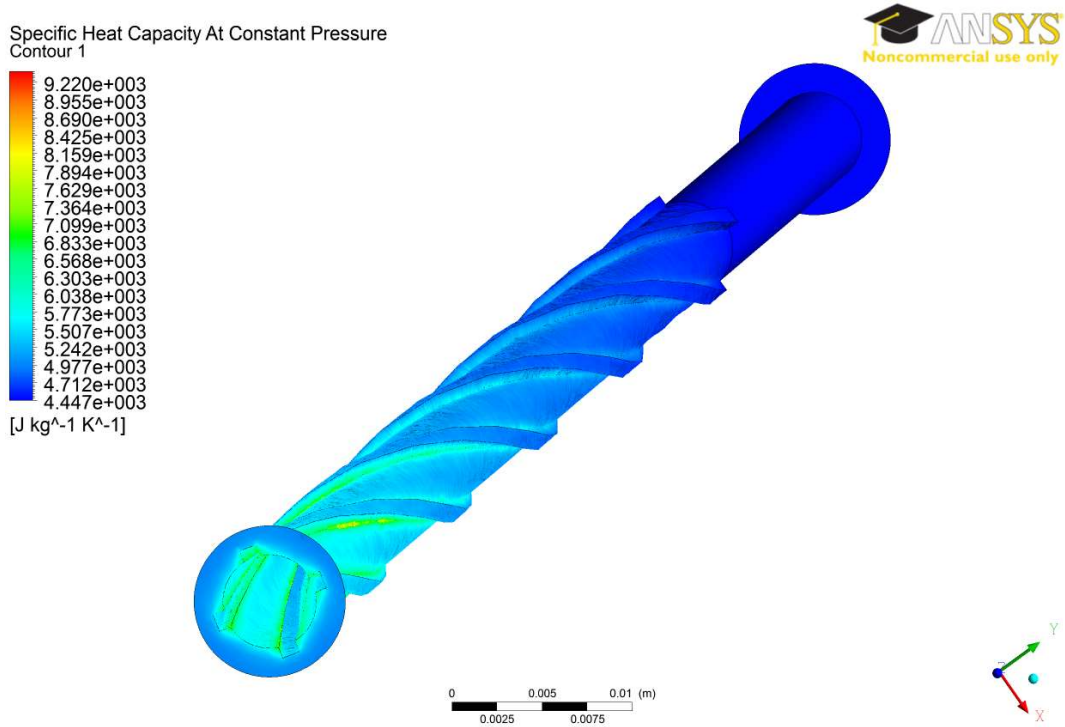


Figure 5-71: Specific heat contours at the heated wall in the annular channel with helical fins (SST model, $P = 22.6$ MPa, $G = 2000$ kg/m²s, $q = 2.547$ MW/m²)

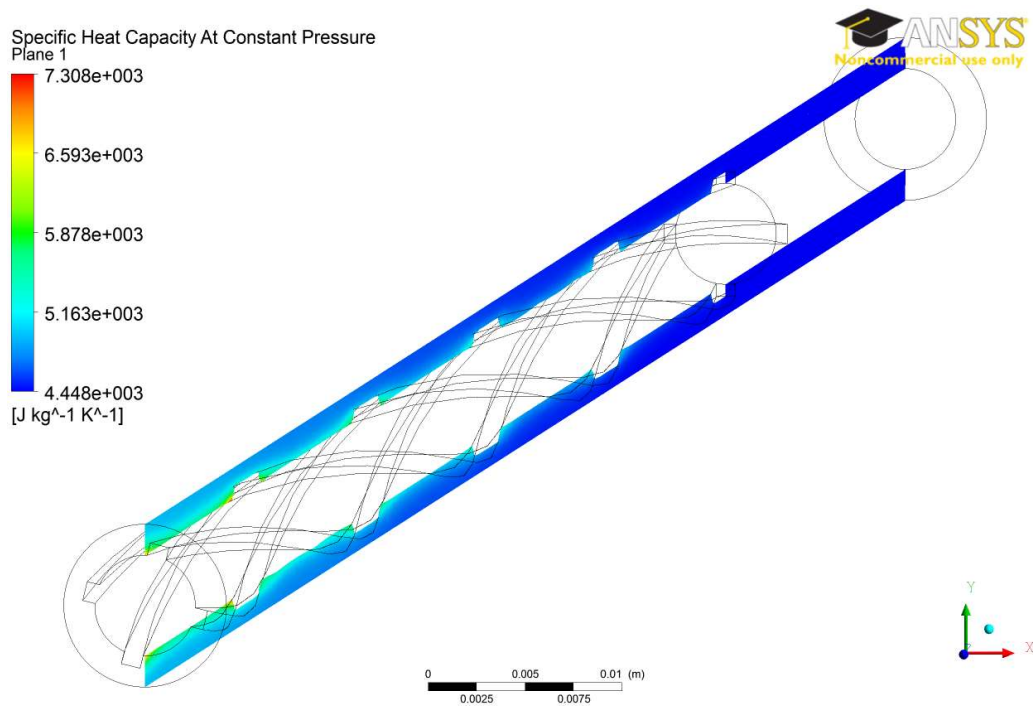


Figure 5-72: Specific heat contours at a longitudinal cross section in the annular channel with helical fins (SST model, $P = 22.6$ MPa, $G = 2000$ kg/m²s, $q = 2.547$ MW/m²)

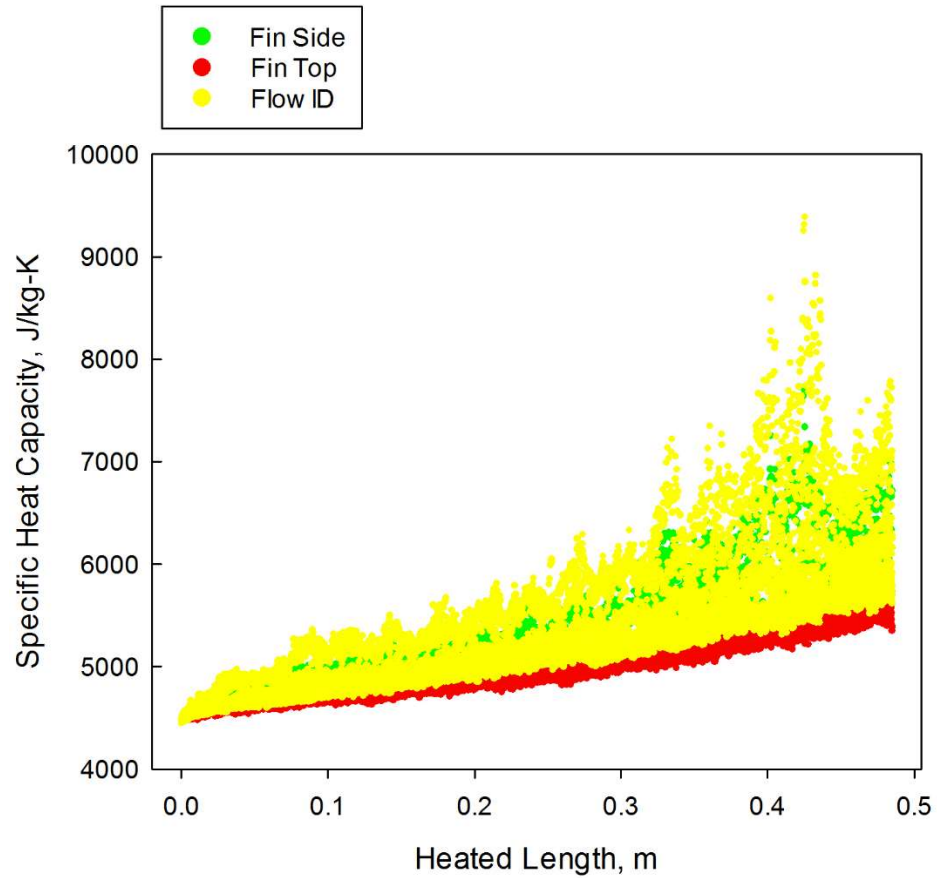


Figure 5-73: Specific heat for the fluid at the heated walls in the annular channel with helical fins (SST model, $P = 22.6$ MPa, $G = 2000$ kg/m²s, $q = 2.547$ MW/m²)

Table 5-2: Specific heat variation with temperature at a constant pressure

Temperature, °C	Pressure, MPa	Cp, kJ/kg-K
375	22.6	55.588
375.5	22.6	101.75
375.8	22.6	274.55
375.9	22.6	492.78
376	22.6	524.11
376.1	22.6	359.54
376.2	22.6	251.01
376.5	22.6	132.01
377	22.6	78.061

5.7 Sources of Uncertainties

Throughout this section, analysis of a complex geometry in the form of an annular channel with helical fins is conducted using an unstructured free mesh for a range of operating conditions. In a numerical analysis with experimental components, some uncertainties arise from both aspects and potentially introduce errors in the results.

Experimentally, the uncertainties mainly arise from the physical structure of the experimental apparatus and the measurement devices used. As the helical pipe is electrically heated, any variation in the thickness of the pipe affects the electrical resistance which in turn affects the heat flux at that point. In addition, the temperature change in the material also affects the electrical resistivity. This means the heat flux out of the heated surfaces is in fact variable. Moreover, as the geometry is inherently variable in thickness; comprising of bare and finned parts, the heat flux out of the surfaces is unlikely to be equal at the fins and the bare surface, as the electrical current will follow the path of least resistance.

As for the measurement devices, the thermocouples used in the experimental apparatus are engraved in a copper plug of the same diameter as the inner rod. The plugs are covered in a silicone resin to provide electrical insulation. Although the authors claim an average temperature is measured at every cross section due to the thermal conductivity of the copper, the measurement point itself is only at the tip of the thermocouple, and there will be variation in the temperature in the copper plug due to the lack of uniformity in the geometry. As shown in the simulation results, the differences between the surface temperatures of the fin top, fin side, and bare tube sections are not insignificant and it is doubtful that the thermocouple measures the true averaged temperature at a given cross section.

Numerically, on the other hand, uncertainty sources are found at every step of the numerical analysis method; geometry creation, meshing, and solving the conservation equations.

During the geometry creation, the assumption is a clean geometry with no variation in thicknesses. There is also an artificial unheated entrance region introduced to develop the flow before entering the heated region. This is likely to represent the true experimental setup, however the length of this entrance region is not reported in the experimental setup description.

During the mesh construction, it was apparent that the ICEM software is not capable of producing a viable mesh (with acceptable quality) using the default 3D blocking method. The only working mesh was attainable using 2D to 3D blocking technique, and only using a free unstructured mesh. The problem with this approach is the amount of RAM needed to create the mesh, which restricts the minimum size of the computational cells, and the inability to build a boundary layer for this type of mesh.

In the solver, using a semi-empirical model (2-equation models such as SST or RKE) means, as the name implies, the introduction of empirical constants, and simplified conservation equations using assumptions to improve the speed at which a solver can produce simulation results. In addition to the turbulence models, the fluid properties at supercritical flow conditions are imported from NIST REFPROP through an interface with the FLUENT solver. REFPROP is a program and not a database, and does not contain any experimental information. The program uses equations for the thermodynamic and transport properties to calculate the state points of the fluid. The uncertainties are not reported for all properties and in many cases they are not known, especially in areas such as the pseudocritical region where steep changes in properties are observed within a very small corresponding temperature change.

As fluid properties are updated whenever new and “more accurate” experimental data are available, the reported properties for any fluid should be taken as the best available option but not necessarily a true representation of reality. And because

REFPROP is in fact a coded program, there will be issues and bugs in the software. Examples of such bugs in the latest version of the software as reported by NIST are: "Calculation of isobars for pure fluids at pressures less than the triple point pressure may incorrectly return properties in the liquid phase rather than the vapor phase" and "Inputs of enthalpy or entropy may not converge, or will converge to the wrong phase" [59]. When CFD simulations call for fluid properties for thousands or millions of computational cells every iteration for potentially thousands of iterations (until convergence is achieved), it is virtually impossible to track and verify the validity of all recalled properties in the solver.

Chapter 6: Sudden Area Change Geometry

This chapter describes the results and analysis for the effects of a sudden area change in SCW flow conditions. Simulations of the tube with a sudden area change were conducted for the normal and deteriorated heat transfer conditions, using the turbulence models developed throughout this work, as shown in the test matrix in Table 3-9.

Figure 6-1 to Figure 6-20 show the 3D plots, contours, and streamlines for a normal heat transfer case with the same parameters as the case studied in Chapter 4: $G = 1002 \text{ kg/m}^2\text{s}$, $q = 391 \text{ kW/m}^2$, $P = 24 \text{ MPa}$, however with the addition of an orifice to the geometry, 10 cm into the entrance region (10 cm before the heated length), as well as the results for a simulation with the orifice 20 cm into the heated length.

The contour in Figure 6-1 shows the temperature distribution in the computational domain, which includes the unheated entrance region and the heated flow section. To analyze the data in a similar manner to the bare tube geometry, a plane is created in the post analysis software (CFD Post), in the center of the geometry - YZ plane - as shown in Figure 6-2.

Figure 6-3 represents the temperature distribution in this central plane, including the unheated region. The figure is built using SigmaPlot software, to show the contour in a color coded scheme. The wall temperature at the outlet reaches roughly 410°C , whereas the contour shown directly from CFD Post (Figure 6-1) shows a maximum of 396°C . To analyze this discrepancy, the raw data was analyzed and sorted, and no temperatures above 396°C were found in the data. Similar issues were found in the rest of the property graphs, such as specific heat, density, and velocity. When the figure type was changed to a scatter plot such as the one in Figure 6-4, it became apparent that the fault was in the interpolation scheme used by SigmaPlot to create the contour mesh. For this reason, the subsequent graphs in this section are shown as 3D scatter plots instead. They show

the same information with the same details, however they are not color-coded for minimum and maximum values.

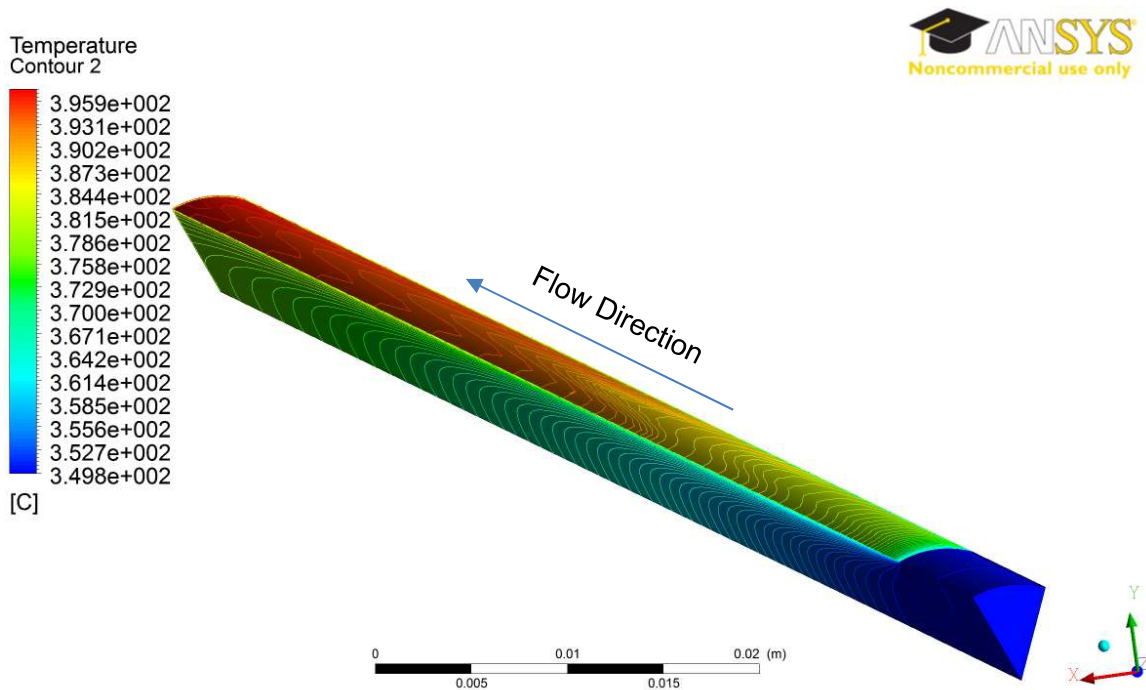


Figure 6-1: 3D temperature contour plot for a tube with an orifice in the entrance region with: $P = 24 \text{ MPa}$, $G = 1002 \text{ kg/m}^2\text{s}$, and $q = 391 \text{ kW/m}^2$, using the RKE model

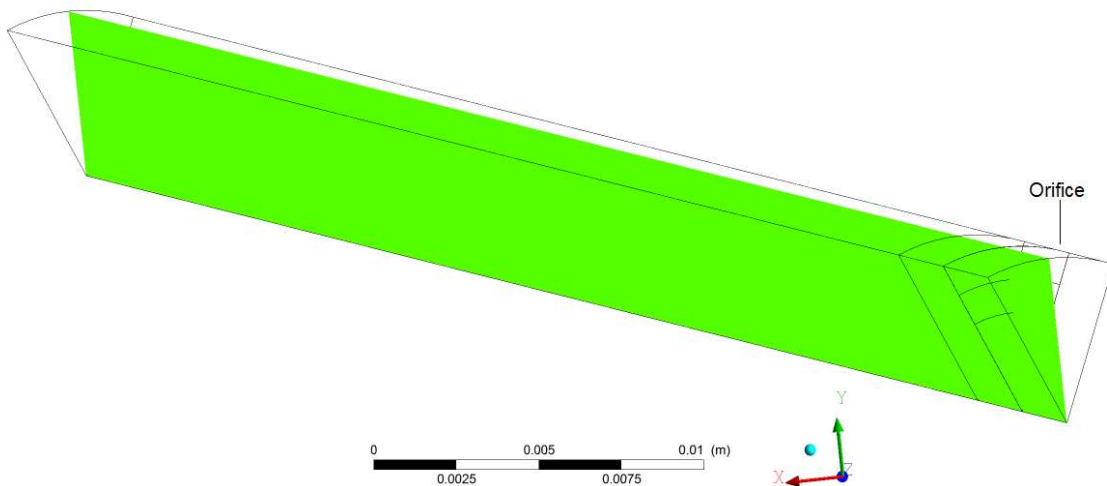


Figure 6-2: Center plane in the 3D mesh of 1/8 tube with an orifice in the entrance region

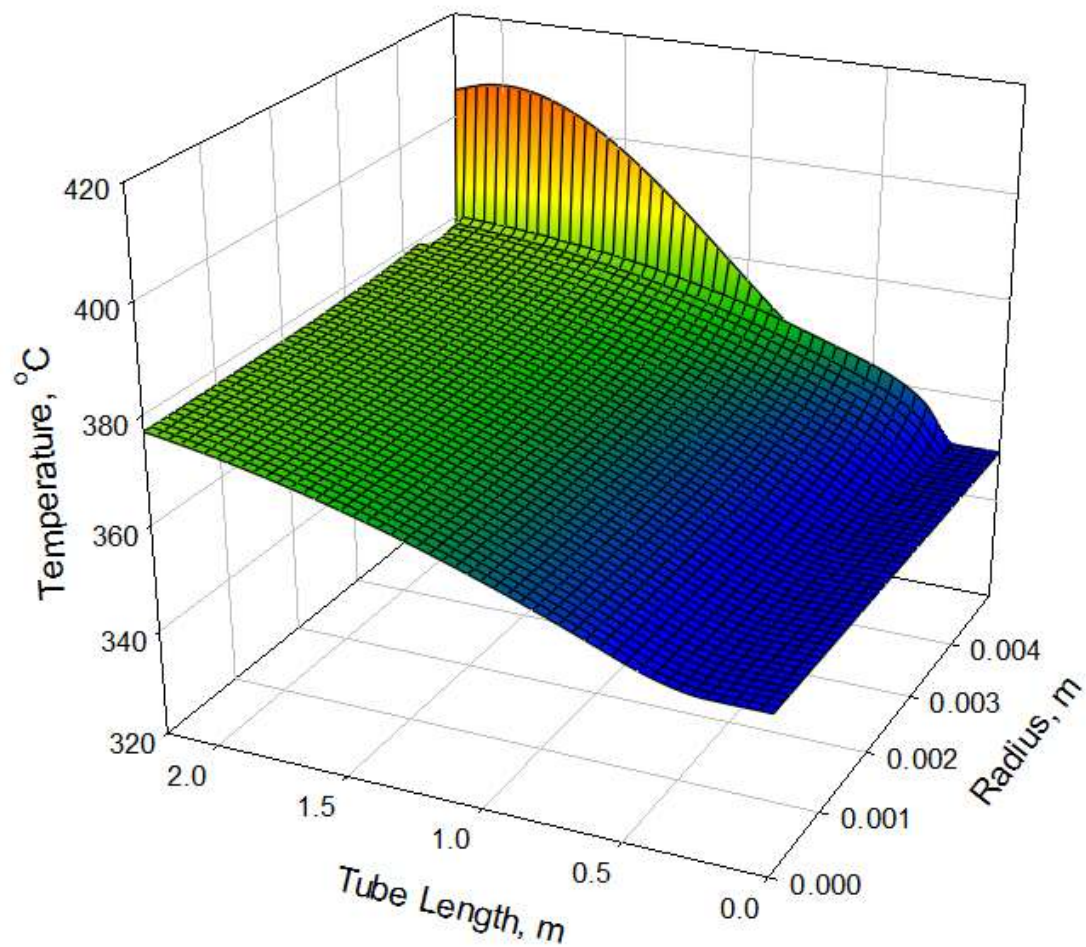


Figure 6-3: 3D temperature plot for a tube with an orifice in the entrance region with: $P = 24 \text{ MPa}$, $G = 1002 \text{ kg/m}^2\text{s}$, and $q = 391 \text{ kW/m}^2$, using the RKE model

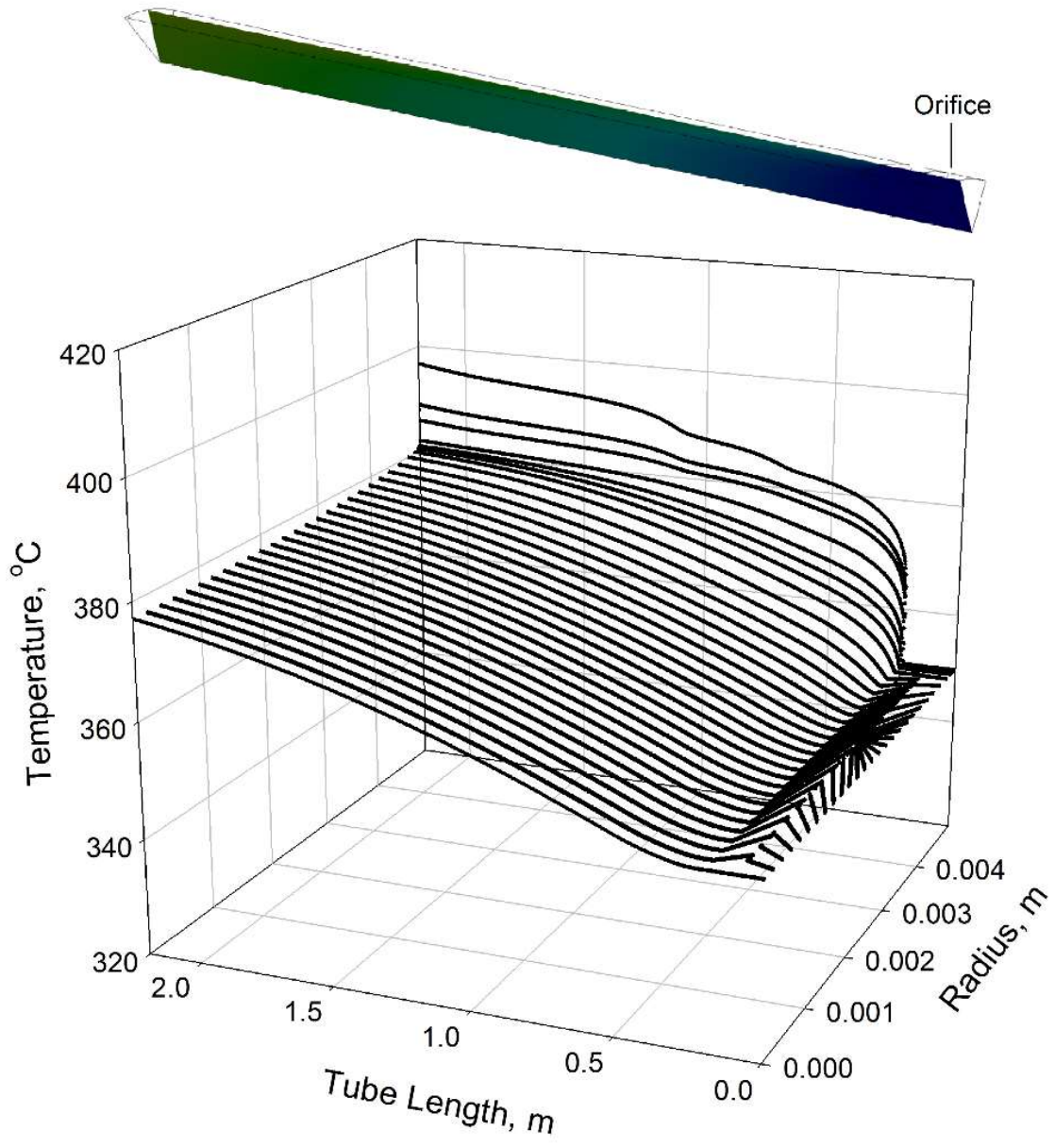


Figure 6-4: 3D temperature scatter plot for a tube with an orifice in the entrance region with: $P = 24$ MPa, $G = 1002$ kg/m²s, and $q = 391$ kW/m², using the RKE model

The temperature shown in the scatter plot follows a similar trend to the simple tube with no perturbation in the entrance region, and reaches similar values throughout the flow region. It can be noticed that nodes have a higher density midway through the entrance region, and to explain the node distribution around the orifice, Figure 6-5 shows a close-up of the mesh in its vicinity. As the boundary layer grows from each of the walls into the flow, there will be a higher density of nodes around the orifice area which has 5 walls in close proximity, resulting in the distribution shown in the figure.

Figure 6-6 shows the turbulent kinetic energy distribution, while Figure 6-7 shows only the heated region, to better depict the changes throughout the flow region which are overshadowed by the change through the orifice, which is two orders of magnitude higher than the rest of the flow. Figure 6-6 shows that there is significant turbulence generated at the orifice but it dissipates shortly afterwards.

The same trends are observed in the turbulence intensity in Figure 6-8 and the cutout without the entrance region in Figure 6-9. Throughout the heated region, the turbulence intensity is on par with that in the bare tubes, as the intensity, which reaches up to 60% through the orifice, dissipates in the next ~15 cm.

Similarly, the specific heat plot in Figure 6-10 and the velocity in Figure 6-11 show similar trends and values to those of the bare tube in the heated region. This means the quick production and dissipation of turbulence does not carry the effects downstream and the resulting property fields resemble that of a tube without the orifice geometry.

Figure 6-12 shows a close-up of the entrance region, showing the velocity changes through the orifice, which can reach 4 times its value through the orifice in the unheated region. The recovery of the velocity back to its mean value occurs within ~7 cm of the orifice, after which, and throughout the flow, the velocity profile resembles that of a bare tube again.

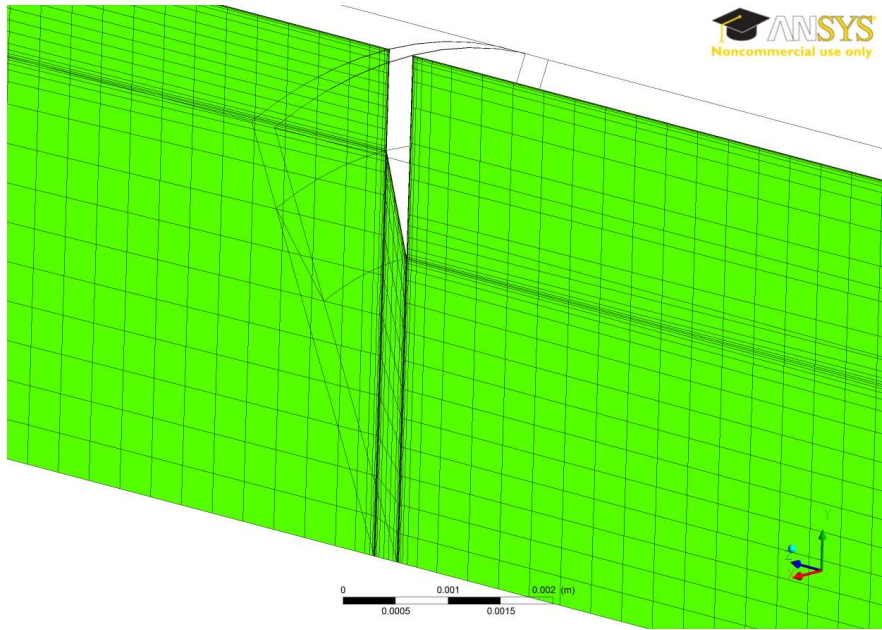


Figure 6-5: Close-up of the orifice geometry with the mesh lines showing the higher density around the orifice walls

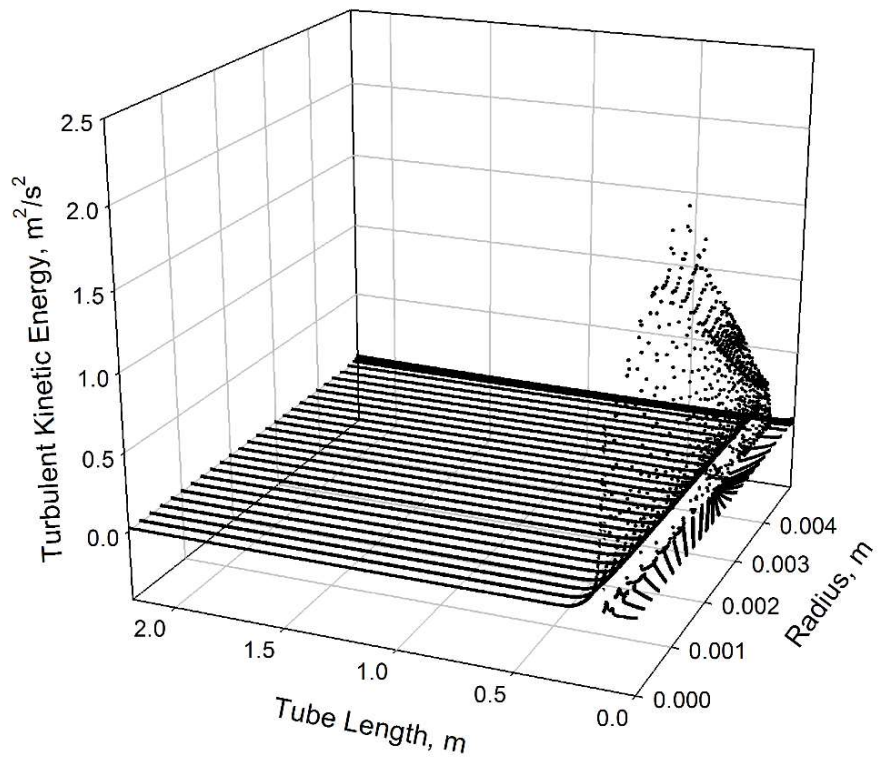


Figure 6-6: 3D turbulent kinetic energy scatter plot for a tube with an orifice in the entrance region: $P = 24$ MPa, $G = 1002$ kg/m²s, and $q = 391$ kW/m², using the RKE model

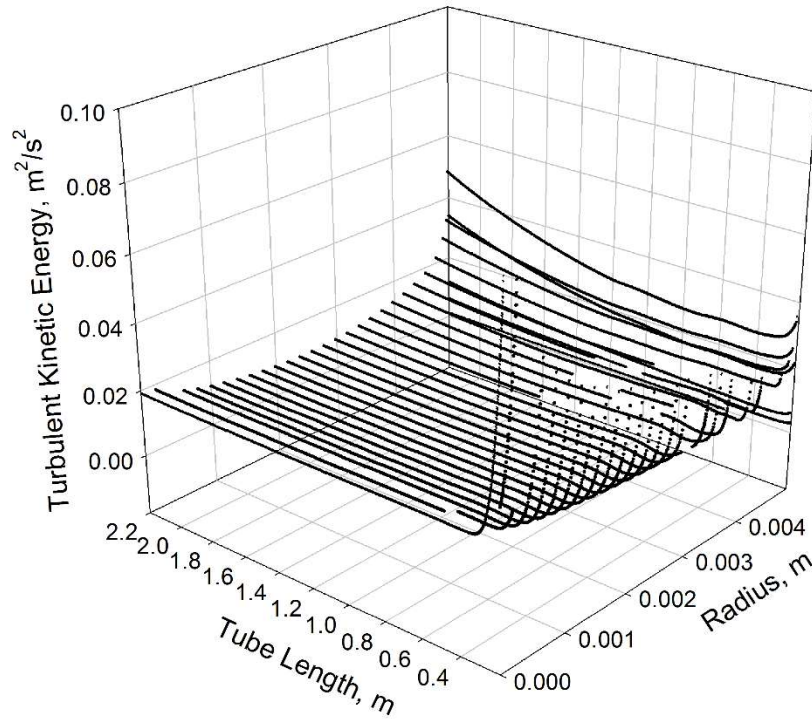


Figure 6-7: 3D cutout of turbulent kinetic energy plot for a tube with an orifice in the entrance region: $P = 24 \text{ MPa}$, $G = 1002 \text{ kg/m}^2\text{s}$, and $q = 391 \text{ kW/m}^2$, RKE model

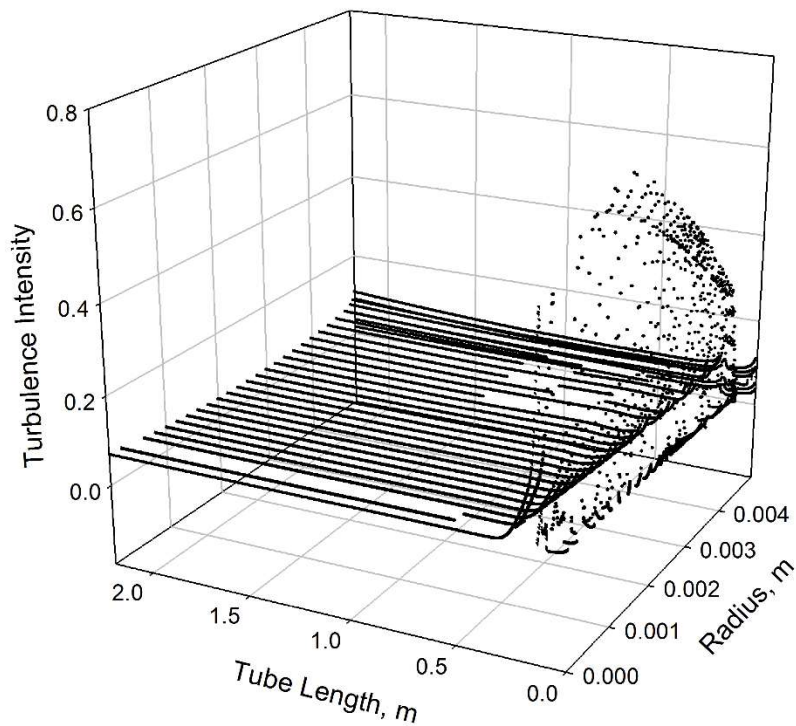


Figure 6-8: 3D 3D turbulence intensity scatter plot for a tube with an orifice in the entrance region: $P = 24 \text{ MPa}$, $G = 1002 \text{ kg/m}^2\text{s}$, and $q = 391 \text{ kW/m}^2$, RKE model

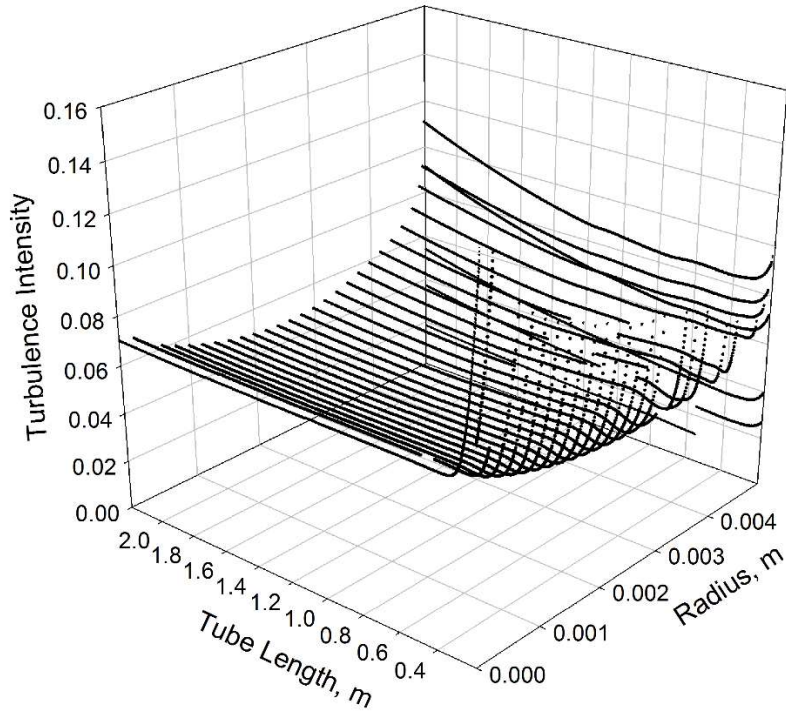


Figure 6-9: 3D cutout of turbulence intensity plot for a tube with an orifice in the entrance region: $P = 24 \text{ MPa}$, $G = 1002 \text{ kg/m}^2\text{s}$, and $q = 391 \text{ kW/m}^2$, RKE model

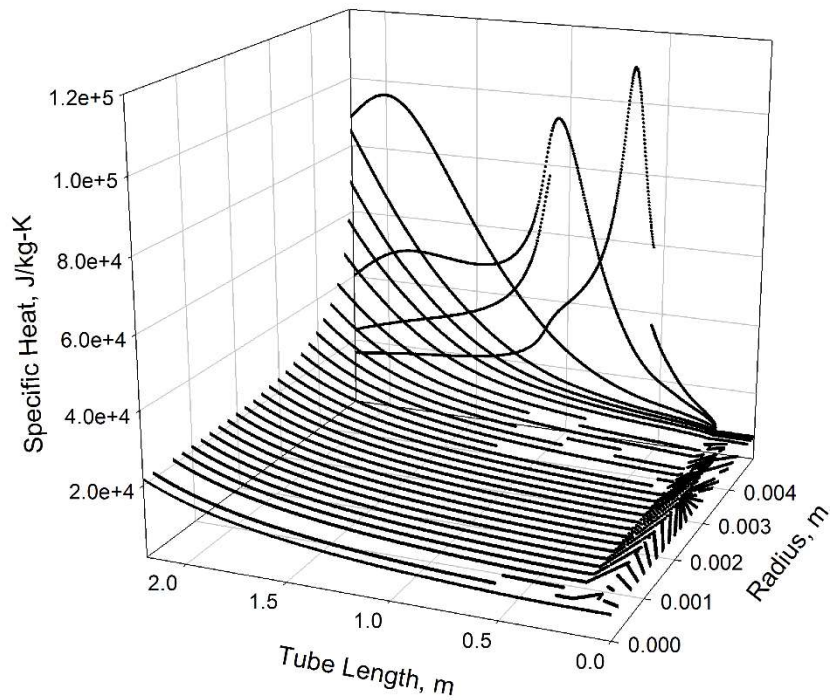


Figure 6-10: 3D Specific heat scatter plot for a tube with an orifice in the entrance region: $P = 24 \text{ MPa}$, $G = 1002 \text{ kg/m}^2\text{s}$, and $q = 391 \text{ kW/m}^2$, RKE model

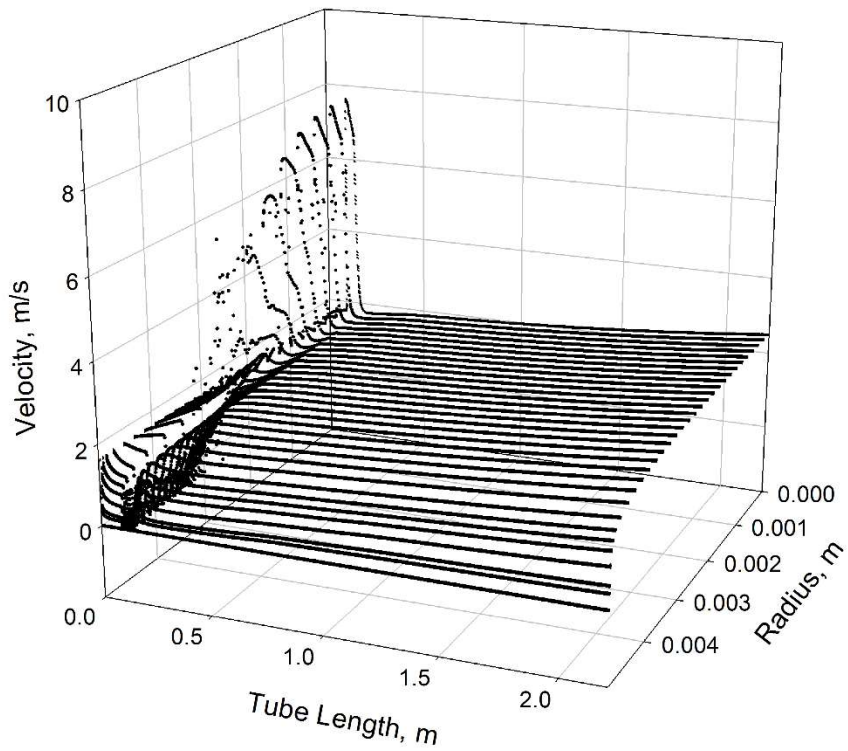


Figure 6-11: 3D Velocity scatter plot for a tube with an orifice in the entrance region: $P = 24$ MPa, $G = 1002$ kg/m²s, and $q = 391$ kW/m², using the RKE model

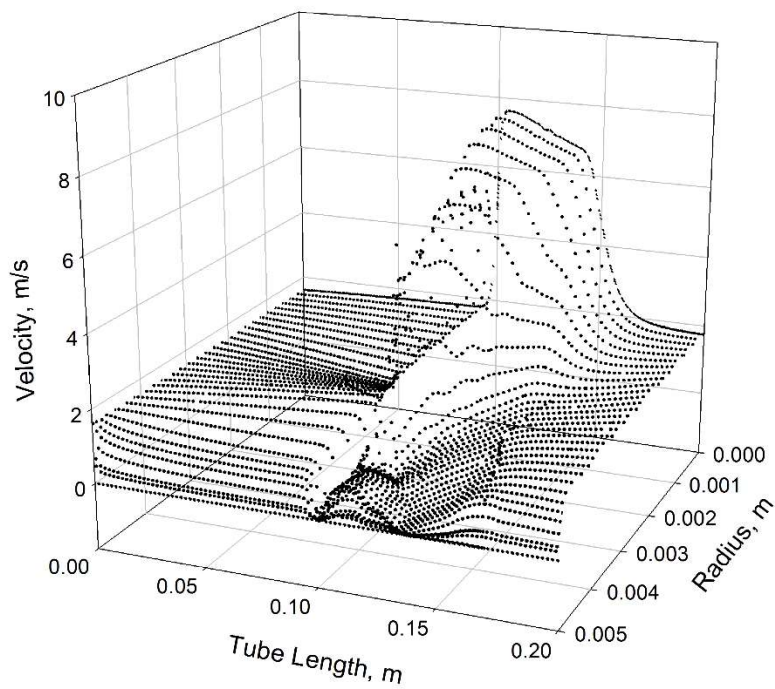


Figure 6-12: 3D Velocity scatter plot for the tube entrance region with an orifice: $P = 24$ MPa, $G = 1002$ kg/m²s, and $q = 391$ kW/m², using the RKE model

After studying the effects of the orifice in the unheated region, it is placed 20 cm in the heated length, to study its effects on heated flow, using the same operating parameters.

Figure 6-13 shows the temperature scatter plot for the same central plane location (YZ plane). The density of nodes around the orifice is also notably higher than the rest of the flow region. The first observation regarding the outlet temperatures is the reduction in wall temperature at the outlet, compared to the bare tube and a tube with an orifice in the entrance region. At 385°C, this is a reduction of 10 °C (or 2.6%).

This can be explained by tracing the temperature distribution back to the orifice, where, due to the high turbulence and mixing in the flow, the heat is transferred to the center of the flow much more efficiently, and just after the orifice, the temperature profile shows a rise in the mean flow fluid temperature and a drop in the wall temperature. This mixing effect carries over until the outlet where the wall temperature is lower than a case without the orifice, and with the orifice in the entrance region, due to the transfer of more heat away from the wall.

It is also notable here, that there is stagnation occurring when the flow hits the orifice, and this results in a temperature increase at that area, as shown by the nodes at a higher temperature at 1.4 m. The temperature at that location is not unreasonably high (it is lower than the exit temperature at the wall), however it should be taken in consideration for operating conditions with higher heat fluxes at the wall.

The specific heat plot in Figure 6-14, shown in this particular case, the fluid does not go through the pseudocritical point as it passes through the orifice. In fact, it only reaches it at the outlet, similar to that in the previously studied cases. The mixing effect helps to keep the fluid temperature at the wall low and thus delays passing through the pseudocritical point.

Figure 6-15 shows a similar velocity profile to that of the orifice in the entrance region, however as the density drops in the heated section, the velocity reaches higher values as shown in the close-up plot in Figure 6-16. Figure 6-17 represents the velocity as streamlines in the vicinity of the orifice, to show the stagnation zone, the acceleration through the contracted area, and the recirculation of the flow afterwards. Figure 6-18 is the same streamlines depiction, but from farther back, to show the entire recirculation and recovery zones. The recovery of flow occurs in this case within 3-4 cm of the orifice, at which point the velocity distribution reverts back to the bare tube distribution studied earlier.

The rapid recovery of the velocity distribution means the flow loses the turbulence generated by the orifice quicker than in the case of the entrance region orifice. And while the effects of the turbulence do propagate throughout the heated region and result in a lower wall temperature at the outlet, it does mean – in the case of fuel channel design – that there might be a need to induce sudden area change geometries more frequently, to maintain the turbulence levels and maintain active cooling of the heated walls.

The turbulence intensity profile in Figure 6-19 shows a higher turbulence level in the flow compared to the orifice in the entrance region (up to 76%), however for the rest of the heated length, the turbulence levels recover to similar values to previous cases as shown in Figure 6-20. The higher levels of turbulence achieved through the orifice, and the fact that it mixes the heated flow, appear to be the main contributors to enhancing the heat transfer

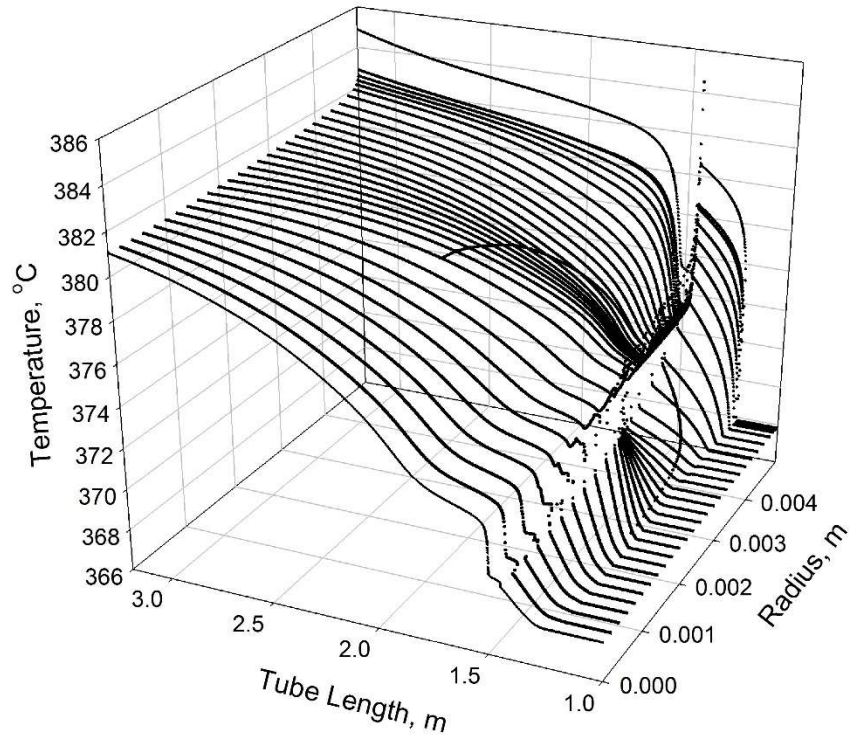


Figure 6-13: 3D Temperature heat plot for a tube with an orifice 20 cm into the heated length with: $P = 24 \text{ MPa}$, $G = 1002 \text{ kg/m}^2\text{s}$, and $q = 391 \text{ kW/m}^2$, using the RKE model

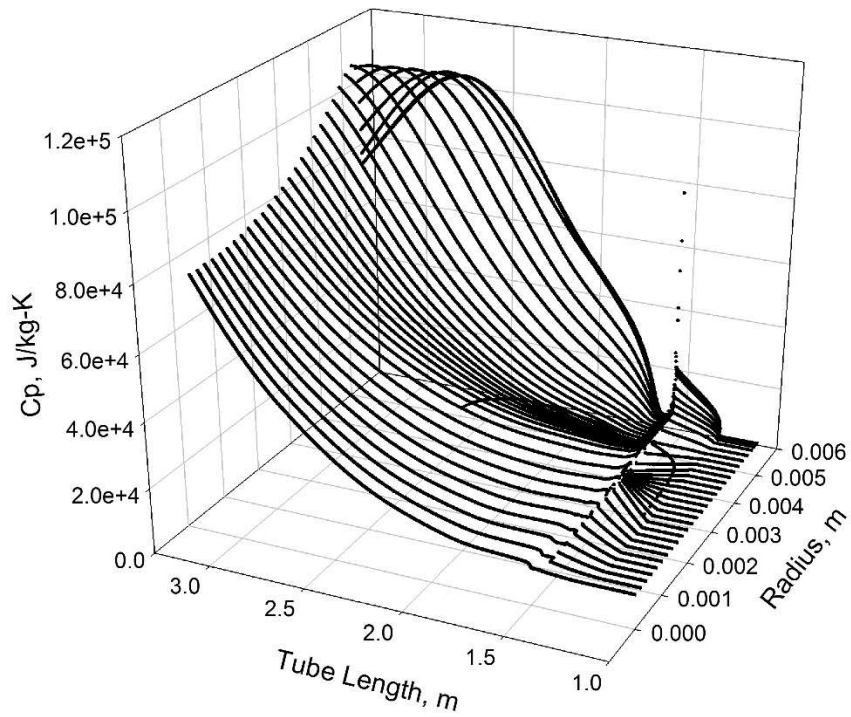


Figure 6-14: 3D Specific heat plot for a tube with an orifice 20 cm into the heated length with: $P = 24 \text{ MPa}$, $G = 1002 \text{ kg/m}^2\text{s}$, and $q = 391 \text{ kW/m}^2$, using the RKE model

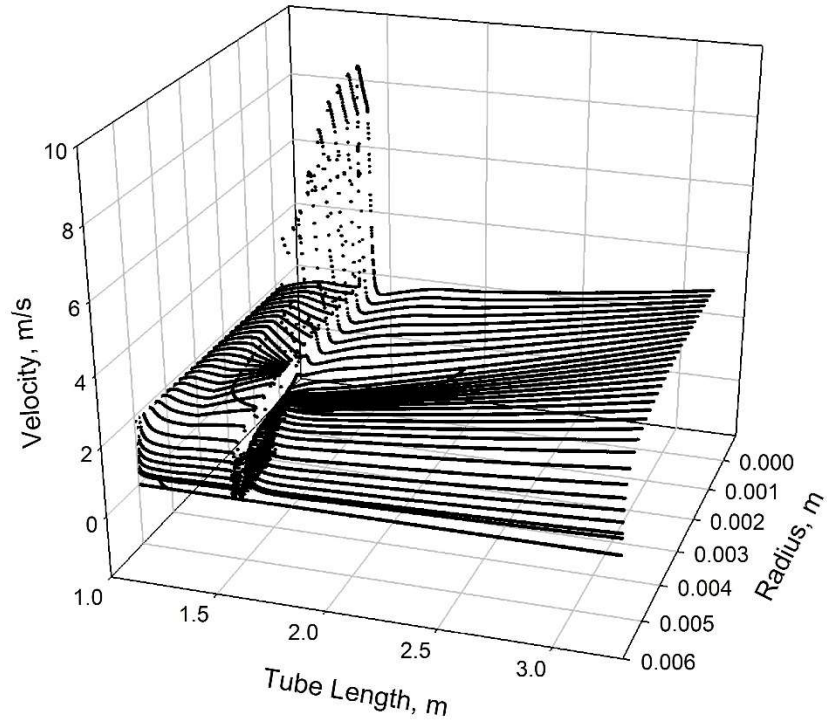


Figure 6-15: 3D Velocity plot for a tube with an orifice 20 cm into the heated length with: $P = 24$ MPa, $G = 1002$ kg/m²s, and $q = 391$ kW/m², using the RKE model

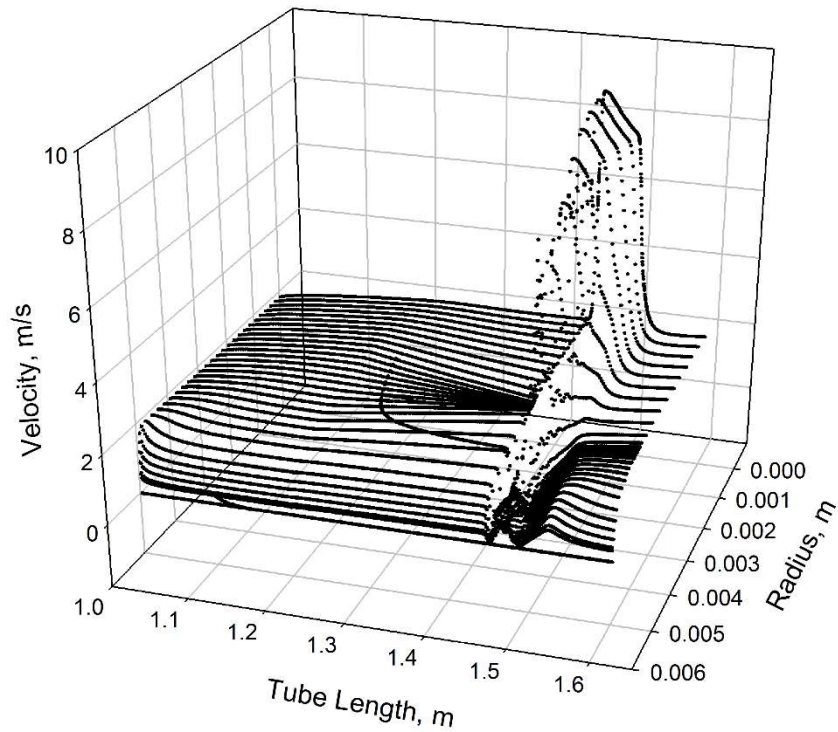


Figure 6-16: 3D cutout of Velocity plot for a tube with an orifice 20 cm into the heated length with: $P = 24$ MPa, $G = 1002$ kg/m²s, and $q = 391$ kW/m², using the RKE model

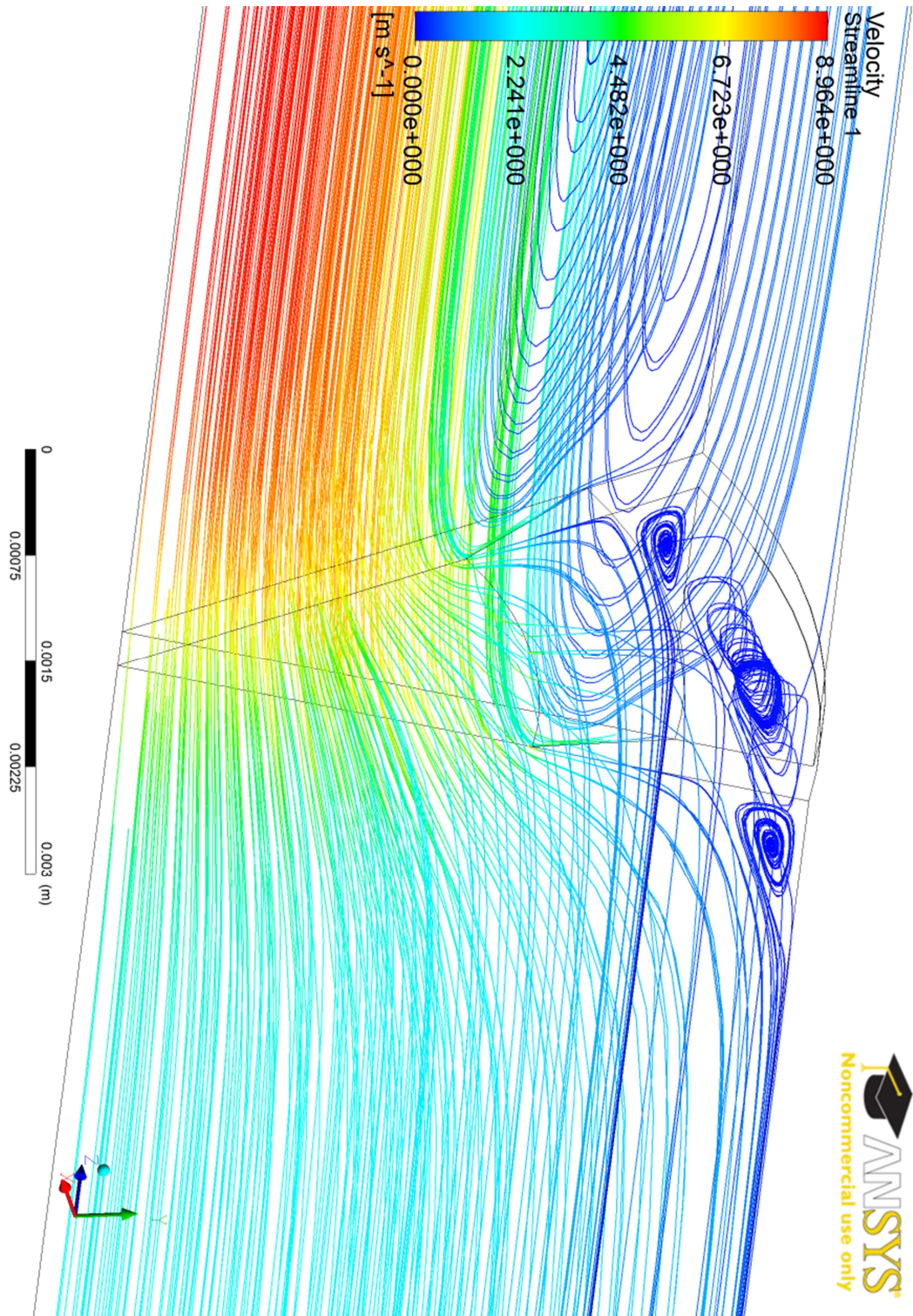


Figure 6-17: Velocity streams visualization around the orifice 20 cm into the heated length with: $P = 24$ MPa, $G = 1002$ kg/m²s, and $q = 391$ kW/m², using the RKE model

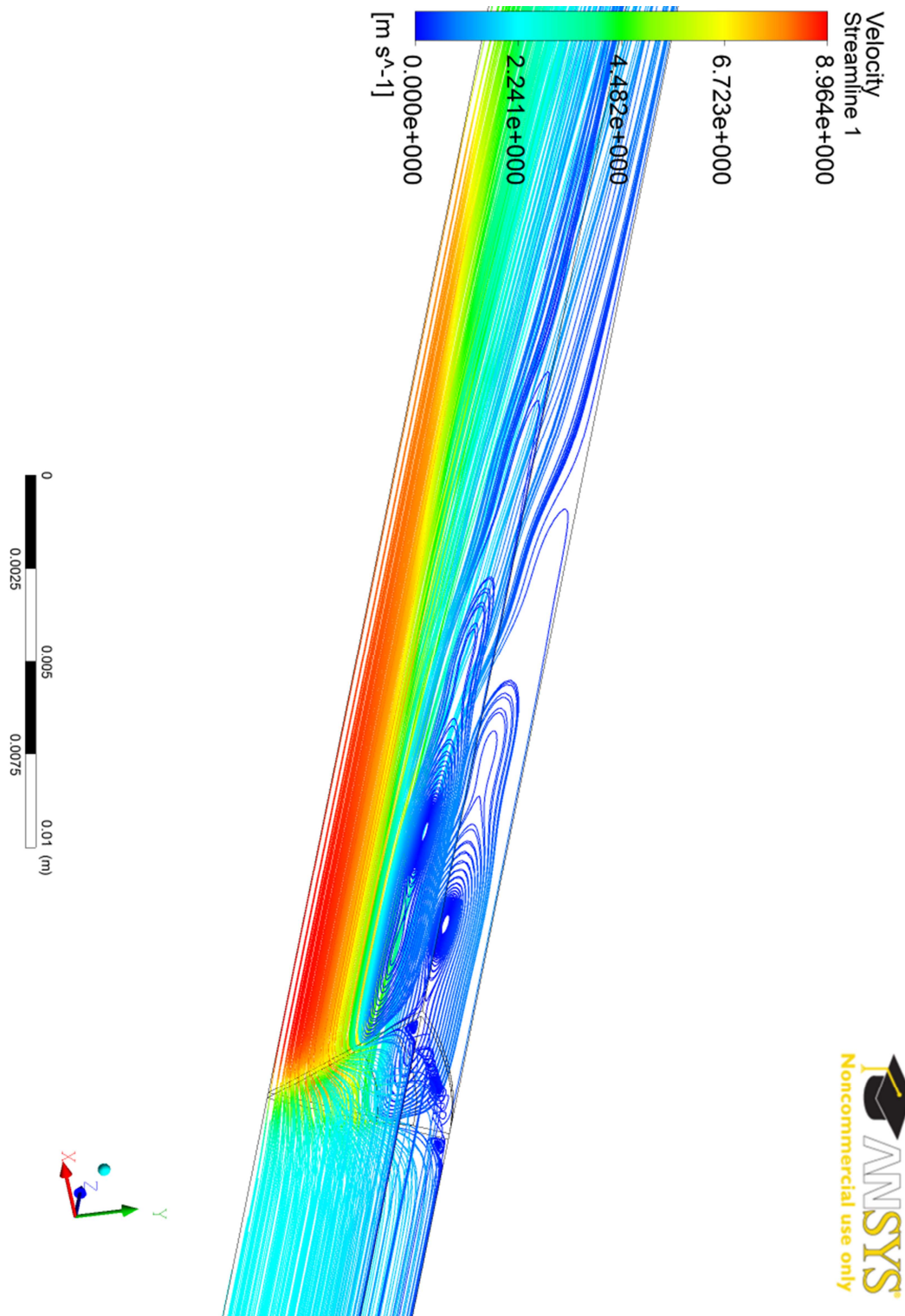


Figure 6-18: Velocity streams visualization around the orifice 20 cm into the heated length with: $P = 24 \text{ MPa}$, $G = 1002 \text{ kg/m}^2\text{s}$, and $q = 391 \text{ kW/m}^2$, using the RKE model

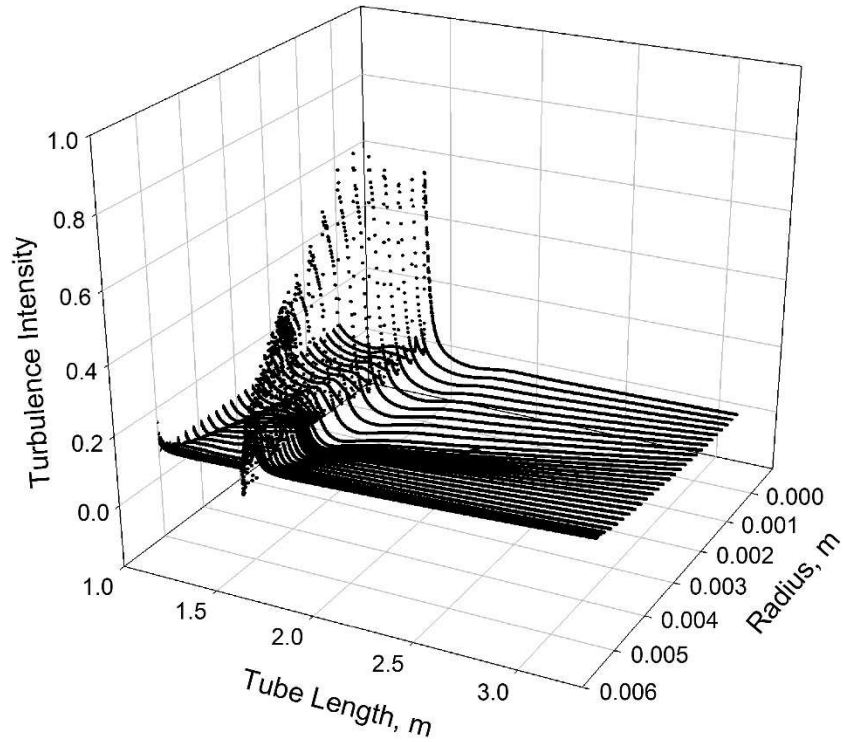


Figure 6-19: 3D Turbulence intensity plot for a tube with an orifice 20 cm into the heated length with: $P = 24 \text{ MPa}$, $G = 1002 \text{ kg/m}^2\text{s}$, and $q = 391 \text{ kW/m}^2$, RKE model

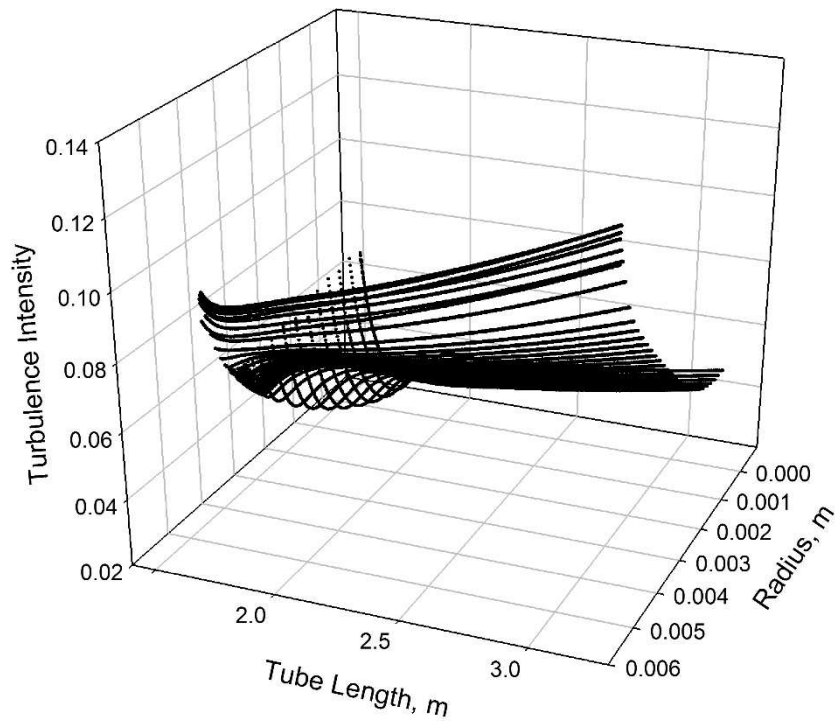


Figure 6-20: 3D Turbulence intensity plot for a tube after the orifice 20 cm into the heated length with: $P = 24 \text{ MPa}$, $G = 1002 \text{ kg/m}^2\text{s}$, and $q = 391 \text{ kW/m}^2$, RKE model

The next step in the study would be to analyze higher heat flux cases reaching into the DHT regime. However, when simulating the DHT case studied earlier in chapter 4, no convergence was reached using any model. In the case of an orifice in the entrance region, low levels of convergence are achieved and the results show large discontinuities in the temperature profiles. In the case of an orifice in the heated section, the recirculation zone at the orifice would lead to wall temperatures in excess of those allowed by the solver, resulting in divergence. To find out where the cutoff region is for the CFD code, Table 6-1 shows some of the simulations conducted on various cases with increasing ratio of heat flux to mass flux. The table also shows the distance between the pseudocritical point for the bulk fluid and the location of the orifice, for tests of 1-3 m and 2-4 m in the heated region respectively.

Table 6-1: Test matrix of tube with orifice geometry simulations

$G, \text{kg/m}^2\text{s}$	$q'', \text{kW/m}^2$	q''/G	convergence	$x_{pc} - x_{orif}$
1002	391	0.4	Yes	~1.9 m, 0.9 m
1500	1022	0.68	Yes	~0.8 m, -0.1 m
1489	1164	0.78	No	~0.45 m, -0.5 m
1496	1235	0.83	No	~0.95 m, -0.05 m

The wall temperature results for the second and third cases are shown in Figure 6-21 and Figure 6-22. The second case is a NHT regime, while the third case shows deterioration in the heat transfer half way through the heated length, as the bulk fluid passes through the pseudocritical point. Of note is the poor prediction of wall temperatures for the DHT case, when the computational domain (1-3 m) includes sections with normal and deteriorated regions. This result can be attributed to the constant turbulent Pr used in the simulation, as it was shown earlier that it takes a different value in the deteriorated region, and thus the same constant value will not capture both phenomena.

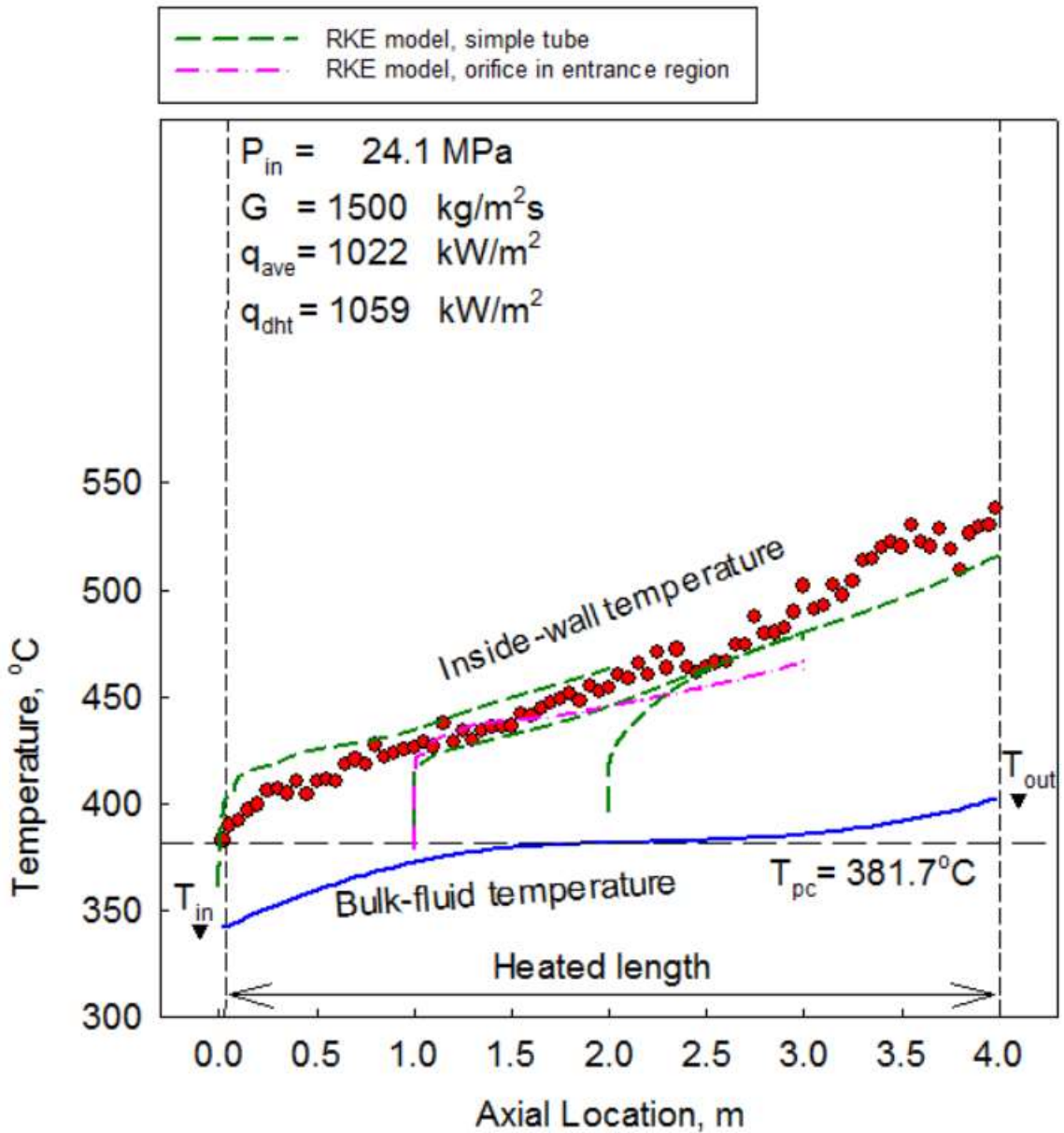


Figure 6-21: Wall temperature results for simple tube and tube with orifice in entrance region, $P = 24.1$, $G = 1500 \text{ kg/m}^2\text{s}$, and $q = 1022 \text{ kW/m}^2$, using the RKE model

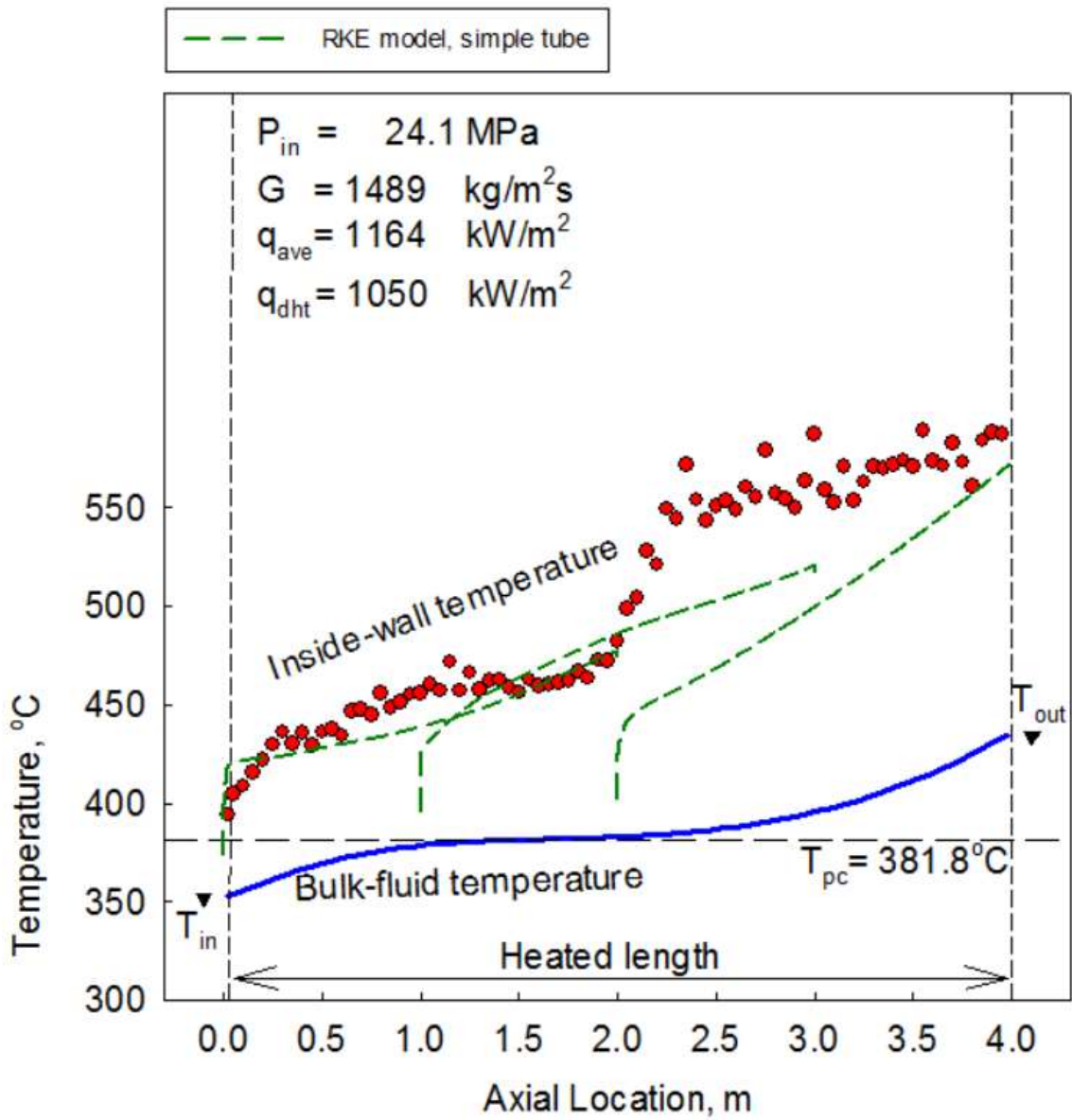


Figure 6-22: Wall temperature results for simple tube and tube with orifice in entrance region, $P = 24.1$, $G = 1489 \text{ kg/m}^2\text{s}$, and $q = 1164 \text{ kW/m}^2$, using the RKE model

Chapter 7: Concluding Remarks and Recommendations

The work presented in this document accomplished the objectives stated in section 1.2. The CFD code FLUENT is benchmarked using the realizable $k-\varepsilon$ (RKE) and Shear Stress Transport $k-\omega$ (SST) on supercritical water flow in vertical bare tubes. The effects of the turbulent Pr number on SCW flow and heat transfer are analyzed and a model is developed to enhance the numerical prediction in the DHT regime. Basic understanding of the various heat transfer regimes is necessary before attempting to study more complex geometries resembling those of a reactor core.

SCW flow has been characterized in helically finned annular channels and sudden area changes in tubes, to establish geometry effects on heat transfer. There is a need to develop a fundamental understanding of SCW behaviour in complex geometries in order to be able to predict its behaviour in a real reactor geometry.

7.1 Concluding Remarks

The following remarks can be ascertained from this work:

- 1- For the turbulent Prandtl number and bare tube geometry: the heat transfer characteristics of SCW flow need to be understood for simple geometries under normal and deteriorated heat transfer regimes. Defaults models of RKE and SST are able to reproduce NHT results with very low errors (<4%), however in the DHT regime higher errors are produced.
- The turbulent Pr number is used as a constant in the CFD models, however it is well known to be variable in value.
- A value of 0.75 for the energy turbulent Pr number in the turbulence production by buoyancy equation, has demonstrated the best fit for DHT conditions using the RKE model. The original value in turbulence models is set at 0.85.

- To reach convergence and continuous accurate prediction of heat transfer in computational domains including both NHT and DHT regimes, a variable Pr_t should be implemented in the CFD code.
 - A lower turbulent Pr indicates an important physical phenomenon in heat transfer under supercritical conditions in upward flows. As heat transfer approaches the onset of deterioration, the influence of buoyancy increases and it works to reduce the turbulent shear stress in the flow, leading to higher wall temperatures.
 - Conversely, the effect of buoyancy is studied in downward flows, and is shown to mitigate the deterioration found in upward flows.
- 2- For the annular flow channel with helical fins: reactor fuel geometries will include geometric perturbations in order to develop turbulence in the flow and enhance heat transfer. Experimental data is available for a helically finned annular flow under SCW flow conditions.
- Using a relatively coarse free mesh to simulate an annular channel with helical fins has shown good agreement with experimental data under NHT conditions.
 - The helicity of the geometry does not induce turbulence in the flow, and the simulations have shown similar results for cases with straight fins.
 - When comparing these results to annular channel geometries with no fins, and equivalent total energy imparted to the fluid, the fins have shown improvement in heat transfer and lower wall temperatures.
 - The CFD models were unable to predict any deterioration in heat transfer in this geometry, in cases where experimental wall temperatures depict an onset of deterioration. This result is attributed to the coarse unstructured mesh not capturing the fine changes as the fluid crosses the pseudocritical point.
- 3- For sudden area change geometry: As the helically finned channel geometry did not produce sufficient levels of turbulence, there was a need to create another geometry which can generate high levels of turbulence to

mimic a real reactor geometry. Orifices exist in fuel channels as a flow control device, and also resemble the sudden area change geometries represented by fuel bundle appendages.

- A sudden area change geometry is studied to show the effects of geometric perturbations on SCW flow and heat transfer. The selected geometry is a thin orifice placed in the unheated and heated sections of a vertical tube.
- Both cases have shown an improvement in the turbulence production in the flow in the NHT regime (roughly 60% turbulence intensity), with the orifice in the heated section showing enhanced mixing leading to a lower outlet temperature at the wall.
- Placing turbulence enhancing appendages in a SCWR fuel geometry is necessary due to the lower HTC's in SCW, and due to the quick dissipation of turbulence under these conditions, the appendages may have to be closely packed (within 15-20 cm of each other), to maintain the high levels of turbulence and lower temperatures at the fuel surfaces.
- The recirculation zones created by the orifice geometry lead to very high wall temperatures in the DHT cases, resulting in divergence in the solver. The limitation in the solver appears to be when the ratio of heat flux to mass flux approach values around 0.78, which corresponds to the onset of DHT regime.
- CFD multidimensional analysis cannot be corroborated without experiments showing those multidimensional traits of the flow under supercritical conditions. Current available experiments only show wall temperature measurements, which do not give sufficient information to reach firm conclusions about the flow and heat transfer phenomena in supercritical fluids.

7.2 Contribution to Knowledge

The contribution to knowledge in the fields of CFD and supercritical water heat transfer from this thesis can be summarized as:

- Determination of the turbulent Pr effect on SCW flow and heat transfer characteristics
- Distinguishing the differences between downward and upward flows on the turbulence production and heat transfer in SCW
- Determining the effect of helical fins geometry on SCW flow and heat transfer
- Analysis of the mechanics of turbulence generation and dissipation and their effect on heat transfer in a sudden area change geometry

Publications related to this contribution to knowledge are listed in Appendix A.

7.3 Future Work

Based on these remarks, the following recommendations are made for future work:

- Experiments are needed to visualize fluid flow properties in supercritical fluids, to validate the findings in CFD simulations. Experimental data have been lacking in detail and consist mainly of 1-D outside-measurements for bare geometries. Techniques such as Schlieren interferometry [69] and Rayleigh scattering [70] has shown some promise in supercritical CO₂ flows, however the data is scarce and isn't available in relevant conditions such as density gradients for flow through the pseudocritical point, or in DHT or IHT conditions. Those experiments could confirm some of the theories proposed to describe DHT, such as the increase in buoyancy forces, creation of pseudo-boiling regimes, and possible separation in flow near and far from the wall.
- Experiments are needed to determine the changes in turbulent Pr in SCW, especially under DHT conditions, to arrive at a description of its variability which will aid future simulations' accuracy, and help make CFD codes valid

for reactor/plant design and analysis purposes. Current proposed methods of implementing the variability of Pr_t are purely functional and are not representative of physical processes occurring in the development of the boundary layer flow. Experimental Pr_t can be derived from measuring values of velocity, temperature, pressure differential, heat flux and shear stress at the wall [66].

- Fluid-to-fluid comparison studies, such as density gradients in supercritical water, CO₂ and Freon, could infer information about the applicability of cheaper and safer modeling fluids for the purposes of reactor design analysis.
- Any real reactor geometry would involve geometric perturbation, likely in the form of a sudden area change, to improve the heat transfer coefficients. Experiments in such geometries are needed to validate CFD codes and understand the phenomena occurring in a geometry such as a fuel bundle/string. Temperature and velocity measurements in such geometries would aid in understanding the turbulence production and dissipation characteristics in SCW flow through geometric perturbations. The proposed geometry in this work provides a simplified platform to study these effects, as it will be used in the SCWR fuel channels and does mimic the fundamental purpose of fuel appendages.

References

- [1] J. Li, G. Jiang, J. Yu and J. Yu, "Assessment of Performance of Turbulence Models of CFX in Predicting Supercritical Water Heat Transfer in a Vertical Tube," in *15th International Topical Meeting on Nuclear Reactor Thermal-Hydraulics (NURETH-15)*, Pisa, Italy, 2013.
- [2] Editor: I.L. Piro, *Handbook of Generation IV Nuclear Reactors*, Duxford, UK: Elsevier - Woodhead Publishing (WP), 2016, p. 940.
- [3] O. Zikanov, *Essential Computational Fluid Dynamics*, Wiley & Sons. Books, 2010.
- [4] I. Piro and R. Duffey, *Heat Transfer and Hydraulic Resistance at Supercritical Pressure in Power-Engineering Application*, New York, NY: ASME, 2007.
- [5] OECD Nuclear Energy Agency, "Technology Roadmap Update for Generation IV Nuclear Energy Systems," 2014.
- [6] B. A. Gabaraev, Y. N. Kuznetsov, I. L. Piro and R. B. Duffey, "Experimental Study on Heat Transfer to Supercritical Water Flowing in 6-m Long Vertical Tubes," in *International Conference on Nuclear Engineering (ICONE-15)*, Nagoya, Japan, 2007.
- [7] B. Shiralkar and P. Griffith, "The Deterioration in Heat Transfer to Fluids at Supercritical Pressure and High Heat Fluxes," Cambridge, 1968.
- [8] H. Zahlan, D. C. Groeneveld and S. Tavoularis, "Look-up Table for Trans-Critical Heat Transfer," in *The 2nd Canada-China Joint Workshop on Supercritical Water Cooled Reactors (CCSC 2010)*, Toronto, ON, Canada, 2010.
- [9] W. Ambrosini, "Continuing Assessment of System and CFD Codes for Heat Transfer and Stability in Supercritical Fluids," in *4th International Symposium on Supercritical Water-Cooled Reactors*, Heidelberg, Germany, 2009.
- [10] X. Cheng, T. Schulenberg, S. Koshizuka, Y. Oka and A. Souyri, "Thermal-hydraulic Analysis of Supercritical Pressures Light Water Reactors," in *Proceedings of ICAPP*, Hollywood, FL, USA, 2002.
- [11] B. V. Dyadyakin and A. S. Popov, "Heat Transfer and Thermal Resistance of Tight Seven-rod Bundle, Cooled with Water Flowing at Supercritical Pressures," *Transactions of VTI*, vol. 11, pp. 244-253, 1977.

- [12] A. Bishop, R. Sandberg and L. Tong, "Forced convection heat transfer to water at near-critical temperatures and super-critical pressures," Pittsburgh, USA, 1964.
- [13] S. Mokry, "Development of a Heat-Transfer Correlation for Supercritical Water in Supercritical Water-Cooled Reactor Applications," University of Ontario Institute of Technology, Oshawa, Canada, 2009.
- [14] H. Swenson, J. Carver and C. Kakarala, "Heat transfer to supercritical water in smooth-bore tubes," *Journal of Heat Transfer*, vol. 87 (4), 1965.
- [15] D. Wilcox, *Turbulence Modeling for CFD*, 3rd ed., La Canada: DCW Industries, 2006.
- [16] S. J. Kline, W. C. Reynolds, F. A. Schraub and P. W. Runstadler, "The Structure of Turbulent Boundary Layers," *J. Fluid Mech*, vol. 30, no. 4, pp. 741-773, 1967.
- [17] Ansys, Inc., "ANSYS FLUENT 12.0 User's Guide," 2009.
- [18] B. E. Launder and W. P. Jones, "The Calculation of Low Reynolds Number Phenomena with a Two-Equation Model of Turbulence," *Int.l J. Heat and Mass Transfer*, vol. 16, no. 6, pp. 1119-1130, 1973.
- [19] D. Wilcox, "Simulation of Transition with a Two-Equation Turbulence Model.," *AIAA Journal*, vol. 32, no. 2, pp. 247-255, 1994.
- [20] F. Menter, "Two-Equation Eddy-Viscosity Turbulence Models for Engineering Applications," *AIAA Journal*, vol. 32, pp. 1598-1605, 1994.
- [21] P. Bradshaw, "The Understanding and Prediction of Turbulent Flow," *Aeronautical Journal*, vol. 76, pp. 403-418, 1971.
- [22] M. B. Sharabi, W. Ambrosini, N. Forgiione and S. He, "Prediction of Experimental Data on Heat Transfer to Supercritical Water with Two-Equation Turbulence Models," in *3rd Int. Symposium on SCWR - Design and Technology*, Shanghai, 2007.
- [23] M. B. Sharabi, "CFD Analyses of Heat Transfer and Flow Instability Phenomena Relevant to Fuel Bundles in Supercritical Water Reactors," in *Tesi di Dottorato di Ricerca in Sicurezza Nucleare Industriale*, Anno, 2008.
- [24] E. N. Pis'menny, V. G. Razumovskiy, A. E. Maevskiy and I. L. Pioro, "Heat Transfer to Supercritical Water in Gaseous State or Affected by Mixed Convection in Vertical Tubes," in *ICONE-14*, Miami, USA, 2006.

- [25] H. Y. Gu, X. Cheng and Y. H. Yang, "CFD Study of Heat Transfer Deterioration Phenomenon in Supercritical Water Through Vertical Tube," in *4th International Symposium on Supercritical Water-Cooled Reactors*, Heidelberg, 2009.
- [26] S. M. Salim and S. C. Cheah, "Wall y^+ Strategy for Dealing with Wall-bounded Turbulent Flows," in *International MultiConference of Engineers and Computer Scientists*, Hong Kong, 2009.
- [27] LEAP Australia, "Turbulence Part 3 - Selection of wall functions and Y^+ to best capture the Turbulent Boundary Layer," April 2013. [Online]. Available: <http://www.computationalfluidynamics.com.au/turbulence-part-3-selection-of-wall-functions-and-y-to-best-capture-the-turbulent-boundary-layer/>.
- [28] ANSYS, Inc., "ANSYS FLUENT 12.1 in Workbench User's Guide," 2009.
- [29] J. Crimaldi, J. Koseff and S. Monismith, "A Mixing-length Formulation for the Turbulent Prandtl Number in Wall-bounded Flows with Bed Roughness and Elevated Scalar Sources," *Physics of Fluids*, vol. 18, p. 9 pages, 2006.
- [30] B. Weigand, J. R. Ferguson and M. E. Crawford, "An Extended Kays and Crawford Turbulent Prandtl Number Model," *International Journal of Heat and Mass Transfer*, vol. 40, no. 17, pp. 4191-4196, 1997.
- [31] M. Mohseni and M. Bazargan, "Effect of Turbulent Prandtl Number on Convective Heat Transfer to Turbulent Flow of a Supercritical Fluid in a Vertical Round Tube," *Journal of Heat Transfer*, vol. 133, p. 10 pages, 2011.
- [32] M. Jaromin and H. Anglart, "A Numerical Study of the Turbulent Prandtl Number Impact on Heat Transfer to Supercritical Water Flowing Upward Under Deteriorated Conditions," in *Proceedings of the 15th International Topical Meeting on Nuclear Reactor Thermalhydraulics (NURETH-15)*, Pisa, Italy, 2013.
- [33] W. Kays, *Turbulent Prandtl Number - Where Are We?*, 1992.
- [34] F. Chen, X. Huai, J. Cai, X. Li and R. Meng, "Investigation on the applicability of turbulent-Prandtl-number models for liquid lead-bismuth eutectic," *Nuclear Engineering and Design*, vol. 257, pp. 128-133, April 2013.
- [35] C.-L. Liu, H.-R. Zhu and J.-T. Bai, "Effect of turbulent Prandtl number on the computation of film-cooling effectiveness," *International Journal of Heat and Mass Transfer*, vol. 51, no. 25-26, pp. 6208-6218, 2008.

- [36] D. M. McEligot and M. F. Taylor, "The turbulent Prandtl number in the near-wall region for low-Prandtl-number gas mixtures," *International Journal of Heat and Mass Transfer*, vol. 39, no. 6, pp. 1287-1295, 1996.
- [37] A. j. Reynolds, "The prediction of turbulent Prandtl and Schmidt numbers," *International Journal of Heat and Mass Transfer*, vol. 18, no. 9, pp. 1055-1069, 1975.
- [38] S. P. Mahulikar and H. Herwig, "Fluid friction in incompressible laminar convection: Reynolds' analogy revisited for variable fluid properties," *European Physics Journal B*, vol. 62, no. 1, pp. 77-86, March 2008.
- [39] B. Weigand, J. R. Ferguson and M. E. Crawford, "An extended Kays and Crawford turbulent Prandtl number model," *International Journal of Heat and Mass Transfer*, vol. 40, no. 17, pp. 4191-4196, 1997.
- [40] M. Jaromin and H. Anglart, "A Numerical Study of the Turbulent Prandtl Number Impact on Heat Transfer to Supercritical Water Flowing Upward Under Deteriorated Conditions," in *The 15th International Topical Meeting on Nuclear Reactor Thermalhydraulics, NURETH-15, Pisa, Italy, 2013*.
- [41] G. Tang, H. Shi, Y. Wu, J. Lu, Z. Li, L. Qing and H. Zhang, "A Variable Turbulent Prandtl Number Model for Simulating Supercritical Pressure CO₂ Heat Transfer," *International Journal of Heat and Mass Transfer*, vol. 12, pp. 1082-1092, 2016.
- [42] Y. Y. Bae, "A New Formulation of Variable Turbulent Prandtl Number for Heat Transfer to Supercritical Fluids," *International Journal of Heat and Mass Transfer*, vol. 92, pp. 792-806, 2016.
- [43] M. Mohseni and M. Bazargan, "A New Correlation for the Turbulent Prandtl Number in Upward Rounded Tubes in Supercritical Fluid Flows," *Journal of Heat Transfer*, vol. 138, p. 9 pages, 2016.
- [44] H. K. Versteeg and W. Malalasekera, *An Introduction to Computational Fluid Dynamics: The Finite Volume Method*, New York: Longman Scientific & Technical, 1995.
- [45] R. Eymard, T. Gallouet and R. Herbin, *Handbook of Numerical Analysis: Finite Volume Methods*, vol 7, pp713-1020 ed., 2006.
- [46] J. H. Bae and J. H. Park, "The effect of a CANDU fuel bundle geometry variation on thermalhydraulic performance," *Annals of Nuclear Energy*, vol. 38, pp. 1891-1899, 2011.

- [47] I. Idelchik, *Handbook of Hydraulic Resistance*, 3rd Ed.: CRC Press, 1994.
- [48] G. L. Brooks, "CANDU Origins and Evolution - Part 3 of 5: "Figure of 8" Heat Transport System Arrangement," AECL, 2001.
- [49] M. Yetisir, M. Gaudet and D. Rhodes, "Development and Integration of Canadian SCWR Concept with Counter-Flow Fuel Assembly," in *The 6th International Symposium on Supercritical Water-Cooled Reactors*, Shenzhen, Guangdong, China, 2013.
- [50] J. Saunders, "CFD Examination of Flow Effects Around a CANFLEX Fuel Bundle in Adiabatic Supercritical Conditions," University of Ontario Institute of Technology, Oshawa, ON., 2011.
- [51] M. Sharabi, W. Ambrosini, N. Forgione and S. He, "SCWR Rod Bundle Thermal Analysis by a CFD Code," in *Proceedings of the 16th International Conference on Nuclear Engineering*, Orlando, Florida, USA, 2008.
- [52] A. Zaretsky, "Simulation of Intersubchannel Mixing in a Triangular Nuclear Fuel Bundle Geometry," McMaster University, Hamilton, Ontario, Canada, 2014.
- [53] P. Kirillov, R. Pometko, A. Smirnov, V. Grabezhaia, I. Pioro, R. Duffey and H. Khartabil, "Experimental study on heat transfer in supercritical water flowing in 1- and 4-m-long vertical tubes," in *Proceedings of GLOBAL'05*, Tsukuba, Japan, 2005.
- [54] A. N. Dominguez, N. Onder, Y. Rao and L. Leung, "Evolution of the Canadian SCWR Fuel-Assembly Concept and Assessment of the 64 Element Assembly for Thermohydraulic Performance," *CNL Nuclear Review*, vol. 5, no. 2, p. 18 pages, 2016.
- [55] F. P. Incropera, D. P. DeWitt, T. L. Bergman and A. S. Lavine, *Fundamentals of Heat and Mass Transfer*, 6th ed., New York, NY: J. Wiley & Sons, 2007.
- [56] V. G. Razumovskiy, E. N. Pis'mennyi, K. Sidawi, I. L. Pioro and A. E. Koloskov, "Experimental Heat Transfer in an Annular Channel and 3-Rod Bundle Cooled with Upward Flow of Supercritical Water," *Journal of Nuclear Engineering and Radiation Science*, vol. 2, p. 8 pages, 2015.
- [57] A. I. C. Hunter, R. G. Nyquist, S. Coller, J. Smith and H. Boice, "Orifice Flow Calculation: Comparison Between Fluid Meter Applications - 6th Edition 1971, ASME PTC 19.5-2004 and ISO 5167 2003," in *Proceedings of the ASME Power Conference - POWER2013*, Boston, Massachusetts, USA, 2013.

- [58] T. Shih, W. W. Liou, A. Shabbir and J. Zhu, "A New k- ϵ Eddy-Viscosity Model for High Reynolds Number Turbulent Flows - Model Development and Validation," *Computers & Fluids*, vol. 24, no. 3, pp. 227-238, 1995.
- [59] National Institute of Standards and Technology (NIST), "NIST Standard Reference Database 23: Reference Fluid Thermodynamic and Transport Properties," 2009.
- [60] A. Farah, "Assessment of FLUENT CFD Code as an Analysis Tool for SCW Applications," University of Ontario Institute of Technology, Oshawa, ON., Canada, 2012, Masters Thesis.
- [61] A. Farah, G. Harvel and I. Piro, "Analysis of CFD Code FLUENT Capabilities for Supercritical Water Heat Transfer Applications in Vertical Bare Tubes," *ASME Nuclear Engineering and Radiation Science Journal*, vol. 2, no. 3, 2016.
- [62] ANSYS, Inc., "ANSYS Fluid Dynamics Verification Manual," Canonsburg, PA, USA, 2013.
- [63] D. E. Kim and M.-H. Kim, "Experimental Investigation of Heat Transfer in Vertical Upward and Downward Supercritical CO₂ Flow in a Circular Tube," *International Journal of Heat and Fluid Flow*, vol. 32, pp. 176-191, 2011.
- [64] C. Zhang, G. Xu, L. Gao, Z. Tao, H. Deng and K. Zhu, "Experimental Investigation on Heat Transfer of a Specific Fuel (RP-3) Flows Through Downward Tubes at Supercritical Pressure," *Journal of Supercritical Fluids*, vol. 72, pp. 90-99, 2012.
- [65] S. Pidaparti, J. McFarland, M. Mikhaeil, M. Anderson and D. Ranjan, "Investigation of Buoyancy Effects on Heat Transfer Characteristics of Supercritical Carbon Dioxide in Heating Mode," *Journal of Nuclear Engineering and Radiation Science*, vol. 1, p. 10, 2015.
- [66] A. L. Snijders, A. M. Koppius and C. Nieuwvelt, "An Experimental Determination of the Turbulent Prandtl Number in the Inner Boundary Layer for Air Flow Over a Flat Plate," *International Journal of Heat and Mass Transfer*, vol. 26, no. 3, pp. 425-431, 1983.
- [67] K. Bremhorst, "Experimentally Determined Turbulent Prandtl Numbers in Liquid Sodium at Low Reynolds Numbers," *International Journal of Heat and Mass Transfer*, vol. 35, no. 2, pp. 351-359, 1992.

- [68] T. Wang, "Experimental Investigation of Turbulent Prandtl Number and Reynolds Analogy in Transitional and Post-Transitional Boundary Layers," Clemson University, Clemson, South Carolina, 1993.
- [69] K. Sakurai, K. Okamoto and H. Madarame, "Visualization Study on Forced Convection Heat Transfer of Super Critical Carbon Dioxide," *Transactions of the Atomic Energy Society of Japan*, vol. 3, no. 1, pp. 34-43, 2004.
- [70] H. Ushifusa, K. Inaba, K. Sugawara, K. Takahashi and K. Kishimoto, "Measurement and Visualization of Supercritical CO₂ in Dynamic Phase Transition," *EPJ Web of Conferences*, vol. 92, p. 6 pages, 2015.

Appendix A: Summary of Publications and Awards

Relevant Publications

34 publications in total: 3 papers in refereed journals, 28 papers in refereed proceedings of international and national conferences and symposiums (12 as a main author), and 3 technical reports.

- Farah, A., Harvel, G., and Pioro, I., 2016. Analysis of CFD Code FLUENT Capabilities for Supercritical Water Heat Transfer Applications in Vertical Bare Tubes, ASME Nuclear Engineering and Radiation Science Journal, Vol. 2, Issue #3.
- Farah, A., Harvel, G., and Pioro, I., 2015. Numerical Assessment and Comparison of Heat Transfer Characteristics of Supercritical Water in Bare Tubes and Tubes with Heat Transfer Enhancing Appendages, Proceedings of the 23rd International Conference on Nuclear Engineering (ICONE-23), May 17 - 21, Chiba, Japan. Best Poster Award
- Farah, A., Harvel, G. and Pioro, I., 2013. Assessment of Fluent Code as a Tool for SCW Heat Transfer Analysis, Proceedings of the 21st International Conference on Nuclear Engineering (ICONE-21), July 29 - August 2, Chengdu, China, Paper #16446, 9 pages.
- Farah, A., Harvel, G. and Pioro, I., 2013. Assessment of Fluent CFD Code as an Analysis Tool for Supercritical-Water Heat-Transfer Applications, Proceedings of the 15th International Topical Meeting on Nuclear Reactor Thermalhydraulics (NURETH-15), Pisa, Italy, May 12 - 15, Paper #118, 13 pages.
- Farah, A., Haines, P., Harvel, G. and Pioro, I., 2013. CFD Analysis of Radial Profiles for Supercritical Water Properties in a Vertical Bare Tube, Proceedings of the 6th International Symposium on Supercritical Water-Cooled Reactors (ISSCWR-6), Shenzhen, Guangdong, China, March 3 - 7, 15 pages.

Awards, Scholarships and Research Grants

- 2016 Canadian Nuclear Society R.E. Jervis Award for outstanding academic accomplishments in nuclear science and technology.
- Best Poster Award, 23rd International Conference on Nuclear Engineering (ICONE-23), Chiba, Japan, (**Farah, A.**, Harvel, G., and Piro, I., 2015. Numerical Assessment and Comparison of Heat Transfer Characteristics of Supercritical Water in Bare Tubes and Tubes with Heat Transfer Enhancing Appendages).
- Akiyama Medal (Award by Japan SME), Awarded to the best overall paper, poster and presentation in the Student Track during the 22nd International Conference on Nuclear Engineering (ICONE-22), Prague, Czech Republic, (Miletic, M., Peiman, W., **Farah, A.**, Samuel, J., and Dragunov, A., 2014. Study on Neutronics and Thermalhydraulics Characteristics of Supercritical Water-cooled Reactors (SCWR)).
- Ph.D. Level Best Paper/Presentation Award, 38th CNS/CAN Student Conference (At the 19th Annual Pacific Basin Nuclear Conference: PBNC-2014), Vancouver, British Columbia, 2014. (**Amjad Farah**, 2014. Life Cycle Assessment for GHG Emissions from an Eskom Pebble Bed Type Modular Reactor).
- Certificate of Appreciation to **Amjad Farah** from the 15th International Topical Meeting on Nuclear Reactor Thermal Hydraulics (NURETH-15), Pisa, Italy, 2013.
- NSERC Postgraduate Scholarship 2013 - Doctoral (PGS D), for 3 years of Ph.D.
- Ontario Graduate Scholarship (OGS), 2012.
- International Atomic Energy Agency (IAEA) Research Agreement #18417 (Coordinated Research Project (CRP) #I31025) "Understanding and Prediction of Thermal-Hydraulics Phenomena Relevant to Supercritical Water-Cooled Reactors (SCWRs)" 2014-2017.
- NSERC Discovery Grants "Advanced Study on Supercritical Fluids in Innovative Technologies Application" 2012-2017.

Appendix B: Bare Tube Results – NHT, RKE Model

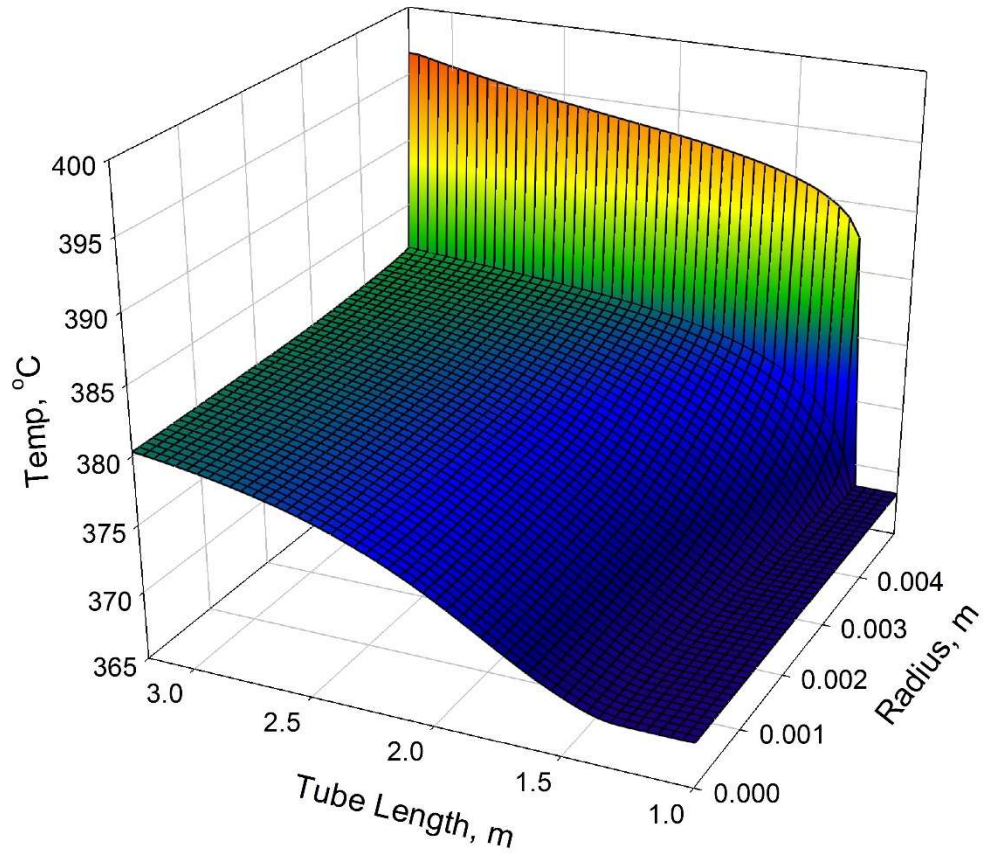


Figure B-1: 3D Temperature plot for a case with: $P = 24$ MPa, $G = 1002$ kg/m²s, and $q = 391$ kW/m², using the RKE model

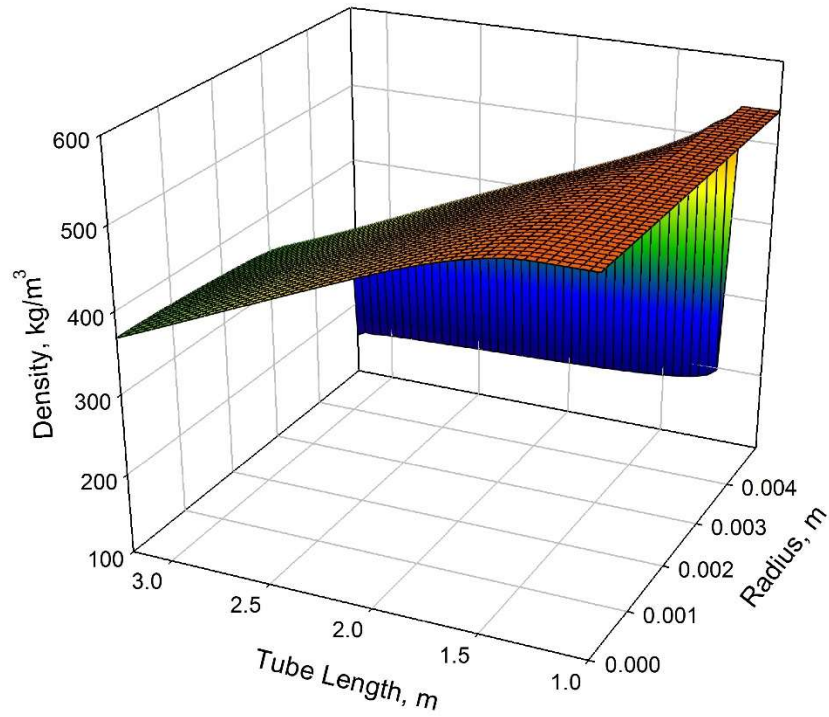


Figure B-2: 3D Density plot for a case with: $P = 24$ MPa, $G = 1002$ kg/m²s, and $q = 391$ kW/m², using the RKE model

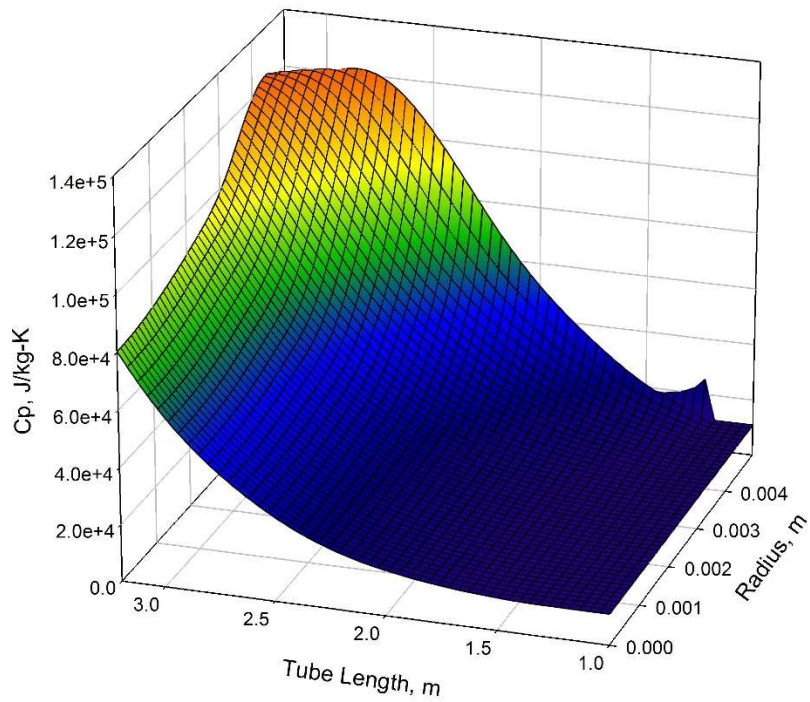


Figure B-3: 3D Specific heat plot for a case with: $P = 24$ MPa, $G = 1002$ kg/m²s, and $q = 391$ kW/m², using the RKE model

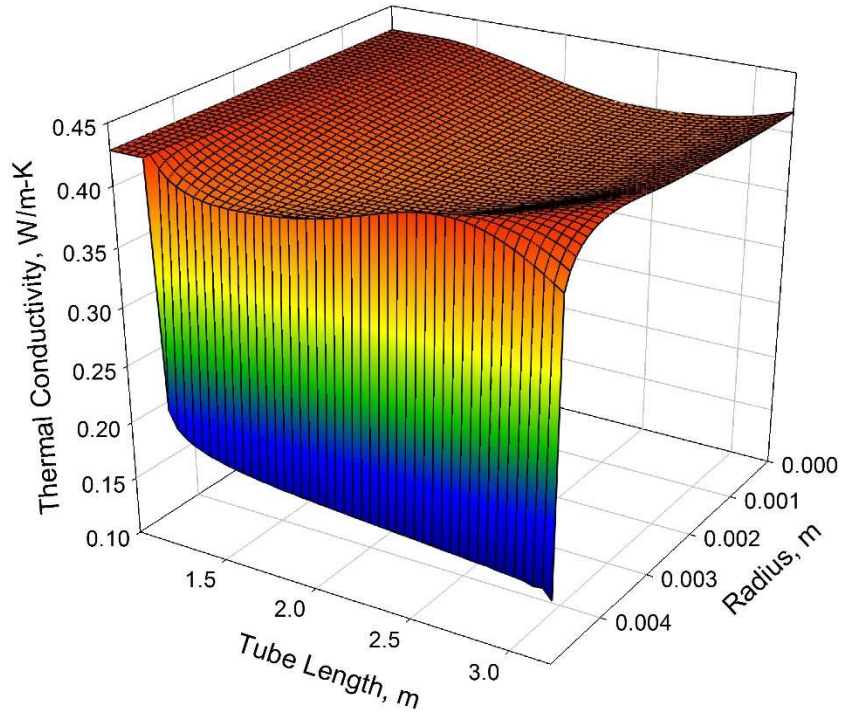


Figure B-4: 3D Thermal conductivity plot for a case with: $P = 24$ MPa, $G = 1002$ kg/m²s, and $q = 391$ kW/m², using the RKE model

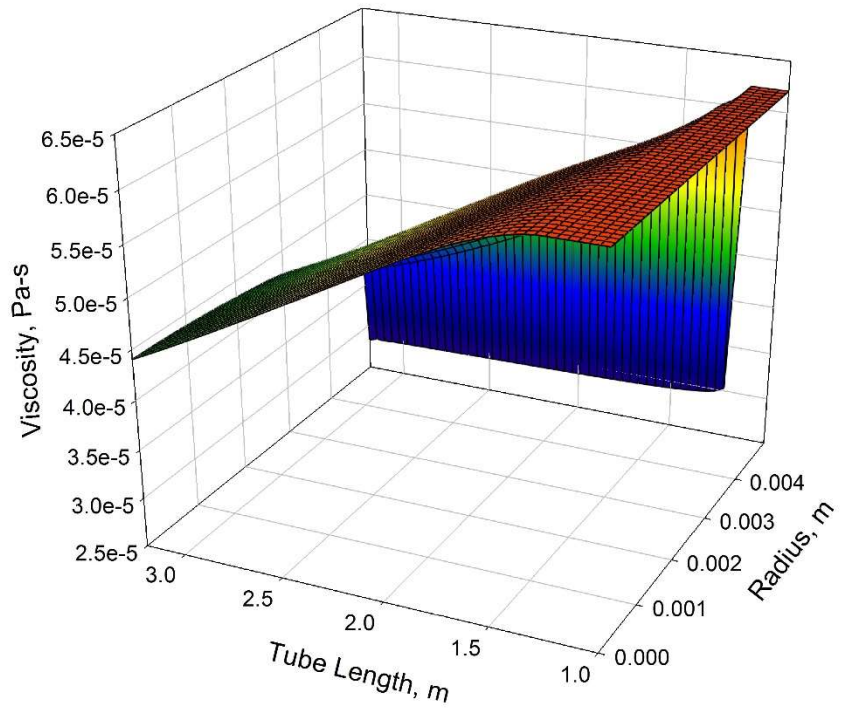


Figure B-5: 3D Viscosity plot for a case with: $P = 24$ MPa, $G = 1002$ kg/m²s, and $q = 391$ kW/m², using the RKE model

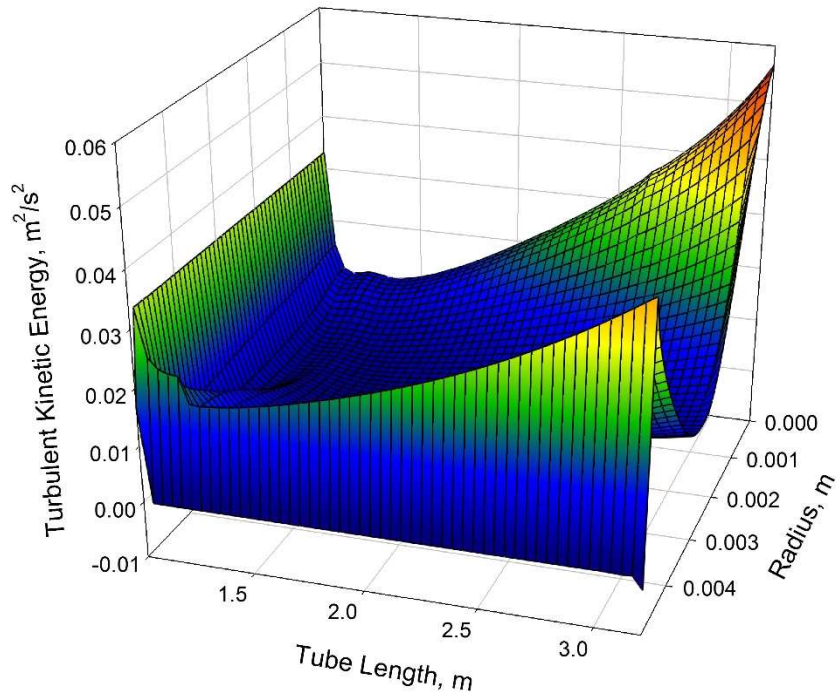


Figure B-6: 3D Turbulence kinetic energy plot for a case with: $P = 24$ MPa, $G = 1002$ kg/m²s, and $q = 391$ kW/m², using the RKE model

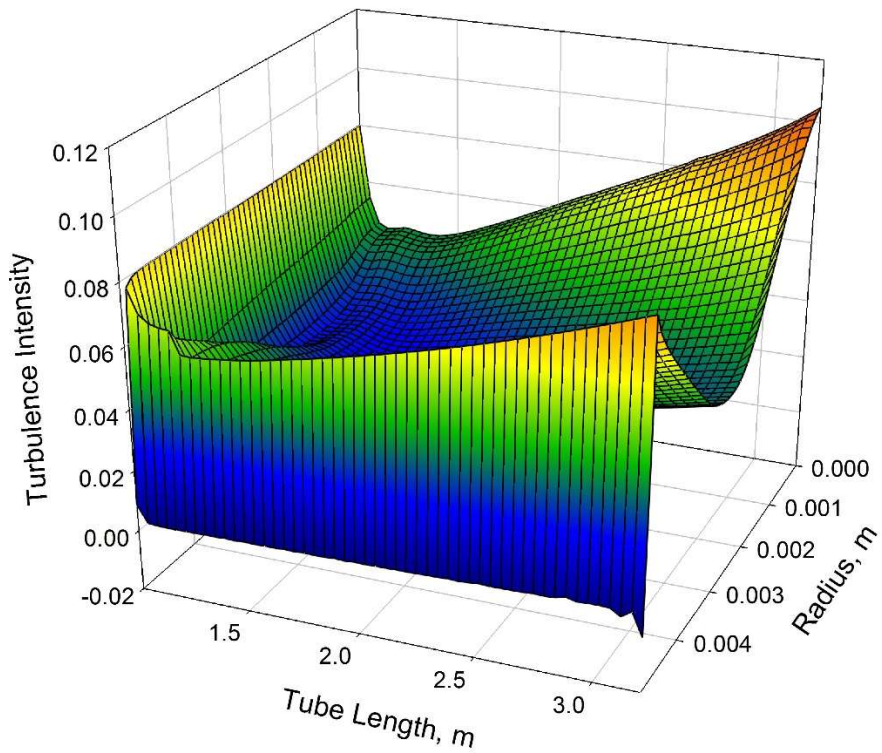


Figure B-7: 3D Turbulence intensity plot for a case with: $P = 24$ MPa, $G = 1002$ kg/m²s, and $q = 391$ kW/m², using the RKE model

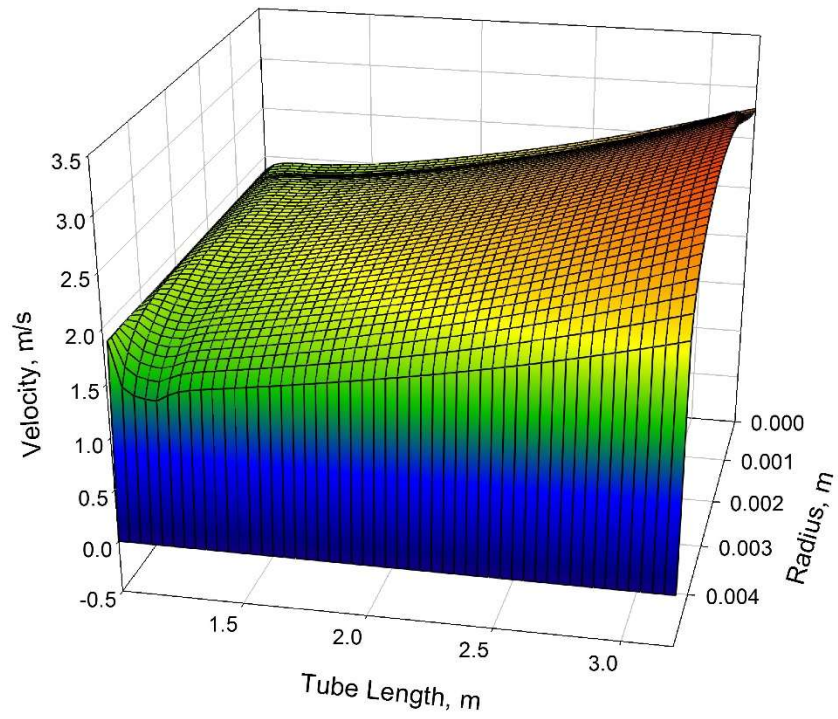


Figure B-8: 3D Velocity plot for a case with: $P = 24$ MPa, $G = 1002$ kg/m²s, and $q = 391$ kW/m², using the RKE model

Appendix C: Turbulent Pr number variations for RKE and SST

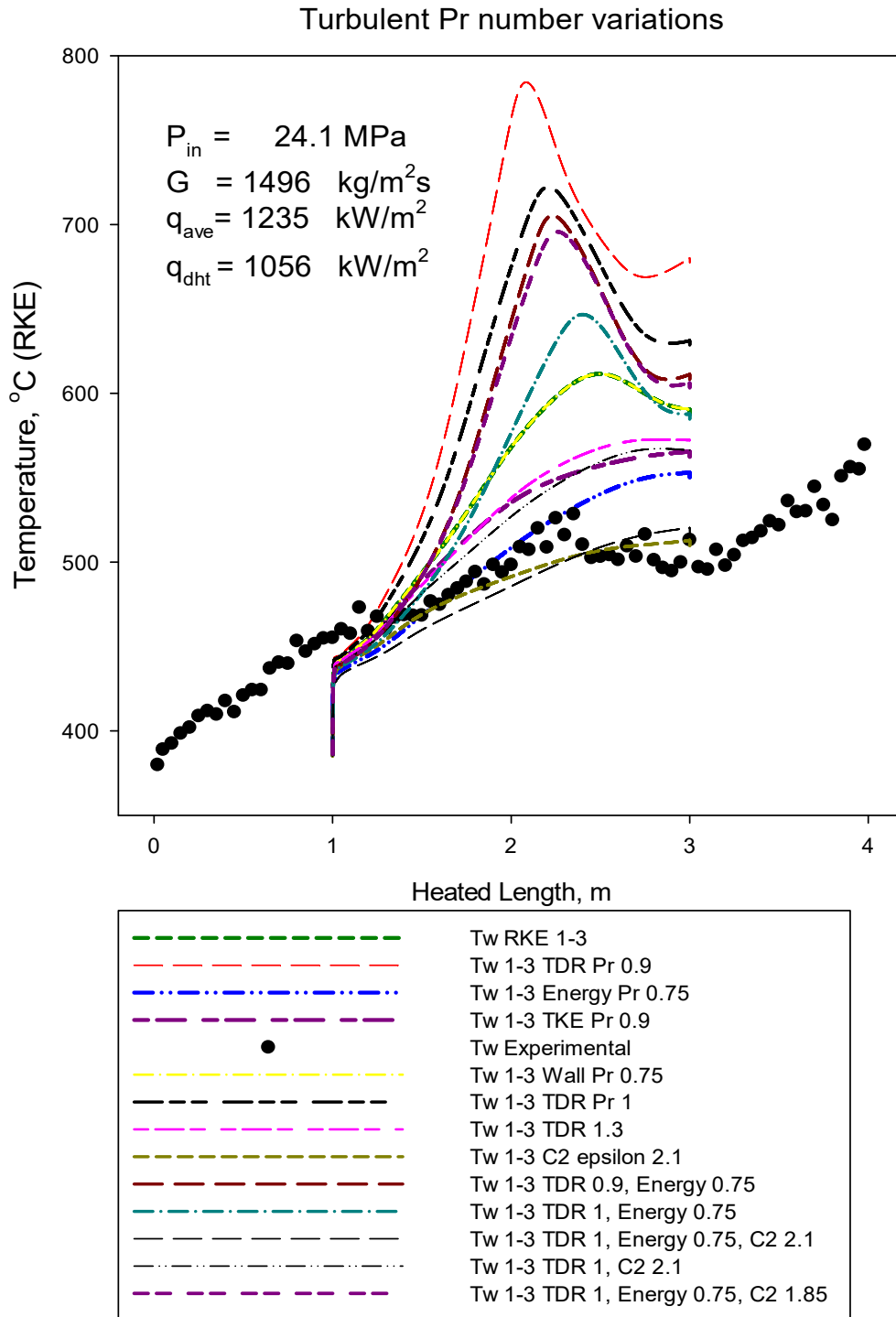


Figure C-1: Effect of Turbulent Pr Number on Wall Temperature Profiles for RKE Model

Turbulent Pr number variations

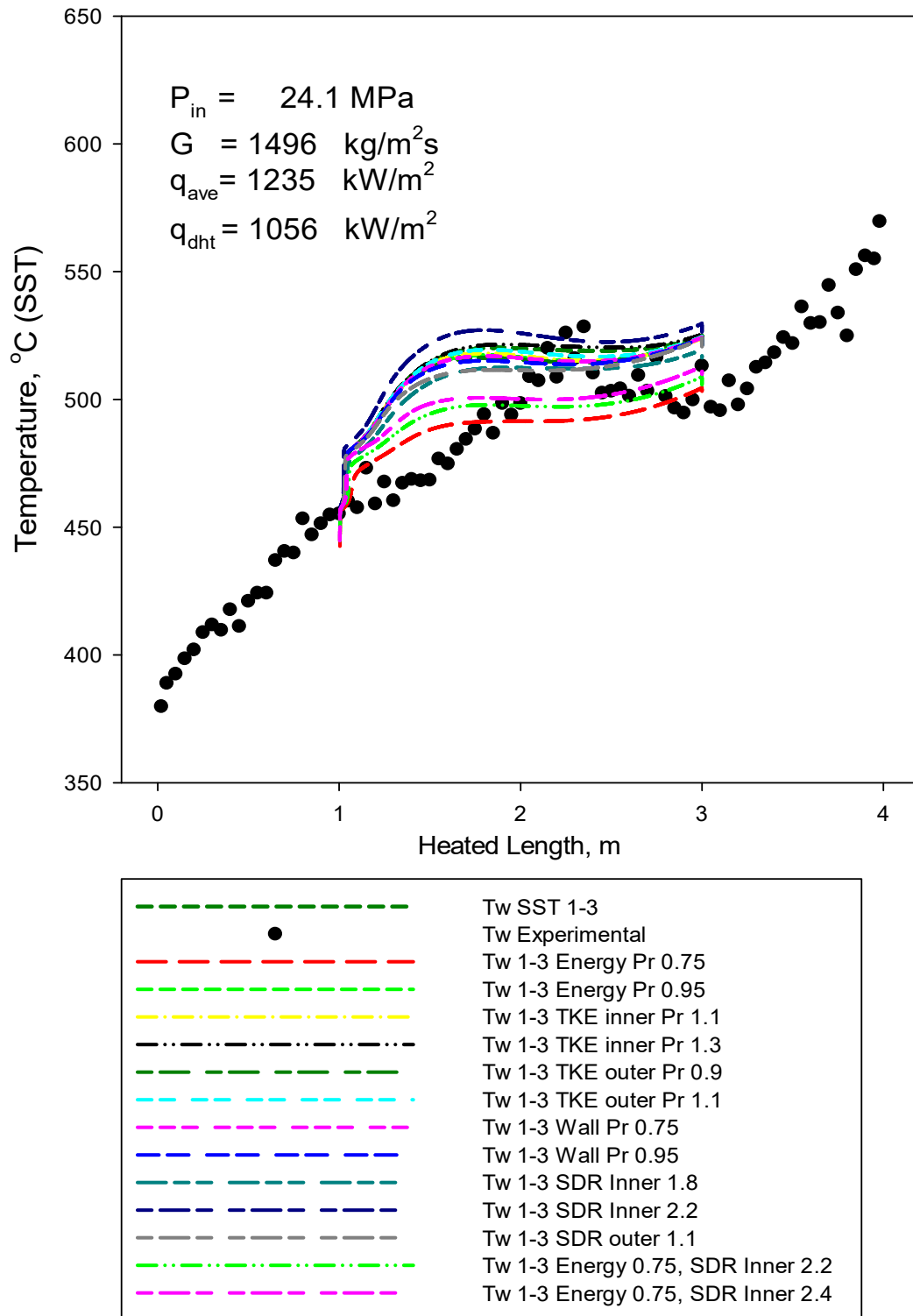


Figure C-2: Effect of Turbulent Pr Number on Wall Temperature Profiles for SST Model

Appendix D: Axial locations of thermocouples in the helically finned annular flow channel



Figure D-1: Cut planes illustrating the axial locations of thermocouples in the helically finned annular flow channel